University of Nevada, Reno

Application of a new method to measure particulate matter concentrations and chemistry to better understand sources of atmospheric pollution to Nevada and the Western United States

A dissertation submitted in partial fulfillment of the requirements for the degree of Doctor of Philosophy in Environmental Sciences

By

Ashley M. Pierce

Dr. Mae Sexauer Gustin/Dissertation Advisor

December 2017

THE GRADUATE SCHOOL

We recommend that the dissertation
prepared under our supervision by

ASHLEY M. PIERCE

Entitled

Application Of A New Method To Measure Particulate Matter Concentrations And Chemistry To Better Understand Sources Of Atmospheric Pollution To Nevada And The Western United States

be accepted in partial fulfillment of the
requirements for the degree of

DOCTOR OF PHILOSOPHY

Mae Sexauer Gustin, Advisor

John N. Christensen, Committee Member

Heather A. Holmes, Committee Member

Richard VanCuren, Committee Member

W. Patrick Arnott, Graduate School Representative

David W. Zeh, Ph. D., Dean, Graduate School

December, 2017

Abstract

The Nevada Rural Ozone Initiative (NVROI) was a project undertaken to understand the spatial and temporal trends of atmospheric ozone (O_3) concentrations and to identify sources of O_3 to rural Nevada. Concentrations at multiple NVROI locations were observed to approach or exceed the current National Ambient Air Quality Standard (NAAQS) for O_3 of 70 ppbv. A need for additional measurements, such as lead isotopes, to aid in identifying the sources of regional and global air masses intercepted in rural Nevada, was identified by the initial findings of the NVROI. To address this need, a method was developed using a Teledyne Advanced Pollution Instrumentation model 602 Beta^{Plus} particulate monitor, to quantify particulate matter < 2.5 µm in aerodynamic diameter ($PM_{2.5}$), on two filter materials that allowed for post-processing of the filter samples for reactive mercury concentrations and lead isotopic ratios. A suite of measurements, including criteria air pollutants, meteorological data, aerosol optical properties, data collected from monitoring agencies, and statistical and back trajectory analyses were also used.

Measurements of reactive mercury indicated that the filters were useful for understanding trends in atmospheric concentrations, but that more research on surface chemistry is needed. Analysis of the lead isotopic data and the results of the statistical and back trajectory analyses indicated that trans-Pacific input of atmospheric pollutants occurred spring through fall of both sample years (2014 and 2015) and was a major source of atmospheric pollutants to Nevada. Reactive mercury was likely removed from air masses due to deposition or conversion to elemental mercury before reaching the sample sites and formation was facilitated by regional sources of oxidants. Other sources

of atmospheric pollutants to Nevada included local and regional urban centers, regional and global wildfires, and subsidence of pollutants aloft. Anomalous particles observed at one high elevation sample site were attributed to corrosion of the sample line tubing during prolonged, high wind events. This research developed a novel method for tracing sources of pollution to aid in understanding the sources, source regions, and physical processes affecting air pollution in the complex terrain of Nevada, USA.

Acknowledgements

I would like to thank my adviser, Dr. Mae Gustin for offering me the opportunity to work on this project. Her commitment to ensuring that I would be able to graduate despite multiple setbacks and challenges with this project was essential to getting me to this point. I would also like to thank my committee members, Dr. Patrick Arnott, Dr. John Christensen, Dr. Heather Holmes, and Dr. Tony VanCuren for their contributions to my academic growth during this project. Thank you particularly to Dr. Arnott for the knowledge he contributed to the fifth chapter, to Dr. Christensen for allowing me to work in his lab at Lawrence Berkeley National Laboratory for several months, to Dr. Holmes for the extensive knowledge she contributed to chapter 4, and to Dr. VanCuren for the use of the rotating drum impactors and help processing the data even though it did not get used and for the knowledge he contributed to the introduction.

Thank you to Dr. Grant Edwards for support and for providing the opportunity to process samples at the Macquarie University Microscopy Laboratory for chapter 5. Thank you also to Sue Lindsay, microscopy unit manager, and to Katrina Macsween for her help running the samples. Thank you to Dr. Rebekka Fine for her initial research on this project and guidance as I was starting. Thank you to Marcela Loría-Salazar for her contributions to chapters 3, 4, and 5 and for all of her support throughout. Thank you to KC King for support and knowledge on various subjects that helped me improve my data processing skills. Thank you also to Dr. Seth Lyman, Dr. Jiaoyan Huang, Dr. Shaun Brown, Dr. Sunni Ivey, Jayne Boehmler and the Gustin Hg group, Matthew Peckham, Jennifer Arnold, Adriel Luippold, and various undergraduates for help during many parts of this research. Thank you to Dr. Christopher Moore and Dr. Daniel Obrist for their

continued support and knowledge. Thank you also to Lauren Every-Wortman, Margaret Mays, my Tang housemates, and my friends in Reno who always support me even when I am too busy with school to be around.

I would like to thank my parents, Frances and Herbert, and my sister, Terra, for always supporting and believing in me. Thank you also to Christopher and Suzanne Pierce for letting me live with them for several months while I analyzed samples. Thank you to Matthieu Miller for his help with setting up and maintaining sample sites, data collection and processing, and for the personal support he provided. Finally, thank you to Bella for always making me smile.

Table of Contents

Chapter 1

Introduction

1. General overview

Air quality is affected by local, regional, and global gas and particulate emissions originating from anthropogenic, biogenic, and natural sources. Air quality degradation can negatively affect human and ecosystem health as well as visibility. Under the United States Environmental Protection Agency (U.S. EPA), states are required to monitor six criteria air pollutants that cause damage to public health and the environment: carbon monoxide (CO), lead (Pb), nitrogen dioxide (NO_2), ozone (O_3), particulate matter (PM; $PM_{2.5}$ and PM_{10}), and sulfur dioxide (SO_2). The Office of Air Quality Planning and Standards (OAQPS) of the U.S. EPA sets National Ambient Air Quality Standards (NAAQS) for the six criteria air pollutants. These include primary standards meant to protect public health, and secondary standards meant to protect public welfare, including animals, crops, vegetation, and built structures

The 1990-amended Clean Air Act requires a network of air monitoring stations in every state using criteria set by the OAQPS. These stations are called the State and Local Air Monitoring Stations (SLAMS) and report an annual summary of monitoring results to the OAQPS. Certain methods, when operated as directed by the manual with quality assurance procedures, are designated by the U.S. EPA as Federal Reference Methods (FRM) or Federal Equivalent Methods (FEM). These methods, for measuring ambient concentrations of the criteria pollutants, are acceptable for use in state or local air quality monitoring systems (U.S. EPA, 2014).

Although air quality is generally monitored in areas of high population density, there are networks focused on measuring air pollution in non-urban areas. The Clean Air Act also requires that visibility in Class I areas be protected and improved. The Interagency Monitoring of PROtected Visual Environments (IMPROVE) network was started in 1985 to track changes in visibility. Class I areas include national parks and wilderness areas, and monitoring involves taking pictures of haze events and measuring extinction, concentration, and chemical composition of fine PM. There are three IMPROVE sites operating in Nevada: in the west at the Walker River Paiute Tribe site, in the east at Great Basin National Park, and in the north east corner in the Jarbidge Wilderness Area.

The Clean Air Status and Trends Network (CASTNET), started in 1991, is a long-term, national, air quality monitoring network that measures air pollutants in order to understand trends in air quality, atmospheric deposition, and ecological effects, to aid in evaluating the effectiveness of pollution control programs. There are more than 85 regional sites throughout the United States and Canada, located in areas with little influence from urban centers. All O_3 monitors in the network were brought into compliance with the Code of Federal Regulations (40 CFR) in 2011, and can therefore be used to determine if an area meets the NAAQS. There are two CASTNET sites in Nevada located in Great Basin National Park and in the Jarbidge Wilderness area.

If a geographic area consistently exceeds the NAAQS or causes another area to exceed the standards, it is considered a nonattainment area. Under the good neighbor provision of the Clean Air Act, if a neighboring state contributes >1% of the relevant NAAQS to a downwind site it is considered out of attainment (U.S. EPA, 2017d). These

areas must then develop a State Implementation Plan (SIP) as required under the amended Clean Air Act that outlines how the state will attain and maintain the standard (US EPA, 2013).

Development of the SIPs require considerable time and money, and can be significant burdens for states. If the state determines that a high concentration event of one of the six criteria pollutants is an exceptional event, it can be exempt from the SIP. An exceptional event is defined as an unusual or naturally occurring event that affects air quality, but is not reasonably controllable using current techniques for attaining the NAAQS (U.S. EPA, 2012a). In order to be exempt from the SIP, the state must supply evidence to the U.S. EPA demonstrating that the state would have been in compliance were it not for a circumstance outside of their ability to control, such as wildfires, stratospheric O_3 intrusions, volcanic and seismic activities, and non-routine international transport (U.S. EPA, 2017d).

In 2014 and 2015, a monitoring site in the U.S. EPA Air Quality System (U.S. EPA AQS) located in Reno, NV, USA was out of attainment for O_3 in 2014 and for $PM_{2.5}$ and PM_{10} in 2014 and 2015 (Washoe County, 2017). The exceedances are under review for exceptional events, mainly wildfires (EPA, 2017). Ozone measurements at Great Basin National Park (GBNP, elevation 2060 m asl), in eastern Nevada, and at three other rural sites in Nevada, have also exceeded the NAAQS for O_3 (Fine et al., 2015a). It is possible that other rural areas across Nevada and areas of other Western States will exceed the NAAQS despite the lack of sources in close proximity. Wildfires, intrusion of O_3 rich stratospheric air, regional urban pollutants, and emissions from other countries contribute to these exceedances (Fine et al., 2015a; Fine et al., 2015b; Lin et al., 2014a;

Miller et al., 2015; Musselman and Korfmacher, 2014). This has important implications for national and global policy making, as pollution attributed to wildfires, stratospheric intrusions, and foreign countries impact states and countries downwind but are not readily controllable by the state or country that is impacted (Lin et al., 2014a; Lin et al., 2012; Pierce et al., 2017). In addition, lack of data in many rural areas makes it difficult to understand the spatial and temporal variability of atmospheric pollutants.

To characterize the spatial and temporal trends in Nevada, and to identify source regions contributing to elevated O_3, the Nevada Rural Ozone Initiative (NVROI) was started in 2011. The NVROI project established 13 sites across Nevada at high elevations (>2000 m asl) and in valleys (<2000 m asl). Results from the project indicated that all rural NVROI sites experience O_3 concentrations approaching the NAAQS, particularly in the spring and early summer, and that as the NAAQS become more stringent, exceedances will increase (Fine et al., 2015a; Miller et al., 2015). O_3 concentrations in rural areas are well correlated with urban areas indicating that processes impacting concentrations across the state are similar, however, site to site variability can be high (Fine et al., 2015a). Long-term increases in O_3 trends at Great Basin National Park are attributable to long-range transport and not increases in regional emissions (Fine et al., 2015a). However, sources of O_3 for discreet events also included wildfires, stratosphere to troposphere exchange (STE), and regional emissions (Fine et al., 2015b; Miller et al., 2015). To aid in identifying the sources and source regions of air masses intercepted in the complex terrain of Nevada, multiple monitoring sites and a suite of trace gas and particulate measurements, supplemented by additional analyses for lead isotope and trace metal composition in atmospheric PM samples was suggested. Pollution sources are

difficult to monitor due to a lack of atmospheric boundaries, chemistry that can occur downwind of a source, and interactions with complex terrain. Determining metal and isotope concentrations of aerosols can facilitate identification of source areas especially when trying to understand a secondary air pollutant such as O_3 (see discussion below).

1.2 Conditions in the Western USA and Nevada affecting air quality

Air pollution in the Western USA is influenced by synoptic scale and mesoscale weather patterns and complex terrain. Pressure gradients cause air to move from high- to low-pressure, balanced by the Coriolis force, generating near-geostrophic winds, particularly in extratropical synoptic-scale disturbances (Holton and Hakim, 2013a; Wallace and Hobbs, 2006). Differential heating at the equator compared to the poles, along with the geostrophic winds, create distinct circulation cells, the Hadley, Ferrel, and Polar cells. In the Northern Hemisphere, winds in the troposphere associated with the Hadley cell travel upwards and east, due to the conservation of angular momentum and the Coriolis force, as air rises and moves from the tropics, poleward. As air cools and sinks at ~30° and moves towards the tropics, it is deflected to the west (trade winds) closer to the surface of the earth (Wallace and Hobbs, 2006). Air in the Ferrel cell, influenced by the Hadley and Polar cells, flows the opposite direction of the Hadley cell, creating the prevailing westerly winds in the mid-latitudes (~30° to 50° N, Holton and Hakim, 2013d). The subtropical jet stream occurs where the Hadley and Ferrel cells converge (~30°), while the polar jet stream occurs where the Ferrel and Polar cells converge (~60°). Jet streams can rapidly transport air in the free troposphere, from west to east (Wallace and Hobbs, 2006). When jet streams deviate toward or away from the

equator, Rossby waves form, with associated high- and low-pressure systems, on either side of a wave (Wallace and Hobbs, 2006). High-pressure systems can cause subsidence of air aloft, generally stable conditions, and a buildup of atmospheric pollutants. Storms associated with low-pressure systems can disperse or scavenge atmospheric pollutants (Wallace and Hobbs, 2006). Nevada can be impacted by the deviating subtropical and polar jet streams (Holton and Hakim, 2013c).

Gradient winds occur when the Coriolis force and the centrifugal force balance the horizontal pressure gradient force (Wallace and Hobbs, 2006). This causes gradient wind speeds in cyclonic flows to be less than the geostrophic wind speed and gradient wind speeds in anticyclonic flows to be greater than the geostrophic wind speed at a given location (Wallace and Hobbs, 2006). Actual wind speed is often better approximated by the gradient wind equation than by the geostrophic wind equation (Holton and Hakim, 2013b).

Mesoscale weather dynamics in Nevada include up/downslope and valley flows. Upslope, or anabatic, flows occur during the day, caused by differential heating of surface air compared to the free atmosphere (Roland, 2006). Downslope, or katabatic, flows occur at night as the air at the surface cools, becomes more dense, and sinks (Roland, 2006). Valley flows are related to the up- and downslope flows. Warming during the day causes air to flow up the valley, while cold air at night pools in the valley and drains down and out of the valley (Roland, 2006; Rotach and Zardi, 2007; Wagner et al., 2015). Airflow around mountains causes a variety of smaller scale phenomena such as flow separation, gap flow winds through mountain passes, acceleration of wind over mountain crests, blocking of low-altitude winds on the windward side, lee-side

circulations, cloud formation, rotors, wake turbulence, downslope windstorms, and hydraulic jumps (McMurdie and Houze, 2006).

Urban areas located in valleys of Nevada are often situated between north-south mountain ranges. Prevailing westerly winds are disrupted by the passage of fronts. As low-pressure systems move from west to east, the systems are lifted over the Sierra Nevada Mountains, causing the air mass to cool and water vapor to condense and precipitate out. As the air mass moves into Nevada, it sinks and warms, causing the rain shadow effect and dry conditions on the leeward side (WRCC, 2014a). Surface lows on the windward side of large mountain ranges may decay, while lee cyclogenesis will replace the surface low on the downwind side (McMurdie and Houze, 2006). The pressure gradient causes air to move towards the low and rise, causing horizontal transport of air from surrounding areas to replace the rising air. The north-south orientation of the mountain ranges and the cyclonic flow of the low-pressure system causes air from the south to be transported north as the low moves over a valley, potentially transporting air from central and southern California and southern Nevada (Fine et al., 2015a; Fine et al., 2015b; McMurdie and Houze, 2006). Westerly downslope flows and geostrophic wind circulating around the low cause these winds to be stronger than the winds on the north side of the low. On the north side of the low-pressure system cyclonic flow causes easterly winds, upslope flows and lifting or anticyclonic flows that are weaker than the flows on the southern edge of the low (McMurdie and Houze, 2006). With the passing of the low-pressure system and associated cold front, higher pressure occurs as cold air sinks behind the cold front, causing air from aloft to subside, potentially bringing pollutants aloft to the surface (Johnson and Viezee, 1981; Knowland

et al., 2015; Kunz and Speth, 1997; Viezee et al., 1983). Wind speeds are high as the front passes and are generally lower and shift from southerly to northerly as the system moves further east (McMurdie and Houze, 2006). These interactions affect airflow and atmospheric pollutants across Nevada.

All of these phenomena contribute to a planetary boundary layer height that varies widely day-to-night and season-to-season. The lower atmosphere, or troposphere (few hundred meters to 10-20 km) contains the planetary boundary layer (few hundred meters to ~2 km), in direct contact with the surface. The boundary layer grows during the day and is shallow at night, due to heating and cooling of air masses. The height of the boundary layer depends on location. In the free troposphere, above the planetary boundary layer, air movement is driven by geostrophic or gradient winds and transport is more rapid than in the planetary boundary layer, where friction affects air movement. At night, there is little convective mixing, and the daytime planetary boundary layer becomes a residual layer, the bottom of which gradually becomes the nocturnal stable boundary layer (Roland, 2006). As solar radiation warms the surface during the day, and air at the surface rises, convective mixing increases the planetary boundary layer height, and entrainment of air from the free troposphere can occur. Entrainment occurs when rising thermals and turbulent eddies from the mixed boundary layer rise through the capping inversion layer, before sinking back into the mixed boundary layer, causing free troposphere air to move down through the capping inversion (Roland, 2006). This input of free tropospheric air can be an important contributor to the composition of the atmosphere in the planetary boundary layer (Wagner et al., 2015; Weiss-Penzias et al., 2009).

Nevada is a large state with a total land area of 2.8 x 10^5 km^2 (WRCC, 2014b), a majority of which is federally owned. The State generally rises in average elevation from south and west to northeast and east, with a mean elevation of 1676 m asl. There are more than 200 named mountain ranges that generally run north-to-south. Nevada is characterized by high solar radiation, resulting in rapid surface heating, low annual precipitation, heavy snowfall in the mountains, relatively clean, dry air, and large ranges of low and high daily temperatures (WRCC, 2014b). The combination of rapid surface heating and complex terrain leads to convective mixing and varying planetary boundary layer heights. Convective mixing can mix pollutants up from valleys and can cause entrainment of free tropospheric air to mix down to valleys (Gustin et al., 2015; Pierce et al., 2017; Rotach and Zardi, 2007; Wagner et al., 2015).

2. Atmospheric pollutants of interest for this research

2.1 Ozone

Ozone is an oxidant that has positive and negative effects on terrestrial and aquatic life on Earth, dependent on its presence in different layers of the atmosphere. In the upper atmosphere, or stratosphere (10-50 km above Earth's surface), O_3 acts as a shield against ultraviolet (UV) radiation from the sun that is harmful to organisms. High-energy UV radiation enters the atmosphere where it can interact with oxygen molecules (O_2) and O_3 present in the stratosphere as seen in reactions 1 through 3 (Chapman, 1930).

1) $O_2 + h\nu \ \ (\lambda < 242\ nm) \rightarrow O + O$

2) $O_3 + \ h\nu\ (\lambda \leq 336\ nm) \rightarrow O + O_2$

3) $O + \ O_2 \overset{M}{\rightarrow} O_3$

These reactions are particularly important because they are the only significant source of O_3 in the stratosphere (Finlayson-Pitts and Pitts Jr, 2000a; Prinn, 2014), which holds about 90% of the world's O_3 (Prinn, 2014). These photochemical reactions that result in high O_3 concentrations, effectively block all radiation at wavelengths less than 290 nm, shielding the lower atmosphere and Earth's surface (Chapman, 1930; Finlayson-Pitts and Pitts Jr, 2000a). This shield is part of the reason that terrestrial life is possible on Earth. This important function came into international spotlight in 1985 with the first reports of O_3 depletion over the Antarctic and the Arctic, extending into high latitude, populated regions in both hemispheres. Loss of stratospheric O_3, and therefore enhanced exposure to UV radiation, increases the potential for tissue damage to terrestrial life forms, such as, cataracts, and reduced immune function in humans (U.S. EPA, 2017c). Loss of stratospheric O_3 also affects the chemistry in the troposphere by increasing the amount of UV radiation available for photochemical reactions at the surface that can generate tropospheric O_3 (U.S. EPA, 2017c).

In the lower atmosphere, or troposphere, which includes the planetary boundary layer and the free troposphere, O_3 is a harmful oxidant and a primary component of photochemical smog (US EPA, 2013). Ozone has detrimental effects on materials, vegetation, and animals (U.S. EPA, 2017c). Because of the harmful effects of ground level O_3, the current NAAQS standard was lowered in 2015, to 70 parts per billion by volume (ppbv) eight hour maximum daily average (MDA8) ground level concentration. To avoid effects of unusual meteorological conditions that may cause periodic, high O_3 concentrations, compliance with the NAAQS is determined based on the three year running average of the annual fourth-highest MDA8 (U.S. EPA, 2017c). The European

Union standard is 60 ppbv MDA8 with 25 allowed exceedances based on the three year average while the World Health Organization standard is 50 ppbv for an 8 h average (European Commission, 2016; WHO, 2016).

Determining sources of boundary layer O_3 is difficult because it is a secondary pollutant. This means that O_3 forms via reactions of primary pollutants, such as nitrogen oxides (NO_x), carbon monoxide (CO), and volatile organic compounds (VOCs). O_3 chemistry in the unpolluted troposphere is dominated by methane (CH_4) and it's degradation products, formaldehyde (HCHO) and CO (NRC, 1991). In the lower troposphere, reactions with biogenic and anthropogenic VOCs and anthropogenic NO_x emissions are dominant (NRC, 1991). Primary pollutants are directly released from a source (anthropogenic or biogenic) and undergo photochemical reactions in sunlight to form O_3 such as reactions 4 through 6 (Finlayson-Pitts and Pitts Jr, 2000e; Prinn, 2014).

4) $NO_2 + h\nu\ (\lambda \leq 430\ nm) \rightarrow O + NO$

5) $O + O_2 \overset{M}{\rightarrow} O_3$

6) $NO + VOCs \rightarrow NO_2\ + RH$ (hydrocarbon)

Reaction 4 and 5 are the major source of anthropogenic O_3. The relationship between O_3, NO_x, and VOC concentrations can be illustrated by isopleth plots of O_3 production as a function of NO_x and VOC concentrations or emission rates that identify two different O_3 regimes; the NO_x-sensitive (low NO_x to VOC ratio) or the NO_x-saturated and VOC-sensitive (high NO_x to VOC ratio) regimes (Finlayson-Pitts and Pitts Jr, 2000g; Sillman, 1999; Thielmann et al., 2001). O_3 concentrations increase with NO_x and are unaffected by increasing VOC concentrations in low NO_x and high VOC conditions (Finlayson-Pitts and Pitts Jr, 2000b). O_3 concentrations decrease with increasing NO_x

(NO_x-saturated) and increase with increasing VOC concentrations (VOC-sensitive) in high NO_x and low VOC conditions (Finlayson-Pitts and Pitts Jr, 2000b). These regimes are determined by sources of NO_x and hydrogen radicals. If hydrogen radicals exceed NO_x sources, then peroxides become a dominant sink and O_3 production is NO_x-sensitive. In areas with high concentrations of NO_x (NO_x-saturated), OH will react with NO_2 to form HNO_3, removing NO_x and decreasing O_3 production, alternatively leading to increasing O_3 production when NO_x is lowered in this regime (Finlayson-Pitts and Pitts Jr, 2000b; NRC, 1991; Prinn, 2014; Sillman, 1999; Thielmann et al., 2001). Reaction 6 recycles NO to NO_2 that can then enter reaction 4. Reaction 6 will vary depending on the reactivity of the VOCs present (NRC, 1991; Sillman, 1999).

Data on sources of NO_x and other O_3 precursors is thus important for understanding where the O_3 may be coming from as well as for understanding destruction of O_3 as seen in reactions 7 and 8 (Finlayson-Pitts and Pitts Jr, 2000e).

7) $NO_2 + O \rightarrow NO + O_2$

8) $NO + O_3 \rightarrow NO_2 + O_2$

Near large emissions of NO, O_3 is removed through NO_x titration. This can occur immediately downwind of large sources of NO_x (point sources, high volume highways), during periods of stagnation when NO_x accumulates, and at nighttime when there is no sunlight to facilitate reaction 4 (Sillman, 1999). O_3 is also highly reactive and will be broken down by reaction with other gases, removed via deposition to particles and droplets in the air, and by deposition to surfaces (Sillman, 1999). O_3 concentrations are therefore, a product of the equilibrium between production and loss processes.

Ozone can be produced at the source or far away from the source of primary pollutants, causing variability in concentrations geographically, temporally, and based on altitude, and extent of anthropogenic influence. Major sources of O_3 precursors, NO_x and VOCs, are heterogeneously distributed and include emissions from industrial facilities and electric utilities, motor vehicle exhaust, gasoline vapors, and chemical solvents and manufacturing (U.S. EPA, 2017c). Natural sources include wildfires, emissions of precursors from vegetation, lightning, and down-mixing from the stratosphere (U.S. EPA, 2017c). The largest sources of NO_x in Nevada are on and off road vehicles, with contributions from fuel combustion and natural sources (U.S. EPA, 2017a). Natural sources are the largest source of VOCs in Nevada (U.S. EPA, 2017a). In Nevada, anthropogenic NO_x emissions were ~16% and VOC emissions were ~28% of those emitted in California in 2014 (U.S. EPA, 2017a). Generally, in urban areas, VOC emissions control the rate of the initial buildup of O_3, while NO_x emissions determine the amount of O_3 formed during downwind chemistry, often affected by the higher rate of biogenic emissions downwind (Sillman, 1999). The rural nature of Nevada means O_3 formation is generally NO_x limited outside of the major urban areas (NRC, 1991).

Increases in anthropogenic emissions of NO_x have increased background concentrations of O_3 from ~10-15 ppbv to 20-55 ppbv with peaks in the most polluted areas reaching as high as 500 ppbv (Finlayson-Pitts and Pitts Jr, 2000d; Fiore et al., 2003; Fiore et al., 2014; Jaffe, 2010; Vingarzan, 2004; Zhang et al., 2014). Pre-industrial measurements of O_3 were made with paper strips containing potassium iodide and starch that changed color when exposed to O_3 and have measurement issues (Tarasick and Slater, 2008). Despite these early issues, a general increasing trend has been observed

(Parrish et al., 2012; Tarasick and Slater, 2008; Vingarzan, 2004). North American Background is a modeled value constructed with zero North American emissions that includes man-made precursor sources outside of North America, while baseline O_3 is defined as aged domestic emissions without recent local emissions (U.S. EPA, 2017c). Accurate measurements of O_3 concentrations are important for understanding air quality trends. As previously mentioned some areas of Nevada exceed the O_3 standard although sources of precursors are limited in Nevada.

Temporal and spatial patterns of O_3 are affected by meteorology, seasonal variability, and elevation. Large-scale climatic variability, such as the El Niño Southern Oscillation (ENSO), affects the distribution of O_3 by enhancing transport from the tropics to the extra-tropics during the warm phase (El Niño events) of the ENSO, especially during spring (Lin et al., 2014b; Rieder et al., 2013a; Rieder et al., 2013b; Zerefos et al., 1992). Springtime O_3 maximums are influenced by STE due to increased storms and a lower tropopause, which allows for better vertical down-mixing from the stratosphere, with larger impacts at high elevation sites (Ambrose et al., 2011; Brodin et al., 2010; Burley and Bytnerowicz, 2011; Fine et al., 2015b; Vingarzan, 2004). Temperature, wind direction, the amount of solar radiation, and surface stability and mixing during different seasons affect surface O_3 concentrations (Vingarzan, 2004).

Increased temperatures due to climate change are also expected to increase O_3 concentrations during the summer time (Fang et al., 2013; Pfister et al., 2014; Ramsey et al., 2014; Rasmussen et al., 2013). This increase is due to increased reaction rates and greater emissions of VOCs at higher temperatures, which then mix with anthropogenic emissions to create O_3. In addition, increasing CH_4, globally increases baseline

concentrations of surface O_3 (Holmes et al., 2013; Pfister et al., 2014; Sanderson et al., 2003; Stevenson et al., 2005). The oxidation of CH_4, as seen in reaction 9, produces CH_3O_2, which can then enter reaction 6, producing more NO_2 (Stevenson et al., 2005).

9) $CH_4 + OH + (O_2) \rightarrow CH_3O_2 + H_2O$

O_3 is both an absorber and emitter of infrared (IR) radiation, which means that increases of ground level O_3 may influence surface temperatures, while loss of stratospheric O_3 cools the stratosphere (Prinn, 2014).

Eurasian long-range transport is strongest in the spring due to increased storm and frontal activity in Eurasia and strong transport of air across the Pacific during this time (Cooper et al., 2010; Knowland et al., 2015; Kunz and Speth, 1997; Vingarzan, 2004). The lifetime of O_3 in the free troposphere is long enough (~22 days) to be transported between continents and across oceans (Stevenson et al., 2006). Transport of O_3 and precursors has elevated background O_3 concentrations in the Western United States by 3 to 15 ppbv with episodic increases during spring up to 30 ppbv (Fine et al., 2015a; Jacob et al., 1999; Jaffe et al., 2003; Langford et al., 2015; Vingarzan, 2004). This influence is projected to increase as Asian countries continue to develop (Christensen et al., 2015; Cooper et al., 2010; Gratz et al., 2015). Species like PAN (peroxyacetyl nitrate, $CH_3COO_2NO_2$) serve as reservoirs for and contribute to the long-range transport of NO_y species, which can then contribute to downwind O_3 concentrations (Fischer et al., 2011).

Due to layers of polluted trans-Pacific air, lofting of pollution produced in California, USA, and stratospheric intrusions, higher elevation sites often observe higher O_3 concentrations than lower elevation sites (Brodin et al., 2010; Burley and Bytnerowicz, 2011; Fine et al., 2015a; Fine et al., 2015b; Gustin et al., 2015; Vingarzan,

2004). Lower elevations sites have greater O_3 removal rates in the boundary layer, particularly nighttime O_3 removal in cities. Nevada routinely intercepts free tropospheric air lofted over the Sierra Nevada Mountains. The predominantly rural nature of the State means monitoring sites located in Nevada are useful for measuring regional air quality trends. In the present work, O_3 production cannot be directly computed, however a suite of measurements are used to evaluate conditions and sources at each monitoring site and to compare across the sites.

2.2 Particulate matter

Natural sources of PM include sea spray, volcanic emissions, wind entrainment of dust, wildfires, gas-to particle conversion of hydrocarbons from plants, and dimethylsulfide from oceans (Buseck and Schwartz, 2014). Anthropogenic sources include land use processes (e.g. agricultural activities), roadways, combustion processes, and biomass burning (Buseck and Schwartz, 2014).

Particles < 2.5 μm in aerodynamic diameter ($PM_{2.5}$), considered fine PM, are a health concern because they can penetrate into the lungs and deposit potentially harmful microscopic solids or liquid droplets (Kleinstreuer and Zhang, 2009; U.S. EPA, 2013). Small particles also impair visibility and are monitored in the IMPROVE network. The primary $PM_{2.5}$ NAAQS for 24 hours is 35 μg m^{-3}, 98th percentile value averaged over three years and the annual primary $PM_{2.5}$ NAAQS is 12 μg m^{-3} annual mean averaged over three years (U.S. EPA, 2013).

Changes in $PM_{2.5}$ mass concentration and composition can occur due to seasonal variables. In winter, during high-pressure systems and increased snow cover, with less

surface heating and therefore less mixing, a buildup of pollution can occur, particularly in valleys. Often the major component of PM during winter is nitrate aerosols. Nitrogen dioxide (NO_2) is removed from the atmosphere when it reacts with a hydroxyl free radical (OH) forming nitric acid (reaction 10; Buseck and Schwartz, 2014; Finlayson-Pitts and Pitts Jr, 2000c). Nitric acid acts as a temporary sink for NO_2 since it can react with OH radicals to produce nitrate (reaction 11) or photochemically, to produce NO_2 (reaction 12). Nitric acid is removed from the atmosphere by precipitation (acid rain), or by reacting with ammonia to produce ammonium nitrate (NH_4NO_3), which is favored by cold temperatures and high humidity (reaction 13). For this reason during winter, high NO_2 tropospheric concentrations tend to correlate with the locations of higher $PM_{2.5}$ concentrations. Wintertime buildup of ammonium nitrate has been observed in valleys in the West (Chen et al., 2012; Green et al., 2015).

10) $NO_2 + OH \rightarrow HNO_3$

11) $OH + HNO_3 \rightarrow H_2O + NO_3$

12) $HNO_3 + h\nu \rightarrow OH + NO_2$

13) $HNO_3 + NH_3 \rightarrow NH_4NO_3$

$PM_{2.5}$ also varies due to topography. A study at high elevation sites in California has shown that the dominate aerosols originate from the Asian continent and are semi-continuous over the year (VanCuren et al., 2005). Nighttime subsidence fumigation from the free troposphere causes a peak in Asian aerosols at these sites (VanCuren et al., 2005). This is important in Nevada due to the high base elevation of much of the State and the many mountain ranges.

Particulate matter has direct and indirect impacts on climate. These impacts vary by region depending on the composition of the $PM_{2.5}$. Direct effects include absorption and scattering of light, which affects visibility. Particles that absorb radiation, such as black carbon, can have a warming effect on the atmosphere, and when deposited to snow and ice surfaces, can increase melting (Heald et al., 2013; U.S. EPA, 2012b). Particles that scatter radiation, such as sulfates and nitrates, can have a cooling effect (Heald et al., 2013). Particulate matter in the West is dominated by carbonaceous and nitrate particles, but will vary by site and local sources (Buseck and Schwartz, 2014; Malm et al., 2011; Malm et al., 2004; Malm and Sisler, 2000; Nguyen et al., 2016)

Indirect effects of airborne particulates include changes in precipitation and changes in cloud albedo and lifetime, which affects radiation and hydrology (Finlayson-Pitts and Pitts Jr, 2000f). Increased reflectivity of clouds due to particles can cause a cooling effect. Reductions in $PM_{2.5}$ emissions may have a mixed effect on the climate; likewise, climate change will have a mixed effect on $PM_{2.5}$ (U.S. EPA, 2012b). Better understanding of the composition and behavior of PM is essential for reducing negative effects on air quality.

2.3 Mercury

The adverse health effects of exposure to mercury (Hg) were brought to international recognition starting in 1956 when Minamata Disease was first discovered in Minamata city in Japan due to contamination from industrial waste released into Minamata Bay (Lofroth, 1978). Hg negatively affects the brain, heart, kidneys, lungs, and immune systems of people of all ages and is capable of crossing biological barriers, such

as the blood-brain barrier and the placental barrier where it causes harm to the developing nervous system (Axelrad et al., 2007; Clarkson and Magos, 2006; U.S. EPA, 2011). Negative impacts have also been documented on behavior and reproductive success of other vertebrates and invertebrates (Hallinger et al., 2010; Jackson et al., 2011; Wyman et al., 2011).

The atmosphere is the main transport and deposition pathway for Hg to enter remote terrestrial and aquatic ecosystems where it can then be converted to the bio-available form, methylmercury (Fitzgerald et al., 1998; Schroeder and Munthe, 1998). There are natural sources of Hg, which include enriched geologic sources, volcanoes, and forest fires (Friedli et al., 2001; Schroeder and Munthe, 1998), but anthropogenic sources are the major contributor of Hg to the atmosphere (Pacyna et al., 2010; Schroeder and Munthe, 1998). Anthropogenic sources include burning coal, oil, and wastes containing Hg, metal smelting, and artisanal gold mining (Pacyna et al., 2006).

Mercury is present in the atmosphere in three forms, gaseous elemental Hg (GEM), gaseous oxidized Hg (GOM), and particulate bound Hg (PBM). GEM represents ~95% of the Hg present in the atmosphere. It is relatively inert, with low solubility in water, and therefore has a long residence time in the atmosphere, which allows it to be transported long distances from sources (Lamborg et al., 2002; Schroeder and Munthe, 1998; Slemr et al., 1985). GOM and PBM have shorter residence times in the atmosphere and are considered local or regional pollutants (Schroeder and Munthe, 1998; Shia et al., 1999; Swartzendruber et al., 2006). The concentrations and chemical compounds of GOM and PBM, collectively referred to as reactive Hg (RM), vary spatially and

temporally, are not well characterized, and require further research on measurement methods (Gustin et al., 2016).

3. Research objectives

The goal of this research was to identify sources, source regions, and processes affecting the concentration of atmospheric pollutants in Nevada, specifically $PM_{2.5}$, RM, and O_3, using Pb isotopic ratios and a suite of measurements, including gaseous data, meteorological data, and aerosol optical properties. In addition, a method was developed and tested due to the need for improved methods for measuring RM and the need for additional measurements and methods for identifying sources of O_3 to rural Nevada.

The first research objective was to develop and deploy a particulate monitor to simultaneously collect $PM_{2.5}$ on two filter materials that could then be post-processed for RM concentrations, and Pb concentrations and isotopes to understand the sources of air pollution to Nevada. The second objective was to use the Pb isotope data from this instrument and a suite of other measurements, to understand sources of elevated O_3 and RM to Nevada. The third objective was to apply a statistical method to the data collected by the particulate monitor to better understand the sources and processes affecting horizontal and vertical heterogeneity of atmospheric pollutants at adjacent valley and peak measurement sites in Nevada. The fourth objective was to investigate the possible sources of anomalous PM collected at one of the sample sites during the sample period.

3.1 Research objective 1

The first research objective was to develop a new method for measuring $PM_{2.5}$ mass concentrations on two filter materials that allowed for post-processing of sample filters for RM and Pb isotope ratios in aerosols to understand sources of $PM_{2.5}$, RM, and O_3. Accurate $PM_{2.5}$ measurements, using the new method, had to be established before analysis of RM or Pb measurements could occur.

Particulate matter is measured for different purposes, including compliance with air quality standards (mass concentration measurements), increased knowledge of chemical and physical processes, impacts on visibility, and impacts on human and ecosystem health. Mass concentration measurements are accomplished by actively drawing sample air through filter material to collect particulates. The most commonly used filter materials include Teflon membranes, quartz fiber filters, nylon membranes, cellulose fiber, Teflon-coated glass fiber, etched polycarbonate membranes, and glass fiber (Watson and Chow, 2011).

Available FRMs for $PM_{2.5}$ include low-volume collectors with gravimetric mass measurement. Sample filters are weighed in temperature- and relative humidity-controlled laboratories before and after sampling. The difference is considered the sample weight, which is then divided by sample volume to attain mass concentration (Watson and Chow, 2011). Federal Reference Methods for measuring PM focus mainly on mass concentration measurements and have a limited ability for continuous sampling or post-processing for particle sizing, hourly and daily continuous sampling, chemical composition, or quantification of volatile aerosols (Watson and Chow, 2011). Positive (e.g. adsorption of organic vapors) and negative (e.g. volatilization of organic aerosols)

sampling artifacts also complicate the collection of samples on filters (Allen 1989, Takahashi 2008). Measurement methods that avoid some of these limitations are, therefore, necessary.

While the IMPROVE network uses gravimetric mass measurement it also uses several different filter types and analysis methods to attain speciated $PM_{2.5}$ and PM_{10} measurements. The IMPROVE setup has four separate sampling inlets: a Teflon filter that collects most of the $PM_{2.5}$ data, a sampling inlet with a nylon filter that measures primarily nitrate and some sulfate and chloride, an inlet with quartz filters that measure carbon in eight temperature fractions, and a PM_{10} (0-10 μm) inlet (IMPROVE, 1995). There is also an option to measure SO_2 on one of the Teflon inlets. Analysis includes gravimetric mass concentrations, X-ray fluorescence (XRF) for elements, ion chromatography (IC) for sulfate, nitrate, nitrite, chloride ions, and estimates of ammonium based on fully neutralized sulfate and nitrate, and thermal/optical reflectance (TOR) protocol for fractionated organic and elemental carbon (IMPROVE, 1995; Solomon et al., 2014; Watson and Chow, 2011). IMPROVE measurements assume no interference from other elements (for all elements except As). According to IMPROVE data analysis, reconstructed particulate mass correlates well with the gravimetric mass, and accounts for most of the fine mass, however ~20% of the missing mass could be due to volatilization of nitrate or residual water on the particles (IMPROVE, 1995). Samples are only collected every one-in-three days from 00:00 to 00:00-local time.

Beta (β) attenuation is a common technique for measuring particulate mass at a finer temporal resolution (hourly) than commonly used gravimetric techniques. Beta rays, emitted from ^{14}C are passed through a filter and measured. Particulate matter is then

collected on the filter and β rays are again passed through the filter. The decrease in β rays through the filter, due to absorption by the deposited particles, is used to calculate the mass of particles deposited to the filter material. Beta attenuation allows for measurement of collected samples directly after sample collection has completed. The β Attenuation Monitor (BAM-1020) is an FEM used at EPA AQS monitoring sites. The Teledyne Advanced Pollution Instrumentation Model 602 Beta^{Plus} particulate monitor (TAPI), also an FEM, was used in this study.

The TAPI was configured to measure $PM_{2.5}$ on two separate filter types that could then be post-processed for RM concentrations, and Pb concentrations and isotopic ratios. This required a different configuration for the two sample inlets of the TAPI than was originally designed. Ensuring that $PM_{2.5}$ measurements from the TAPI, in the new configuration, were comparable to FRM and other FEM instruments (BAM-1020) was critical before RM or Pb could be measured using the $PM_{2.5}$ samples. $PM_{2.5}$ and RM were addressed in the first research objective; Pb was addressed in the second research objective.

GEM is reliably measured by pre-concentrating atmospheric samples on gold traps and analyzed using cold vapor atomic fluorescent spectroscopy (CVAFS). Co-located instruments measuring GEM have been shown to have an average systematic uncertainty of ~10% and in some cases up to 20% (Slemr, 2014). Measurements of GOM and PBM are operationally defined and do not have standards available for calibration that are relevant for ambient concentrations. The commercially available method that is widely used collects GOM and PBM, separately. GOM is collected on a potassium chloride (KCl) coated annular denuder for 1 h while PBM (<2.5 μm in diameter) is

collected on quartz chips for 1 h. The annular denuder is desorbed at 500° C and the quartz chips are desorbed at 800° C. GEM is released during desorption and collected on gold traps where it is then analyzed using CVAFS. Temporal resolution is 1 h, every other hour.

Another method for collecting RM, used in this study, is sample collection on cation exchange membranes (CEM) and post-processing following U.S. EPA method 1631 for total Hg concentrations in aqueous samples. Filters are digested to remove Hg from the filter surface; all Hg present is oxidized to ensure all forms are the soluble Hg^{II} form, Hg is then reduced to volatile GEM. GEM is purged from the aqueous samples and collected on gold traps, thermally desorbed from the traps, and measured by CVAFS.

The collection efficiency of GOM and PBM on the annular denuder and quartz chips is affected by O_3 concentrations, relative humidity, temperature, interferences from other atmospheric constituents, and for GOM, the form present in the atmosphere (Huang and Gustin, 2015; Huang et al., 2013; Jaffe et al., 2014; Luke, 2016; Lyman et al., 2010; Malcolm and Keeler, 2007; McClure et al., 2014; Rutter and Schauer, 2007). GOM measurements from the annular denuder have been shown to be biased low by 2 to 13 times compared to filter measurements (Gustin et al., 2013; Huang and Gustin, 2015; Huang et al., 2013). Developing novel measurement methods is therefore critical for improving our understanding of the global Hg cycle.

3.2 Research objective 2:

The second research objective was to use aerosol chemistry for determining sources of RM and O_3 to Nevada using Pb isotopic ratios from $PM_{2.5}$, combined with

gaseous measurements (O_3, CO, NO_x, NO_y, SO_2), meteorological data, and back trajectory analysis. Once it was established that the TAPI measured $PM_{2.5}$ concentrations similar to those measured using FRM and FEM monitors, the $PM_{2.5}$ data could be used to identify sources of air masses based on Pb isotopic ratios and back trajectory analyses.

Although Pb is a criteria air pollutant, the removal of leaded gasoline in North America in the 1970s, has resulted in a dramatic decrease in atmospheric Pb concentrations (Nriagu and Pacyna, 1988; Reuer and Weiss, 2002). Decreases in Pb concentrations from anthropogenic sources mean that observed concentrations in the USA are usually much lower than the NAAQS (0.15 μg m^{-3}, three month running average), making it easier to distinguish influence from sources outside of the USA (Bollhöfer and Rosman, 2002; U.S. EPA, 2016). Lead occurs naturally in soil with a mean of 17 ppm (range of 10 to 700 ppm) in the Western USA and can be emitted to the air when the soil is disturbed (Shacklette and Boerngen, 1984). Lead in soils can be enhanced by historic leaded gasoline vehicle exhaust, naturally occurring lead in fly ash from burning of coal, leaded paint, and contaminated sites such as lead smelters (U.S. EPA, 2017b). Lead is emitted from the use of fossil fuels, and industrial and metallurgical processes that also emit O_3 precursors (Li et al., 2012; U.S. EPA, 2017b). Pollutants, including fine aerosol Pb, can be transported long distances, such as across oceans (Fiore et al., 2002; Heald et al., 2006; Jaffe et al., 1999; VanCuren, 2003; VanCuren et al., 2005; Wilkening et al., 2000). Aerosols collected on filters can then be analyzed for Pb isotopic ratios to determine sources of the aerosols (Bollhöfer and Rosman, 2001; Bollhöfer and Rosman, 2002; Christensen et al., 2015; Ewing et al., 2010).

Isotopic ratio analysis of radiogenic samples has traditionally been performed using thermal ionization mass spectrometry (TIMS). However, TIMS analyses have low precision and reproducibility due to mass-dependent isotopic fractionation during analysis (White et al., 2000). Fractionation in TIMS analysis occurs during evaporation and ionization of the samples, which preferentially ionizes lighter isotopes and is time-dependent. Generally, this is corrected for by observing the fractionation of two non-radiogenic isotopes whose ratio is known in nature and is assumed to be invariant (Walder and Freedman, 1992; White et al., 2000). This correction is not possible for Pb isotopic analysis with only one non-radiogenic isotope (^{204}Pb), and therefore the observed fractionation for a standard reference material is assumed to be the same as for the analysis of unknown samples and is used for mass-fractionation correction (Walder and Freedman, 1992; White et al., 2000).

ICP-MS has larger fractionation than TIMS, due to space-charge effects in low electrostatic field regions of the instrument (e.g. ion beam), creating different ion focusing efficiencies as the ions enter the mass analyzer. This fractionation is essentially time-independent and should be primarily independent of the chemical properties of an ion and therefore only mass-dependent, which allows for use of an element with a similar mass to correct for mass fractionation (White et al., 2000). Samples were therefore spiked with thallium (5:1 ratio of Pb to Tl) with known isotopic composition (^{205}Tl:^{203}Tl) to adjust for instrumental mass fractionation of Pb during analysis for this research. MC ICP-MS is an improvement over quadrupole ICP-MS (Q ICP-MS), which has lower precision compared to TIMS due to poor ion peak shape (rounded instead of flat), low ion count rates, and instability of the plasma ion source (Hill, 2007; Taylor, 2001a; Walder

and Freedman, 1992; White et al., 2000). Q ICP-MS can also only measure one ion mass at a time. The flat topped peaks of the MC ICP-MS allows for high precision measurements, while the multiple Faraday collectors allows for simultaneous measurement of ions of different masses, removing source instability and further improving precision (Becker, 2005; Walder and Freedman, 1992; White et al., 2000).

For this research objective, Pb from $PM_{2.5}$ samples collected on Teflon filters is leached from the filters using acid solutions and run through resin columns for ion exchange chemistry to separate Pb and remove other constituents that may produce mass interferences or affect the mass fractionation behavior. The sample is then nebulized into a desolvation system to reduce water vapor in the aerosol and therefore oxide interferences. For these measurements an Apex isotope ratio [IR] sample introduction system with an actively cooled membrane [ACM] desolvation for Apex inlet system attached (by ESI), were used to produce a dry aerosol that is then introduced into the argon plasma stream. The plasma breaks down the aerosol, dissociates the molecules, and creates singly-charge ions (Taylor, 2001b). Faraday cups collect and measure the currents generated by the collected mass-separated ion beams. When ions impact on a Faraday cup they transfer their charge to the cup and are neutralized (Taylor, 2001a). The cup is an element in a circuit and the current created by the impacting ions can be measured and related to the number of ions intercepted by the cup with high sensitivity (Taylor, 2001a). A double-focusing sector field mass spectrometer directs ions to an array of Faraday cups, allowing for simultaneous collection of multiple, separated isotopic masses. The mass spectrometer uses a magnet and an electrostatic filter to focus ions with the same mass to charge ratios using both the kinetic energy and angular dispersions (Bradshaw et

al., 1989; Walder and Freedman, 1992). The separate ion signals collected from Faraday cup detectors set for masses of interest are amplified by current amplifiers. The ion signal can then be compared to the ion signal from a standard to determine concentration.

The natural abundance of Pb isotope is not fixed in nature, ^{204}Pb is the only primordial stable isotope with a constant abundance, and the other Pb isotopes are radiogenic. Radiogenic isotopes are products of natural radioactive decay of a parent isotope (^{235}U to ^{207}Pb, ^{238}U to ^{206}Pb, ^{232}Th to ^{208}Pb). This means that Pb isotopic ratios vary geographically depending on the source of the Pb and can therefore be attributed to different source regions (Bollhöfer and Rosman, 2001; Bollhöfer and Rosman, 2002; Ewing et al., 2010; Komárek et al., 2008). Atmospheric processes and concentrations of aerosols and Pb do not alter the isotopic composition of Pb as it is transported away from a source, making it a useful tool for tracing sources of pollutants. Previous studies have demonstrated the use of Pb isotopic ratios for identifying trans-Pacific input of pollutants (Ewing et al., 2010), and specifically O_3, to the Western USA (Christensen et al., 2015).

Combining Pb isotope data with back trajectory analyses aided in identifying general source regions of air masses intercepted at the measurement sites in Nevada. A Lagrangian back trajectory model for particle dispersion was used to follow theoretical particles observed at a measurement site, back in time based on meteorological inputs to the model (Stohl et al., 2002; Stohl et al., 2003). A large number of back trajectories, each representing a single particle, allow for a residence time calculation of all the particles in an area of interest, normalized by the total number of particles modeled in the back trajectories (Stohl et al., 2003). This calculation gives an estimate of the contribution of that area to the measurements observed at a site. Residence times and Pb

isotope analysis were then used to attribute enhancements of O_3 in Nevada to different source regions.

3.3 Research objective 3:

The third research objective was to use data collected using the particulate monitor developed for the first two research objectives for use in a statistical method. The quadrant method, a data exploration tool, developed to understand sources and physical processes affecting the relationship between columnar aerosol optical depth (AOD) and surface $PM_{2.5}$ measurements, was applied using the $PM_{2.5}$ data collected with the TAPI. ANOVA one-way statistical analysis was applied to quantify statistically significant differences in the means of meteorological variables, aerosol optical properties, vertical structure, stability measures, and O_3 concentrations to identify the sources and physical processes affecting the relationship between ground-based, columnar AOD and surface $PM_{2.5}$ observations.

The complex terrain, mixture of synoptic and mesoscale weather patterns that govern airflow in the Western USA, and input from local, regional, and long-range sources create horizontal and vertical gradients of pollutants that can be difficult to characterize. Furthermore, many urban centers in the intermountain west are located in valleys, where large populations are affected by atmospheric pollution emissions and valley airflow dynamics (Fernando, 2010). It is therefore necessary to quantify pollutant gradients to assess human and ecosystem exposure to potentially harmful concentrations and to develop air quality management policies.

In 2010, the U.S. EPA implemented a near-road monitoring program for NO_2, CO, and $PM_{2.5}$ to assess pollutant exposure in cities with >500,000 people, located within 50 m, and ideally 20 m, of the nearest high-traffic lane (Batterman, 2013; EPA, 2016). Atmospheric pollutants from traffic interact with urban point and non-point sources of pollutants, and undergo reactions that affect concentrations at different times and distances from emission sources (Karner et al., 2010). While proximity and traffic intensity is important for assessing exposure to near-road pollutants, much of the complexity of the processes is lost without an understanding of site meteorology and physical processes, vehicle emissions, time-activity patterns, and confounding sources (Karner et al., 2010; Zhang and Batterman, 2013). Additionally, traffic-related air pollution, particularly secondary pollutants, affects areas downwind of urban centers (Batterman, 2013; Karner et al., 2010).

The complexity of airflow in the Western USA, discussed previously, means that pollutants can exist within and above the planetary boundary layer, sometimes in filamentous layers (Fine et al., 2015b; Lin et al., 2012; Stohl et al., 2003). Vertical heterogeneity of pollutants will affect valley and high elevation sites differently depending on the site-specific sources and physical processes present. Surface monitoring stations provide valuable information, but only capture a small spatial picture in the complex environment of the Western USA.

Satellites capture data at large spatial scales and are therefore useful in addressing the lack of data in rural and remote areas across the world. Measurements from the Moderate Resolution Imaging Spectroradiometer (MODIS), the Multi-angle Imaging SpectroRadiometer (MISR), and the Cloud-Aerosol Lidar with Orthogonal Polarization

(CALIOP), located on different satellites (Terra, Aqua, and CALIPSO), have been used to collect AOD. Aerosol optical depth is a measure of the light extinction caused by scattering and absorption of aerosols in the atmospheric column at different wavelengths. Two different algorithms, the Dark Target and the Deep Blue, are used to calculate AOD from the collected satellite data over land. Deep Blue was developed to retrieve AOD over bright surfaces, and uses different spectral channels than Dark Target to accomplish this (Hsu et al., 2013; Hsu et al., 2006; Martin, 2008; Sayer et al., 2013; Sorek-Hamer et al., 2015).

Retrievals of columnar AOD have several challenges: retrievals are only available during daylight and clear sky conditions and retrievals by satellites are difficult over bright or reflective surfaces, such as deserts and snow (Gupta et al., 2006; Husar, 2011; Lee et al., 2016; Loría-Salazar et al., 2016; Nguyen et al., 2016; Sorek-Hamer et al., 2015; Sorek-Hamer et al., 2013; van Donkelaar et al., 2006; Wang and Christopher, 2003). Furthermore, comparisons between satellite and ground-based columnar AOD also show biases due to differences in calibration, presence of clouds, surface parameterization, aerosol measurement assumptions, and heterogeneous vertical distribution of aerosols in the atmospheric column (Engel-Cox et al., 2004; Li et al., 2014a; Li et al., 2014b; Li et al., 2014c; Loría-Salazar et al., 2017; Zhang and Reid, 2006).

Ground-based retrievals of AOD from the AErosol RObotic NETwork (AERONET) consist of direct, collimated solar radiation measurements from a sun photometer. Direct sun measurements are made at eight wavelengths, 340, 380, 440, 500, 670, 870, 940, and 1020 nm (Holben et al., 1998; NASA, 2007). Extinction of direct

radiation is calculated based on the Beer-Bouguer Law for each wavelength, using top of the atmosphere spectral irradiance obtained from a sun photometer located at Mauna Loa Observatory in Hawaii as the initial irradiance value and an air mass factor to account for the slant path through the atmosphere (Holben et al., 1998; NASA, 2007). Extinction due to Rayleigh scatter, absorption by O_3, and other gaseous pollutants (NO_2, CO_2, CH_4) are removed to calculate AOD. Data is then screened for cloud contamination and corrected using pre- and post-field deployment calibrations (Holben et al., 1998; NASA, 2007).

Several studies have focused on deriving $PM_{2.5}$ concentrations using empirical statistical correlations (linear and multivariate) with τ_{ext}, land use information, other satellite products, and information from chemical transport models, with some success (Engel-Cox et al., 2004; Gupta et al., 2006; Liu et al., 2009; Liu et al., 2004; Strawa et al., 2013; van Donkelaar et al., 2006; Wang and Christopher, 2003). Previous studies have identified relationships between columnar AOD and surface $PM_{2.5}$ measurements that are not well correlated (Li et al., 2015; Loría-Salazar et al., 2017). The use of statistical methods, such as the quadrant method, aid in identifying the sources and physical processes influencing periods when columnar measurements are not associated with surface measurements. Information gained using this method can then be applied to identify exceptional events at measurement sites and for improving models that use columnar data to estimate surface $PM_{2.5}$ and health exposure with large spatial coverage.

3.4 Research objective 4:

The fourth objective was to investigate the possible reasons for anomalous particulate data collected at one measurement site during the measurement campaign.

Particles were collected on a sample filter that were > 2.5 µm in aerodynamic diameter, which is the cut point size of the inlet for the TAPI. These samples indicated that either the observed particles had unique dimensions that allowed them to bypass a PM_{10} pre-impactor and $PM_{2.5}$ cyclone inlet or that there was an issue with the particulate monitor.

For the purposes of measuring PM in ambient air, assumptions are made about the size and shape of particles, and therefore their behavior as they move through a measurement instrument. Ambient PM measurements are based on the behavior of an ideal spherical particle with a density of ~1000 kg m^{-3} (Kulkarni et al., 2011a). For particles that are non-spherical, equivalent diameters are used to approximate the particle behavior. More than one equivalent diameter is often necessary to understand the behavior of non-spherical particles. Aerodynamic equivalent diameter (D_a), or the diameter of a sphere of unit specific gravity that settles at the same terminal velocity as the particle, is the most common equivalency measure used in ambient PM measurements (Marple and Olson, 2011).

Impactors and cyclones are designed to use inertial separation to separate particles of different aerodynamic diameters (Kulkarni et al., 2011b). Impactors use an impactor plate to create an abrupt change in airflow direction, causing particles too large to move with the airflow to cross streamlines and deposit onto the impactor surface (Kulkarni and Baron, 2011; Marple and Olson, 2011). Cyclones create a swirling pattern in the airflow that causes large particles to deposit out of the air stream due to centrifugal force (Kulkarni and Baron, 2011; Marple and Olson, 2011). Particles with less inertia will remain in the airflow and continue to the sample surface. Collected particles can be

primary particles, or monomers, or collections of monomers into an agglomerate or aggregate.

Aggregates are classified as particle-cluster aggregation (diffusion limited aggregation, DLA) or cluster-cluster aggregation (diffusion limited cluster aggregation, DLCA). DLA occurs when single monomers diffuse and stick to a growing, stationary cluster and have a fractal dimension (D_f) of ~2.5. DLCA occurs when clusters diffuse and stick together (D_f ~ 1.75 to 2.15) when they randomly come in contact and is known to occur in the atmosphere (Kulkarni et al., 2011a). Soot aggregates are formed during incomplete combustion via DLCA. The fractal dimension describes the relationship between linear and volumetric size (which is related to the primary particles that make up the aggregates) and is a quantitative description of the density of an aggregate (Kulkarni et al., 2011a).

If the aerodynamic diameter of an aggregate is low and the fractal dimension is high, indicative of low density, high porosity aggregates, it is possible for these aggregates to deposit past inlets such as the PM_{10} pre-impactor and $PM_{2.5}$ cyclone used by the TAPI (Chakrabarty et al., 2014; Kearney and Pierce, 2012). If these particles are present in the atmosphere they could potentially be harmful to organisms, as the mobility of the particles would allow them to penetrate deeper into the lungs than an equivalent spherical particle (Kleinstreuer and Zhang, 2009). However, if these aggregates are an instrument artifact, then $PM_{2.5}$ measurements could be artificially biased high during conditions that facilitate the formation of aggregates within the sample line.

4. Chapter overview

The following chapters address the four research objectives. Chapter 2 describes the development and deployment of a particulate monitor to quantify $PM_{2.5}$, RM, and Pb isotopes and how it compares to other methods for measuring $PM_{2.5}$ and RM. The third chapter applies Pb isotopic analyses and a suite of other measurements to understand elevated O_3, RM, and sources of pollution to three sites in Nevada. Chapter 4 uses data from the particulate monitor in a statistical method to better understand the sources and physical processes affecting atmospheric pollutants in Nevada. In Chapter 5, the possible sources of anomalous PM collected on filters during the sample period are investigated. Chapter 6 summarizes the findings of each chapter and presents conclusions and recommendations for future research.

References

IMPROVE Data Guide. In: University of California D, editor. University of California, Davis, University of California, Davis, 1995, pp. 13.

Ambrose JL, Reidmiller DR, Jaffe DA. Causes of high O3 in the lower free troposphere over the Pacific Northwest as observed at the Mt. Bachelor Observatory. Atmospheric Environment 2011; 45: 5302-5315.

Axelrad DA, Bellinger DC, Ryan LM, Woodruff TJ. Dose-Response Relationship of Prenatal Mercury Exposure and IQ: An Integrative Analysis of Epidemiologic Data. Environmental Health Perspectives 2007; 115: 609-615.

Batterman S. The Near-Road Ambient Monitoring Network and Exposure Estimates for Health Studies. EM (Pittsburgh, Pa.) 2013; 2013: 24-30.

Becker SJ. Recent developments in isotope analysis by advanced mass spectrometric techniques Plenary lecture. Journal of Analytical Atomic Spectrometry 2005; 20: 1173-1184.

Bollhöfer A, Rosman KJR. Isotopic source signatures for atmospheric lead: the Northern Hemisphere. Geochimica et Cosmochimica Acta 2001; 65: 1727-1740.

Bollhöfer A, Rosman KJR. The temporal stability in lead isotopic signatures at selected sites in the Southern and Northern Hemispheres. Geochimica et Cosmochimica Acta 2002; 66: 1375-1386.

Bradshaw N, Hall EFH, Sanderson NE. Communication. Inductively coupled plasma as an ion source for high-resolution mass spectrometry. Journal of Analytical Atomic Spectrometry 1989; 4: 801-803.

Brodin M, Helmig D, Oltmans S. Seasonal ozone behavior along an elevation gradient in the Colorado Front Range Mountains. Atmospheric Environment 2010; 44: 5305-5315.

Burley JD, Bytnerowicz A. Surface ozone in the White Mountains of California. Atmospheric Environment 2011; 45: 4591-4602.

Buseck PR, Schwartz SE. 5.4 - Tropospheric Aerosols. In: Holland HD, Turekian KK, editors. Treatise on Geochemistry (Second Edition). Elsevier, Oxford, 2014, pp. 95-137.

Chakrabarty RK, Beres ND, Moosmuller H, China S, Mazzoleni C, Dubey MK, et al. Soot superaggregates from flaming wildfires and their direct radiative forcing. Sci. Rep. 2014; 4.

Chapman S. A Theory of Upper-Atmospheric Ozone. Vol 3: Memoirs of the Royal Meteorological Society, 1930.

Chen LWA, Watson JG, Chow JC, Green MC, Inouye D, Dick K. Wintertime particulate pollution episodes in an urban valley of the Western US: a case study. Atmos. Chem. Phys. 2012; 12: 10051-10064.

Christensen JN, Weiss-Penzias P, Fine R, McDade CE, Trzepla K, Brown ST, et al. Unraveling the sources of ground level ozone in the Intermountain Western United States using Pb isotopes. Science of The Total Environment 2015; 530–531: 519-525.

Clarkson TW, Magos L. The Toxicology of Mercury and Its Chemical Compounds. Critical Reviews in Toxicology 2006; 36: 609-662.

Cooper O, R., Parrish D, D., Stohl A, Trainer M, Nedelec P, Thouret VC, J. P. Oltmans, S. J. Johnson, B. J. Tarasick, D. Leblanc, T. McDermid, I. S. Jaffe, D. Gao, R. Stith, J. Ryerson, T. Aikin, K. Campos, T. Weinheimer, A. Avery, M. A. Increasing springtime ozone mixing ratios in the free troposphere over western North America. Nature 2010; 463: 344-348.

Engel-Cox JA, Holloman CH, Coutant BW, Hoff RM. Qualitative and quantitative evaluation of MODIS satellite sensor data for regional and urban scale air quality. Atmospheric Environment 2004; 38: 2495-2509.

EPA USEPA. Exceptional events documents ozone - Washoe, NV. 2017, 2017.

European Commission. Air Quality Standards. 2017, 2016.

Ewing SA, Christensen JN, Brown ST, Vancuren RA, Cliff SS, Depaolo DJ. Pb Isotopes as an Indicator of the Asian Contribution to Particulate Air Pollution in Urban California. Environmental Science & Technology 2010; 44: 8911-8916.

Fang Y, Mauzerall DL, Liu J, Fiore AM, Horowitz LW. Impacts of 21st century climate change on global air pollution-related premature mortality. Climatic Change 2013; 121: 239-253.

Fernando HJS. Fluid Dynamics of Urban Atmospheres in Complex Terrain. Annual Review of Fluid Mechanics 2010; 42: 365-389.

Fine R, Miller MB, Burley J, Jaffe DA, Pierce RB, Lin M, et al. Variability and sources of surface ozone at rural sites in Nevada, USA: Results from two years of the Nevada Rural Ozone Initiative. Science of The Total Environment 2015a; 530–531: 471-482.

Fine R, Miller MB, Yates EL, Iraci LT, Gustin MS. Investigating the influence of long-range transport on surface O3 in Nevada, USA, using observations from multiple measurement platforms. Science of The Total Environment 2015b; 530–531: 493-504.

Finlayson-Pitts BJ, Pitts Jr JN. Chapter 4 - Photochemistry of Important Atmospheric Species. In: Finlayson-Pitts BJ, Pitts JN, editors. Chemistry of the Upper and Lower Atmosphere. Academic Press, San Diego, 2000a, pp. 86-129.

Finlayson-Pitts BJ, Pitts Jr JN. Chapter 6 - Rates and Mechanisms of Gas-Phase Reactions in Irradiated Organic −NOx—Air Mixtures. In: Finlayson-Pitts BJ, Pitts JN, editors. Chemistry of the Upper and Lower Atmosphere. Academic Press, San Diego, 2000b, pp. 179-263.

Finlayson-Pitts BJ, Pitts Jr JN. Chapter 9 - Particles in the Troposphere. In: Finlayson-Pitts BJ, Pitts JN, editors. Chemistry of the Upper and Lower Atmosphere. Academic Press, San Diego, 2000c, pp. 349-435.

Finlayson-Pitts BJ, Pitts Jr JN. Chapter 11 - Analytical Methods and Typical Atmospheric Concentrations for Gases and Particles. In: Finlayson-Pitts BJ, Pitts JN, editors. Chemistry of the Upper and Lower Atmosphere. Academic Press, San Diego, 2000d, pp. 547-656.

Finlayson-Pitts BJ, Pitts Jr JN. Chapter 12 - Homogeneous and Heterogeneous Chemistry in the Stratosphere. In: Finlayson-Pitts BJ, Pitts JN, editors. Chemistry of the Upper and Lower Atmosphere. Academic Press, San Diego, 2000e, pp. 657-726.

Finlayson-Pitts BJ, Pitts Jr JN. Chapter 14 - Global Tropospheric Chemistry and Climate Change. In: Finlayson-Pitts BJ, Pitts JN, editors. Chemistry of the Upper and Lower Atmosphere. Academic Press, San Diego, 2000f, pp. 762-843.

Finlayson-Pitts BJ, Pitts Jr JN. CHAPTER 16 - Applications of Atmospheric Chemistry: Air Pollution Control Strategies and Risk Assessments for Tropospheric Ozone and Associated Photochemical Oxidants, Acids, Particles, and Hazardous Air Pollutants. Chemistry of the Upper and Lower Atmosphere. Academic Press, San Diego, 2000g, pp. 871-942.

Fiore A, Jacob DJ, Liu H, Yantosca RM, Fairlie TD, Li Q. Variability in surface ozone background over the United States: Implications for air quality policy. Journal of Geophysical Research: Atmospheres 2003; 108: 4787.

Fiore AM, Jacob DJ, Bey I, Yantosca RM, Field BD, Fusco AC, et al. Background ozone over the United States in summer: Origin, trend, and contribution to pollution episodes. Journal of Geophysical Research: Atmospheres 2002; 107: ACH 11-1-ACH 11-25.

Fiore AM, Oberman JT, Lin MY, Zhang L, Clifton OE, Jacob DJ, et al. Estimating North American background ozone in U.S. surface air with two independent global models: Variability, uncertainties, and recommendations. Atmospheric Environment 2014; 96: 284-300.

Fischer EV, Jaffe DA, Weatherhead EC. Free tropospheric peroxyacetyl nitrate (PAN) and ozone at Mount Bachelor: potential causes of variability and timescale for trend detection. Atmospheric Chemistry & Physics 2011; 11: 5641-5654.

Fitzgerald WF, Engstrom DR, Mason RP, Nater EA. The Case for Atmospheric Mercury Contamination in Remote Areas. Environmental Science & Technology 1998; 32: 1-7.

Friedli HR, Radke LF, Lu JY. Mercury in smoke from biomass fires. Geophys. Res. Lett. 2001; 28: 3223-3226.

Gratz LE, Jaffe DA, Hee JR. Causes of increasing ozone and decreasing carbon monoxide in springtime at the Mt. Bachelor Observatory from 2004 to 2013. Atmospheric Environment 2015; 109: 323-330.

Green MC, Chow JC, Watson JG, Dick K, Inouye D. Effects of Snow Cover and Atmospheric Stability on Winter PM2.5 Concentrations in Western U.S. Valleys. Journal of Applied Meteorology and Climatology 2015; 54: 1191-1201.

Gupta P, Christopher SA, Wang J, Gehrig R, Lee Y, Kumar N. Satellite remote sensing of particulate matter and air quality assessment over global cities. Atmospheric Environment 2006; 40: 5880-5892.

Gustin MS, Fine R, Miller M, Jaffe D, Burley J. The Nevada Rural Ozone Initiative (NVROI): Insights to understanding air pollution in complex terrain. Science of The Total Environment 2015; 530–531: 455-470.

Gustin MS, Huang J, Miller MB, Peterson C, Jaffe DA, Ambrose J, et al. Do We Understand What the Mercury Speciation Instruments Are Actually Measuring? Results of RAMIX. Environmental Science & Technology 2013; 47: 7295-7306.

Gustin MS, Pierce AM, Huang J, Miller MB, Holmes H, Loria-Salazar SM. Evidence for different reactive Hg sources and chemical compounds at adjacent valley and high elevation locations. Environmental Science & Technology 2016.

Hallinger KK, ZabransKy DJ, Kazmer KA, Cristol DA. Birdsong differs between mercury-polluted and reference sites. Los Cantos de Aves Diieren entre Sitios Contaminados con Mercurio y Sitios de Referencia. 2010; 127: 156-161.

Heald CL, Jacob DJ, Park RJ, Alexander B, Fairlie TD, Yantosca RM, et al. Transpacific transport of Asian anthropogenic aerosols and its impact on surface air quality in the United States. Journal of Geophysical Research: Atmospheres 2006; 111: n/a-n/a.

Heald CL, Ridley DA, Kroll JH, Barrett SRH, Cady-Pereira KE, Alvarado MJ, et al. Beyond direct radiative forcing: the case for characterizing the direct radiative effect of aerosols. Atmos. Chem. Phys. Discuss. 2013; 13: 32925-32961.

Hill SJaFAaFM. Basic Concepts and Instrumentation for Plasma Spectrometry. 2007: 61--97.

Holben BN, Eck TF, Slutsker I, Tanré D, Buis JP, Setzer A, et al. AERONET—A Federated Instrument Network and Data Archive for Aerosol Characterization. Remote Sensing of Environment 1998; 66: 1-16.

Holmes CD, Prather MJ, Sovde OA, Myhre G. Future methane, hydroxyl, and their uncertainties: key climate and emission parameters for future predictions. Atmospheric Chemistry and Physics 2013; 13: 285-302.

Holton JR, Hakim GJ. Chapter 2 - Basic Conservation Laws. An Introduction to Dynamic Meteorology (Fifth Edition). Academic Press, Boston, 2013a, pp. 31-66.

Holton JR, Hakim GJ. Chapter 3 - Elementary Applications of the Basic Equations. An Introduction to Dynamic Meteorology (Fifth Edition). Academic Press, Boston, 2013b, pp. 67-93.
Holton JR, Hakim GJ. Chapter 6 - Quasi-geostrophic Analysis. An Introduction to Dynamic Meteorology (Fifth Edition). Academic Press, Boston, 2013c, pp. 171-211.
Holton JR, Hakim GJ. Chapter 10 - The General Circulation. An Introduction to Dynamic Meteorology (Fifth Edition). Academic Press, Boston, 2013d, pp. 325-375.
Hsu NC, Jeong MJ, Bettenhausen C, Sayer AM, Hansell R, Seftor CS, et al. Enhanced Deep Blue aerosol retrieval algorithm: The second generation. Journal of Geophysical Research: Atmospheres 2013; 118: 9296-9315.
Hsu NC, Tsay SC, King MD, Herman JR. Deep Blue Retrievals of Asian Aerosol Properties During ACE-Asia. IEEE Transactions on Geoscience and Remote Sensing 2006; 44.
Huang J, Gustin MS. Uncertainties of Gaseous Oxidized Mercury Measurements Using KCl-Coated Denuders, Cation-Exchange Membranes, and Nylon Membranes: Humidity Influences. Environmental Science & Technology 2015; 49: 6102-6108.
Huang J, Miller MB, Weiss-Penzias P, Gustin MS. Comparison of Gaseous Oxidized Hg Measured by KCl-Coated Denuders, and Nylon and Cation Exchange Membranes. Environmental Science & Technology 2013; 47: 7307-7316.
Husar RB. Satellite-Based Measurement of Atmospheric Aerosols. Aerosol Measurement. John Wiley & Sons, Inc., 2011, pp. 667-680.
Jackson AK, Evers DC, Etterson MA, Condon AM, Folsom SB, Detweiler J, et al. Mercury exposure affects the reproductive success of a free-living terrestrial songbird, the Carolina Wren (Thryothorus ludovicianus). La Exposición al Mercurio Afecta el Éxito Reproductivo de Thryothorus ludovicianus, un Ave Canora Terrestre Silvestre. 2011; 128: 759-769.
Jacob DJ, Logan JA, Murti PP. Effect of rising Asian emissions on surface ozone in the United States. Geophysical Research Letters 1999; 26: 2175-2178.
Jaffe D. Relationship between Surface and Free Tropospheric Ozone in the Western U.S. Environmental Science & Technology 2010; 45: 432-438.
Jaffe D, Anderson T, Covert D, Kotchenruther R, Trost B, Danielson J, et al. Transport of Asian air pollution to North America. Geophysical Research Letters 1999; 26: 711-714.
Jaffe D, Price H, Parrish D, Goldstein A, Harris J. Increasing background ozone during spring on the west coast of North America. Geophysical Research Letters 2003; 30: n/a-n/a.
Jaffe DA, Lyman S, Amos HM, Gustin MS, Huang J, Selin NE, et al. Progress on Understanding Atmospheric Mercury Hampered by Uncertain Measurements. Environmental Science & Technology 2014; 48: 7204-7206.
Johnson WB, Viezee W. Stratospheric ozone in the lower troposphere —I. Presentation and interpretation of aircraft measurements. Atmospheric Environment (1967) 1981; 15: 1309-1323.
Karner AA, Eisinger DS, Niemeier DA. Near-Roadway Air Quality: Synthesizing the Findings from Real-World Data. Environmental Science & Technology 2010; 44: 5334-5344.
Kearney SP, Pierce F. Evidence of soot superaggregates in a turbulent pool fire. Combustion and Flame 2012; 159: 3191-3198.
Kleinstreuer C, Zhang Z. Airflow and Particle Transport in the Human Respiratory System. Annual Review of Fluid Mechanics 2009; 42: 301-334.
Knowland KE, Doherty RM, Hodges KI. The effects of springtime mid-latitude storms on trace gas composition determined from the MACC reanalysis. Atmos. Chem. Phys. 2015; 15: 3605-3628.

Komárek M, Ettler V, Chrastný V, Mihaljevič M. Lead isotopes in environmental sciences: A review. Environment International 2008; 34: 562-577.

Kulkarni P, Baron PA. An Approach to Performing Aerosol Measurements. Aerosol Measurement. John Wiley & Sons, Inc., 2011, pp. 55-65.

Kulkarni P, Baron PA, Sorenson CM, Harper M. Nonspherical Particle Measurement: Shape Factor, Fractals, and Fibers. Aerosol Measurement. John Wiley & Sons, Inc., 2011a, pp. 507-547.

Kulkarni P, Baron PA, Willeke K. Introduction to Aerosol Characterization. Aerosol Measurement. John Wiley & Sons, Inc., 2011b, pp. 1-13.

Kunz H, Speth P. Variability of Near-Ground Ozone Concentrations During Cold Front Passages – a Possible Effect of Tropopause Folding Events. Journal of Atmospheric Chemistry 1997; 28: 77-95.

Lamborg CH, Fitzgerald WF, Damman AWH, Benoit JM, Balcom PH, Engstrom DR. Modern and historic atmospheric mercury fluxes in both hemispheres: Global and regional mercury cycling implications. Global Biogeochem. Cycles 2002; 16: 1104.

Langford AO, Senff CJ, Alvarez Ii RJ, Brioude J, Cooper OR, Holloway JS, et al. An overview of the 2013 Las Vegas Ozone Study (LVOS): Impact of stratospheric intrusions and long-range transport on surface air quality. Atmospheric Environment 2015; 109: 305-322.

Lee HJ, Chatfield RB, Strawa AW. Enhancing the Applicability of Satellite Remote Sensing for PM2.5 Estimation Using MODIS Deep Blue AOD and Land Use Regression in California, United States. Environmental Science & Technology 2016; 50: 6546-6555.

Li J, Carlson BE, Lacis AA. Application of spectral analysis techniques in the intercomparison of aerosol data. Part II: Using maximum covariance analysis to effectively compare spatiotemporal variability of satellite and AERONET measured aerosol optical depth. Journal of Geophysical Research: Atmospheres 2014a; 119: 153-166.

Li J, Carlson BE, Lacis AA. Application of spectral analysis techniques in the intercomparison of aerosol data: Part III. Using combined PCA to compare spatiotemporal variability of MODIS, MISR, and OMI aerosol optical depth. Journal of Geophysical Research: Atmospheres 2014b; 119: 4017-4042.

Li J, Carlson BE, Lacis AA. Application of spectral analysis techniques to the intercomparison of aerosol data – Part 4: Synthesized analysis of multisensor satellite and ground-based AOD measurements using combined maximum covariance analysis. Atmos. Meas. Tech. 2014c; 7: 2531-2549.

Li J, Carlson BE, Lacis AA. How well do satellite AOD observations represent the spatial and temporal variability of PM2.5 concentration for the United States? Atmospheric Environment 2015; 102: 260-273.

Li Q, Cheng H, Zhou T, Lin C, Guo S. The estimated atmospheric lead emissions in China, 1990–2009. Atmospheric Environment 2012; 60: 1-8.

Lin J, Pan D, Davis SJ, Zhang Q, He K, Wang C, et al. China's international trade and air pollution in the United States. Proceedings of the National Academy of Sciences 2014a; 111: 1736-1741.

Lin M, Fiore AM, Horowitz LW, Cooper OR, Naik V, Holloway J, et al. Transport of Asian ozone pollution into surface air over the western United States in spring. Journal of Geophysical Research: Atmospheres 2012; 117: D00V07.

Lin M, Horowitz LW, Oltmans SJ, Fiore AM, Fan S. Tropospheric ozone trends at Mauna Loa Observatory tied to decadal climate variability. Nature Geosci 2014b; 7: 136-143.

Liu Y, Paciorek CJ, Koutrakis P. Estimating Regional Spatial and Temporal Variability of PM(2.5) Concentrations Using Satellite Data, Meteorology, and Land Use Information. Environmental Health Perspectives 2009; 117: 886-892.

Liu Y, Park RJ, Jacob DJ, Li Q, Kilaru V, Sarnat JA. Mapping annual mean ground-level PM2.5 concentrations using Multiangle Imaging Spectroradiometer aerosol optical thickness over the contiguous United States. Journal of Geophysical Research: Atmospheres 2004; 109: n/a-n/a.

Lofroth G. Minamata Disease. Methylmercury poisoning in Minamata and Niigata Japan. The Quarterly Review of Biology 1978; 53: 353-354.

Loría-Salazar SM, Holmes HA, Patrick Arnott W, Barnard JC, Moosmüller H. Evaluation of MODIS columnar aerosol retrievals using AERONET in semi-arid Nevada and California, U.S.A., during the summer of 2012. Atmospheric Environment 2016; 144: 345-360.

Loría-Salazar SM, Panorska A, Arnott WP, Barnard JC, Boehmler JaM, Holmes HA. Toward Understanding Atmospheric Physics Impacting the Relationship between Columnar Aerosol Optical Depth and Near-Surface PM2.5 Mass Concentrations in Nevada and California, U.S.A., During 2013. Atmospheric Environment 2017.

Luke W. 2016 NOAA report. 2016, 2016.

Lyman SN, Jaffe DA, Gustin MS. Release of mercury halides from KCl denuders in the presence of ozone. Atmos. Chem. Phys. 2010; 10: 8197-8204.

Malcolm EG, Keeler GJ. Evidence for a sampling artifact for particulate-phase mercury in the marine atmosphere. Atmospheric Environment 2007; 41: 3352-3359.

Malm WC, Schichtel BA, Pitchford ML. Uncertainties in PM2.5 gravimetric and speciation measurements and what we can learn from them. J Air Waste Manag Assoc 2011; 61: 1131-49.

Malm WC, Schichtel BA, Pitchford ML, Ashbaugh LL, Eldred RA. Spatial and monthly trends in speciated fine particle concentration in the United States. Journal of Geophysical Research: Atmospheres 2004; 109: D03306.

Malm WC, Sisler JF. Spatial patterns of major aerosol species and selected heavy metals in the United States. Fuel Processing Technology 2000; 65–66: 473-501.

Marple VA, Olson BA. Sampling and Measurement Using Inertial, Gravitational, Centrifugal, and Thermal Techniques. Aerosol Measurement. John Wiley & Sons, Inc., 2011, pp. 129-151.

Martin RV. Satellite remote sensing of surface air quality. Atmospheric Environment 2008; 42: 7823-7843.

McClure CD, Jaffe DA, Edgerton ES. Evaluation of the KCl Denuder Method for Gaseous Oxidized Mercury using HgBr2 at an In-Service AMNet Site. Environmental Science & Technology 2014; 48: 11437-11444.

McMurdie WL, Houze RA. 8 - Weather Systems. Atmospheric Science (Second Edition). Academic Press, San Diego, 2006, pp. 313-373.

Miller MB, Fine R, Pierce AM, Gustin MS. Identifying sources of ozone to three rural locations in Nevada, USA, using ancillary gas pollutants, aerosol chemistry, and mercury. Science of The Total Environment 2015; 530–531: 483-492.

Musselman RC, Korfmacher JL. Ozone in remote areas of the Southern Rocky Mountains. Atmospheric Environment 2014; 82: 383-390.

NASA GSFC. AERONET Aerosol Robotic Network system description. 2017, 2007.

Nguyen TKV, Ghate VP, Carlton AG. Reconciling satellite aerosol optical thickness and surface fine particle mass through aerosol liquid water. Geophysical Research Letters 2016; 43: 11,903-11,912.

NRC NRC. Rethinking the Ozone Problem in Urban and Regional Air Pollution. Washington, DC: The National Academies Press, 1991.

Nriagu JO, Pacyna JM. Quantitative assessment of worldwide contamination of air, water and soils by trace metals. Nature 1988; 333: 134-139.

Pacyna EG, Pacyna JM, Steenhuisen F, Wilson S. Global anthropogenic mercury emission inventory for 2000. Atmospheric Environment 2006; 40: 4048-4063.

Pacyna EG, Pacyna JM, Sundseth K, Munthe J, Kindbom K, Wilson S, et al. Global emission of mercury to the atmosphere from anthropogenic sources in 2005 and projections to 2020. Atmospheric Environment 2010; 44: 2487-2499.

Parrish DD, Law KS, Staehelin J, Derwent R, Cooper OR, Tanimoto H, et al. Long-term changes in lower tropospheric baseline ozone concentrations at northern mid-latitudes. Atmos. Chem. Phys. 2012; 12: 11485-11504.

Pfister GG, Walters S, Lamarque JF, Fast J, Barth MC, Wong J, et al. Projections of future summertime ozone over the U.S. Journal of Geophysical Research: Atmospheres 2014: 2013JD020932.

Pierce AM, Gustin MS, Christensen JN, Loría-Salazar SM. Use of multiple tools including lead isotopes to decipher sources of ozone and reactive mercury to urban and rural locations in Nevada, USA. Science of The Total Environment 2017; 615: 1411-1427.

Prinn RG. 5.1 - Ozone, Hydroxyl Radical, and Oxidative Capacity. In: Holland HD, Turekian KK, editors. Treatise on Geochemistry (Second Edition). Elsevier, Oxford, 2014, pp. 1-18.

Ramsey NR, Klein PM, Moore Iii B. The impact of meteorological parameters on urban air quality. Atmospheric Environment 2014; 86: 58-67.

Rasmussen DJ, Hu J, Mahmud A, Kleeman MJ. The Ozone–Climate Penalty: Past, Present, and Future. Environmental Science & Technology 2013; 47: 14258-14266.

Reuer MK, Weiss DJ. Anthropogenic lead dynamics in the terrestrial and marine environment. Philosophical Transactions of the Royal Society of London. Series A: 				Mathematical, Physical and Engineering Sciences 2002; 360: 2889.

Rieder HE, Frossard L, Ribatet M, Staehelin J, Maeder JA, Di Rocco S, et al. On the relationship between total ozone and atmospheric dynamics and chemistry at mid-latitudes - Part 2: The effects of the El Niño/Southern Oscillation, volcanic eruptions and contributions of atmospheric dynamics and chemistry to long-term total ozone changes. Atmospheric Chemistry and Physics 2013a; 13: 165-179.

Rieder HE, Frossard L, Ribatet M, Staehelin J, Maeder JA, Di Rocco S, et al. On the relationship between total ozone and atmospheric dynamics and chemistry at mid-latitudes – Part 2: The effects of the El Niño/Southern Oscillation, volcanic eruptions and contributions of atmospheric dynamics and chemistry to long-term total ozone changes. Atmos. Chem. Phys. 2013b; 13: 165-179.

Roland S. 9 - The Atmospheric Boundary Layer. Atmospheric Science (Second Edition). Academic Press, San Diego, 2006, pp. 375-417.

Rotach MW, Zardi D. On the boundary-layer structure over highly complex terrain: Key findings from MAP. Quarterly Journal of the Royal Meteorological Society 2007; 133: 937-948.

Rutter AP, Schauer JJ. The effect of temperature on the gas–particle partitioning of reactive mercury in atmospheric aerosols. Atmospheric Environment 2007; 41: 8647-8657.
Sanderson MG, Jones CD, Collins WJ, Johnson CE, Derwent RG. Effect of Climate Change on Isoprene Emissions and Surface Ozone Levels. Geophysical Research Letters 2003; 30: 1936.
Sayer AM, Hsu NC, Bettenhausen C, Jeong MJ. Validation and uncertainty estimates for MODIS Collection 6 “Deep Blue” aerosol data. Journal of Geophysical Research: Atmospheres 2013; 118: 7864-7872.
Schroeder WH, Munthe J. Atmospheric mercury - An overview. Atmospheric Environment 1998; 32: 809-822.
Shacklette HT, Boerngen JG. Element Concentrations

in Soils and Other Surficial Materials of the Conterminous United

States. U.S. Geological Survey Professional Paper 1270, U.S.

Government Printing Office, Washington D.C., 1984.
Shia R-L, Seigneur C, Pai P, Ko M, Sze ND. Global simulation of atmospheric mercury concentrations and deposition fluxes. J. Geophys. Res. 1999; 104: 23747-23760.
Sillman S. The relation between ozone, NOx and hydrocarbons in urban and polluted rural environments. Atmospheric Environment 1999; 33: 1821-1845.
Slemr F, Schuster G, Seiler W. Distribution, speciation, and budget of atmospheric mercury. Journal of Atmospheric Chemistry 1985; 3: 407-434.
Slemr FA, H. Dommergue, A. Magand, O. Barret, M. Weigelt, A. Ebinghaus, R. Brunke, E.-G. Pfaffhuber, K. Edwards, G. Howard, D. Powell, J. Keywood, M. Wang, F. Comparison of mercury concentrations measured at several sites in the Southern Hemisphere. Atmospheric Chemistry and Physics Discussions 2014; 14: 30611-30637.
Solomon PA, Crumpler D, Flanagan JB, Jayanty RKM, Rickman EE, McDade CE. U.S. National PM2.5 Chemical Speciation Monitoring Networks—CSN and IMPROVE: Description of networks. Journal of the Air & Waste Management Association 2014; 64: 1410-1438.
Sorek-Hamer M, Kloog I, Koutrakis P, Strawa AW, Chatfield R, Cohen A, et al. Assessment of PM2.5 concentrations over bright surfaces using MODIS satellite observations. Remote Sensing of Environment 2015; 163: 180-185.
Sorek-Hamer M, Strawa AW, Chatfield RB, Esswein R, Cohen A, Broday DM. Improved retrieval of PM2.5 from satellite data products using non-linear methods. Environmental Pollution 2013; 182: 417-423.
Stevenson D, Doherty R Fau - Sanderson M, Sanderson M Fau - Johnson C, Johnson C Fau - Collins B, Collins B Fau - Derwent D, Derwent D. Impacts of climate change and variability on tropospheric ozone and its precursors. 2005.
Stevenson DS, Dentener FJ, Schultz MG, Ellingsen K, van Noije TPC, Wild O, et al. Multimodel ensemble simulations of present-day and near-future tropospheric ozone. Journal of Geophysical Research: Atmospheres 2006; 111: n/a-n/a.
Stohl A, Eckhardt S, Forster C, James P, Spichtinger N, Seibert P. A replacement for simple back trajectory calculations in the interpretation of atmospheric trace substance measurements. Atmospheric Environment 2002; 36: 4635-4648.

Stohl A, Forster C, Eckhardt S, Spichtinger N, Huntrieser H, Heland J, et al. A backward modeling study of intercontinental pollution transport using aircraft measurements. Journal of Geophysical Research: Atmospheres 2003; 108: n/a-n/a.

Strawa AW, Chatfield RB, Legg M, Scarnato B, Esswein R. Improving retrievals of regional fine particulate matter concentrations from Moderate Resolution Imaging Spectroradiometer (MODIS) and Ozone Monitoring Instrument (OMI) multisatellite observations. Journal of the Air & Waste Management Association 2013; 63: 1434-1446.

Swartzendruber PC, Jaffe DA, Prestbo EM, Weiss-Penzias P, Selin NE, Park R, et al. Observations of reactive gaseous mercury in the free troposphere at the Mount Bachelor Observatory. Journal of Geophysical Research: Atmospheres 2006; 111: n/a-n/a.

Tarasick DW, Slater R. Ozone in the troposphere: Measurements, climatology, budget, and trends. Atmosphere-Ocean 2008; 46: 93-115.

Taylor HE. Chapter 4 - Instrumentation. Inductively Coupled Plasma-Mass Spectrometry. Academic Press, San Diego, 2001a, pp. 29-51.

Taylor HE. Chapter 5 - Sample Introduction. Inductively Coupled Plasma-Mass Spectrometry. Academic Press, San Diego, 2001b, pp. 53-90.

Thielmann A, Prévôt ASH, Grüebler FC, Staehelin J. Empirical ozone isopleths as a tool to identify ozone production regimes. Geophysical Research Letters 2001; 28: 2369-2372.

U.S. EPA. National Ambient Air Quality Standards (NAAQS) for lead (Pb). 2017, 2016.

U.S. EPA USEPA. Mercury. 2012, 2011.

U.S. EPA USEPA. National Ambient Air Quality Standards (NAAQS). 2014, 2012a.

U.S. EPA USEPA. Our Nation's Air: status and trends through 2010, Research Triangle Park, NC, 2012b.

U.S. EPA USEPA. Particulate Matter (PM). 2014, 2013.

U.S. EPA USEPA. List of designated reference and equivalent methods. Office of Research and Development, Research Triangle Park, NC, USA, 2014.

U.S. EPA USEPA. 2014 National Emissions Inventory (NEI) Data. 2017, 2017a.

U.S. EPA USEPA. Lead. 2017, 2017b.

U.S. EPA USEPA. Ozone, 2017c.

U.S. EPA USEPA. Treatment of air quality data influenced by exceptional events. 2017, 2017d.

US EPA USEPA. Ozone, 2013.

van Donkelaar A, Martin RV, Park RJ. Estimating ground-level PM2.5 using aerosol optical depth determined from satellite remote sensing. Journal of Geophysical Research: Atmospheres 2006; 111: n/a-n/a.

VanCuren RA. Asian aerosols in North America: Extracting the chemical composition and mass concentration of the Asian continental aerosol plume from long-term aerosol records in the western United States. Journal of Geophysical Research: Atmospheres 2003; 108: 4623.

VanCuren RA, Cliff SS, Perry KD, Jimenez-Cruz M. Asian continental aerosol persistence above the marine boundary layer over the eastern North Pacific: Continuous aerosol measurements from Intercontinental Transport and Chemical Transformation 2002 (ITCT 2K2). Journal of Geophysical Research: Atmospheres 2005; 110: D09S90.

Viezee W, Johnson WB, Singh HB. Stratospheric ozone in the lower troposphere—II. Assessment of downward flux and ground-level impact. Atmospheric Environment (1967) 1983; 17: 1979-1993.

Vingarzan R. A review of surface ozone background levels and trends. Atmospheric Environment 2004; 38: 3431-3442.

Wagner JS, Gohm A, Rotach MW. The impact of valley geometry on daytime thermally driven flows and vertical transport processes. Quarterly Journal of the Royal Meteorological Society 2015; 141: 1780-1794.

Walder AJ, Freedman PA. Communication. Isotopic ratio measurement using a double focusing magnetic sector mass analyser with an inductively coupled plasma as an ion source. Journal of Analytical Atomic Spectrometry 1992; 7: 571-575.

Wallace JM, Hobbs PV. 7 - Atmospheric Dynamics. Atmospheric Science (Second Edition). Academic Press, San Diego, 2006, pp. 271-311.

Wang J, Christopher SA. Intercomparison between satellite-derived aerosol optical thickness and PM2.5 mass: Implications for air quality studies. Geophysical Research Letters 2003; 30: n/a-n/a.

Washoe County N. Air Quality Trends (2007-2016). Washoe County Heath District Air Quality Management Division, 2017.

Watson JG, Chow JC. Ambient Aerosol Sampling. Aerosol Measurement. John Wiley & Sons, Inc., 2011, pp. 591-613.

Weiss-Penzias P, Gustin MS, Lyman SN. Observations of speciated atmospheric mercury at three sites in Nevada: Evidence for a free tropospheric source of reactive gaseous mercury. Journal of Geophysical Research-Atmospheres 2009; 114: -.

White WM, Albarède F, Télouk P. High-precision analysis of Pb isotope ratios by multi-collector ICP-MS. Chemical Geology 2000; 167: 257-270.

WHO WHO. Ambient (outdoor) air quality and health. 2017, 2016.

Wilkening KE, Barrie LA, Engle M. Trans-Pacific Air Pollution. Science 2000; 290: 65.

WRCC WRCC. Climate of Nevada. 2014, 2014a.

WRCC WRCC. Climate of Nevada. 2014, 2014b.

Wyman KE, Rodenhouse NL, Bank MS. Mercury Bioaccumulation, speciation, and influence on web structure in orb-weaving spiders from a forested watershed. Environmental Toxicology and Chemistry 2011; 30: 1873-1878.

Zerefos CS, Bais AF, Ziomas IC, Bojkov RD. On the relative importance of quasi-biennial oscillation and El Nino/Southern Oscillation in the revised Dobson total ozone records. Journal of Geophysical Research: Atmospheres 1992; 97: 10135-10144.

Zhang J, Reid JS. MODIS aerosol product analysis for data assimilation: Assessment of over-ocean level 2 aerosol optical thickness retrievals. Journal of Geophysical Research: Atmospheres 2006; 111: n/a-n/a.

Zhang K, Batterman S. Air pollution and health risks due to vehicle traffic. Science of The Total Environment 2013; 450: 307-316.

Zhang L, Jacob DJ, Yue X, Downey NV, Wood DA, Blewitt D. Sources contributing to background surface ozone in the US Intermountain West. Atmos. Chem. Phys. 2014; 14: 5295-5309.

Chapter 2

Development of a particulate mass measurement system for quantification of ambient reactive mercury

Ashley M. Pierce*, Mae Sexauer Gustin

Department of Natural Resources and Environmental Sciences, University of Nevada, Reno, 1664 N. Virginia St. Reno, NV, USA 89557
*Corresponding Author: Ashley M. Pierce, ash.pie4@gmail.com, phone: (775) 784-4020, fax: (775) 784-4583

Published: *Environmental Science & Technology* (Web: 2016, Print: 2017)

Appendix A: Supplemental Information, 26 pages, 3 Tables, and 19 Figures

Table of Contents Graphic

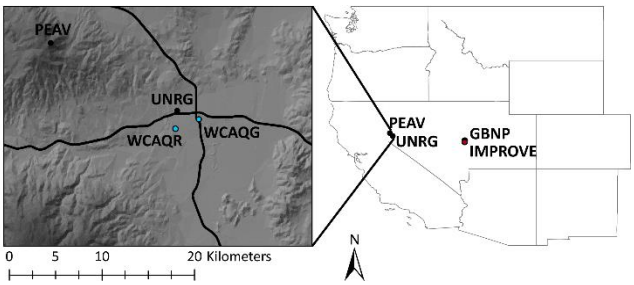

Abbreviations:

BAM: β Attenuation Method
CEM: Cation exchange membrane
CVAFS: Cold vapor atomic fluorescence spectroscopy
EBAM: Environmental β Attenuation Method
FEM: Federal equivalent method
FRM: Federal reference method
GBNP: Great Basin National Park, NV
GOM: Gaseous oxidized mercury
IMPROVE: Interagency Monitoring of Protected Environments Network
NDEP: Nevada Department of Environmental Protection
PBM: Particulate bound mercury
PEAV: Peavine Peak, NV
PM: Particulate matter
$PM_{2.5}$: Particulate matter (<2.5 μm in diameter)
RM: Reactive mercury (PBM+GOM)
TAPI: Teledyne Advanced Pollution Instrumentation
UNRG: University of Nevada, Reno Agricultural Experiment Station Greenhouse Facilities
UNRRMAS: University of Nevada, Reno-Reactive Mercury Active System
WCAQG: Washoe County Air Quality, Galletti monitoring site
WCAQR: Washoe County Air Quality, Reno monitoring site

Abstract:

The Teledyne Advanced Pollution Instrumentation (TAPI) Model 602 Beta^{Plus} particulate system provides non-destructive analysis of particulate matter ($PM_{2.5}$) mass concentration. This instrument was used to determine if measurements made with cation exchange membranes (CEM) were comparable to standard methods, the β attenuation method at two locations in Reno, NV, USA and an environmental β attenuation method and gravimetric method at Great Basin National Park, NV, USA. TAPI $PM_{2.5}$ CEM measurements were statistically similar to the other three $PM_{2.5}$ methods. Once this was established, the second objective, a destructive method for measurement of reactive mercury (RM=gaseous oxidized and particulate bound Hg), was tested. Samples collected at 16.7 liters per min (Lpm) for 24 h on CEM from the TAPI were compared to those measured by the University of Nevada, Reno-Reactive Mercury Active System (UNRRMAS, 1 Lpm) CEM and a Tekran® 2537/1130/1135 system (7 Lpm). Given the use of CEM in the TAPI and UNRRMAS, we hypothesized that both should collect RM. Due to the high flow rate and different inlets, TAPI data were systematically lower than the UNRRMAS. Correlation between RM concentrations demonstrated that the TAPI may be used to estimate 24 h resolution RM concentrations in Nevada.

Keywords: Beta attenuation, $PM_{2.5}$, UNRRMAS, Tekran, intercomparison

Introduction:

Recent studies involving the standard instrument (Tekran 2537/1130/1135), applied across the globe, to measure gaseous elemental mercury (GEM), gaseous oxidized mercury (GOM), and particulate bound mercury (PBM), are problematic[1-9]. Concentrations are operationally defined, and in the case of GOM and PBM, no standards are available for use in calibration[7, 10]. Experiments with co-located Tekran 2537 instruments measuring GEM have shown an average systematic uncertainty of about 10% and in some extreme cases up to 28%[8, 11]. The KCl-coated denuder in the Tekran 1130 unit for measuring GOM collects different compounds of GOM (Hg II and possibly I) with different efficiencies, and has interferences with ozone and water vapor[3, 5, 7-10]. There is also evidence of uncertain PBM measurements due to evaporation, temperature, and interference with other atmospheric constituents[7, 9, 12, 13]. It is possible that Tekran measurements can be adjusted for the low concentration bias; however, calibration and improvement of measurement techniques and development of new sampling methods are critical[6, 7, 14, 15].

The 602 Beta^{Plus} particulate system (Model 602, Teledyne® Advanced Pollution Instrumentation [TAPI]) is a unique instrument that allows collection of particulate matter (PM) on a filter analyzed for PM mass concentration non-destructively via β attenuation[16]. Knowledge of the chemical composition of PM sampled is not necessary for instrument calibration or measurements.

The β attenuation method allows analyses of PM mass concentration directly after a sample has been collected. Immediate analysis is important due to positive (e.g. adsorption of organic vapors) and negative (e.g. volatilization of organic aerosols)

sampling artifacts that occur with filter samples[17-19]. β attenuation instruments have been shown to measure 20-50% higher $PM_{2.5}$ mass concentration than collocated FRM (Federal Reference Method) samplers, such as gravimetric methods, due to moisture accumulation on particulate matter during periods of high relative humidity (RH)[20]. Due to this, β attenuation instruments generally include heaters to maintain RH at certain levels during measurement.

Negative artifacts are particularly important for comparison with gravimetric measurements (used in the Interagency Monitoring of Protected Environments [IMPROVE] network) where filters (Teflon) are weighed in temperature- and RH-controlled laboratories prior to deployment and after a sample is collected[21]. But because filters are processed days to weeks after sample collection, volatilization of chemical compounds can occur (e.g. ammonium nitrate and ammonium chloride), and therefore lower measurements have been observed on filter samples that remain at room temperature for extended periods before processing[19, 22].

For this project, TAPI $PM_{2.5}$ measurements using CEM were compared to established methods, gravimetric and beta attenuation, which use Teflon and glass fiber filters, respectively. The CEM is not the standard filter used in this method and the instrument had to be adjusted to correct for the pressure drop across the CEM that differed from that associated with the glass fiber filters. Comparisons were done to verify that $PM_{2.5}$ collected with the CEM in the TAPI were comparable to other instruments typically used in the field. In addition, the non-destructive nature of β attenuation allows for post-processing of filter material to understand chemistry and potential sources of

$PM_{2.5}$. Samples were post-processed for Hg concentrations. This system was tested as a potentially new way of measuring ambient GOM and PBM.

There were two research hypotheses for this study: (1) if the CEM (instead of conventional glass fiber filters) in the TAPI measured $PM_{2.5}$ accurately compared to established methods, then data collected on these filters could be used to quantify specific constituents present in the $PM_{2.5}$ samples, in this case RM concentrations; and (2) due to different analytical configurations (i.e. flow rates, inlets, and sampling methods) RM concentrations measured by the different instruments will not be the same. Additionally, given the resolution of the TAPI measurement (24 h), RM and further post-processing of a second inlet filter for Pb isotope ratios (not presented here) could aid in elucidation of sources of pollution.

$PM_{2.5}$ data from the TAPI CEM measurements at the University of Nevada, Reno Agriculture Experiment Station Greenhouse Facilities (UNRG) were compared with those collected using a β Attenuation Monitor (BAM-1020, MetOne instruments, Inc. Grants Pass, OR, USA) located at the Washoe County Air Quality Management sites in Reno (Galletti and Reno; WCAQG, WCAQR). TAPI $PM_{2.5}$ data from Great Basin National Park (GBNP), NV, USA were compared to an Environmental β Attenuation Monitor (EBAM-9800 Rev L, MetOne Instruments, Inc.) and gravimetrically measured $PM_{2.5}$ data from the IMPROVE network (Table 1).

Reactive Hg data from the TAPI CEM measurements collected at UNRG were compared with those collected using CEM in the University of Nevada, Reno-Reactive Mercury Active System (UNRRMAS) and a Tekran 2537/1130/1135 speciation system (Tekran Inc., Toronto, Canada). Data from the TAPI RM measurements collected at

Peavine Peak (PEAV), just outside of Reno, were compared with those collected using the UNRRMAS. Data were collected with a TAPI located at GBNP for six months.

Measurement sites:

See Table 1, the supplemental information (Fig. SI 1) and graphical abstract for more detailed information.

Table 1: Measurement sites and measurements made at each, $PM_{2.5}$ and RM median concentrations and range.

Site	Elevation (m) Lat (N), Lon (W)	Code	Measurements (n)	Sample Period	$PM_{2.5}$ ($\mu g\ m^{-3}$) Median (range)	RM ($pg\ m^{-3}$) Median (range)
Nevada Agricultural Experiment Station Greenhouse Facilities, Reno	1371 39.5374, 119.8044	UNRG	TAPI 131 (n=387)	04/2014, 06/2014-10/2015	7 (0.0-63)	22 (0.1-121)
			TAPI 135 (n=114)	11/2013, 04/2014, 05/2014 11/2014-03/2015	8 (0.4-33)	-
			UNRRMAS (n=42)	06/2014-10/2015	-	71 (19-213)
			Tekran (n=310)	06/2014-10/2015	-	24 (0.0-156)
Peavine Peak, Reno	2513 39.5895, 119.9290	PEAV	TAPI 135 (n=158)	06/2014-11/2014	5 (0.0-75)	36 (1.4-147)
			UNRRMAS (n=12)	06/2014-11/2014	-	129 (48-288)
Great Basin National Park	2061 39.0052, 114.2161	GBNP	TAPI 135 (n=171)	03/2015-10/2015	4 (0.3-21)	38 (3-134)
			IMPROVE (n=72)		3 (0.8-19)	-
			E-BAM (n=388)		3 (0.2-14)	-
Washoe County Air Quality Management Galletti	1369 39.5320, 119.7850	WCAQG	BAM (n=381)	06/2014-11/2014	6 (0.5-100)	-
Washoe County Air Quality Management Reno	1368 39.5251, 119.8077	WCAQR	BAM (n=698)	06/2014-present	7 (0.1-101)	-

The University of Nevada, Reno Agricultural Experiment Station Greenhouse Facilities (UNRG, 1371 m, Table 1) is located in the Reno/Sparks metropolitan area 0.1 km north of Interstate 80, 1.5 km west of U.S. Route 395, and 1.3 km northeast of downtown Reno (39.5374 N, 119.8044 W; see graphical abstract and Fig. SI 1). Reno is

located in a topographic bowl that experiences winter inversions and high convective mixing through the year that promotes down mixing of free tropospheric air[23].

Peavine Peak, Reno (PEAV, 2513 m, Table 1) is located above tree level in a sage/steppe ecosystem at the summit, ~15 km east of the Sierra Nevada Mountain range and ~12 km northwest of UNRG (39.5895 N, 119.9290 W, see graphical abstract).

Great Basin National Park, Nevada (GBNP) is located in eastern Nevada, close to the Utah border on the east side of the Snake Range (Table 1). The sampling site was located at the convergence of two valleys with airflow in the area influenced by solar radiation and upslope/downslope flows. Surrounding vegetation consists of pinyon/juniper forest vegetation (39.0052 N, 114.2161 W, see graphical abstract). The UNR/Nevada Division of Environmental Protection (NDEP) air-sampling trailer was located next to a National Park System operated IMPROVE site.

The Washoe County Air Quality Galletti (WCAQG) site was located 0.6 km south of Interstate 80, 0.15 km east of U.S. Route 395, and 1.9 km southeast of UNRG. The Washoe County Air Quality Reno (WCAQR) site is located 1.3 km south of I-80, 2 km west of U.S. Route 395 and 1.4 km southwest of UNRG. The WCAQ Galletti site, though closer to UNRG site with similar sources, went offline on November 18, 2014, which is why both the Galletti and Reno WCAQ sites were used here.

Methods

Particulate measurements

The TAPI 602Beta^{Plus} measured $PM_{2.5}$ through two separate inlets. $PM_{2.5}$ concentrations were based on recovery of β particles emitted by ^{14}C passing through the

CEM filter measured with a Geiger-Müller counter (see Fig. 1 and SI for more detail). Inlets consisted of a 10 µm pre-impactor and a 2.5 µm cyclone in series connected to 2.1 and 1.7 m long anodized aluminum (25.4 mm outer diameter [O.D.]) sample inlets. Sample inlets had a condensation water trap just above a sample line heater used to maintain RH of the sample air stream. The sample line heater was preset to activate at 40% RH and deactivate at 30% RH[16]. The instrument was set to make measurement through a CEM filter every 24h, and then the sample was rotated out and stored in a filter holder (unloader, Fig 1). This provided a means of storing samples for up to four weeks. These filters were then available for further processing.

In this instrument, ambient air was collected for 24 h at a flow rate of 16.7 liters per min (Lpm) simultaneously on two filter mediums, 47 mm cation exchange membranes for RM (CEM; Pall Corporation, PN: MSTGS3R; pore size: 0.2 µm) and 47 mm Teflon for Pb (data not discussed here). This differs from the typical deployment scheme that uses glass fiber filters. Thus, for both filters Teledyne needed to make adjustments and test for an adequate pressure drop across both membranes. Nylon membranes (0.2 µm pore, Cole Parmer) did not work. To further account for RH a reference CEM filter was automatically used throughout the sample process to allow for correction of humidity effects on the sample filter[16]. The manufacturer reported detection limit for $PM_{2.5}$ measurements was 0.3 µg m^{-3} for 24 h[16].

Leak tests of the pneumatic circuit, span checks of the β source, and calibration of the flow rate system occurred automatically at the start of each sampling period for both sample lines. Sample inlets were cleaned monthly, and pumps rebuilt every 6 months following instructions from the instrument manual[16]. The TAPI is a Federal Equivalent

Method (FEM) and has been reported by the manufacturer to produce similar observations as the FRM methods[16]. Individual CEM filters were loaded into cartridges specific to the TAPI and then placed in the loader for sampling (Fig. 1) Filters were collected from the unloader filter holder every one to four weeks, depending on the ease of access to sites. Filters were removed from cartridges using clean tweezers, into a 125 mL soda-lime glass jar and then stored in a freezer at -22 º C until analyzed. Data during maintenance or other data collection issues were not used.

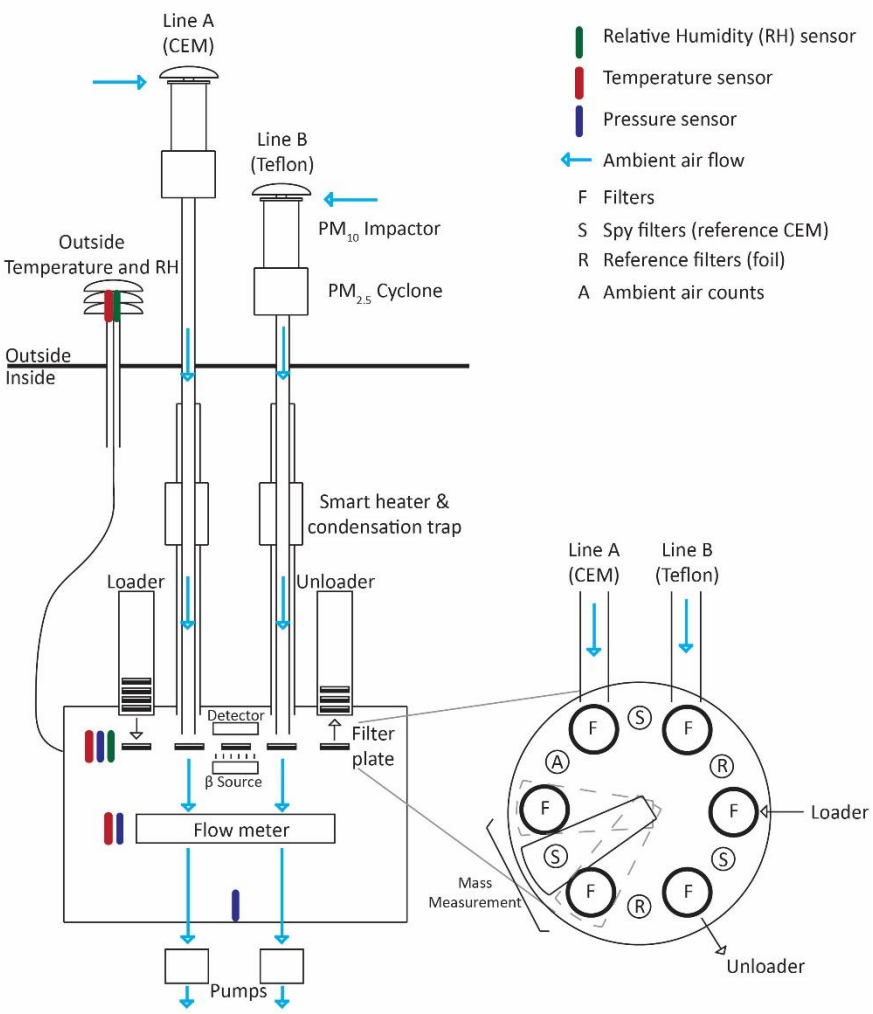

Figure 1: Diagram of the Teledyne Advanced Pollution Instrumentation (TAPI) Model 602 Beta^{Plus} particulate system. The TAPI consists of two inlets with PM_{10} impactors and $PM_{2.5}$ cyclones. The loader adds filters to the filter plate. After sampling and mass measurement, samples were moved to the unloader for collection. The filter plate holds six filters (F) at a time. The plate rotates as needed. Spy filters (S) consist of CEM material and were used to adjust for RH throughout sampling. Reference filters (R) consist of two different aluminum membranes with known surface mass density used for β calibration (β span test). Ambient air β counts (A) are measured through a hole in the filter plate. The mass measurement setup rotates between two filters and a spy filter while another two filters collect sample. Filters five and six are loaded and unloaded as necessary.

$PM_{2.5}$ data collected using the TAPI with CEM was compared with three methods. 1) The automatic β attenuation monitor (BAM-1020) manufactured by MetOne Instruments is an FEM for measuring PM. Particulate matter is collected at 16.7 Lpm for 24 h on glass fiber filter tape (pore size 0.2 µm). The BAM-1020 measured β particles emitted by ^{14}C decay through the filter with a scintillation device located in a photomultiplier tube using the same theory as the TAPI above (also see SI). The BAM-1020 consists of a smart heater that maintains RH, at the measurement point, at or below 35% to address measurement biases due to RH[20]. The BAM-1020 has a reported detection limit of <1.0 µg m^{-3} for 24 h averaged measurements[20]. Washoe County Air Quality Management, following regulations for monitoring criteria pollutants set by the U.S. EPA, operated BAM-1020s.

2) The Environmental β Attenuation Monitor (EBAM-9800), a portable version of the BAM-1020, also uses β attenuation to collect β particles from a ^{14}C source. A scintillation detector counted the β particles coming through the glass fiber filter tape (pore size 0.2 µm) at 16.7 Lpm. The E-BAM is not currently designated as a FEM for continuous $PM_{2.5}$ monitoring, but it is designed to estimate FRM or FEM concentration measurements when operated according to the manual[24]. The E-BAM also had a smart heater that maintained RH, at the measurement point, at or below 45% to address measurement biases due to RH[24]. The system was set up to measure for 24 h. The reported detection limit of the E-BAM was <1.2 µg m^{-3} for 24 h averaged measurements[24]. Operational limitations, listed in the manual, include an elevated particulate concentration value during increased levels of RH. An E-BAM $PM_{2.5}$ unit was

operated at GBNP by the Nevada Division of Environmental Protection (NDEP) during this study.

3) The Clean Air Act requires the National Park Service and other Federal Land Managers to protect visibility in Class I areas. This includes National Parks and Wilderness Areas. IMPROVE is considered an FRM for $PM_{2.5}$ measurements. According to IMPROVE data analyses, reconstructed particulate mass correlates well with gravimetric mass, and accounts for most of the fine mass, however about 20% of the missing mass could be nitrate or residual water on the particles[25]. Data from the inlet with a Teflon filter that collects most of the $PM_{2.5}$ data were used here[25]. Ambient air was sampled each week on Wednesday and Saturday from midnight to midnight, local time. Sample filters are weighed in temperature- and RH- controlled laboratories before and after sampling, the difference being $PM_{2.5}$ mass that is divided by sample volume to attain the air concentration[21].

Mercury Measurements

Two TAPI instruments ID#s 131 and 135 were used. CEM in these instruments were used to quantify RM after $PM_{2.5}$ measurements. Cation exchange membranes are generally used for separation purposes in aqueous phase applications[26, 27]; however, recent studies have used CEM for measurement of atmospheric Hg[5, 28, 29]. CEM in this study were a hydrophilic, polyethersulfone membrane with a neutral surface designed for proton exchange[5]. TAPI samples were collected every 24 h automatically by the instrument and stored.

The UNRRMAS measured RM by continuously pulling sample air, at 1 Lpm, through two CEM filters in-line held in separate filter packs[5, 15] An adjustable t-joint was used to adjust flow to 1 Lpm (Fig. SI 2). The flow rate was measured before and after sampling by a calibrated flow meter (Sierra Instruments Top Trak 820). Filters were collected every one to four weeks using clean tweezers, stored in individual 125 mL soda-lime glass jars until analyzed.

CEM filters were digested and then analyzed using an automated Tekran 2600 instrument following EPA method 1631 for total Hg concentrations. See SI for more detailed information. The method detection limit for the CEM (3 x standard deviation of blanks, excluding outliers using the 75th percentile as a specific value) was 0.3 ng[15].

The Tekran Hg measurement system consists of separate units for analyzing GEM (2537), GOM (1130), and PBM (1135) concentrations as operationally defined. The Tekran 2537 is a semi-continuous Hg analyzer that uses gold amalgamation to pre-concentrate ambient GEM on two gold traps sequentially for 5 min. Traps were heated to thermally desorb the GEM into a stream of inert carrier gas (argon) for analysis via cold vapor atomic fluorescence spectroscopy (CVAFS). The Tekran 2537 has a reported detection limit of 0.1 ng m^{-3} at a 5 min time resolution[30].

The Tekran 1130 consists of a KCl-coated annular denuder that collected GOM from ambient air for 1 h. Mercury on the denuder is then desorbed at 500 ºC to remove GOM from the denuder as GEM and then analyzed by the 2537 unit. The Tekran 1135 collected PBM on quartz chips in a pyrolyzer that was heated to 800 ºC to convert PBM to GEM, again analyzed by the 2537 unit. The desorption cycle was 1 h, creating a 2 h sample cycle. The reported detection limit for the 1130 and 1135 is 2 pg m^{-3} for a 2 h

sample[30]. There are significant concerns with measurements from these instruments as discussed in the introduction[7].

CEM tests

To test for the potential loss of RM to the TAPI inlet, tests were performed to compare measurements made with shorter inlets using filter packs designed to hold two filters inline (Savillex, Eden Praire, MN, USA, P/N: 402-21-47-22-21-2) deployed adjacent to the TAPI inlet. Filter pack inlets consisted of a 2.5 cm length Teflon tube to reduce surface area for RM and $PM_{2.5}$ to deposit. A vacuum pressure pump (Thermo Scientific, P/N: 420-1901) pulled ambient air through the two CEM in each filter pack at 16.7 Lpm. An adjustable t-joint controlled flow, measured by a flow meter (BGI MesaLabs, Butler, NJ, USA, TetraCal). Filters were collected after 24 h using clean tweezers and stored in individual 125 mL soda-lime glass jars at -22 °C until analyzed.

Experiments were performed to understand breakthrough behavior of RM on the CEM. Due to the 0.2 µm pore size of the filters, breakthrough will most likely consist of volatile GOM species, not PBM. Breakthrough on this system is therefore an effective breakthrough that will differ due to possible differences in chemical species with space and time. This effective breakthrough will be referred to as breakthrough for the remainder of the study. Breakthrough was calculated as the percent of total RM collected on the second filter in the UNRRMAS. Gustin et al. found this to be 25%[15]. This was checked using an automated calibrator developed by Lyman et al.[14]. This instrument allowed automatic permeation of two different RM compounds ($HgCl_2$ and $HgBr_2$) in ambient air with two CEM filters in two separate filter packs in-line. A vacuum pressure

pump pulled ambient air and the permeation flow through the filters at 1 Lpm for different lengths of time, creating different concentrations of RM. Breakthrough greater than 40% of the total RM collected was considered bad data most likely due to a ripped filter or a loose filter pack (see SI for more detail).

Retention of RM on the CEM over time was investigated by loading filters using the automated calibration system. Fifteen CEM filters were loaded with $HgCl_2$ for 20 seconds using the calibrator. Three filters were analyzed immediately to determine how much $HgCl_2$ was collected on the filters. Three blank filters were also analyzed immediately. Three of the loaded filters were kept in jars for one week, and three for two weeks. Six inlets (ambient air at 1 Lpm) were setup to collect ambient air through three loaded filters for one week and three inlets for two weeks with unloaded back up filters (total of six loaded CEM and six back up unloaded CEM). The UNRRMAS system was setup to collect ambient air through three inlets for one week and three inlets for two weeks with back up filters (total of six ambient CEM and six back up CEM). This allowed us to compare ambient measurements to measurements from the loaded filters with ambient air pulled through for the same sample period (one week and two weeks). Filters were analyzed immediately after collection to determine RM concentrations.

Meteorological data

Meteorological data at the UNRG were obtained from the Western Regional Climate Center (WRCC) UNR Valley Road Weather Station in hourly and daily averages (Figure SI 1). The WRCC station was located on the north and opposite side of the

UNRG from the TAPI instruments and highways. Specific humidity (SH) was calculated using RH, temperature, and pressure from the WRCC and TAPI data (See Eq. SI 2).

Data processing

Python, Microsoft Excel, the R program, and Adobe Illustrator provided data visualization and statistical analysis. ArcGIS provided map visualization. Although ambient air data in this study were not normally distributed (See Fig. SI 3 and Table SI 1, 2, and 3), ANOVA tests compare means and are generally robust to the assumption of normality with large enough datasets.

Results and Discussion

Table 1 contains median and concentration ranges for $PM_{2.5}$ and RM at all sites.

Tests of the TAPI reconfiguration for $PM_{2.5}$ measurements

ANOVA single factor tests for the TAPI instruments at UNRG compared to the BAM-1020 located at the WCAQ Galletti and Reno locations had p-values >0.05 indicating that the $PM_{2.5}$ data were similar. Data from TAPI 131 and 135, and the WCAQ stations were significantly correlated. Data from TAPI 131 and the WCAQ Galletti and Reno stations had r^2 of 0.89 (p-value<0.05, n=141, Fig. SI 4a) and 0.84 (p-value<0.05, n=385, Fig. SI 4b), respectively. The TAPI 135 and the WCAQ Galletti and Reno had r^2=0.83 (p-value<0.05, n=25, Fig. SI 4c) and 0.63 (p-value<0.05, n=114, Fig. SI 4d), respectively.

The TAPI 135 and the EBAM run by NDEP at GBNP means were similar (ANOVA $p>0.05$) and had good correlation ($r^2=0.63$, p-value<0.05, n=120, Fig. SI 5).

The TAPI 135 at GBNP and IMPROVE data had good correlation ($r^2=0.96$, p-value<0.05, n=59, Fig. SI 6) and similar means (ANOVA p-value>0.05).

These $PM_{2.5}$ similarities and correlations support the first hypothesis that the CEM in the TAPI measured $PM_{2.5}$ accurately compared to established methods. The second hypothesis could then be tested with respect to whether data collected on these filters could be used to quantify different constituents present in the $PM_{2.5}$ samples, such as RM.

Comparison of the UNRG TAPI $PM_{2.5}$ and RM data

Flow rate and length of measurement (24 h versus 4 day) affected the RM concentrations on the TAPI system. When the TAPI operated for 24 h, RM concentrations were higher than when the TAPI operated at longer time intervals (three or four day periods, ANOVA, p-value<0.01, n=9, data not shown). Because of the apparent loss of RM over time, 24 h measurements were carried out for the remainder of the study.

The two TAPI instruments showed good agreement measuring $PM_{2.5}$ when both instruments were located at UNRG ($r^2=0.87$, p-value < 0.05, n=77, Fig. SI 7a). The two instruments operated for 24 h sample periods in April 2014 ($r^2=0.80$, p-value < 0.05, n=6, Fig. SI 7b) and in November 2014 to March 2015 ($r^2=0.88$, p-value<0.05, n=71, Fig. SI 7c). In addition, means for $PM_{2.5}$ were similar (ANOVA $p>0.05$).

However, comparison of RM measured with the two instruments indicated poor correlation and different means (r^2 of 0.28, p-value<0.05, n=57, single-factor ANOVA p-value<0.05, Fig. SI 8). The TAPI 135 had higher RM concentrations (75% of the time, 43 of 57 data points) compared to the TAPI 131. The greater RM concentrations for TAPI 135 were attributed to positioning of the two TAPIs (Fig. SI 1). Due to power and space constraints, TAPI 135 was located in a temporary trailer between two of the UNR Greenhouse bays, where significant RM sources were handled (mine tailings)[31]. Wind speed did not affect the concentrations of TAPI 135 RM (Fig SI 9), however we believe this was due to the positioning of the TAPI 135 temporary trailer (Fig. SI 1). TAPI 131 was located in a permanent trailer setup away from the UNRG bays and closer to the highway. Since the two TAPIs measured statistically similar $PM_{2.5}$ concentrations, this indicated that GOM emanating from the surrounding area was influencing TAPI 135 data.

There was no correlation between all $PM_{2.5}$ and RM data when both TAPIs (131 and 135) were located at UNRG (Fig. SI 10 and 11). Spring and winter (Fig. SI 10b and e) had lower RM and $PM_{2.5}$ concentrations compared to summer and fall (Fig. SI 10c and d) for TAPI 131. Limited data for TAPI 135 at UNRG showed a slight correlation (r^2=0.24, p-value<0.05, n=77) between $PM_{2.5}$ and RM in the winter (Fig. SI 11d).

Comparison of the PEAV TAPI $PM_{2.5}$ and RM data

When TAPI 135 was moved to Peavine Peak, the high elevation site (2515 m) just outside the urban Reno area, the single factor ANOVA p-value was <0.05 when comparing the $PM_{2.5}$ data from the instrument at UNRG, indicating that the means were

different. UNRG $PM_{2.5}$ mass concentrations were weakly correlated (r^2=0.33, p-value<0.05, n=131, Fig. SI 12) and higher than concentrations at PEAV (84% of the time, 110 of 131 data points), likely due to proximity to the two highways. On several occasions PEAV $PM_{2.5}$ mass concentration was higher than UNRG (16% of the time, 21 of 131 data points), likely due to transport of pollution aloft that does not reach UNRG[15].

RM concentrations were correlated between UNRG and PEAV (r^2=0.5, p-value<0.05, n=134, Fig. 2a). The single factor ANOVA p-value was >0.05 indicating the mean RM concentrations for the two datasets were similar[15].

There was no correlation between $PM_{2.5}$ and RM data when located at PEAV (Fig. SI 13a). Summer and fall (Fig. SI 13b and d) at PEAV had similar patterns and ranges (summer $PM_{2.5}$: 1-57 µg m^{-3} range, median=5, n=88; summer RM: 15-140 pg m^{-3} range, median=41, n=88; fall $PM_{2.5}$: 0-75 µg m^{-3} range, median=4, n=70; fall RM: 1-147 pg m^{-3} range, median=27, n=73). When data points impacted by fires were removed (Fig. SI 13c and e) the $PM_{2.5}$ range decreased and the RM was unaffected (summer $PM_{2.5}$: 1-11 µg m^{-3} range, median=5, n=64; summer RM: 16-140 pg m^{-3} range, median=47, n=60; fall $PM_{2.5}$: 0-13 µg m^{-3} range, median=2, n=44; fall RM: 1-147 pg m^{-3} range, median=24, n=33).

Comparison of the GBNP TAPI $PM_{2.5}$ and RM data

TAPI 135 was located at GBNP (2061 m) from March to October 2015. UNRG $PM_{2.5}$ mass concentrations were typically > GBNP (82% of the time, 98 of 120 data points). The single factor ANOVA p-value was <0.01 indicating that $PM_{2.5}$ mean concentrations for the two datasets were different and the two sites were not correlated

(r^2=0.06, p-value<0.05, n=120, Fig. SI 14). Days with higher $PM_{2.5}$ at GBNP occurred more frequently during March, April, and May than in June, July, and September (not enough data in August to compare) when compared to UNRG data. This may be due to long-range transport of aerosols associated with free tropospheric air movement in the spring[23, 32].

RM concentrations were correlated between UNRG and GBNP (r^2=0.58, p-value<0.05, n=118, Fig. 2b). The single factor ANOVA p-value was <0.05 indicating the mean RM concentrations for the two datasets were different. GBNP RM was higher 65% of the time (77 of 118 data points). GBNP's location provides a unique setting for impacts by regional and global pollution[23, 33].

There was no correlation between $PM_{2.5}$ and RM concentrations at GBNP (Fig. SI 15a). In spring (Fig. SI 15b), GBNP $PM_{2.5}$ ranged from 0.3 to 12 μg m^{-3} with a median of 3 μg m^{-3} while RM ranged from 3 to 70 pg m^{-3} with a median of 12 pg m^{-3}. Highest RM concentrations occurred in May. In summer (Fig. SI 15c), GBNP $PM_{2.5}$ ranged from 1 to 21 μg m^{-3} with a median of 4 μg m^{-3} while RM ranged from 17 to 134 pg m^{-3} with a median of 59 pg m^{-3}. Days with the highest $PM_{2.5}$ concentrations occurred at GBNP in the summer time during the month of August when smoke from wildfires in the region was impacting the site. If these points are removed (Fig. SI 15d), the $PM_{2.5}$ range changed to 1 to 7 μg m^{-3} with a median of 4 μg m^{-3} while RM concentrations did not change.

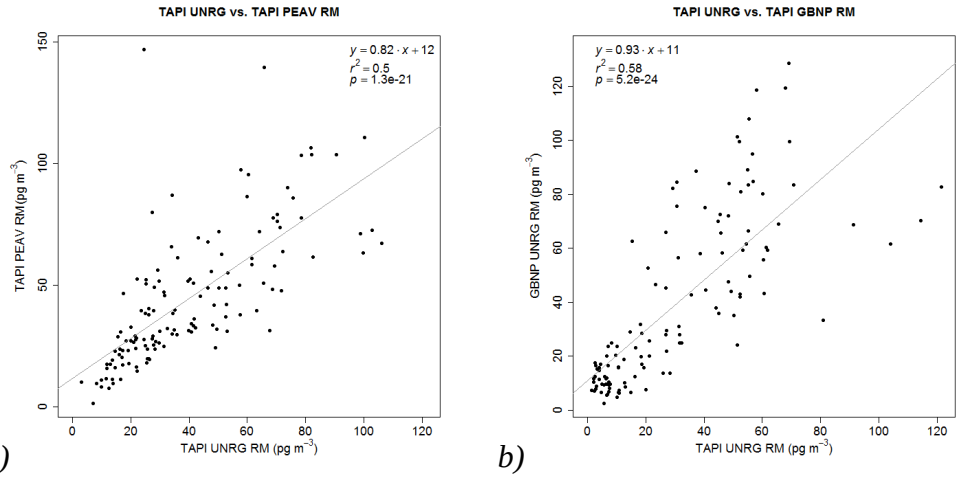

a) *b)*

Figure 2: a) Linear regression for UNRG TAPI RM and PEAV TAPI RM and b) linear regression for UNRG TAPI RM and GBNP TAPI RM.

CEM tests

Despite limited data here, observed trends are interesting and future investigation is needed. Means between the TAPI and two CEM filters in a single filter pack with shorter inlet (2.5 cm length Teflon tube with ambient air pulled through two CEM at 16.7 Lpm) were statistically different (single factor ANOVA p-value<0.05). Relative percent difference between the TAPI RM and co-located inlet CEM filter RM concentrations ranged from 5 to 105% (n=7) with only one instance where the inlet CEM mean concentration had less RM than the TAPI on the same day (Fig. SI 16). Since the short inlet CEM had no PM 10 µm pre-impactor or PM 2.5 µm cyclone, we expected measurements from this system to be higher than the TAPI.

Total RM collected with the short inlet setup increased with WRCC SH (r^2=0.6, p-value<0.05, Fig. SI 17c), while breakthrough decreased with increasing WRCC SH

(r^2=0.2, p-value>0.05, Fig. SI 17d). This indicated more efficient collection of RM by the short inlet CEM with higher SH.

During this time TAPI RH measured at the inlet (external) and within the measurement container (internal) was used with external and internal pressure and temperature measurements to calculate SH. TAPI RM increased with internal SH (r^2=0.53, p=value=0.06, Fig. SI 18a) and increased with internal temperature (r^2=0.77, p=value<0.05, Fig. SI 18b). TAPI RM increased with external SH (r^2=0.84, p=value<0.05, Fig. SI 18c) and increased with external temperature (r^2=0.80, p=value<0.05, Fig. SI 18d). According to the TAPI RH measurements, the smart heater on the inlet never came on to adjust RH in the sample line. Due to the location of the WRCC UNRG meteorological station, the internal and external monitors on the TAPI were more informative for instrument behavior. These indicated that TAPI RM concentrations increased with SH and temperature. Increased uptake of RM by the CEM has previously been observed with increasing RH[4].

Breakthrough tests using the calibration system (1 Lpm) to permeate RM compounds ranged from 0 to 27% of total RM collected (n=18, Fig. SI 19). However, permeations occurred for 20, 30, and 40 s and flushed for a total of 130, 140, and 160 s into ambient air whereas ambient measurements were made for 24 h to two weeks. Inlet tests with two membranes in one filter pack with a flow rate of 16.7 Lpm resulted in median breakthrough of 15% (range: 7 to 36%).

Median breakthrough with the UNRRMAS at a flow rate of 1 Lpm was 25% (range: 0-40%) at UNRG and 13% (range: 2-26%) at PEAV. This may be due to different RM compounds at each location with different polarizability; Hg-sulfur and -nitrogen

compounds were prevalent at UNRG, while $HgCl_2$/$HgBr_2$ compounds were prevalent at PEAV[15].

For GOM retention tests, ~0.2 ng of $HgCl_2$ was permeated onto the filters. For a one-week period of ambient air measurements 0.2 ng is ~10% of the total RM collected. For a two-week period of ambient air measurements, that is ~5% of the total RM collected. Blanks were consistent and did not increase in RM when held in jars for one- and two-week periods. Loaded filters in jars averaged 0.25 ± 0.09 ng (mean ± 1 std, n = 9) for the one-week period and 0.18 ± 0.01 ng (n = 4) for the two-week period. Total ambient RM for one-week was 2.3 ± 0.15 ng. Total ambient RM collected for 2 two-week periods was 4.6 ± 0.3 and 3.6 ± 0.4 ng. Total RM from loaded filters with ambient air for the same periods were 3.8 ± 0.7, 6.8 ± 0.7, and 4.6 ± 0.2 ng. Expected total RM on the loaded filters after ambient air for these periods was 2.5, 4.9, and 3.8 ng. Breakthrough ranged from 4 to 10% of total RM collected and was not affected by loaded filters. These preliminary tests showed that RM was not gained or lost from loaded filters, held in jars, over one- and two-week periods. When loaded filters had ambient air drawn through, total RM was statistically higher (two sample t-test assuming equal variances for all three periods, p-value < 0.05) than expected based on the amount of RM permeated and the ambient air membrane concentrations collected at the same time, indicating that filters with loaded RM may take up more RM over time. Loaded filters did not affect breakthrough in this setup. More tests are needed to understand these processes.

Comparison of the RM measurement methods

Comparison of data collected at UNRG indicated that the Tekran speciation unit measured statistically different RM concentrations relative to the TAPI 131 over 24 h (two-factor ANOVA without replication; r^2=0.02, p-value<0.05, n=216, Fig. 3a) and over weekly samples (two-factor ANOVA without replication; r^2=0.06, p-value<0.05, n=28, Fig. 3b) corresponding to UNRRMAS sample periods. In the winter-spring (January to May 2014; n=73), Tekran RM concentrations were higher than those measured by the TAPI (two-factor ANOVA p-value<0.05), the median SH was 0.0046 kg kg^{-1} (RH=41%). In summer (June to August 2014; n=107) Tekran RM concentrations were lower than the TAPI (two-factor ANOVA p-value<0.05), the median SH was 0.0065 kg kg^{-1} (RH=33%). In fall to winter (September to December 2014; n=34) the two-factor ANOVA p-value was >0.05, indicating the means were similar for Tekran RM and the TAPI, the median SH was 0.0055 kg kg^{-1} (RH=36%).

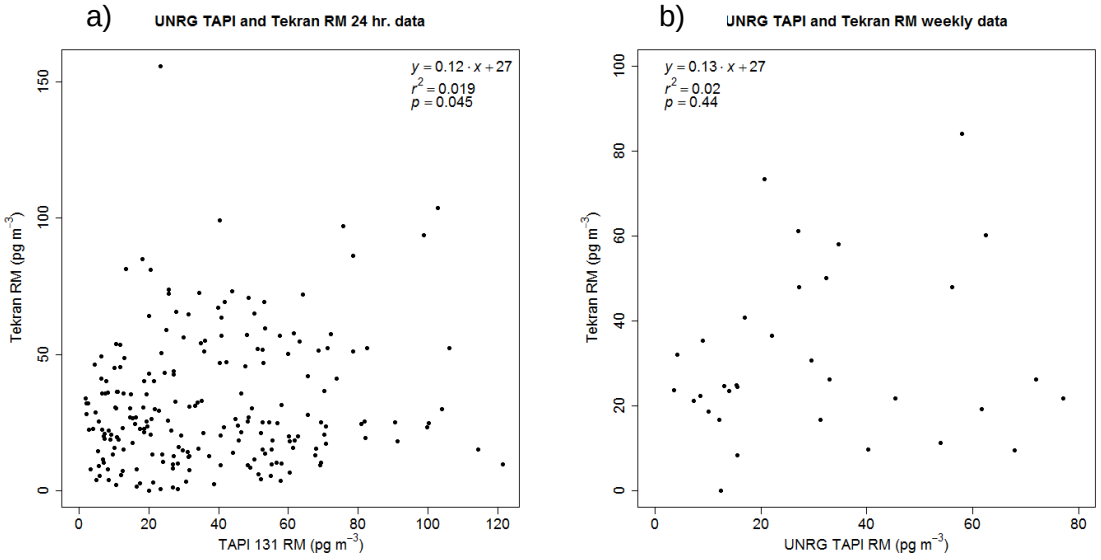

Figure 3: a) Scatter plot for UNRG TAPI 131 and Tekran RM for 24 h data and b) scatter plot for UNRG TAPI 131 and Tekran RM for weekly data corresponding to UNRRMAS sample periods.

The TAPI 131 and the UNRRMAS at UNRG compare well in general trends of RM concentrations, however the UNRRMAS consistently measured higher concentrations than the TAPI 131 (p-value<0.05, n=31) and were significantly correlated (r^2=0.52, p-value<0.05, Fig. 4a). This difference was also the case at PEAV where the UNRRMAS measured higher RM concentrations than the TAPI 135 (p-value<0.05, n=12) and were significantly correlated (r^2=0.58, p-value<0.05, Fig. 4b). When the two datasets are combined the slope was 2.4, the intercept was 30 pg m^{-3} with an r^2 of 0.57 and a p-value<0.05.

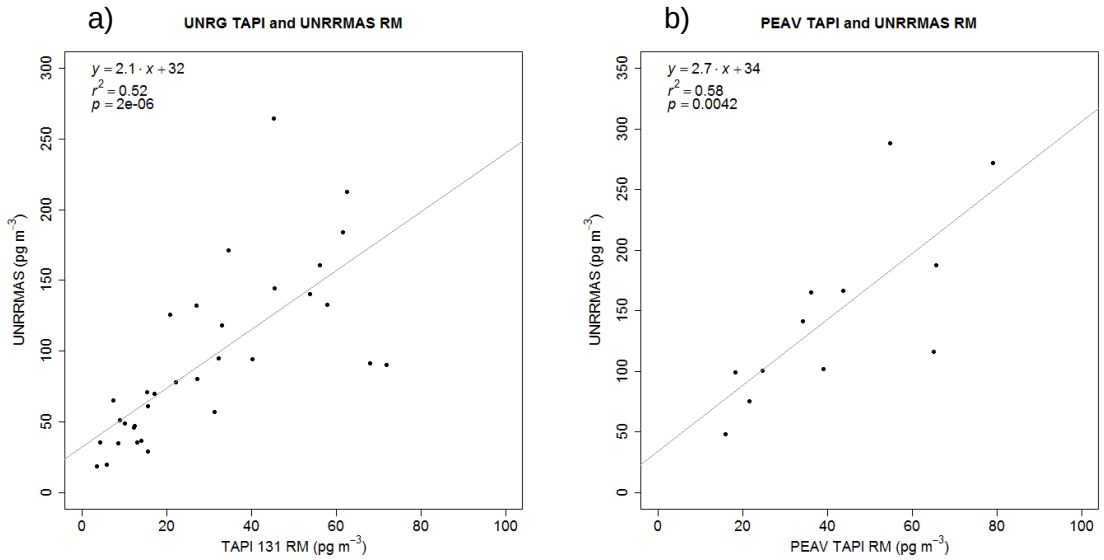

Figure 4: a) Linear regression for UNRG TAPI 131 RM and UNRG UNRRMAS RM weekly data and b) linear regression for PEAV TAPI 135 RM and the PEAV UNRRMAS RM weekly data.

At UNRG the three Hg systems measured different RM concentrations overall. These differences changed depending on season. Theoretically, both the TAPI system and the UNRRMAS should collect RM on the CEM filters; however, the TAPI, as

configured, had the following collection issues: lost RM to the inlet and the CEM could have measured PBM or only certain forms of GOM. The two systems should be correlated as they both used CEM. The intercepts for the TAPI compared to the UNRRMAS at UNRG and PEAV were similar indicating that the UNRRMAS measured ~30 pg m^{-3} of RM above the TAPI when the data from both sites were combined. These two sites have been shown to have different dominant forms of GOM ($HgBr_2$/$HgCl_2$ at PEAV and Hg-sulfur and -nitrogen compounds at UNRG[15]). These data support our second hypothesis that due to different analytical configurations, different RM concentrations were measured. The equation (r^2 = 0.57) between the TAPI and UNRRMAS for both locations combined was:

$$\text{TAPI (pg m}^{-3}\text{)} + 30 \text{ (pg m}^{-3}\text{)} + \text{breakthrough} = \text{ambient RM (pg m}^{-3}\text{)} \qquad \text{Eq. 1}$$

There was significant breakthrough on the CEM in both configurations (UNRRMAS and TAPI). The TAPI, with only one CEM filter inline, under collects 0 to 40% of the total RM due to breakthrough. Breakthrough should be quantified at each sample location as it may differ from site to site depending on prevalent forms of RM and environmental conditions.

Implications

This study demonstrated that the TAPI using CEM measured $PM_{2.5}$ statistically similar to FEM and FRM measurements, as well as between two TAPI instruments. Due to this similarity in $PM_{2.5}$, differences in the RM concentrations were attributed to

proximity to local RM emissions from mining material and not differences between the two TAPI instruments. The advantage of the TAPI instrument for sampling RM is the higher temporal resolution compared to the UNRRMAS. Higher temporal resolution is important for understanding sources of pollution to an area. However, this method significantly underestimated RM due to high flow rate and inlet configuration, and possibly differences in RM compounds at different sites. In addition, there were seasonal differences associated with TAPI RM concentrations and those measured by the Tekran associated with SH. Higher SH (0.0065 kg kg^{-1}) occurred in the summer when the TAPI measured higher concentrations relative to the Tekran RM and lower SH (0.0046 kg kg^{-1}) in the winter-spring when the TAPI measured lower than the Tekran RM. Intermediate SH values (0.0055 kg kg^{-1}) in the fall to winter occurred when the TAPI and Tekran RM measured statistically similar values. Thus, seasonal variation in meteorological conditions affected not only Tekran measurements, but also TAPI data. However, seasonal RM concentration ranges were not affected by the presence or absence of fires, a finding that supports previous studies indicating fires influence GEM and PBM, but not GOM[34]. This finding and the lack of correlation between $PM_{2.5}$ and RM suggests that we are measuring primarily GOM.

Preliminary GOM retention tests indicated that CEM do not gain or lose RM over time when held in jars. Loaded filters may retain more RM than expected, which may impact samples with high RM concentrations early in a sample period. A better understanding of breakthrough and retention of RM on the CEM along with the difference between the UNRRMAS and the TAPI could improve measurements while giving a higher temporal resolution. The CEM show higher collection efficiency for RM

than the Tekran in the UNRRMAS system and during high specific humidity in the TAPI system. Future studies should include more long-term behavior and breakthrough tests of the CEM. The calibrator system is a useful tool for permeating repeatable concentrations of different RM compounds for testing methods for measuring RM. Understanding the surface chemistry on the filters is also important for understanding the SH effects, the behavior of different RM compounds, and the retention of RM at different flow rates.

Appendix A: Supplemental Information, 25 pages, 3 Tables, and 19 Figures.

Acknowledgements:

We would like to acknowledge the Nevada Division of Environmental Protection (NDEP), the UNR College of Biotechnology and Natural Resources, and a USDA-HATCH grant for supporting this project. We would also like to acknowledge a National Science Foundation (NSF) grant (629679) funding for the UNRRMAS and Tekran data. Thank you to Teledyne Advanced Pollution Instrumentation for their collaboration on the TAPI setup and technical support. Thank you to Rebekka Fine for the initial research on the TAPI system for use in this setup. Thank you to Dr. Seth Lyman for use of the automatic calibration system. Thank you to Jiaoyan Huang and Keith Heidecorn for collection of data from the UNRRMAS and the Tekran speciation system. Thank you to Dr. Mary Peacock for assistance. We would also like to acknowledge the members of the Gustin Hg group laboratory who are instrumental in keeping everything running: Matthieu Miller, Matthew Peckham, Jennifer Arnold, Adriel Luippold, Jonathon Heywood, and Logan Distefano.

References

1. Jaffe, D. A.; Lyman, S.; Amos, H. M.; Gustin, M. S.; Huang, J.; Selin, N. E.; Levin, L.; ter Schure, A.; Mason, R. P.; Talbot, R.; Rutter, A.; Finley, B.; Jaeglé, L.; Shah, V.; McClure, C.; Ambrose, J.; Gratz, L.; Lindberg, S.; Weiss-Penzias, P.; Sheu, G.-R.; Feddersen, D.; Horvat, M.; Dastoor, A.; Hynes, A. J.; Mao, H.; Sonke, J. E.; Slemr, F.; Fisher, J. A.; Ebinghaus, R.; Zhang, Y.; Edwards, G., Progress on Understanding Atmospheric Mercury Hampered by Uncertain Measurements. *Environmental Science & Technology* **2014,** *48*, (13), 7204-7206.
2. McClure, C. D.; Jaffe, D. A.; Edgerton, E. S., Evaluation of the KCl Denuder Method for Gaseous Oxidized Mercury using HgBr2 at an In-Service AMNet Site. *Environmental Science & Technology* **2014,** *48*, (19), 11437-11444.
3. Lyman, S. N.; Jaffe, D. A.; Gustin, M. S., Release of mercury halides from KCl denuders in the presence of ozone. *Atmos. Chem. Phys.* **2010,** *10*, (17), 8197-8204.
4. Huang, J.; Gustin, M. S., Uncertainties of Gaseous Oxidized Mercury Measurements Using KCl-Coated Denuders, Cation-Exchange Membranes, and Nylon Membranes: Humidity Influences. *Environmental Science & Technology* **2015,** *49*, (10), 6102-6108.
5. Huang, J.; Miller, M. B.; Weiss-Penzias, P.; Gustin, M. S., Comparison of Gaseous Oxidized Hg Measured by KCl-Coated Denuders, and Nylon and Cation Exchange Membranes. *Environmental Science & Technology* **2013,** *47*, (13), 7307-7316.
6. Gustin, M. S.; Evers, D. C.; Bank, M. S.; Hammerschmidt, C. R.; Pierce, A.; Basu, N.; Blum, J.; Bustamante, P.; Chen, C.; Driscoll, C. T.; Horvat, M.; Jaffe, D.; Pacyna, J.; Pirrone, N.; Selin, N., Importance of Integration and Implementation of Emerging and Future Mercury Research into the Minamata Convention. *Environmental Science & Technology* **2016,** *50*, (6), 2767-2770.
7. Gustin, M. S.; Amos, H. M.; Huang, J.; Miller, M. B.; Heidecorn, K., Measuring and modeling mercury in the atmosphere: a critical review. *Atmos. Chem. Phys.* **2015,** *15*, (10), 5697-5713.
8. Gustin, M. S.; Huang, J.; Miller, M. B.; Peterson, C.; Jaffe, D. A.; Ambrose, J.; Finley, B. D.; Lyman, S. N.; Call, K.; Talbot, R.; Feddersen, D.; Mao, H.; Lindberg, S. E., Do We Understand What the Mercury Speciation Instruments Are Actually Measuring? Results of RAMIX. *Environmental Science & Technology* **2013,** *47*, (13), 7295-7306.
9. Malcolm, E. G.; Keeler, G. J., Evidence for a sampling artifact for particulate-phase mercury in the marine atmosphere. *Atmospheric Environment* **2007,** *41*, (16), 3352-3359.
10. Jaffe, D. A.; Lyman, S.; Amos, H. M.; Gustin, M. S.; Huang, J.; Selin, N. E.; Levin, L.; ter Schure, A.; Mason, R. P.; Talbot, R.; Rutter, A.; Finley, B.; Jaeglé, L.; Shah, V.; McClure, C.; Ambrose, J.; Gratz, L.; Lindberg, S.; Weiss-Penzias, P.; Sheu, G.-R.; Feddersen, D.; Horvat, M.; Dastoor, A.; Hynes, A. J.; Mao, H.; Sonke, J. E.; Slemr, F.; Fisher, J. A.; Ebinghaus, R.; Zhang, Y.; Edwards, G., Progress on Understanding Atmospheric Mercury Hampered by Uncertain Measurements. *Environmental Science & Technology* **2014**.

11. Slemr, F. A., H. Dommergue, A. Magand, O. Barret, M. Weigelt, A. Ebinghaus, R. Brunke, E.-G. Pfaffhuber, K. Edwards, G. Howard, D. Powell, J. Keywood, M. Wang, F., Comparison of mercury concentrations measured at several sites in the Southern Hemisphere. *Atmospheric Chemistry and Physics Discussions* **2014,** *14*, (22), 30611-30637.
12. Rutter, A. P.; Schauer, J. J., The effect of temperature on the gas–particle partitioning of reactive mercury in atmospheric aerosols. *Atmospheric Environment* **2007,** *41*, (38), 8647-8657.
13. Luke, W. 2016 NOAA report. ftp://ftp.arl.noaa.gov/.mercury-workshop (June 2016),
14. Lyman, S.; Jones, C.; O'Neil, T.; Allen, T.; Miller, M.; Gustin, M. S.; Pierce, A. M.; Luke, W.; Ren, X.; Kelley, P., Automated Calibration of Atmospheric Oxidized Mercury Measurements. *Environmental Science & Technology* **2016**.
15. Gustin, M. S.; Pierce, A. M.; Huang, J.; Miller, M. B.; Holmes, H.; Loria-Salazar, S. M., Evidence for different reactive Hg sources and chemical compounds at adjacent valley and high elevation locations. *Environmental Science & Technology* **2016**.
16. TAPI, T. A. P. I., Operation Manula: Model 602 BETA PLUS particle measurement system. In Teledyne Advanced Pollution Instrumentation: San Diego, CA, 2012; p 180.
17. Hauck, H.; Berner, A.; Gomiscek, B.; Stopper, S.; Puxbaum, H.; Kundi, M.; Preining, O., On the equivalence of gravimetric PM data with TEOM and beta-attenuation measurements. *Journal of Aerosol Science* **2004,** *35*, (9), 1135-1149.
18. Malm, W. C.; Schichtel, B. A.; Pitchford, M. L., Uncertainties in PM2.5 gravimetric and speciation measurements and what we can learn from them. *J Air Waste Manag Assoc* **2011,** *61*, (11), 1131-49.
19. Takahashi, K.; Minoura, H.; Sakamoto, K., Examination of discrepancies between beta-attenuation and gravimetric methods for the monitoring of particulate matter. *Atmospheric Environment* **2008,** *42*, (21), 5232-5240.
20. Gobeli, D.; Schloesser, H.; Pottberg, T., Met One Instruments BAM-1020 Beta Attenuation Mass Monitor US-EPA PM2.5 Federal Equivalent Method Field Test Results. **2008**.
21. Watson, J. G.; Chow, J. C., Ambient Aerosol Sampling. In *Aerosol Measurement*, John Wiley & Sons, Inc.: 2011; pp 591-613.
22. Allen, A. G.; Harrison, R. M.; Erisman, J.-W., Field measurements of the dissociation of ammonium nitrate and ammonium chloride aerosols. *Atmospheric Environment (1967)* **1989,** *23*, (7), 1591-1599.
23. Gustin, M. S.; Fine, R.; Miller, M.; Jaffe, D.; Burley, J., The Nevada Rural Ozone Initiative (NVROI): Insights to understanding air pollution in complex terrain. *Science of The Total Environment* **2015,** *530–531*, (0), 455-470.
24. MetOne Instruments, I. *E-BAM particulate monitor operation manual: E-BAM-9800 REV L*; 2008; p 75.
25. *IMPROVE Data Guide*; University of California, Davis: University of California, Davis, 1995; p 13.
26. Xu, T., Ion exchange membranes: State of their development and perspective. *Journal of Membrane Science* **2005,** *263*, (1–2), 1-29.

27. Yee, R. S. L.; Rozendal, R. A.; Zhang, K.; Ladewig, B. P., Cost effective cation exchange membranes: A review. *Chemical Engineering Research and Design* **2012,** *90*, (7), 950-959.
28. Mason, R. P.; Lawson, N. M.; Sullivan, K. A., The concentration, speciation and sources of mercury in Chesapeake Bay precipitation. *Atmospheric Environment* **1997,** *31*, 3541-3550.
29. Lyman, S. N.; Gustin, M. S.; Prestbo, E. M.; Kilner, P. I.; Edgerton, E.; Hartsell, B., Testing and Application of Surrogate Surfaces for Understanding Potential Gaseous Oxidized Mercury Dry Deposition. *Environmental Science & Technology* **2009,** *43*, (16), 6235-6241.
30. Tekran Unique features of the Tekran Model 2537B. http://www.tekran.com/files/Tekran-2537B-Unique-Features.r103.pdf
31. Eckley, C. S.; Gustin, M.; Miller, M. B.; Marsik, F., Scaling Non-Point-Source Mercury Emissions from Two Active Industrial Gold Mines: Influential Variables and Annual Emission Estimates. *Environmental Science & Technology* **2011,** *45*, (2), 392-399.
32. Fine, R.; Miller, M. B.; Burley, J.; Jaffe, D. A.; Pierce, R. B.; Lin, M.; Gustin, M. S., Variability and sources of surface ozone at rural sites in Nevada, USA: Results from two years of the Nevada Rural Ozone Initiative. *Science of The Total Environment* **2015,** *530–531*, (0), 471-482.
33. Fine, R.; Miller, M. B.; Yates, E. L.; Iraci, L. T.; Gustin, M. S., Investigating the influence of long-range transport on surface O3 in Nevada, USA, using observations from multiple measurement platforms. *Science of The Total Environment* **2015,** *530–531*, (0), 493-504.
34. Friedli, H. R.; Radke, L. F.; Lu, J. Y.; Banic, C. M.; Leaitch, W. R.; MacPherson, J. I., Mercury emissions from burning of biomass from temperate North American forests: laboratory and airborne measurements. *Atmospheric Environment* **2003,** *37*, (2), 253-267.

Chapter 3

Use of multiple tools including lead isotopes to decipher sources of ozone and reactive mercury to urban and rural locations in Nevada, USA

Ashley M. Pierce[a,*], Mae Sexauer Gustin[a,*], John N. Christensen[b], S. Marcela Loría-Salazar[c]

*Corresponding author: ash.pie4@gmail.com; mgustin@cabnr.unr.edu

[a]Department of Natural Resources and Environmental Sciences, University of Nevada Reno, NV, USA 89557

[b]Energy Geosciences Division, Lawrence Berkeley National Laboratory, Berkeley, CA, USA 94720

[c]Atmospheric Science Program, Department of Physics, University of Nevada, Reno, Nevada, USA 89557

Published: *Science of the Total Environment* (Web: 2017, Print: 2018)

Appendix B: Supplemental Information, 72 pages, 40 Tables, and 38 Figures

Table of Contents Graphic

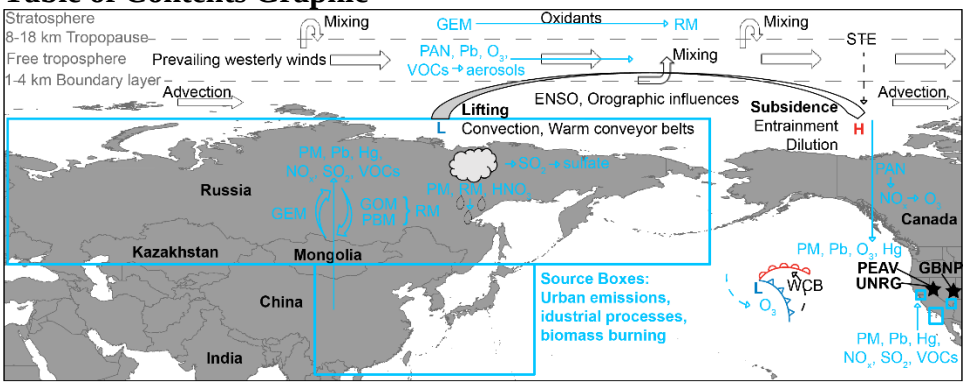

Highlights:

- The lower USA EPA NAAQS for O_3 (70 ppbv) will affect attainment in many areas.
- 24 h $PM_{2.5}$ was collected on two filter types for Hg and Pb to trace O_3 sources.
- Trans-Pacific, regional, and local sources affected O_3 in spring and fall.
- Reactive Hg was negatively correlated with trans-Pacific air masses and Asian lead.
- Comprehensive studies in Western USA are needed to understand complex dynamics.

Abstract:

Ambient air particulate matter (<2.5 µm in diameter) samples were collected on two different filter types in 2014 and 2015 over 24 h periods and analyzed for reactive mercury (gaseous oxidized mercury + particulate bound mercury) concentrations and lead isotopes to determine sources of pollution to three sites in Nevada, USA. Two sites were located on the western edge of Nevada (Reno, urban, 1370 m and Peavine Peak, rural, high elevation, 2515 m); the third location was ~485 km east in rural Great Basin National Park, NV (2061 m). Reactive mercury samples were collected on cation exchange membranes simultaneously with lead samples, collected on Teflon membranes.

Lead isotopic ratios have previously identified trans-Pacific lead sources based on the 206/207 and 208/207 lead ratios. Influence from trans-Pacific air masses was higher from March to June associated with long-range transport of pollutants. Spring months are well known for increased transport across the Pacific; however, fall months were also influenced by trans-Pacific air masses in this study.

Western North American background ozone concentrations have been measured and modeled at 50 to 55 ppbv. Median ozone concentrations at both rural sites in Nevada were within this range. Sources leading to enhancements in ozone of 2 to 18 ppbv above monthly medians in Nevada included emissions from Eurasia, regional urban centers, and global and regional wildfires, resulting in concentrations close to the USA air quality standard. At the high elevation locations, ozone was derived from pollutants being transported in the free troposphere that originate around the globe; however, Eurasia and Asia were dominant sources to the Western USA.

Negative correlations between reactive mercury and percent Asian lead, Northern Eurasia and East Asia trajectories indicated reactive mercury concentrations at the two high elevation sites were produced by oxidants from local, regional, and marine boundary layer sources.

Keywords:

$PM_{2.5}$, MC-ICPMS, Long-range transport, Pollution sources, Complex terrain

1. Introduction:

Determining sources of pollution in complex terrains, such as the Western United States of America (USA), is difficult due to a combination of complicated meteorological conditions (e.g. complex planetary boundary layer processes, El Niño/Southern oscillation, and jet streams), stratospheric-tropospheric exchange (STE), and long-range transport of air masses. Moreover, determining sources of ozone (O_3) is particularly complex as it is a secondary pollutant that forms downwind of primary pollution sources. These factors provide multiple challenges for regulators given the task of determining measures for meeting the National Ambient Air Quality Standard (NAAQS) for O_3 in the Western USA (Cooper et al., 2015). This research was conducted with the purpose of understanding sources of O_3 and reactive mercury (RM) to Nevada, USA in 2014 and 2015, using lead (Pb) isotopes and a suite of other measurements.

In the troposphere, O_3 is a harmful oxidant that has detrimental effects on materials (such as rubber), leaves and therefore crops and forests, and mucous membranes and respiratory tissues in organisms (U.S. EPA, 2017). Ozone also affects climate change because it absorbs infrared radiation (Finlayson-Pitts and Pitts Jr, 2000a; Finlayson-Pitts and Pitts Jr, 2000b). The current USA Environmental Protection Agency (EPA) NAAQS is set to 70 parts per billion (ppbv) 8 h maximum (max) daily average (MDA8) concentration and determined based on the 3-year running average of the annual fourth-highest MDA8 (called the design value, U.S. EPA, 2017). The European Union standard is set to 60 ppbv MDA8 with 25 exceedance days averaged over 3 years (European Commission, 2016). Washoe County, in which two field sites in this study,

Reno and Peavine Peak reside, was out of attainment for O_3 for the 2014 to 2016 averaging years, due to several large fires during this time (EPA, 2017).

Spring and summer maximums of O_3 are often observed across the Northern Hemisphere due to increased photochemical reactions with accumulated NO_x, increased STE, and long-range transport of precursors from other continents (Prinn, 2014; Vingarzan, 2004; Wilkening et al., 2000; Zhang et al., 2014). Springtime O_3 concentrations in mid-latitudes are also influenced by El Niño/Southern Oscillation, especially during strong El Niño events in which O_3 is transported from the tropics to the extra-tropics (Lin et al., 2012; Rieder et al., 2013). Stratospheric-tropospheric exchange is greatest over North America in the spring, due to increased storm activity and a low tropopause allowing for better vertical down mixing from the stratosphere (Ambrose et al., 2011; Dempsey, 2014; Fine et al., 2015a; Johnson and Viezee, 1981; Langford et al., 2012; Langford et al., 2015a; Langford et al., 2015b; Langford, 2017; Lin et al., 2015; Stohl et al., 2000; Tang and Prather, 2010; Viezee et al., 1983; Vingarzan, 2004). Summer in the Western USA also means increased wildfires, which can increase summer mean MDA8 O_3 by 0.3-1.5 ppbv with episodic increases of 10-20 ppbv (Lu et al., 2016).

Research has demonstrated that long-range transport of gases and particulate matter (PM) from Eurasia impacts air quality in the Northeast Pacific and North America (Bertschi and Jaffe, 2005; Christensen et al., 2015; Ewing et al., 2010; Fine et al., 2014; Jaffe et al., 1999; Jaffe et al., 1997; Jaffe et al., 2003; Lin et al., 2012; Price et al., 2004; Teakles et al., 2017; VanCuren, 2003; VanCuren et al., 2005; Weiss-Penzias et al., 2007; Weiss-Penzias et al., 2006). Trans-Pacific atmospheric pollutants are predominant in the spring due to increased storm, and frontal activity in Eurasia, facilitating transport of air

across the Pacific (Cooper et al., 2010; Knowland et al., 2015; Kunz and Speth, 1997; Vingarzan, 2004). Increased fires in Eurasia in the spring also add pollutants to the atmosphere for trans-Pacific transport (Cooper et al., 2010; Vingarzan, 2004). Total annual area burned of boreal fires in Eurasia has been shown to significantly impact O_3 and CO summer seasonal means, explaining 42 to 86% inter-annual variability across sites in Western North America (Jaffe et al., 2004). To understand contributions to North American O_3 concentrations baseline and background levels need to be quantified. Baseline O_3 is defined as that which does not include recent local emissions, but includes aged domestic emissions, while North American Background is a modeled value constructed with zero North America emissions that does include man made precursor sources outside of North America (U.S. EPA, 2017). In the Western USA, trans-Pacific O_3 has been estimated with models and shown with observations to increase surface O_3 concentrations by 3 to 15 ppbv and contributed to exceedances of 70 ppbv springtime MDA8 O_3 concentrations (Fiore et al., 2002; Fiore et al., 2014; Jacob et al., 1999; Jaffe et al., 2004; Jaffe et al., 2003; Langford et al., 2015b; Lin et al., 2012; Vingarzan, 2004). This influence will increase as Asian countries continue to develop, affecting Western USA, rural O_3 by ~0.5 ppbv/yr (Christensen et al., 2015; Cooper et al., 2010; Gratz et al., 2015).

Higher O_3 concentrations have been measured at high elevation sites in Western USA, compared to nearby lower elevations, due to layers of polluted trans-Pacific air, lofting of pollution produced in California into the free troposphere, and stratospheric intrusions (Brodin et al., 2010; Burley and Bytnerowicz, 2011; Fine et al., 2015a; Fine et al., 2015b; Fiore et al., 2002; Gustin et al., 2015b; Jaffe et al., 2003; Lin et al., 2012;

VanCuren, 2015; Vingarzan, 2004). Sites in California and Nevada have shown a strong relationship between site altitude and maximum (max) 1 h O_3 indicating an increase of 13 ppbv for every km of elevation in the summer, and 7 to 10 ppbv/km in other seasons (Fine et al., 2015b). Previous data and models indicated that high elevation, rural sites in Western USA, such as Great Basin National Park, NV, exceeded the NAAQS design value concentration and will continue to exceed if sources and processes remain constant or increase (Fine et al., 2015a; Lin et al., 2012).

Mercury (Hg) is a global pollutant and neurotoxin that can negatively affect ecosystems as it bio-accumulates in the food web. The Global Mercury Assessment, updated in 2015, estimated that ~40% of global anthropogenic Hg emissions come from East and Southeast Asia generally in the form of gaseous elemental Hg (GEM, AMAP/UNEP, 2015; Jaffe et al., 2005). Reactive Hg (RM), considered to be gaseous oxidized Hg (GOM) and particulate bound Hg (PBM), has a shorter residence time in the boundary layer (a day to a week, Schroeder and Munthe, 1998) compared to GEM (6 months to a year). GEM is considered a global pollutant that is transported far from sources and can then be oxidized by a variety of gases and deposited (Weiss-Penzias et al., 2003). RM will undergo reactions or deposit close to sources and can also be formed in dry upper altitude air due to photo-oxidation of GEM near the tropopause and in the stratosphere (Lyman and Jaffe, 2012). Positive correlations between RM and O_3 have been previously observed and interpreted as photo-oxidation in upper altitude air (Weiss-Penzias, 2015). It has also been demonstrated that RM dry deposition is higher at higher elevation sites in California and Nevada (Huang and Gustin, 2015).

The Minamata Convention, adopted in 2013, commits signatories to better understanding atmospheric Hg sources and to reducing emissions to the environment (UNEP, 2017). RM measurements are currently under review due to uncertainties in widely used, commercially available, measurement methods (Gustin et al., 2015a; Gustin et al., 2013; Huang and Gustin, 2015; Huang et al., 2013; Jaffe et al., 2014). A better understanding of the atmospheric cycling of Hg, the main pathway into environments, is necessary for fulfilling the goals of the Minamata Convention.

Lead isotope analysis has previously been used to identify sources of pollution (Ewing et al., 2010), and specifically O_3, to the Western USA (Christensen et al., 2015). Using Pb isotopic ratios in particulate matter, collected on filters, provides a means of identifying sources. As air masses move away from sources, pollutant chemistry changes but Pb isotope ratios do not. There are systematic, geographic differences in Pb isotopic compositions of the four stable isotopes; ^{208}Pb (52%), ^{207}Pb (23%), ^{206}Pb (24%), and ^{204}Pb (1%), of which the three heaviest are produced from radioactive decay that occurs over billions of years (Komárek et al., 2008). Pb associated with Asian aerosols has been shown to have an isotopic composition distinct from Pb in Western North America (Bollhöfer and Rosman, 2002; Ewing et al., 2010), specifically, a higher proportion of ^{208}Pb in ^{208}Pb/^{207}Pb versus ^{206}Pb/^{207}Pb isotopic ratios (Bollhöfer and Rosman, 2001). Analysis of PM collected on filters for Pb isotope ratios can therefore elucidate where air masses originate.

From 2001 to 2009, coal combustion was the largest emission source of Pb in China (Li et al., 2012). The USA is a net exporter of coal, of which ~20% goes to Asia (2014: exports = 88 billion kg, imports = 10 billion kg, 2015: exports = 67 billion kg,

imports = 10 billion kg of coal, U.S. Energy Information Administration, 2017). Although imported coal is a small amount of the total coal used in the USA (<2%) or in Asia (<0.5%), transport in isolated parcels of air (Fine et al., 2015b) may complicate the Pb isotopic signature by adding isotopes that are not representative of the source region (U.S. Energy Information Administration, 2017). In addition, some coals are low in Pb and will therefore, not have discernable isotopic signatures.

In 2011, data collection for the Nevada Rural Ozone Initiative (NVROI) was initiated. The goal of this study was to understand sources of O_3 to the complex terrain and rural areas of the Western USA (Gustin et al., 2015b). This component of the project investigated the use of aerosol concentration and chemistry to understand sources of air masses. Three of the NVROI sites housed modified Teledyne Advanced Pollution Instrumentation (TAPI) particulate measurement systems to quantify particulate matter <2.5 µm in diameter ($PM_{2.5}$), RM (GOM+PBM) concentrations, and Pb concentration and isotopes. Multiple sources of data were used to understand sources of pollutants in air masses delivered to Nevada in summer through fall 2014 and spring to fall 2015. Given that Nevada, with the exception of Reno and Las Vegas, is a rural state with complex terrain, high elevation, and limited sources of O_3 precursors, we hypothesized a component of the O_3 and RM was from long-range transport across the Pacific Ocean.

2. Site descriptions:

Data were collected at three sites with two sites being simultaneously operated at a time. The goal was to understand sources of O_3 to individual locations. More detailed site descriptions are provided in Fine et al. (2015a), Gustin et al. (2015b), Miller et al. (2015),

and in Table 1. The Nevada Agricultural Experiment Station Greenhouse Facility (UNRG; 1371 m, Table 1) is located at the Valley Road field laboratory and Greenhouse complex of the University of Nevada, Reno (UNR) in the topographic bowl of the Reno/Sparks metropolitan area. Data collected from April 2014 to October 2015 were used from this site. The Peavine Peak (PEAV; 2515 m, Table 1) site is situated above the tree line at the peak summit, just east of the Sierra Nevada Mountains (~15 km) and northwest of Reno (~12 km). Data from June to November 2014 were used from this site. The third site, Great Basin National Park (GBNP; 2060 m, Table 1), is located ~485 km due east of Reno in eastern NV at the Utah border. The measurement station is located on the east side of the Snake Range in a forested area, mainly pinyon-juniper, near the Lehman Visitor Center where two canyons merge in a slight topographic bowl. Data were collected from March to October 2015 at this location.

Site	Code	Elevation (m asl)	Measurements	Other	Latitude (N)	Longitude (W)
Great Basin National Park, NV, USA	GBNP	2060	TAPI, CO, SO_2, NO_x, NO_y, Met, E-BAM	IMPROVE (speciated $PM_{2.5}$), CASTNET (O_3)	39.0050	114.2161
Nevada Agricultural Experiment Station Greenhouse Facilities, Reno. NV, USA	UNRG	1371	TAPI, O_3, CO, NO_x	WCAQ (Reno3, O_3, CO, NO_x), WRCC (Met)	39.5374	119.8044
Peavine Peak, Reno, NV, USA	PEAV	2515	TAPI, O_3, CO, Met		39.5895	119.9290

Table 1: Measurement sites and the measurements made at each. Abbreviations are explained under the table with sample resolution in parentheses.

asl – above sea level
CASTNET - Clean Air Status and Trends Network (1 h)
CO – carbon monoxide (1 h)
E-BAM – Environmental Beta Attenuation Monitor ($PM_{2.5}$, 1 h)
IMPROVE - Interagency Monitoring of Protected Visual Environments (24 h once every 3 days)
Met – meteorological data (1 h)
NO – nitrogen oxide (1 h)
NOx – nitrogen oxide compounds (1 h)
NOy – total reactive nitrogen (1 h)
SO_2 – sulfur dioxide (1 h)
TAPI – Teledyne Advanced Pollution Instrumentation Model 602 $Beta^{Plus}$ $PM_{2.5}$ monitor (24 h)
WCAQ – Washoe County Air Quality (1 h)
WRCC – Western Regional Climate Center (1 h)

3. Methods:

Data from multiple platforms (described below) were collected for each site at hourly, 24 h, or once daily resolution and compared at 24 h, 1 h max values, or 8 h max running averages. Filters collected using two TAPI Beta^{Plus} particulate measurement systems for $PM_{2.5}$ samples were post-processed for Pb isotopic composition and RM concentrations. Statistical tests were performed to illustrate differences between sites and to identify significant relationships. Trajectory analyses were applied to identify possible sources of air masses. Specific periods based on exceedances of monthly medians were then chosen for more in depth analysis.

3.1 Teledyne Advanced Pollution Instrumentation (TAPI) Beta^{Plus} Particulate Monitor

Two TAPI Beta^{Plus} particulate measurement systems (Model 602, San Diego, CA, USA) were used to collect $PM_{2.5}$. RM concentrations, and Pb concentrations and isotope ratios were determined. The TAPI Beta^{Plus} particulate measurement system was modified to collect RM on 47 mm cation exchange membranes (CEM; Pall Corporation, PN: MSTGS3R) and Pb on 47 mm Teflon (Pall Corporation, PN: EW-36329-08) for 24 h. Mass concentration was measured using beta attenuation, leaving filters intact and available for further processing (see SI and Gustin (2016) for more detail). Pierce and Gustin (2017) showed that $PM_{2.5}$ measurements using CEM filters were statistically similar to Federal Reference (FRM) and Federal Equivalent methods (FEM). At 24 h the TAPI Beta^{Plus} particulate measurement system has a $PM_{2.5}$ detection limit of 0.3 μg m^{-3} (TAPI, 2012).

3.2 Lead isotope analysis

Teflon filters were processed at Lawrence Berkeley National laboratory (LBNL) in class 100 laminar fume hoods, following Ewing et al. (2010) and Christensen et al. (2015) and analyzed with a multi-collector inductively coupled plasma mass spectrometer (MC-ICPMS Neptune). See SI for details on sample processing.

Percent of Pb attributed to Asia was calculated using methodology developed in Ewing et al. (2010) and applied in Christensen et al. (2015). Wintertime aerosol samples from the Chabot Observatory in California define the "California Array" (blue line and blue squares, Fig. 1, slope = 1.22). Chinese aerosol and loess data define the "Asia Array" (black line and black triangles and squares, Fig 1, slope = 1.09). The horizontal divergence (Δ^{208}Pb) from California array ^{208}Pb/^{207}Pb isotope data towards Asia array ^{208}Pb/^{207}Pb isotope data at a specific observed ^{206}Pb/^{207}Pb isotope value is calculated. The Δ^{208}Pb is then divided by the total distance between the two arrays to determine the percent of the Pb that can be attributed to Asian sources (Ewing et al., 2010). Data from previous studies collected from aerosol and ore samples were used to compare to samples collected in this study. Aerosol samples from different years may have differing isotope ratios over time and direct isotopic composition comparison of ores to aerosols, due to source and supplier differences, is difficult, however these provide an estimate of isotopic ratios in different areas.

3.3 Ozone

Hourly O_3 concentrations were measured at all three sites using UV absorption instruments. O_3 measurements at PEAV were made using a TAPI T400E UV absorption

O_3 analyzer. UNRG had a Thermo 49i (Thermo Fisher Scientific, Inc. Franklin, MA, USA). When O_3 data were missing from UNRG it was supplemented with data from a TAPI 400E at the Reno site (Reno3, site ID: 32-031-0016, 301A State St. Reno) of Washoe County Air Quality Management (WCAQ). At GBNP, O_3 data were collected using a TAPI T400E UV absorption O_3 analyzer operated by the Nevada Department of Environmental Protection (NDEP) and a Thermo 49c operated by the National Park Service (NPS) Clean Air Statuses and Trends Network (CASTNET).

WCAQ and UNRG O_3 data were statistically different (ANOVA $p<0.05$), but positively correlated ($r^2 = 0.72$, $p<0.05$), this is due to distance from a highway (manuscript in preparation). Due to the positive correlation, variations in daily means compared to monthly medians at WCAQ reflect the overall trends in the valley housing Reno, if not the specific concentrations at UNRG, and were used to supplement when UNRG data were unavailable. At GBNP, CASTNET and NDEP O_3 were statistically similar and therefore positively correlated (ANOVA $p>0.05$, $r^2 = 0.93$, $p<0.05$), CASTNET data supplemented periods when NDEP data were not available.

Here we discuss MDA8 as the max 8 h average for a day, but do not compare to the MDA8 NAAQS design value (3-year running average of the annual fourth highest MDA8). Ozone data were compiled and compared with other data as 24 h daily averages, MDA8 values for each day, and the max 1 h O_3 values for each day. The second two values are more likely to capture transport events that may occur within a shorter time scale than a 24 h daily average and are not affected by the smoothing effect that 24 h daily averages have on concentrations (Fine et al., 2015b; Langford, 2017).

3.4 Mercury

CEM filters were digested and then analyzed using an automated Tekran 2600 Hg analyzer following EPA method 1631 for total Hg concentrations. The RM method detection limit was 0.3 ng. See SI and Pierce & Gustin (2017) for further detail.

3.5 Auxiliary Gas and Meteorological data

Measured auxiliary gases are listed in Table 1 and described in Fine et al. (2015a), Gustin et al. (2015b), and Miller et al. (2015), as is meteorological data. All gas instruments at PEAV and GBNP (NDEP) were trace level. Vertical potential temperature from atmospheric balloon soundings were used to calculate the height of the atmospheric boundary layer, termed the atmospheric boundary layer height (ABLH). This data came from soundings released from the National Weather Service in Reno, NV (REV) at 16:00 PST. Late afternoon vertical profiles illustrate the maximum height that the ABLH can potentially reach. Data collected by other organizations, including Washoe County Air Quality Management (WCAQ), Western Regional Climate Center (WRCC), Interagency Monitoring of Protected Visual Environments (IMPROVE), and the Clean Air Status and Trends Network (CASTNET) monitoring networks were also used (Table 1).

3.6 Hybrid Single Particle Lagrangian Integrated Trajectory (HYSPLIT) Model

The NOAA Air Resources Lab HYSPLIT v.4 model (Draxler and Hess, 1997) using the 1° Global Data Assimilation System (GDAS, 23 vertical layers) from the National Center for Environmental Prediction (NCEP, http://ready.arl.noaa.gov/archives.php) was used to compile 240 h back trajectories from

all three sites. Back trajectories were initiated every 4 h (00:00, 04:00, 08:00, 12:00, 16:00, 20:00 PST) from 9 points within a 0.5°x0.5° horizontal grid centered on each site with four arrival heights (500, 1000, 1500, 2000 m agl), generating 216 trajectories a day, or 51,840 hourly trajectory points. Back trajectories give a general indication of a source region and are less useful for vertical motion: however, generating large numbers of trajectories gives a general representation of air mass transport (Stohl et al., 2002; Stohl et al., 2003; Weiss-Penzias et al., 2006).

Trajectory residence times (TRT) were calculated as the percent of the total hourly trajectory points (out of 240 h) that a trajectory resided in a 3 dimensional source box. There were five defined source boxes (see TOC graphic and SI Table 1): Northern Eurasia (N. Eurasia), East Asia (E. Asia), San Francisco, CA (SF), Los Angeles, CA (LA), and Las Vegas, NV (LV). Trajectory resident times for air parcels occurring <3 km, total (<10 km), and >3 km were used for N. Eurasia and E. Asia source boxes. Due to difficulties the HYSPLIT model has with resolving boundary layer to free troposphere exchange in distant source boxes, <3 km, total (<10 km), and >3 km trajectory residence times were used to represent air masses in direct and indirect contact with these source regions (Stohl, 1998; Weiss-Penzias et al., 2006). Trajectory points <1 km over SF, LA, and LV were used as indicators of sources from those areas. Trajectory residence times >3 km over SF were used as an indicator of transport from over the marine boundary layer (MBL) and of high-altitude air, where China has been shown to be a dominant source of O_3 precursors (Cooper et al., 2011). TRT percentages were used in the Pearson correlation (R), discussed in section 3.8, to determine influence from the different source boxes on the three measurement sites.

3.7 Moderate Resolution Imaging Spectroradiometer (MODIS)

Fire Radiative Power (FRP) retrievals from the Terra (morning overpass) and Aqua (afternoon overpass) satellites were used as an indicator of fire frequency and intensity from the N. Eurasia source box and from Western North America including Canada (latitude: 30 to 60 and longitude: -124 to -100°). FRP retrievals from the two satellites were averaged for each day. Daily number (n), minimum (min), maximum (max), mean, standard deviation, and median were calculated for the sample periods. FRP days were chosen based on the first and last day during a 10-day back trajectory in which a trajectory resided in the N. Eurasia source box or Western North America. If a trajectory was within the Western North America bounds for 240 h, the middle day in that time was also used.

3.8 Data analyses:

Data were processed using Python, the R program, Matlab, and Excel. ESRI ArcGIS was used for map creation. Monthly means, daily means, and maximums were calculated from hourly data for each sample period. Data were used if >50% of the data were available. When NVROI data were unavailable, they were supplemented by other data sources (WCAQ, CASTNET). Monthly means were compared using ANOVA (two factor without replication) to determine if the two sites differed. Pearson correlation was used to assess correlation and significance for variables for the sample period at each site and for observations at the sites for days with Pb data using daily means for each variable. Statistical tests were considered significant at $\alpha<0.05$, unless otherwise noted.

4. Results:

During both study periods, median $PM_{2.5}$ concentrations were higher at the urban location than at PEAV or GBNP (Table 1). Median concentrations of RM were higher at GBNP than UNRG. The higher elevation locations (PEAV and GBNP) had higher 24 h average O_3 compared to UNRG. PEAV had higher max 1 h and MDA8 O_3 than UNRG. Average Δ208 Pb for all samples was 7.2±4.7 with an average uncertainty of 0.12±0.080, which corresponds to an average % Asian Pb of 29±19% and an average uncertainty of 0.47±0.32%. Uncertainty for individual measurements can be found in SI Table 2. Pb concentrations were less than the concentration used for the NAAQS design value (0.15 μg m^{-3} or 150 ng m^{-3}) at all sites.

Table 2: Sample statistics for a) PEAV and UNRG June to November 2014 and GBNP and UNRG March to October 2015 and b) for all sites June to October. Site means ± one standard deviation, medians, number of days (n), and range of data.

a) All data

Site	Statistics	$PM_{2.5}$ (µg m^{-3})	RM (pg m^{-3})	O_3 (ppbv)	Max 1 h O_3 (ppbv)	MDA8 O_3 (ppbv)	Total Pb (ng m^{-3})	Asian Pb (ng m^{-3})	% Asian Pb
PEAV 2014	Mean ± StDev	5.94±6.1	43±27	48±7.2	56±8.4	53±7.6	0.34±0.15	0.090±0.089	26±15
	Median (n)	4.9 (141)	38 (153)	49 (158)	56 (158)	53 (158)	0.32 (19)	0.065 (19)	23 (19)
	Range	0.0-42	1.4-147	25-69	40-80	39-78	0.13-0.72	0.0025-0.38	0.51-58
UNRG 2014	Mean ± StDev	8.9±7.7	41±23	26±10	46±14	40±12	0.76±0.61	0.24±0.43	24±17
	Median (n)	7.1 (133)	34 (132)	26 (117)	48 (117)	42 (117)	0.60 (19)	0.11 (19)	21 (19)
	Range	0.0-63	8.4-106	2.6-49	7.4-77	13-65	0.20-3.1	-0.024-1.9	-2.4-63
GBNP 2015	Mean ± StDev	4.4±2.9	45±33	48±7.2	56±8.0	53±7.5	0.26±0.13	0.081±0.071	31±22
	Median (n)	3.8 (171)	38 (174)	47 (169)	54 (169)	52 (169)	0.25 (23)	0.062 (23)	30 (23)
	Range	0.30-21	2.5-134	32-81	35-82	35-82	0.12-0.70	-0.069-0.27	-28-74
UNRG 2015	Mean ± StDev	6.7±3.9	30±24	36±11	58±12	52±12	1.5±1.2	0.69±0.88	35±23
	Median (n)	6.1 (162)	22 (154)	34 (194)	57 (194)	50 (194)	1.1 (11)	0.34 (11)	25 (11)
	Range	1.7-35	1.5-121	15-71	29-92	25-85	0.35-4.4	0.032-2.9	9.0-74

b) June-October

Site	Statistics	$PM_{2.5}$ (µg m^{-3})	RM (pg m^{-3})	O_3 (ppbv)	Max 1 h O_3 (ppbv)	MDA8 O_3 (ppbv)	Total Pb (ng m^{-3})	Asian Pb (ng m^{-3})	% Asian Pb
PEAV 2014	Mean ± StDev	10±6.6	48±26	50±6.6	58±8.1	55±7.5	0.33±0.13	0.070±0.060	23±14
	Median (n)	5.3 (105)	42 (117)	50 (119)	57 (119)	54 (119)	0.33 (16)	0.06 (16)	20 (16)
	Range	0.80-42	1.9-140	34-69	42-80	39-78	0.13-0.63	0.0-0.26	0.51-58
UNRG 2014	Mean ± StDev	9.6±8.7	48±22	27±9.9	47±15	41±13	0.62±0.24	0.13±0.12	21±15
	Median (n)	7.4 (98)	44 (98)	29 (86)	48 (86)	42 (86)	0.59 (16)	0.10 (16)	21 (16)
	Range	0.0-63	8.4-106	8.9-49	19-77	14-65	0.20-1.0	-0.024-0.40	-2.4-47
GBNP 2015	Mean ± StDev	4.76±3.4	64±28	48±7.9	56±8.7	54±8.2	0.25±0.090	0.080±0.055	32±18
	Median (n)	4.1 (107)	59 (107)	47 (120)	54 (120)	52 (120)	0.26 (19)	0.062 (19)	26 (19)
	Range	1.1-21	17-134	32-81	35-82	35-82	0.12-0.46	0.022-0.21	6.68-74
UNRG 2015	Mean ± StDev	7.9±5.1	50±20	32±6.8	53±9.6	46±7.9	1.2±0.88	0.42±0.56	27±21
	Median (n)	6.7 (73)	49 (73)	31 (122)	53 (122)	46 (122)	0.82 (8)	0.24 (8)	21 (8)
	Range	2.7-35	21-121	19-44	34-85	29-65	0.35-2.4	0.032-1.7	9.0-74

GBNP – Great Basin National Park, NV, USA
Max 1 h O_3 – maximum 1 h average of each day
MDA8 O_3 – maximum daily average (8 h) for each day
O_3 – ozone
Pb - lead.
PEAV – Peavine Peak, Reno, NV, USA
$PM_{2.5}$ – particulate matter <2.5 µm in diameter
ppbv – parts per billion by volume
RM – reactive Hg

4.1 PEAV and UNRG 2014

During summer and fall (June to November 2014) when TAPI Beta^{Plus} particulate measurement systems were located at UNRG and at PEAV, O_3 monthly means and monthly MDA8 O_3 means were statistically higher at PEAV for all months. $PM_{2.5}$ and RM monthly means were not statistically different between the two sites. Chemical composition of RM (except for mid-to-late June) at UNRG were primarily nitrogen and sulfur compounds, while at PEAV compounds were primarily halogen based Hg compounds with periodic appearances of Hg-O, nitrogen-, and sulfur-based compounds, indicating the sites were often isolated from each other.

Daily $PM_{2.5}$ mass concentrations were statistically higher at UNRG. CO monthly means were lower at PEAV. Percent Asian Pb for the two sites was similar, median Pb mass concentration was higher at UNRG. Wind speed monthly means were higher at PEAV. Monthly mean temperature was lower at PEAV, while RH monthly means were not statistically different between the two sites. These comparisons reflect the fact that PEAV is a high elevation location impacted by the free troposphere and that UNRG is adjacent to a highway, where increased levels of $PM_{2.5}$, Pb, and other pollutants (e.g. CO, NO_x, SO_2) are experienced.

Diel patterns of CO at PEAV (SI Fig. 1) indicate upslope convective mixing; increasing CO by ~60 ppbv in the afternoon. There was a small increase in O_3 (by ~2 ppbv) at this time as well. Positive correlation between O_3 and <1 km trajectories from San Francisco and negative correlation with RH indicate that for this period, regional air from the west (prevailing wind direction) transported O_3 (SI Tables 3-6). Positive

correlations between O_3 and ABLH and the diel patterns indicate impacts from upslope flow of pollutants from Reno, NV as the valley warmed (SI Fig. 1). However, given the small increase in O_3 (3%), PEAV likely had access to O_3 aloft and limited photochemical production of O_3, indicating the Reno/Sparks valley was not the primary source. Long-range transport and southern Nevada did not increase daily averages of O_3. Max 1 h and MDA8 O_3 often occurred with increased pollutants ($PM_{2.5}$ and CO), and drier, high, fast moving conditions, indicating long-range transport events occurred at a shorter time scale than 24 h.

RM at PEAV (SI Table 3) was positively correlated with O_3 and negatively correlated with N. Eurasia trajectories. This indicates the importance of local and regional sources of oxidants for formation. The >3 km trajectories from San Francisco and halogenated RM species ($HgBr_2$ and $HgCl_2$) measured at PEAV indicate that reactions in the marine boundary layer during this time influenced this site (Gustin et al., 2016; Timonen et al., 2013). Positive correlations between O_3 (daily average, max 1 h, MDA8 [$p<0.1$]), temperature, pressure, and ABLH also indicate that local sources could periodically influence RM, bringing up pollutants from the Reno/Sparks valley.

For the days with Pb isotope analysis at PEAV (19 days, SI Tables 7-11), % Asian Pb was correlated with trajectories from E. Asia; however, this was not correlated with O_3. Total Asian Pb and % Asian Pb were derived using data from Asia (China), a large emitter of Pb due to industrial processes, so the positive correlation with E. Asia trajectories is reasonable. This correlation demonstrates that Asia was a significant source of Pb to this high elevation site. Pb isotopes measured at PEAV during this time were located on the California Array and on a mixing line that had a slope of 0.92 ($r^2 = 0.90$)

and intercepted and overlapped ores from Russia, Mongolia, and Kazakhstan (Fig. 1a). Based on meteorology, other sites in Nevada will also experience significant amounts of Pb from Asia (Christensen et al., 2015; Gustin et al., 2015b). RM was not correlated with % Asian Pb further supporting regional impacts of oxidants on RM concentrations and formation.

At UNRG, CO and NO_x increased during the morning commute (05:00 to 08:00 PST); O_3 started to increase at 07:00 and stayed elevated until 20:00 (SI Fig. 2). The morning increase was due to local sources, while the afternoon elevation was due to down mixing from the free troposphere, similar to what has been observed in valleys of Nevada, including Reno (Gustin et al., 2015b; Gustin et al., 2013) and in California (Burley and Bytnerowicz, 2011). The same diel pattern was observed at UNRG in 2014 and 2015 (SI Fig. 2 and 3). This site is located <30 m from a highway and the pattern of criteria pollutants at this location show an association with local mobile sources (SI Fig. 2 and SI Tables 12-15). During the 2014 sample period at UNRG, O_3 (daily average) was impacted by regional transport bringing air pollution from San Francisco, Sacramento, and the San Joaquin Valley up the I-80 corridor (CARB, 2001) and through the Yuba River gap, indicated by the short-term O_3 measurements (max 1 h, MDA8) being positively correlated with SO_2 and NO. O_3 (daily average, max 1 h, MDA8) was also impacted by long-range transport, indicated by positive correlations with N. Eurasia and E. Asia trajectories.

RM compounds at UNRG were primarily indicative of quick oxidation reactions associated with highway pollutants (nitrogen and sulfur compounds, Gustin et al., 2016); however, a mixture of compounds was observed, including halogenated compounds

($HgBr_2$ and $HgCl_2$). RM was negatively correlated with all trajectories from N. Eurasia and E. Asia, and with O_3 ($p<0.1$), max 1 h O_3, MDA8 O_3 (SI Table 12) indicating RM did not arrive with trans-Pacific air masses, but halogenated compounds suggest a marine boundary contribution and local and regional oxidants impacting concentrations. Both PEAV and UNRG had little influence from the Las Vegas source box.

For the days with Pb isotope data at UNRG (19 days, SI Tables 16-20), Pb measured at UNRG was also impacted by long-range transport from E. Asia. Pb isotopes measured at UNRG during this time were located on the California Array, again on a mixing line that had a different slope from PEAV (slope=1.04, $r^2 = 0.83$) and overlapped ores from Russia, Mongolia, and Kazakhstan towards the Asia array (Fig. 1a). UNRG and PEAV Pb days were analyzed for the same day at both sites due to the proximity of the two sites. UNRG had ~1.9 times the amount of Pb and ~1.5 times the amount of Asian Pb compared to PEAV, confirming that PEAV is more rural but may intercept long-range air masses. Additional Pb isotopic data from Eurasia (Fig. 1 grey data points from: Bollhöfer and Rosman, 2001; Bollhöfer and Rosman, 2002; Brown, 1962; Doe, 1970; Hopper and Ross, 1991) show that N. Eurasian sources need to be considered.

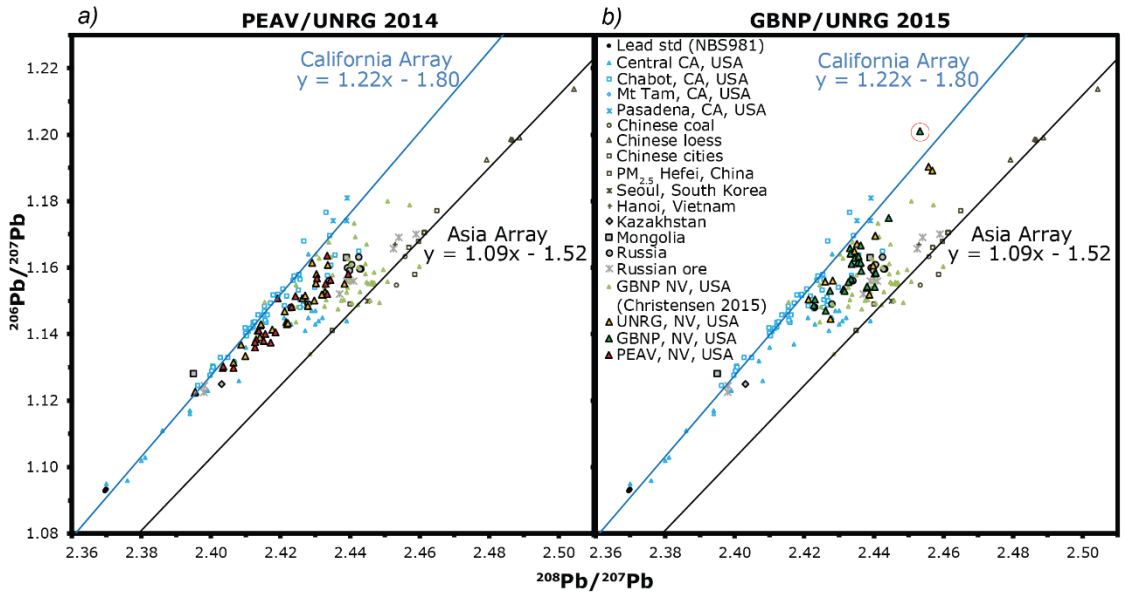

Figure 1: Plot of $^{206}Pb/^{207}Pb$ vs. $^{208}Pb/^{207}Pb$ for 2014 data at a) UNRG and PEAV 2014, and b) UNRG and GBNP 2015, including data from previous studies. Data from California is in blue, Asia in black, UNRG in yellow, PEAV in red, GBNP in green, and N. Eurasia in grey. Data include Mt. Tamalpais, Chabot science center, CA, central CA, Chinese Loess and Hefei, China (Ewing et al., 2010), Eurasian aerosols (Bollhöfer and Rosman, 2001; Bollhöfer and Rosman, 2002), Chinese coal (Díaz-Somoano et al., 2009; Tan et al., 2006), Chinese Loess (Jones et al., 2000), Russian ores (Brown, 1962; Doe, 1970; Hopper and Ross, 1991), and Great Basin National Park, NV (Christensen et al., 2015). Red circle indicates anomalous data point.

4.2 GBNP and UNRG 2015

The diel pattern at GPNP during spring and fall 2015 (SI Fig. 4), shows an increase in O_3 of ~6 ppbv starting at 05:00 to 11:00 PST that stayed elevated until 16:00 as air was mixed down to this high elevation location. When looking at the fine resolution data (SI Fig. 4b), CO (120 ppb) and NO_x (0.55 ppb) concentrations increased by 12 ppb and 0.6 ppb, respectively, at 06:00 PST, then declined and increased again mid-morning (10:00 PST), and then declined and increased again mid-afternoon (16:00 and 18:00 PST, respectively), suggesting local source impacts, also seen in previous work (Miller et al.,

2015). Mean O_3 at GBNP during this period (48±9 ppbv) was also similar to previous studies (46±9 ppbv, Miller et al., 2015).

For this sample period at GBNP (SI Tables 21-24), O_3 (daily average, max 1 h, MDA8) was positively correlated with $PM_{2.5}$, CO, temperature, solar radiation, total and >3 km trajectories from N. Eurasia, >3 km trajectories from E. Asia, and >3 km trajectories from over San Francisco and negatively correlated with NO_x and RH. This indicates that GBNP O_3 was impacted by long-range transport, with some impact from regional and local sources. GBNP experiences differing conditions based on season (Fine et al., 2015a; Fine et al., 2015b; Gustin et al., 2015b). Air masses often approach GBNP from the southwest in the spring, particularly during cyclonic flow that disrupts prevailing westerly wind patterns (Fine et al., 2015a; Fine et al., 2015b; VanCuren and Gustin, 2015), bringing regional pollution from Los Angeles and Las Vegas (SI Table 25). In summer, GBNP has more local tourist activity. Increased photochemical reactions and convective mixing in the summer also facilitate interception of trans-Pacific air masses, and stronger positive correlations with long-range air masses (SI Table 26)

RM at GBNP (SI Table 21) was positively correlated with $PM_{2.5}$, O_3 (daily average, max 1 h, MDA8), temperature, solar radiation, and trajectories from Los Angeles and Las Vegas. RM was negatively correlated with NO_x, RH, and all trajectories from N. Eurasia and E. Asia. This indicates that regional sources were facilitating production of RM and that RM from Eurasia was lost due to deposition or conversion to GEM, this is also supported by the a negative correlation between % Asian Pb and RM (SI Table 24).

For the days with Pb isotope analysis at GBNP (22 days, SI Tables 27-31), total Pb mass and total Asian Pb mass were positively correlated with O_3. Percent Asian Pb was positively correlated with total and >3 km trajectories from E. Asia, and negatively correlated with <1 km trajectories from Los Angeles and <1 km ($p<0.1$) trajectories from Las Vegas, indicating the importance of Asian sources of Pb to GBNP. Pb isotopes measured at GBNP during this time were located on the California Array and on a mixing line towards the Asia array that had a slope of 0.79 ($r^2 = 0.44$, Fig. 1b)

For this sample period, at UNRG (SI Tables 32-35), significant positive correlations between O_3 and ABLH, N. Eurasia and E. Asia indicated that daily average, max 1 h, MDA8 O_3 at UNRG during this period were influenced by long-range transport (SI Table 35). $PM_{2.5}$ was positively correlated with other pollutants (RM, CO, NOx, and NO), highlighting the urban nature of this site.

RM at UNRG during this period (SI Table 32) was positively correlated with $PM_{2.5}$, solar radiation, temperature, and <1 km trajectories from San Francisco. RM was negatively correlated with O_3 (daily average, max 1 h, MDA8), and all trajectories from N. Eurasia, and from E. Asia. Again, indicating local and regional impacts were greater than long-range impacts, supported by nitrogen and sulfur based RM compounds measured during this time (Gustin et al., 2016).

For days with Pb isotope analysis at UNRG (11 days, SI Tables 36-40), daily average O_3, max 1 h O_3 ($p<0.1$), and MDA8 O_3 were positively correlated with % Asian Pb. Filters analyzed for Pb were biased towards understanding O_3 events (noted below), so this correlation makes sense. At UNRG during this time, total and Asian Pb mass was greater, but the % Asian Pb was similar to that measured at GBNP. It is important to note the

differences in samples between UNRG (n=11) and GBNP (n=23). Pb isotope ratios for UNRG lie between the Asia and California arrays on a mixing line that had a slope of 1.17 (r^2 = 0.77), and indicate a Eurasian influence (Fig. 1b). There is one anomalous point from GBNP on September 3, 2015 with -28% Asian Pb (circled in red in Fig. 1b). Trajectories for this time (SI Fig. 5) remain over the Pacific Ocean, southern California, and western Mexico, with minor transport from N. Eurasia and central USA. It is uncommon to have trajectories in this area track over central USA, which could explain the anomalous data; however, HYSPLIT only indicates two trajectories out of 216 from this area. Two days at UNRG during the same time (August 31 and September 2) had similar high 208/207 Pb ratios but lower 206/207 Pb ratios, and previous data from California (Fig. 1, blue squares) also occur to the left of the California array. The September 3, 2015 data point was not included in the Pearson correlation analyses or in the linear fit in the data but is included in Table 2 and Fig 1b.

5. Discussion:

5.1 Case studies

Complex weather dynamics affect the transport of atmospheric pollutants in the Western USA. To understand this phenomenon, specific events were assessed as case studies. These case studies were selected based on % Asian Pb, concentrations of O_3 (daily average, max 1 h, MDA8), RM, CO, and RH values. Days were selected when these values were above the monthly median (RH below monthly median), indicating pollution transport events and compared to days below the monthly median.

5.1.1 June 2014

Pb samples were analyzed for June 6, 12, and 17, 2014 at PEAV and UNRG (SI Fig. 6). During this time, weather maps indicated a low-pressure system at the surface (SI Fig. 7a-d) and cyclonic flow at 500 mb moved from W to E across the top of Nevada (SI Fig. 8a-d), while a cold front associated with the low moved W to E across Nevada. Pressure measured at PEAV dropped across this period and temperature decreased (16, 12, and 3° C on the 3 days). ABLH measured at 16:00 PST lowered from 3.2 to 1.9 km, and then returned to 3.5 km. Wind speed at PEAV and UNRG was higher on June 12 at 16 m s^{-1} and 3.7 m s^{-1} compared to median monthly values of 3.1 m s^{-1} and 2.0 m s^{-1}, respectively. RH was lower than the monthly median on June 6 and 12 at both PEAV and UNRG and higher than the monthly median on June 17 (SI Fig. 9 and 10). Influence from the total E. Asia trajectory box on these days, decreased from 1.0% to 0.019%, and then increased to 0.15%. At the same time, influence from N. Eurasia decreased and increased 5.0%, 1.8%, and 16%. Trajectories for June 12 (Fig. 2a and 3b) resided mainly over the Pacific Ocean. On June 9 and 10 at PEAV, there was an increase in $PM_{2.5}$, O_3 (daily average, max 1 h, MDA8), RM, CO, and influence from N. Eurasia and E. Asia trajectories (SI Fig. 9). Influence from N. Eurasia remained elevated through June. It is likely that air masses being transported over the Pacific Ocean at this time were polluted and the low-pressure system and associated cold front brought this air to the surface along with air from the San Francisco area.

On June 12, % Asian Pb was 41%, higher than the 75th percentile (36%) at PEAV. $PM_{2.5}$, O_3 (daily average, max 1 h, MDA8), and RM increased on June 12 above the monthly medians for each measurement. During this period, RM compounds differed

slightly between the two sites with HgO, $HgCl_2$, and $HgBr_2$ seen at PEAV, and $HgCl_2$ and $HgBr_2$ at UNRG (Gustin et al., 2016). RM compounds appear to be influenced by interaction with the MBL. CO at PEAV was below the monthly median for all 3 days as the front moved through (SI Fig. 9b).

On June 12 at UNRG, % Asian Pb was 47%, higher than the 75^{th} percentile (42%) for Pb samples at UNRG in 2014. $PM_{2.5}$, WCAQ O_3 (daily average, max 1 h, MDA8), and RM increased on June 12 above the monthly medians for each measurement. CO was above the monthly median for June 6 and 12, and below on June 17 (SI Fig. 10b). This is an example of input of Trans-Pacific pollution associated with frontal activity as described by Knowland et al. and VanCuren et al. (2015; 2005). For June 2014, both PEAV and UNRG had halogenated RM compounds and elevated influence from >3 km trajectories from over San Francisco. MDA8 O_3 was enhanced by 2 to 7 ppbv above the monthly median at PEAV and 4 to 9 ppbv at UNRG.

a)

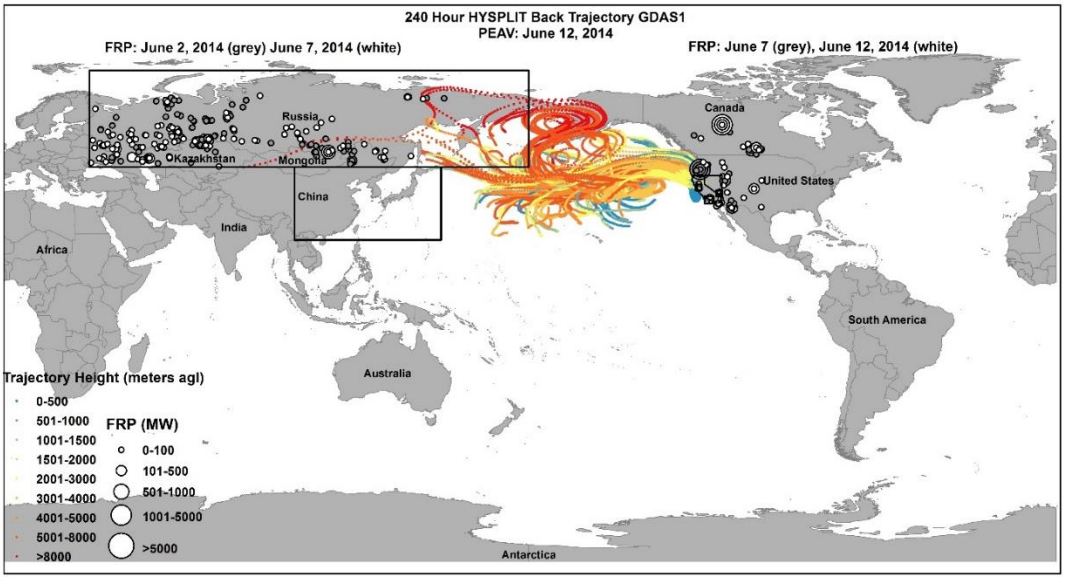

b)

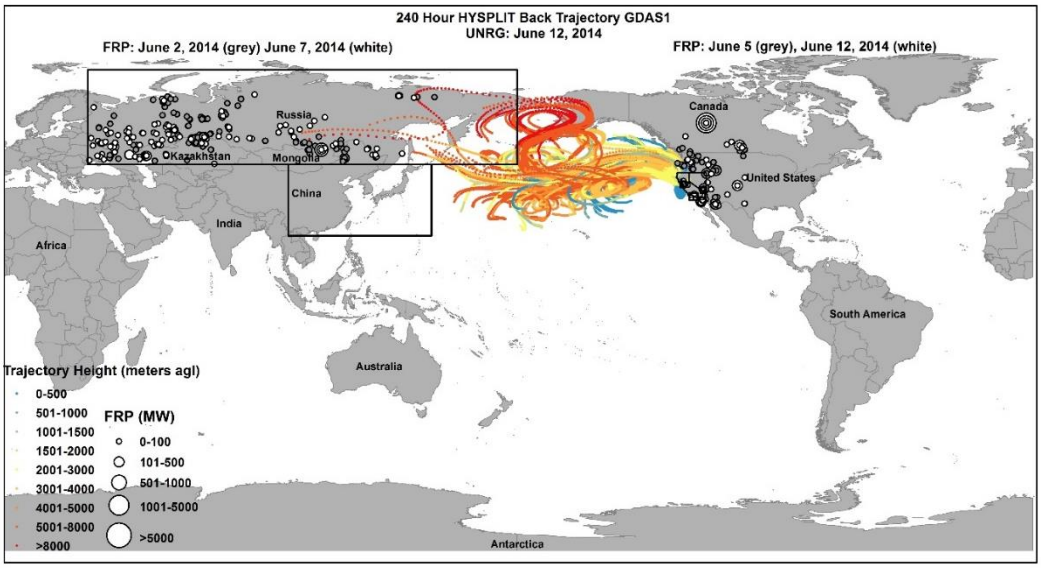

Figure 2a and b: HYSPLIT 10-day back trajectories for a) PEAV and b) UNRG June 12, 2014. Trajectory points are colored by altitude height (m agl). FRP points are sized based on power (MW), white circles indicate the most recent day back, light grey circles indicate an intermediate day back, and grey circles indicate the furthest day back. Black boxes indicate the five source boxes.

5.1.2 September/October 2014

From September 13 to October 31, 2014, the King Fire burned over 390 km^2 in California, southwest of Reno, NV (CA, 2017). On September 22 and 24, $PM_{2.5}$, O_3, CO were all above monthly medians (SI Fig. 11 and 12) at PEAV and at UNRG on September 22 due to influence from this fire, seen in SI Fig. 13 from the Naval Research Laboratory Aerosol Analysis and Prediction System (NAAPS, https://www.nrlmry.navy.mil/aerosol/). RH on September 22 was higher than the monthly median at PEAV and UNRG due to emission of water vapor associated with biomass burning (SI Fig. 11a & 12a, Parmar et al., 2008). RM at both sites was lower than the monthly median. RM compounds at the end of September were not discernible at PEAV. At this time, UNRG had nitrogen and sulfur RM compounds (Gustin et al., 2016). Influence from local (King fire) and regional sources dominated this period. Previous large fires west of Nevada have also impacted air quality in Nevada (Rim Fire 2013, Miller et al., 2015).

On September 27, October 15, and 17, Pb samples at PEAV were > 36% Asian Pb (SI Fig. 14). September 27, October 9, and October 17 Pb samples at UNRG were greater than or equal to 42% (SI Fig. 14). Although September 27 had high % Asian Pb (58% at PEAV and 42% at UNRG), there was moderate input of air from N. Eurasia and San Francisco, which may reflect previously deposited Asian Pb being re-mobilized during the fire and mixed with local and regional sources. Precipitation was observed that day, likely lowering pollutant concentrations; $PM_{2.5}$, O_3, CO, and RM were all below monthly medians. RM compounds were different during the end of September and start of October, PEAV had $HgCl_2$, $HgBr_2$, and nitrogen compounds indicating input from the

marine boundary layer, while UNRG had nitrogen and sulfur RM compounds (Gustin et al., 2016). October 15 and 17 at PEAV had $PM_{2.5}$, above the monthly median and RM below the monthly median. October 17 had O_3 (daily average, max 1 h, MDA8) and CO concentrations higher than the monthly medians (there were no CO measurements for October 15). Temperature on October 17 was higher, while wind speed was lower than October 15. N. Eurasia and E. Asia TRTs doubled from October 15 to October 17 (Fig. 3a and b). A low-pressure system and cold front moved through the area between October 15 and 17 (SI Fig. 15), bringing down drier air from the free troposphere and stratosphere, demonstrating that trans-Pacific air masses can influence the Western USA in the fall. In September 2014, MDA O_3 at PEAV was initially suppressed ~12 ppbv while UNRG stayed at the monthly median during heavy fire impacts and then enhanced ~18 ppbv at PEAV and UNRG as the fire plume aged. In October, PEAV MDA O_3 was enhanced 5 to 7 ppbv, while UNRG saw little enhancement during this time.

a)

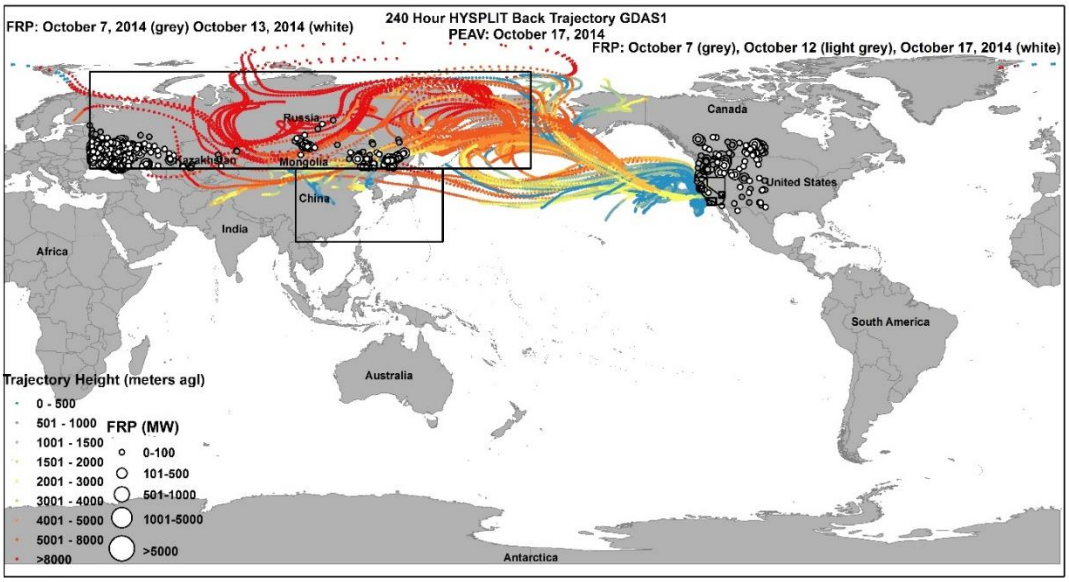

b)

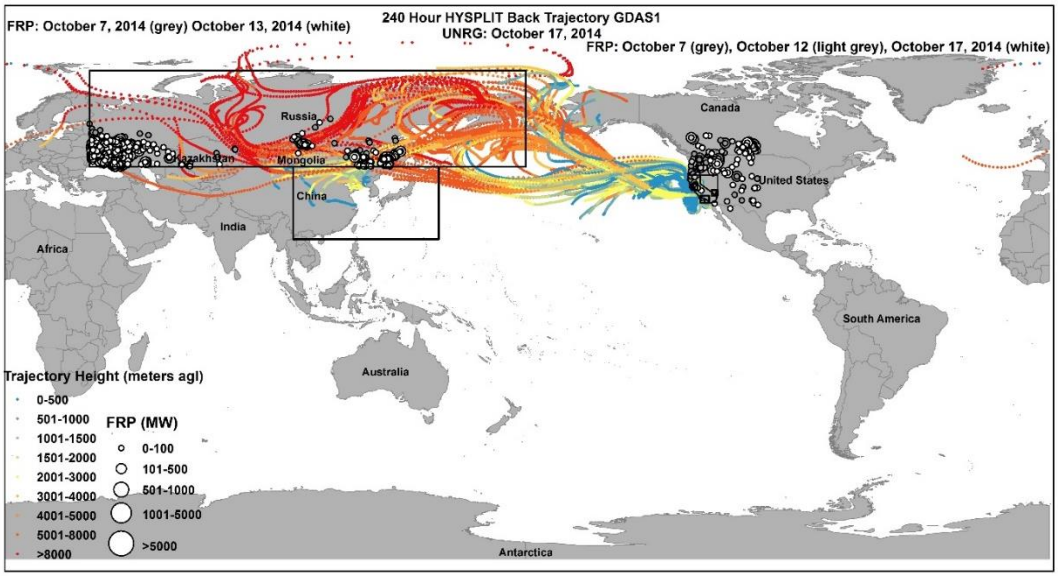

Figure 3a and b: HYSPLIT 10-day back trajectories for a) PEAV and b) UNRG October 17, 2014. Trajectory points are colored by altitude height (m agl). FRP points are sized based on power (MW), white circles indicate the most recent day back, light grey circles indicate an intermediate day back, and grey circles indicate the furthest day back. Black boxes indicate the five source boxes.

5.1.3 March 2015

Two low-pressure systems moved NW to SE, and an associated cold front moved across the state from March 28 to 29, and March 31 to April 1 (SI Fig. 16). There were no CO or NO_x measurements for this period at GBNP. March 27 at GBNP had lower $PM_{2.5}$, O_3 (daily average, max 1 h, MDA8), and RM than monthly medians and RH only slightly lower than the monthly median. March 31 had higher $PM_{2.5}$, O_3 (daily average, max 1 h, MDA8), and RM than the monthly median and RH was half of the monthly median (SI Fig. 17). On March 31, there was influence from the E. Asia source box greater than the 75th percentile for the site and three times March 27, which doubled the next day as the low continued to move through. There was also influence from the San Francisco source box above the 75th percentile on March 31. March 31 had the highest Pb mass (0.70 ng m^{-3}) of the 22 days analyzed for Pb, but was only 38% Asian Pb compared to March 27 (0.15 ng m^{-3}), which was 65% Asian Pb (SI Fig. 18). As the low-pressure system moved west to east, there was an increase in trans-Pacific, Los Angeles, and Las Vegas trajectory influence at GBNP while UNRG had increases in trans-Pacific and >3 km trajectories from over San Francisco.

UNRG had a similar pattern for March 28 and March 31 for $PM_{2.5}$ and CO. O_3 (daily average, max 1 h, MDA8) for both days was higher than the monthly median (SI Fig. 19). RH was lower than the monthly median for both days. RM was higher than the monthly median on March 31. Influence from N. Eurasia and E. Asia were both higher than the 75th percentile for this period, there was elevated influence from San Francisco as well.

HYSPLIT back trajectories for March 27 from GBNP and March 28 from UNRG (Fig. 4a and 4b) show minimal trajectories through E. Asia and most of the trajectories stayed low above the Pacific Ocean. The NAAPS optical depth maps (SI Fig. 20) show a plume with moderately high optical depth moving from W to E across the Pacific towards Western North America, March 30 to March 31, 2015. HYSPLIT back trajectories for March 31 at GBNP and UNRG (Fig. 4c and 4d) show air masses moving very quickly, several of which made it around from Greenland and Eastern North America. Trajectories coming into GBNP stayed mostly south of the N. Eurasian source box in the E. Asian source box while trajectories coming into UNRG had a mix of E. Asia and N. Eurasian influence. Percent Asian Pb was lower on March 31 due to the combination of local sources and long-range transport from Eurasia as well as the Eastern USA.

MODIS FRP (Fig. 4c and 5d) shows multiple large fires in the N. Eurasia source box and east of Nevada, occurring during this time. IMPROVE data (SI Fig. 21) for March 31 at GBNP shows elevated potassium (K) over the monthly mean, a tracer for biomass burning, as well as aluminum (Al), chloride (Cl-), chlorine (Cl), iron (Fe), magnesium (Mg), sea salt, silicon (Si), sodium (Na), and soil. Although March 31 was influenced by trans-Pacific air, the fast moving air likely picked up many sources of pollution including local and regional (SI Fig. 22), contributing to O_3 concentrations at GBNP and UNRG (67 and 69 ppbv, respectively) approaching the NAAQS concentration for the design value. MDA8 O_3 was enhanced by 2 to 16 ppbv above the monthly median at GBNP and 5 to 14 ppbv at UNRG during these events.

a)

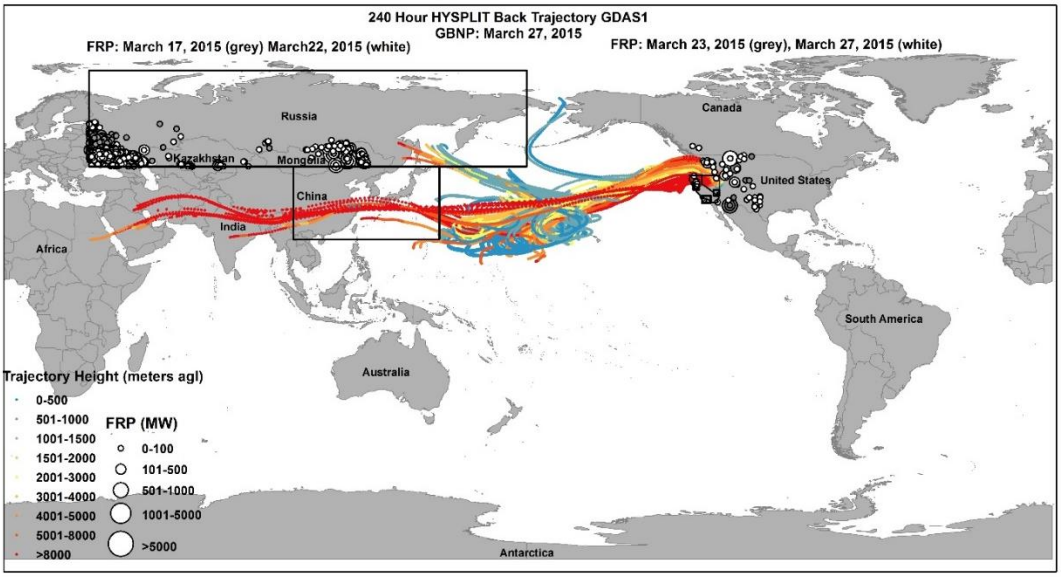
240 Hour HYSPLIT Back Trajectory GDAS1
GBNP: March 27, 2015
FRP: March 17, 2015 (grey) March22, 2015 (white)
FRP: March 23, 2015 (grey), March 27, 2015 (white)
Russia
Canada
Kazakhstan
Mongolia
China
United States
India
Africa
South America
Australia
Antarctica
Trajectory Height (meters agl)
0-500
501-1000
1001-1500
1501-2000
2001-3000
3001-4000
4001-5000
5001-8000
>8000
FRP (MW)
0-100
101-500
501-1000
1001-5000
>5000

b)

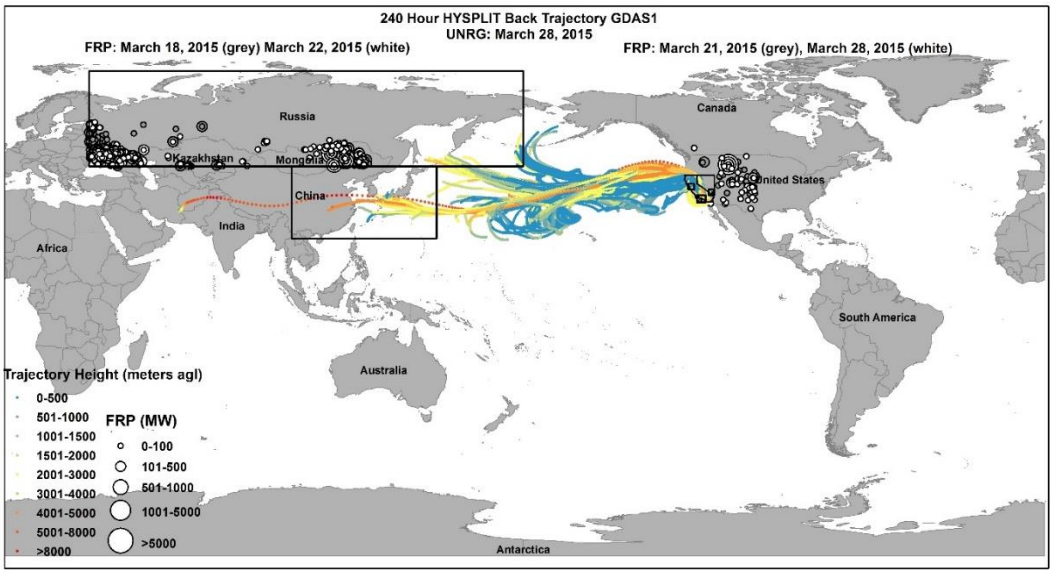
240 Hour HYSPLIT Back Trajectory GDAS1
UNRG: March 28, 2015
FRP: March 18, 2015 (grey) March 22, 2015 (white)
FRP: March 21, 2015 (grey), March 28, 2015 (white)
Russia
Canada
Kazakhstan
Mongolia
China
United States
India
Africa
South America
Australia
Antarctica
Trajectory Height (meters agl)
0-500
501-1000
1001-1500
1501-2000
2001-3000
3001-4000
4001-5000
5001-8000
>8000
FRP (MW)
0-100
101-500
501-1000
1001-5000
>5000

c)

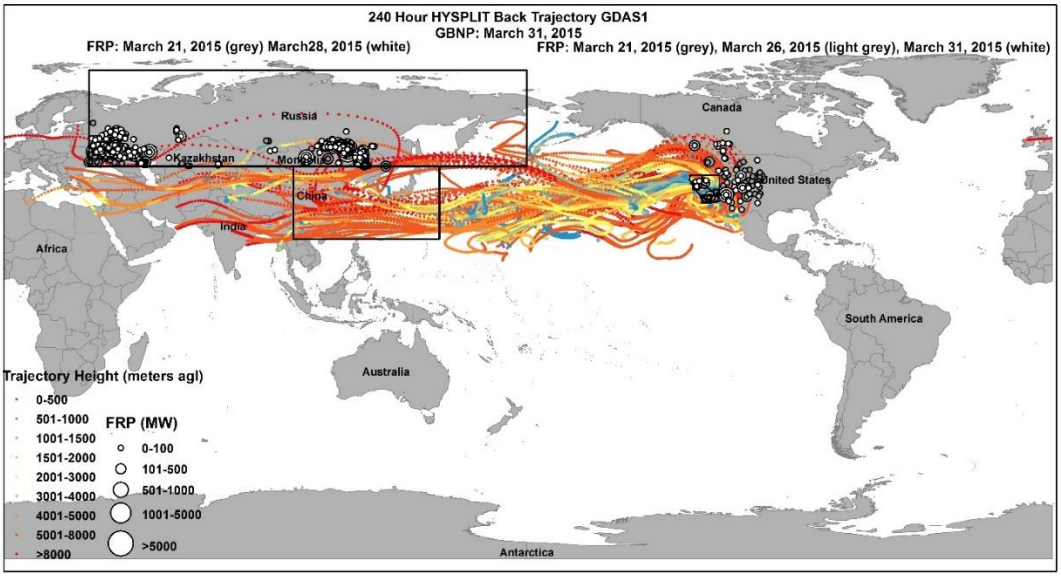

d)

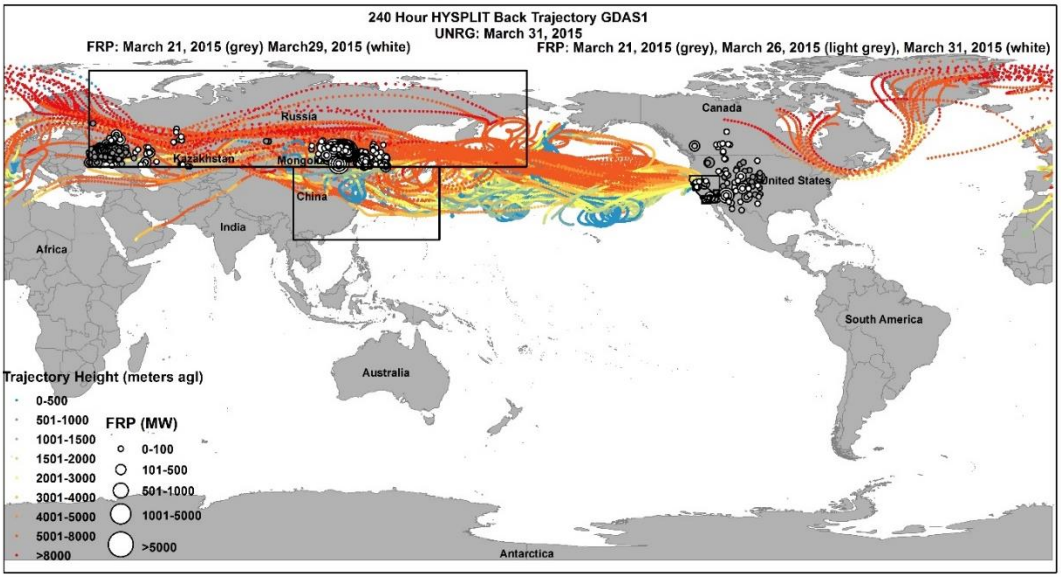

Figure 4a, b, c, and d: HYSPLIT 10-day back trajectories for GBNP March 27 (a), 31 (c) and UNRG March 28 (b), 31 (d), 2015. Trajectory points are colored by altitude height (m agl). FRP points are sized based on power (MW), white circles indicate the most recent day back, light grey circles indicate an intermediate day back, and grey circles indicate the furthest day back. Black boxes indicate the five source boxes.

5.1.4 June 2015

June had the highest mean monthly O_3 (56 ppbv daily, 65 ppbv max 1 h, 62 ppbv MDA8) concentrations of the six-month study period at GBNP. Eight days in June were analyzed for Pb isotopes (SI Fig. 23). On June 8 and 9 at GBNP MDA8 was above the 70 ppbv concentration used for the NAAQS, decreasing from June 8 to June 9. CO, NO_x, and NO were all above the monthly median. $PM_{2.5}$ was below the monthly median but decreased further on June 9, RM also decreased. RH dropped from 38% on June 8 to 29% on June 9; both days were below the monthly median (SI Fig. 24), there was a small amount of precipitation on June 8. Influence from the N. Eurasia and E. Asia source boxes decreased by half, both below the 75th percentile. There was no influence from the <1 km San Francisco box and minimal influence from the <1 km Los Angeles and Las Vegas boxes, air mainly arrived >3 km over these source boxes (Fig. 5a and b). From June 8 to June 9, a high-pressure area stagnated over Nevada and the rest of the inland Western USA, while low pressure occurred over California and a weak cyclonic system remained at the 500 mb level over Nevada (SI Fig. 25 and 26), bringing air aloft down to the surface. Speciated $PM_{2.5}$ IMPROVE data (SI Fig. 27) had elevated sulfate (SO_4, NH_4SO_4), Si, and sulfur (S) on June 8, generally considered tracers of long-range transport of pollutants associated with combustion from Asia (Christensen et al., 2015). Total Pb mass decreased slightly, but percent Asian Pb stayed the same (61%) for both days.

At UNRG, as the high-pressure system remained over Nevada ($PM_{2.5}$, O_3 daily average, max 1 h O_3, MDA8 O_3, and CO), pollutant concentrations increased from June 8 to June 9 (SI Fig. 28). NO_x decreased and RH increased with some precipitation. Solar

radiation decreased, wind speed and temperature were similar. RM concentrations did not change between the two days. Influence from N. Eurasia and E. Asia decreased over the two days at similar magnitudes as the TRTs for GBNP. Influence from San Francisco trajectories increased. Trajectories from Las Vegas and Los Angeles were similar for the two days (~1.1% and 0.03%, respectively), both were higher than the 75th percentile for the sample period (~0.03% and 0.0%, respectively). Total Pb mass increased and % Asian Pb went from 40% to 74% between the two days. During this period, the Western USA was influenced by regional sources, long-range transport and possibly STE as air aloft subsided.

At GBNP, on June 17 and 18, max 1 h O_3 was over 70 pbb and MDA8 O_3 was 67 and 68 ppbv respectively, all higher than the monthly medians. $PM_{2.5}$ on June 17 was slightly higher than the monthly median and dropped below on June 18. CO, NO_x, and NO increased across the two days, NO_x on the second day and NO on both days were above the monthly medians. RH was below the monthly median on both days (SI Fig. 24). Influence from >3 km trajectories over the N. Eurasia source box dropped by half over the two days but were ~3 and 2 times higher than the 75th percentile value (Fig. 5c). Influence from <1 km from San Francisco decreased over the two days but was higher than the 75th percentile on both. Trajectories <1 km from Los Angeles and Las Vegas decreased but were below the 75th percentile. Total Pb mass was similar on the two days as was % Asian Pb (~40%). There was a high-pressure system that moved across the state, June 16 to 17, and lows surrounding the state. Cyclonic flow at the 500 mb pressure height remained over the state on June 17 and 18 (SI Fig. 29 and 30). IMPROVE data (SI Fig. 31) from June 17 had elevated Al, nitrates (NH_4NO_3, NO_3), sulfates (NH_4SO_4, SO_4),

calcium (Ca), Cl-, Fe, Mg, sea salt, Si, and soil, above the monthly mean, pointing to local and long-range pollution sources. During this period, the Western USA was influenced by long-range transport and possibly STE as air aloft subsided as well as regional pollutants from Los Angeles and Las Vegas (SI Fig. 24c and 28c). The trajectory residences times clearly illustrate trans-Pacific air masses peaking at UNRG ~2 days before peaking at GBNP (SI Fig. 24c and 28c) as the high-pressure system moved across the state. In June 2015, MDA8 O_3 was enhanced by 4 to 10 ppbv above the monthly median at GBNP, and 7 to 9 ppbv at UNRG.

a)

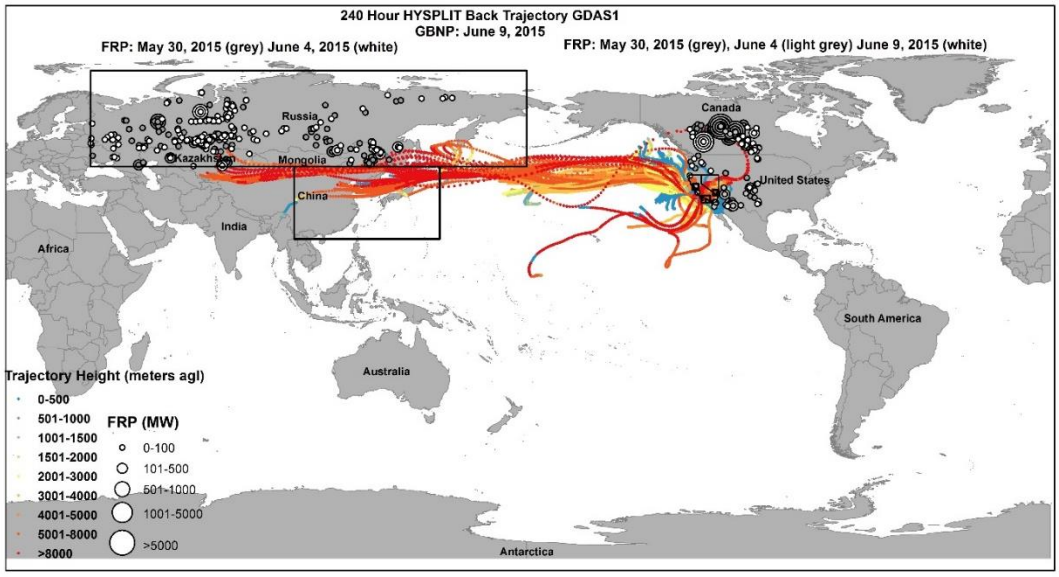

b)

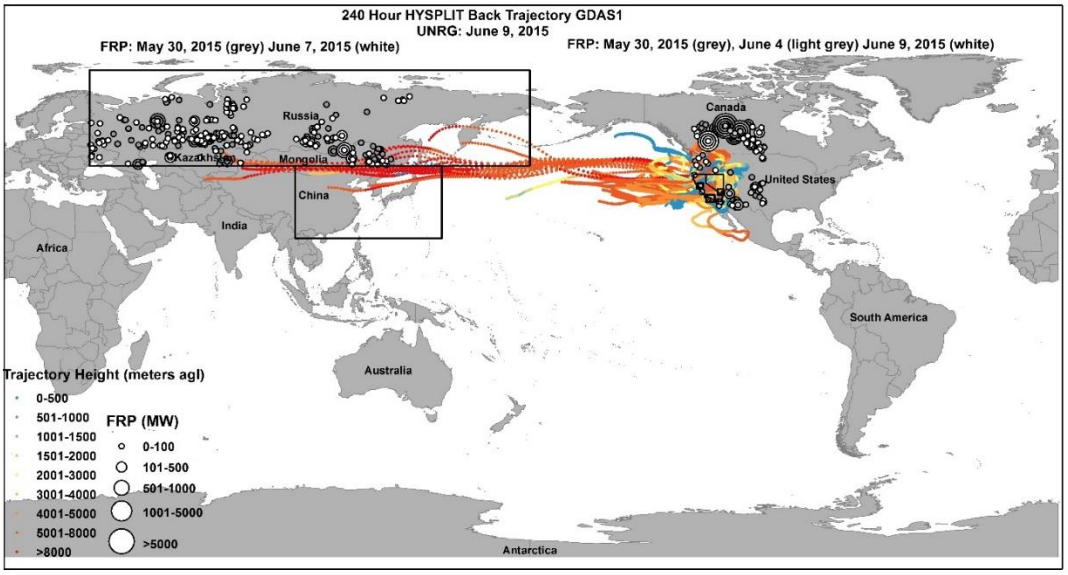

c)

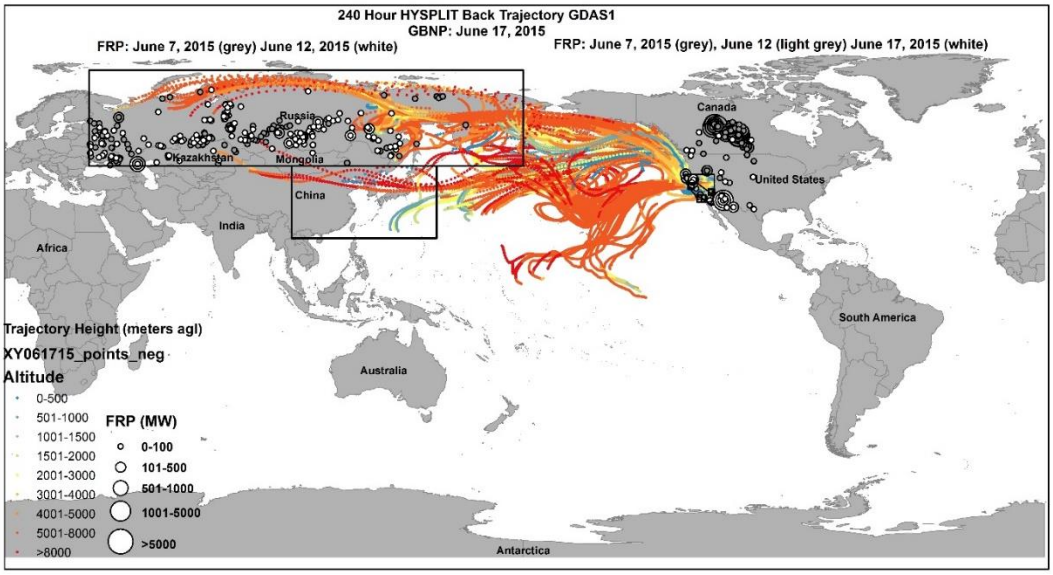

Figure 5: HYSPLIT 10-day back trajectories for (a) GBNP June 9, (b) UNRG June 9, and (c) GBNP June 17, 2015. Trajectory points are colored by altitude height (m agl). FRP points are sized based on power (MW), white circles indicate the most recent day back, light grey circles indicate an intermediate day back, and grey circles indicate the furthest day back. Black boxes indicate the five source boxes.

5.1.5 September 2015

On September 10, 2015 at GBNP, $PM_{2.5}$, O_3 (daily average, max 1 h, MDA8), CO, RM were all elevated above the monthly medians (SI Fig. 32). RH was below the monthly median. N. Eurasia trajectories were above the 75th percentile. TRT from the E. Asia source box decreased from the previous two days; however, percent Asian Pb was 74% (SI Fig. 32c and 33). TRTs from San Francisco were greater than the 75th percentile while trajectories from Los Angeles and Las Vegas (<1 km) were zero (SI Fig. 32c). FRP data show several fires in the trajectory paths with high FRP in the N. Eurasia source box and large FRP values in California (Fig. 6). Trajectories also arrived from over Canada and Alaska.

Surface weather maps show a high (SI Fig. 34) over Nevada and a weak cyclonic flow at the 500 mb level (SI Fig. 35); indicating that air aloft was mixed down to the ground. Before the high-pressure formed, Los Angeles trajectories had a strong influence on GBNP, which decreased with the high-pressure system (SI Fig. 32c). IMPROVE data (SI Fig. 36) shows elevated organic mass (OMC), due to local smoke (SI Fig. 37). Although O_3 concentrations were not approaching the NAAQS concentration on this day, concentrations were elevated above the monthly medians (SI Fig. 32), again demonstrating that long-range transport of air masses can influence pollutants in the Western USA outside of the spring months. Local sources, such as wildfires, may complicate the signature of long-range transport. In September 2015, MDA O_3 was enhanced by 17 ppbv above monthly medians at GBNP, with little enhancement at UNRG (SI Fig. 38).

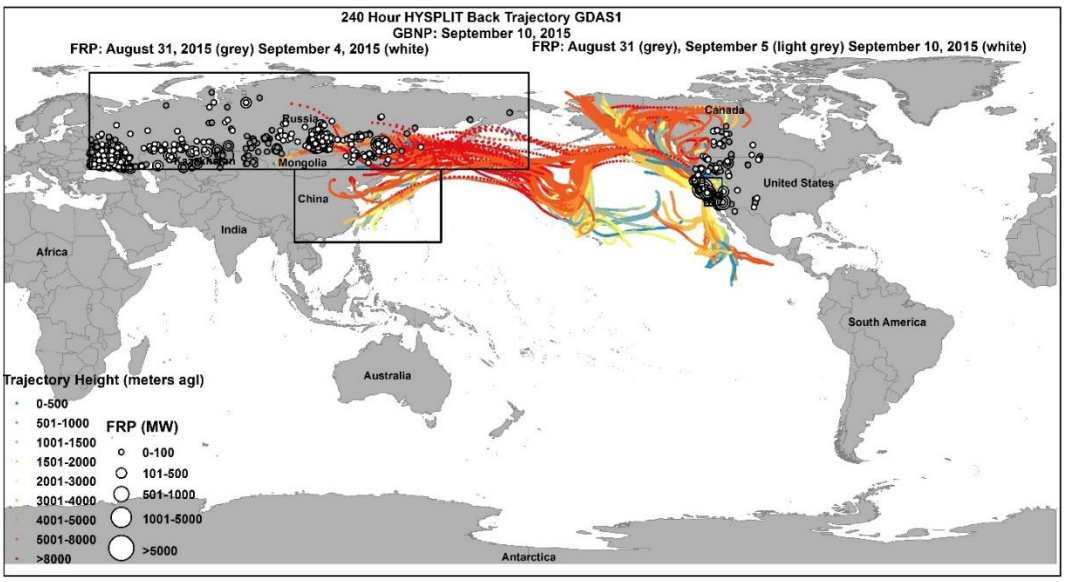

Figure 6: HYSPLIT 10-day back trajectories for GBNP September 10, 2015. Trajectory points are colored by altitude height (m agl). FRP points are sized based on power (MW), white circles indicate the most recent day back, light grey circles indicate an intermediate day back, and grey circles indicate the furthest day back. Black boxes indicate the five source boxes.

6. Conclusions:

Diel patterns of O_3 at the two high elevation sites had smaller ranges (<10 ppbv) and elevated O_3 compared to the lower elevation, urban site (>30 ppbv) similar to previous studies (Fine et al., 2015a). At both high elevation sites, max 1 h O_3 was positively correlated with $PM_{2.5}$ and CO, indicative of transport of pollutants from regional and long-range sources. Lower concentrations of $PM_{2.5}$ and CO at the two high elevation sites illustrated the rural nature compared to UNRG. Ozone was positively correlated with RM at both sites while RM was negatively correlated with RH, similar to free tropospheric data from Weiss-Penzias et al. (2015), indicating formation of RM from photo-oxidation of GEM in dry upper altitude air. Total Pb mass, total Asian Pb mass, and % Asian Pb were generally positively correlated with trajectories from E. Asia.

GBNP air was influenced by Las Vegas and Los Angeles during the sample period, while western Nevada sites were not.

UNRG had different conditions between the sample year (2014 versus 2015), and from the two high elevation sites. Ozone (daily average, max 1 h, MDA8) was negatively correlated with RM for both sample periods at UNRG. This may be due to rapid deposition of HgO, created as O_3 increased, reducing measured RM. RM at UNRG was generally negatively correlated with N. Eurasia and E. Asia trajectories and positively correlated with >3 km (2014) and <1 km (2015) trajectories from San Francisco. RM measurements consisted of nitrogen- and sulfur-based compounds with periodic halogen species, indicating influence from regional sources and the MBL. At UNRG in 2014 (summer and fall), total Pb mass, total Asian Pb mass, and % Asian Pb were positively correlated with trajectories from E. Asia; however, this was not the case in 2015 (spring-summer-fall) sample period, possibly due to the difference in sample period. Differences in RM compounds at PEAV and UNRG further support that the high elevation site differs from the urban, lower elevation site and that air quality can differ between two sites located close together (~12 km) due to differences in transport between a valley and a high elevation site.

The case studies demonstrated that in a 240 h back trajectory period, air masses can pass though the E. Asia source box as well as through other parts of Eurasia and Eastern North America. Trans-Pacific air masses not only influenced the Western USA in spring, but also in the fall (September 2014 and 2015). Ozone was often elevated following passage of low-pressure systems and associated cold front also seen in Knowland et al. (2015) and Lin et al. (2012) and when there was a high-pressure system

at the surface and cyclonic flow aloft, bringing O_3 down to the surface seen in Cooper et al. (2011). Increased trans-Pacific air masses contributed to elevated O_3 above monthly medians. The ubiquitous influence of Eurasian Pb and positive correlations between Pb mass and O_3 at the two high elevation sites indicates long-range transport of pollutants. During pollution events, long-range transport not only affects baseline and background concentrations, but can also be the primary reason for increased concentrations associated with discrete pollution plumes traveling in the free troposphere that may or may not be delivered to the surface in the Western USA (Fine et al., 2015b; Langford et al., 2015b).

In spring (end of March 2015), low-pressure systems moved west to east with associated cold fronts impacting measurements at GBNP and UNRG, marked by a decrease in RH and increases in RM, O_3, and $PM_{2.5}$ concentrations all above monthly medians. Increased frontal activity in the Western USA facilitated entrainment of drier air aloft combined with increasing temperatures and photochemical reactions. In summer, higher overall concentrations of O_3 occurred in both years. In June 2014 there was frontal activity causing entrainment, while June 2015 was characterized by high-pressure systems in the area causing subsidence of air bringing pollutants aloft to the surface. In fall, September/October 2014, a low-pressure system and cold front also moved through the area, bringing down drier air from the free troposphere and stratosphere, demonstrating that trans-Pacific air masses can influence the Western USA in the fall. In September 2015, there was a high over Nevada and a weak cyclonic flow at the 500 mb level; indicating that air aloft was mixed down to the ground, supported by the large influence of >3 km trajectories from over San Francisco at UNRG.

Fiore et al. (2014) modeled baseline O_3 (no recent local emissions, but includes aged domestic emissions) and North American Background (NAB, constructed with zero North America emissions, but includes manmade sources outside of North America) MDA8 O_3 for a typical year at high elevation intermountain western sites (>1.5 km). Baseline was modeled at 60 ± 7 while NAB was 48 ± 8 using the GFDL AM3 model and 54 ± 6 and 42 ± 5 respectively for the GEOS-Chem model. These modeled baseline and background numbers agree well with other observational and modeling studies (Baylon et al., 2016; Cooper et al., 2011; Dolwick et al., 2015; Fine et al., 2015a; Fiore et al., 2003; Lin et al., 2012; Zhang et al., 2011). Asian enhancement events to surface observations and modeled Asian enhancements can contribute 8 to 15 ppbv at high-elevation sites in the Western USA when MDA8 O_3 exceeds 60 ppbv (Lin et al., 2012). Observed enhancements during strong trans-Pacific events, such as in March 2015, agree with this enhancement range.

Negative correlations between RM and % Asian Pb, N. Eurasia trajectories, and E. Asia trajectories suggests RM was removed from these air masses before reaching the sample sites due to deposition or conversion to GEM as suggested by Weiss-Penzias et al. (2015). RM at GBNP was also positively correlated with trajectories from Los Angeles and Las Vegas, indicating that regional oxidant sources facilitated production of RM. Reinemann et al. (2014), using sediment cores, also found that lakes in the Great Basin area were influenced by regional sources of Hg. Ozone at GBNP has also previously been shown to correlate better with southern Nevada sites (Fine et al., 2015a).

Monitoring sites are typically concentrated in urban centers or sensitive natural environments, leaving significant data gaps in rural areas, such as much of Nevada. This

gap in data leads to poor understanding of air pollution sources influencing a region. Long-term monitoring sites with regular measurements are necessary for quantifying international atmospheric inputs that affect national standards and goals for international conventions. The TAPI Beta^{Plus} particulate measurement system may be too elaborate for long-term measurements at higher spatial density; however, it is useful for targeted experiments. Filter measurements are useful, low-cost methods for making multiple measurements ($PM_{2.5}$, RM, and Pb isotopes) simultaneously. Better understanding of the global cycling of pollutants will affect national and global policies, as standards to protect human and ecosystem health become more stringent, it will be necessary to understand the sources and processes influencing production and transport of atmospheric pollutants, particularly in areas far from sources, located in complex terrain, such as the Western USA.

Acknowledgments:

We acknowledge the Nevada Division of Environmental Protection (NDEP), the UNR College of Biotechnology and Natural Resources, and a USDA-HATCH grant for supporting this project. Thank you to Teledyne Advance Pollution Instrumentation (TAPI) for their collaboration on the TAPI Beta^{Plus} particulate measurement system setup and technical support. The FRP data used in this study is freely available from NASA. Balloon sounding data is available from Atmospheric Soundings Wyoming Weather Web. Thank you to Dr. Rebekka Fine for initial research on the TAPI Beta^{Plus} particulate measurement systems for use in this project; to Matthieu Miller for site support, data collection, and processing; to Dave Metts for allowing access to and support at the

Peavine Peak site; to Kristien King for assistance with data processing; to Shaun Brown at LBNL for assistance; and to Christopher and Suzanne Pierce for support during sample analysis at LBNL. Support for the Center for Isotope Geochemistry at LBNL is provided by the Department of Energy, Office of Basic Energy Sciences through contract DE-AC02-05CH11231 to LBNL.

References:

AMAP/UNEP. Global Mercury Modelling: Update of Modelling Results in the Global Mercury Assessment 2013. Arctic Monitoring and Assessment Programme, Oslo, Norway/UNEP Chemicals Branch, Geneva, Switzerland, 2015.

Ambrose JL, Reidmiller DR, Jaffe DA. Causes of high O3 in the lower free troposphere over the Pacific Northwest as observed at the Mt. Bachelor Observatory. Atmospheric Environment 2011; 45: 5302-5315.

Baylon PM, Jaffe DA, Pierce RB, Gustin MS. Interannual Variability in Baseline Ozone and Its Relationship to Surface Ozone in the Western U.S. Environmental Science & Technology 2016; 50: 2994-3001.

Bertschi IT, Jaffe DA. Long-range transport of ozone, carbon monoxide, and aerosols to the NE Pacific troposphere during the summer of 2003: Observations of smoke plumes from Asian boreal fires. Journal of Geophysical Research: Atmospheres 2005; 110: n/a-n/a.

Bollhöfer A, Rosman KJR. Isotopic source signatures for atmospheric lead: the Northern Hemisphere. Geochimica et Cosmochimica Acta 2001; 65: 1727-1740.

Bollhöfer A, Rosman KJR. The temporal stability in lead isotopic signatures at selected sites in the Southern and Northern Hemispheres. Geochimica et Cosmochimica Acta 2002; 66: 1375-1386.

Brodin M, Helmig D, Oltmans S. Seasonal ozone behavior along an elevation gradient in the Colorado Front Range Mountains. Atmospheric Environment 2010; 44: 5305-5315.

Brown JS. Ore leads and isotopes. Economic Geology 1962; 57: 673.

Burley JD, Bytnerowicz A. Surface ozone in the White Mountains of California. Atmospheric Environment 2011; 45: 4591-4602.

CA SoCG. 2014 Large Fires List. In: Fire C, editor. Incident Information. 2017, 2017.

CARB CARB. Ozone Transport Assessment 2001. 2017, 2001.

Christensen JN, Weiss-Penzias P, Fine R, McDade CE, Trzepla K, Brown ST, et al. Unraveling the sources of ground level ozone in the Intermountain Western United States using Pb isotopes. Science of The Total Environment 2015; 530–531: 519-525.

Cooper O, R., Parrish D, D., Stohl A, Trainer M, Nedelec P, Thouret VC, J. P. Oltmans, S. J. Johnson, B. J. Tarasick, D. Leblanc, T. McDermid, I. S. Jaffe, D. Gao, R. Stith, J. Ryerson, T. Aikin, K. Campos, T. Weinheimer, A. Avery, M. A. Increasing springtime ozone mixing ratios in the free troposphere over western North America. Nature 2010; 463: 344-348.

Cooper OR, Langford AO, Parrish DD, Fahey DW. Challenges of a lowered U.S. ozone standard. Science 2015; 348: 1096-1097.

Cooper OR, Oltmans SJ, Johnson BJ, Brioude J, Angevine W, Trainer M, et al. Measurement of western U.S. baseline ozone from the surface to the tropopause and assessment of downwind impact regions. Journal of Geophysical Research: Atmospheres 2011; 116: D00V03.

Dempsey F. Observations of stratospheric O3 intrusions in air quality monitoring data in Ontario, Canada. Atmospheric Environment 2014; 98: 111-122.

Doe BR. Lead Isotopes: Springer-Verlag Berlin Heidelberg, 1970.

Dolwick P, Akhtar F, Baker KR, Possiel N, Simon H, Tonnesen G. Comparison of background ozone estimates over the western United States based on two separate model methodologies. Atmospheric Environment 2015; 109: 282-296.

Draxler RR, Hess GD. Description of the HYSPLIT_4 modeling system. NOAA Technical Memorandum ERL ARL-224, 1997, pp. 24.

Díaz-Somoano M, Kylander ME, López-Antón MA, Suárez-Ruiz I, Martínez-Tarazona MR, Ferrat M, et al. Stable Lead Isotope Compositions In Selected Coals From Around The World And Implications For Present Day Aerosol Source Tracing. Environmental Science & Technology 2009; 43: 1078-1085.

EPA USEPA. Exceptional events documents ozone - Washoe, NV. 2017, 2017.

European Commission. Air Quality Standards. 2017, 2016.

Ewing SA, Christensen JN, Brown ST, Vancuren RA, Cliff SS, Depaolo DJ. Pb Isotopes as an Indicator of the Asian Contribution to Particulate Air Pollution in Urban California. Environmental Science & Technology 2010; 44: 8911-8916.

Fine R, Miller MB, Burley J, Jaffe DA, Pierce RB, Lin M, et al. Variability and sources of surface ozone at rural sites in Nevada, USA: Results from two years of the Nevada Rural Ozone Initiative. Science of The Total Environment 2014.

Fine R, Miller MB, Burley J, Jaffe DA, Pierce RB, Lin M, et al. Variability and sources of surface ozone at rural sites in Nevada, USA: Results from two years of the Nevada Rural Ozone Initiative. Science of The Total Environment 2015a; 530–531: 471-482.

Fine R, Miller MB, Yates EL, Iraci LT, Gustin MS. Investigating the influence of long-range transport on surface O3 in Nevada, USA, using observations from multiple measurement platforms. Science of The Total Environment 2015b; 530–531: 493-504.

Finlayson-Pitts BJ, Pitts Jr JN. Chapter 4 - Photochemistry of Important Atmospheric Species. In: Finlayson-Pitts BJ, Pitts JN, editors. Chemistry of the Upper and Lower Atmosphere. Academic Press, San Diego, 2000a, pp. 86-129.

Finlayson-Pitts BJ, Pitts Jr JN. Chapter 14 - Global Tropospheric Chemistry and Climate Change. In: Finlayson-Pitts BJ, Pitts JN, editors. Chemistry of the Upper and Lower Atmosphere. Academic Press, San Diego, 2000b, pp. 762-843.

Fiore A, Jacob DJ, Liu H, Yantosca RM, Fairlie TD, Li Q. Variability in surface ozone background over the United States: Implications for air quality policy. Journal of Geophysical Research: Atmospheres 2003; 108: 4787.

Fiore AM, Jacob DJ, Bey I, Yantosca RM, Field BD, Fusco AC, et al. Background ozone over the United States in summer: Origin, trend, and contribution to pollution episodes. Journal of Geophysical Research: Atmospheres 2002; 107: ACH 11-1-ACH 11-25.

Fiore AM, Oberman JT, Lin MY, Zhang L, Clifton OE, Jacob DJ, et al. Estimating North American background ozone in U.S. surface air with two independent global models: Variability, uncertainties, and recommendations. Atmospheric Environment 2014; 96: 284-300.

Gratz LE, Jaffe DA, Hee JR. Causes of increasing ozone and decreasing carbon monoxide in springtime at the Mt. Bachelor Observatory from 2004 to 2013. Atmospheric Environment 2015; 109: 323-330.

Gustin MS, Amos HM, Huang J, Miller MB, Heidecorn K. Successes and challenges of measuring and modeling atmospheric mercury at the part per quadrillion level: a critical review. Atmos. Chem. Phys. Discuss. 2015a; 15: 3777-3821.

Gustin MS, Fine R, Miller M, Jaffe D, Burley J. The Nevada Rural Ozone Initiative (NVROI): Insights to understanding air pollution in complex terrain. Science of The Total Environment 2015b; 530–531: 455-470.

Gustin MS, Huang J, Miller MB, Peterson C, Jaffe DA, Ambrose J, et al. Do We Understand What the Mercury Speciation Instruments Are Actually Measuring? Results of RAMIX. Environmental Science & Technology 2013; 47: 7295-7306.

Gustin MS, Pierce AM, Huang J, Miller MB, Holmes H, Loria-Salazar SM. Evidence for different reactive Hg sources and chemical compounds at adjacent valley and high elevation locations. Environmental Science & Technology 2016.

Hopper JF, Ross HB. Regional source discrimination of atmospheric aerosols in Europe using the isotopic composition of lead. Tellus B 1991; 43: 45-60.

Huang J, Gustin MS. Uncertainties of Gaseous Oxidized Mercury Measurements Using KCl-Coated Denuders, Cation-Exchange Membranes, and Nylon Membranes: Humidity Influences. Environmental Science & Technology 2015; 49: 6102-6108.

Huang J, Miller MB, Weiss-Penzias P, Gustin MS. Comparison of Gaseous Oxidized Hg Measured by KCl-Coated Denuders, and Nylon and Cation Exchange Membranes. Environmental Science & Technology 2013; 47: 7307-7316.

Jacob DJ, Logan JA, Murti PP. Effect of rising Asian emissions on surface ozone in the United States. Geophysical Research Letters 1999; 26: 2175-2178.

Jaffe D, Anderson T, Covert D, Kotchenruther R, Trost B, Danielson J, et al. Transport of Asian air pollution to North America. Geophysical Research Letters 1999; 26: 711-714.

Jaffe D, Bertschi I, Jaeglé L, Novelli P, Reid JS, Tanimoto H, et al. Long-range transport of Siberian biomass burning emissions and impact on surface ozone in western North America. Geophysical Research Letters 2004; 31: n/a-n/a.

Jaffe D, Mahura A, Kelley J, Atkins J, Novelli PC, Merrill J. Impact of Asian emissions on the remote North Pacific atmosphere: Interpretation of CO data from Shemya, Guam, Midway and Mauna Loa. Journal of Geophysical Research: Atmospheres 1997; 102: 28627-28635.

Jaffe D, McKendry I, Anderson T, Price H. Six 'new' episodes of trans-Pacific transport of air pollutants. Atmospheric Environment 2003; 37: 391-404.

Jaffe D, Prestbo E, Swartzendruber P, Weiss-Penzias P, Kato S, Takami A, et al. Export of atmospheric mercury from Asia. Atmospheric Environment 2005; 39: 3029-3038.

Jaffe DA, Lyman S, Amos HM, Gustin MS, Huang J, Selin NE, et al. Progress on Understanding Atmospheric Mercury Hampered by Uncertain Measurements. Environmental Science & Technology 2014; 48: 7204-7206.

Johnson WB, Viezee W. Stratospheric ozone in the lower troposphere —I. Presentation and interpretation of aircraft measurements. Atmospheric Environment (1967) 1981; 15: 1309-1323.

Jones CE, Halliday AN, Rea DK, Owen RM. Eolian inputs of lead to the North Pacific. Geochimica et Cosmochimica Acta 2000; 64: 1405-1416.

Knowland KE, Doherty RM, Hodges KI. The effects of springtime mid-latitude storms on trace gas composition determined from the MACC reanalysis. Atmos. Chem. Phys. 2015; 15: 3605-3628.

Komárek M, Ettler V, Chrastný V, Mihaljevič M. Lead isotopes in environmental sciences: A review. Environment International 2008; 34: 562-577.

Kunz H, Speth P. Variability of Near-Ground Ozone Concentrations During Cold Front Passages – a Possible Effect of Tropopause Folding Events. Journal of Atmospheric Chemistry 1997; 28: 77-95.

Langford AO, Brioude J, Cooper OR, Senff CJ, Alvarez RJ, Hardesty RM, et al. Stratospheric influence on surface ozone in the Los Angeles area during late spring and early summer of 2010. Journal of Geophysical Research: Atmospheres 2012; 117: n/a-n/a.

Langford AO, Pierce RB, Schultz PJ. Stratospheric intrusions, the Santa Ana winds, and wildland fires in Southern California. Geophysical Research Letters 2015a; 42: 6091-6097.

Langford AO, Senff CJ, Alvarez Ii RJ, Brioude J, Cooper OR, Holloway JS, et al. An overview of the 2013 Las Vegas Ozone Study (LVOS): Impact of stratospheric intrusions and long-range transport on surface air quality. Atmospheric Environment 2015b; 109: 305-322.

Langford AOaARJaBJaFRaGMSaLMYaMRD. Entrainment of stratospheric air and Asian pollution by the convective boundary layer in the southwestern U.S. Journal of Geophysical Research: Atmospheres 2017: n/a--n/a.

Li Q, Cheng H, Zhou T, Lin C, Guo S. The estimated atmospheric lead emissions in China, 1990–2009. Atmospheric Environment 2012; 60: 1-8.

Lin M, Fiore AM, Horowitz LW, Cooper OR, Naik V, Holloway J, et al. Transport of Asian ozone pollution into surface air over the western United States in spring. Journal of Geophysical Research: Atmospheres 2012; 117: D00V07.

Lin M, Fiore AM, Horowitz LW, Langford AO, Oltmans SJ, Tarasick D, et al. Climate variability modulates western US ozone air quality in spring via deep stratospheric intrusions. Nature Communications 2015; 6: 7105.

Lu X, Zhang L, Yue X, Zhang J, Jaffe DA, Stohl A, et al. Wildfire influences on the variability and trend of summer surface ozone in the mountainous western United States. Atmos. Chem. Phys. 2016; 16: 14687-14702.

Lyman SN, Jaffe DA. Formation and fate of oxidized mercury in the upper troposphere and lower stratosphere. Nature Geoscience 2012; 5: 114-117.

Miller MB, Fine R, Pierce AM, Gustin MS. Identifying sources of ozone to three rural locations in Nevada, USA, using ancillary gas pollutants, aerosol chemistry, and mercury. Science of The Total Environment 2015; 530–531: 483-492.

Parmar RS, Welling M, Andreae MO, Helas G. Water vapor release from biomass combustion. Atmos. Chem. Phys. 2008; 8: 6147-6153.

Pierce AM, Gustin MS. Development of a Particulate Mass Measurement System for Quantification of Ambient Reactive Mercury. Environmental Science & Technology 2016.

Pierce AM, Gustin MS. Development of a Particulate Mass Measurement System for Quantification of Ambient Reactive Mercury. Environmental Science & Technology 2017; 51: 436-445.

Price HU, Jaffe DA, Cooper OR, Doskey PV. Photochemistry, ozone production, and dilution during long-range transport episodes from Eurasia to the northwest United States. Journal of Geophysical Research: Atmospheres 2004; 109: n/a-n/a.

Prinn RG. 5.1 - Ozone, Hydroxyl Radical, and Oxidative Capacity. In: Holland HD, Turekian KK, editors. Treatise on Geochemistry (Second Edition). Elsevier, Oxford, 2014, pp. 1-18.

Reinemann SA, Porinchu DF, Gustin MS, Mark BG. Historical trends of mercury and spheroidal carbonaceous particle deposition in sub-alpine lakes in the Great Basin, United States. Journal of Paleolimnology 2014; 52: 405-418.

Rieder HE, Frossard L, Ribatet M, Staehelin J, Maeder JA, Di Rocco S, et al. On the relationship between total ozone and atmospheric dynamics and chemistry at mid-latitudes - Part 2: The effects of the El Niño/Southern Oscillation, volcanic eruptions and contributions of atmospheric dynamics and chemistry to long-term total ozone changes. Atmospheric Chemistry and Physics 2013; 13: 165-179.

Schroeder WH, Munthe J. Atmospheric mercury - An overview. Atmospheric Environment 1998; 32: 809-822.

Stohl A. Computation, accuracy and applications of trajectories—A review and bibliography. Atmospheric Environment 1998; 32: 947-966.

Stohl A, Eckhardt S, Forster C, James P, Spichtinger N, Seibert P. A replacement for simple back trajectory calculations in the interpretation of atmospheric trace substance measurements. Atmospheric Environment 2002; 36: 4635-4648.

Stohl A, Forster C, Eckhardt S, Spichtinger N, Huntrieser H, Heland J, et al. A backward modeling study of intercontinental pollution transport using aircraft measurements. Journal of Geophysical Research: Atmospheres 2003; 108: n/a-n/a.

Stohl A, Spichtinger-Rakowsky N, Bonasoni P, Feldmann H, Memmesheimer M, Scheel HE, et al. The influence of stratospheric intrusions on alpine ozone concentrations. Atmospheric Environment 2000; 34: 1323-1354.

Tan MG, Zhang GL, Li XL, Zhang YX, Yue WS, Chen JM, et al. Comprehensive Study of Lead Pollution in Shanghai by Multiple Techniques. Analytical Chemistry 2006; 78: 8044-8050.

Tang Q, Prather MJ. Correlating tropospheric column ozone with tropopause folds: the Aura-OMI satellite data. Atmospheric Chemistry and Physics 2010; 10: 9681-9688.

TAPI TAPI. Operation Manula: Model 602 BETA PLUS particle measurement system. Teledyne Advanced Pollution Instrumentation, San Diego, CA, 2012, pp. 180.

Teakles AD, So R, Ainslie B, Nissen R, Schiller C, Vingarzan R, et al. Impacts of the July 2012 Siberian fire plume on air quality in the Pacific Northwest. Atmos. Chem. Phys. 2017; 17: 2593-2611.

Timonen H, Ambrose JL, Jaffe DA. Oxidation of elemental Hg in anthropogenic and marine airmasses. Atmos. Chem. Phys. 2013; 13: 2827-2836.

U.S. Energy Information Administration. Coal. Quarterly Coal Report 2015. 2017. U.S. Department of Energy, 2017.

U.S. EPA USEPA. Ozone, 2017.

UNEP. Minamata Convention on Mercury. 2017, 2017.

VanCuren R. Transport aloft drives peak ozone in the Mojave Desert. Atmospheric Environment 2015; 109: 331-341.

VanCuren R, Gustin MS. Identification of sources contributing to PM2.5 and ozone at elevated sites in the western U.S. by receptor analysis: Lassen Volcanic National Park, California, and Great Basin National Park, Nevada. Science of The Total Environment 2015; 530–531: 505-518.

VanCuren RA. Asian aerosols in North America: Extracting the chemical composition and mass concentration of the Asian continental aerosol plume from long-term aerosol records in the western United States. Journal of Geophysical Research: Atmospheres 2003; 108: 4623.

VanCuren RA, Cliff SS, Perry KD, Jimenez-Cruz M. Asian continental aerosol persistence above the marine boundary layer over the eastern North Pacific: Continuous aerosol measurements from Intercontinental Transport and Chemical Transformation 2002 (ITCT 2K2). Journal of Geophysical Research: Atmospheres 2005; 110: D09S90.

Viezee W, Johnson WB, Singh HB. Stratospheric ozone in the lower troposphere—II. Assessment of downward flux and ground-level impact. Atmospheric Environment (1967) 1983; 17: 1979-1993.

Vingarzan R. A review of surface ozone background levels and trends. Atmospheric Environment 2004; 38: 3431-3442.

Weiss-Penzias P, Jaffe D, Swartzendruber P, Hafner W, Chand D, Prestbo E. Quantifying Asian and biomass burning sources of mercury using the Hg/CO ratio in pollution plumes observed at the Mount Bachelor observatory. Atmospheric Environment 2007; 41: 4366-4379.

Weiss-Penzias P, Jaffe DA, McClintick A, Prestbo EM, Landis MS. Gaseous Elemental Mercury in the Marine Boundary Layer: Evidence for Rapid Removal in Anthropogenic Pollution. Environmental Science & Technology 2003; 37: 3755-3763.

Weiss-Penzias P, Jaffe DA, Swartzendruber P, Dennison JB, Chand D, Hafner W, et al. Observations of Asian air pollution in the free troposphere at Mount Bachelor Observatory during the spring of 2004. J. Geophys. Res. 2006; 111: D10304.

Weiss-Penzias PA, H. M. Selin, N. E. Gustin, M. S. Jaffe, D. A. Obrist, D. Sheu, G.-R. Giang, A. Use of a global model to understand speciated atmospheric mercury observations at five high-elevation sites. Atmospheric Chemistry and Physics 2015; 15: 1161-1173.

Wilkening KE, Barrie LA, Engle M. Trans-Pacific Air Pollution. Science 2000; 290: 65.

Zhang L, Jacob DJ, Downey NV, Wood DA, Blewitt D, Carouge CC, et al. Improved estimate of the policy-relevant background ozone in the United States using the GEOS-Chem global model with 1/2° × 2/3° horizontal resolution over North America. Atmospheric Environment 2011; 45: 6769-6776.

Zhang L, Jacob DJ, Yue X, Downey NV, Wood DA, Blewitt D. Sources contributing to background surface ozone in the US Intermountain West. Atmos. Chem. Phys. 2014; 14: 5295-5309.

Chapter 4

Investigating horizontal and vertical pollution gradients in the atmosphere associated with an urban location in complex terrain, Reno, Nevada, USA

Ashley M. Pierce[a,*], S. Marcela Loría-Salazar[b], Heather A. Holmes[b], Mae Sexauer Gustin[a]

*Corresponding author: ash.pie4@gmail.com

[a]Department of Natural Resources and Environmental Sciences, University of Nevada Reno, NV, USA 89557

[b]Atmospheric Sciences Program, Department of Physics, University of Nevada Reno, NV, USA 89557

Submitted: *Atmospheric Environment*

Appendix C: Supplemental Information, 31 pages, 10 Tables, and 23 Figures

Abstract:

A new statistical method, the quadrant method, was developed to aid in identifying different conditions affecting the relationship between columnar aerosol optical depth (τ_{ext}) and concentrations of particulate matter (< 2.5 μg m^{-3} in aerodynamic diameter, $PM_{2.5}$) at the surface. Understanding this relationship has the potential to improve our ability to estimate surface $PM_{2.5}$ concentrations from satellite retrievals of τ_{ext} in the Western USA, where complex terrain, diverse climates, and large fluctuations in the planetary boundary layer height affect the vertical distribution of aerosol concentrations. The objective of this study was to identify air pollution sources and atmospheric physics affecting gradients of atmospheric pollutants observed at two valley sites (~1370 m) and a high elevation site (2515 m) located in and adjacent to Reno, Nevada, USA. The two valley sites were used to investigate the horizontal gradient of pollutants associated with mobile sources from high volume highways. Results indicate statistically significant differences in concentrations of criteria air pollutants between the valley sites, where one site is located 0.03 km from a major highway.

Meteorological variables, aerosol optical properties, vertical structure of the atmosphere, measures of atmospheric stability, and ozone concentrations were used to determine the conditions influencing the relationship between τ_{ext} and surface $PM_{2.5}$ concentrations. Vertical gradients were impacted by air pollution sources and atmospheric boundary layer stability. During periods when τ_{ext} and surface $PM_{2.5}$ concentrations were associated, emissions from wildfires and local pollutants in a well-mixed boundary layer dominated the relationship. During periods of no association, stable boundary layer conditions and pollution aloft created vertical heterogeneity.

Transport of trans-Pacific pollutants and regional wildfire plumes aloft created challenges for separating these sources of pollutants at the measurement sites, therefore use of other indicators of air pollution sources above the atmospheric boundary layer are necessary. Results show that the quadrant method, developed for hourly data, can be used with 24 h data and that it is a useful tool for identifying air pollution sources and atmospheric physics driving pollution gradients.

Keywords:

Quadrant method; aerosol optical depth; $PM_{2.5}$; atmospheric stability; vertical heterogeneity; near-road pollution gradients

Highlights:

- Statistical analysis of atmospheric sources and physics affecting pollution gradients
- A method used to understand relationships between τ_{ext} and surface $PM_{2.5}$
- Horizontal pollution gradients in the valley were influenced by highways
- Stability, transport aloft, and wildfires drove vertical heterogeneity of pollution
- Quadrant method was successfully applied to 24 h data

Abbreviations:

AEE – Ångström Extinction Exponent
AERONET - AErosol RObotic NETwork
AOD – Aerosol Optical Depth (τ_{ext})
AOH – Apparent Optical Height (km)
AQS – Air Quality Station
CO – Carbon monoxide (ppbv)
DRI – Desert Research Institute, Reno, NV, USA
FARM – Nevada Agricultural Experiment Station Farm Facilities of the University of Nevada, Reno, NV, USA
GALE – Galena, NV, USA
HD – Heat Deficit (MJ m^{-2})
Max 1 h O_3 – Maximum 1 h ozone for each day (ppbv)
MDA8 O_3 – Maximum daily 8 h average (ppbv)
NAAQS - National Ambient Air Quality Standards
NO – Nitrogen monoxide (ppbv)
NO_x – Oxides of nitrogen (ppbv)
NRL NAAPS – Naval Research Laboratory Aerosol Analysis and Prediction System
NWS – National Weather Service
O_3 – Ozone (ppbv)
PBL – Planetary Boundary Layer
PBLH – Planetary Boundary Layer Height
PEAV – Peavine Peak, NV, USA
$PM_{2.5}$ – Particulate Matter < 2.5 µg m^{-3} in diameter
PM_{10} – Particulate Matter < 10 µg m^{-3} in diameter
RH – Relative Humidity (%)
SO_2 – Sulfur dioxide (ppbv)
UNRG – Nevada Agricultural Experiment Station Greenhouse Facilities of the University of Nevada, Reno, USA
U.S. EPA – United States Environmental Protection Agency
VOCs – Volatile Organic Compounds
WCAQ – Washoe County Air Quality Management
WHO – World Health Organization
WRCC – Western Regional Climate Center
WS – Wind speed (m s^{-1})

1. Introduction

Many urban centers in the intermountain west are located in valleys and experience horizontal and vertical gradients of atmospheric pollution. The atmospheric processes affecting boundary layer stability and, therefore, transport and accumulation of air pollution in intermountain areas is influenced by synoptic flow patterns and mesoscale thermal circulation, such as local heating and cooling, generating valley and up/downslope flows (Fernando, 2010; Li et al, 2015). The large number of mountain ranges, high solar radiation, and semi-arid climate of Nevada, USA, contribute to planetary boundary layer heights (PBLH) that vary widely between seasons (Fine et al, 2015; Gustin et al, 2015; McMurdie & Houze, 2006; Nguyen et al, 2016; Pierce et al, 2017).

Mobile sources are dominant sources of atmospheric pollutants in urban areas and contribute to strong horizontal gradients of atmospheric pollution near major roadways. Motor vehicles contribute to elevated pollutant concentrations of both primary and secondary pollutants in the atmosphere (Colvile et al, 2001; HEI, 2010). Exposure to pollutants from mobile sources has adverse health effects related to respiratory, cardiovascular, cognitive functioning, and birth outcomes (Hao H. et al, 2016; HEI, 2010). Spatial gradients of air pollution concentrations, and therefore exposures, in urban areas are important to quantify as ~54% of the total population in 2014 lived in urban areas (WHO, 2017).

During winter, stable atmospheric conditions and persistent temperature inversions cause cold, denser air to sink to the valley floor, trapping pollutants near the surface. These events, are referred to as cold air pools, and are characterized by low

temperatures, wind speeds, and PBLH, as well as high surface pressure and relative humidity (RH) in the valley (Chemel et al, 2016; Whiteman et al, 2001). The difference in temperature, relative to the upper atmosphere, results in decoupling of air in valleys from air aloft, isolating the valleys from stronger, prevailing winds and suppressing vertical mixing, sometimes for multiple days (Chemel et al, 2016). Cold air pools, enhanced by cloud and snow cover, allow pollutants to buildup, at times to concentrations above the United States Environmental Protection Agency (U.S. EPA) National Ambient Air Quality Standards (NAAQS), specifically for particulate matter ([PM], Chemel et al, 2016; Chen et al, 2012; Green et al, 2015; Silcox et al, 2012; Whiteman et al, 2014).

Atmospheric pollutants, such as $PM_{2.5}$ (particulate matter < 2.5 μm in aerodynamic diameter), can exist within the planetary boundary layer (PBL) (e.g. in cold air pools), and above the PBL, (e.g. long-range transport in the free troposphere). This vertical heterogeneity makes it challenging to reconcile ground and columnar observations (Bergin et al, 2000; Corbin et al, 2002; Fine et al, 2015; Langford et al, 2015; Li et al, 2015; Loría-Salazar, 2014). $PM_{2.5}$ aloft will increase columnar aerosol optical depth (τ_{ext}) but will not necessarily increase surface $PM_{2.5}$, creating periods when the two observations are not associated (Campbell et al, 2003; Crosbie et al, 2014; Loría-Salazar et al, 2017). Satellite retrievals of τ_{ext} have been used to estimate surface $PM_{2.5}$ concentrations because of the large spatial coverage. However, vertical heterogeneity of atmospheric pollution caused by complex terrain, diverse climates, and large fluctuations in PBL creates challenges for using retrievals of τ_{ext} to estimate surface $PM_{2.5}$ concentrations in the Western USA (Levy et al, 2013; Loría-Salazar et al, 2017; Nguyen

et al, 2016). Statistical models of satellite-derived $PM_{2.5}$ often rely on linear relationships between τ_{ext} and surface $PM_{2.5}$ observations, however there are large biases in the estimated $PM_{2.5}$ (Engel-Cox et al, 2004; Gupta et al, 2006; Lee et al, 2016; Liu et al, 2009; Sorek-Hamer et al, 2013; Sorek-Hamer et al, 2015). Therefore, an examination of the physical processes in the atmosphere is required prior to using health effects studies or risk assessments that rely on statistical data fusion models and retrievals from satellite remote sensing. To address some of these challenges, Loría-Salazar et al. (2017) developed a statistical data exploration technique, called the quadrant method, to identify atmospheric physics influencing the relationship between τ_{ext} and surface $PM_{2.5}$ observations without prior knowledge of the measurement sites.

Results from Loría-Salazar et al. (2017) at three inland sites in the Western USA found four relationships between τ_{ext} and surface $PM_{2.5}$ observations: 1) low aerosol pollution at the surface and in the column, related to local sources of pollution in a well-mixed PBL; 2) high aerosol pollution at the surface and low aerosol pollution in the column, identified as stable conditions and local pollution sources; 3) high aerosol pollution at the surface and in the column, identified as wildfire plumes transported at the surface in a well-mixed PBL; and 4) low aerosol pollution at the surface and high aerosol pollution in the column, identified as transport of regional or global pollution aloft and/or entrainment of pollution, due to a poorly mixed PBL and interactions with complex terrain. This method proved useful for investigating the atmospheric physics affecting the relationship between τ_{ext} and surface $PM_{2.5}$ concentrations in the Western USA.

The main goal of the current study was to identify atmospheric physics affecting air pollution gradients at three sites in and adjacent to Reno, Nevada, USA. Two valley

sites were located in a metropolitan area in close proximity (~0.03 to 2.1 km) to two, high volume, interstate highways. A mountain peak site was located ~12 km northwest and ~1.2 km higher in elevation than the valley sites. We first investigated horizontal gradients of atmospheric pollutant concentrations different distances from the highways. We then apply the quadrant method, developed by Loría-Salazar et al. (2017), to 24 h data from the two valley sites to categorize air pollution sources and physical processes affecting the vertical heterogeneity of pollutants into four conditions: *unstable conditions and mixing of local pollution sources, stable atmospheric conditions and accumulation of local pollutants, transport and mixing of smoke plumes, and transport of pollution aloft.*

2. Site descriptions and instrumentation

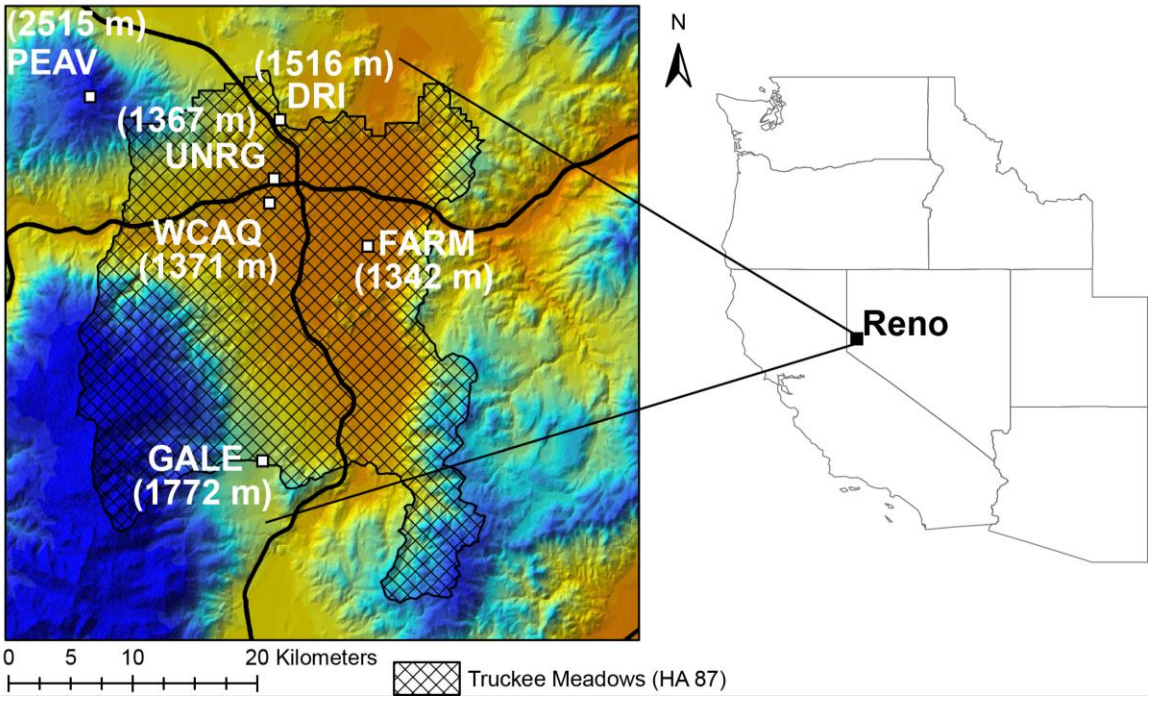

Figure 1: Map of the data sites and elevation (m asl). Checkered area indicates Truckee Meadows (Hydrographic Area 87). Bold black lines indicate Interstate-80 that runs east/west and Interstate-580 (U.S. 395) that runs north/south. Abbreviations for each location are identified in Table 1

Site	Code	Elevation asl (m)	Measurements	Other	Latitude (N)	Longitude (W)
Nevada Agricultural Experiment station Farm Facilities, Reno, NV, USA (WRCC)	FARM	1342	Met		39.5029	119.7379
Nevada Agricultural Experiment Station Greenhouse Facilities, Reno, NV, USA	UNRG	1367	O_3, CO, NO_x, SO_2, TAPI $PM_{2.5}$	WRCC Met	39.5373	119.8043
Washoe County Air Quality, Reno3, NV, USA	WCAQ	1371	O_3, CO, NO_x, SO_2, $PM_{2.5}$, Met	SLAMS, NCore	39.5250	119.8077
Desert Research Institute, Reno, NV, USA (WRCC)	DRI	1516	Met	NWS Balloon soundings	39.5708	119.8016
Galena, NV, USA (WRCC)	GALE	1772	Met	RAWS	39.3816	119.8150
Peavine Peak, NV, USA	PEAV	2515	CO, O_3, TAPI $PM_{2.5}$, Met		39.5895	119.9290

Table 1: Measurement sites in order of increasing elevation and the measurements made at each.

Met – Meteorological data
NCore – National Core Multi-Pollutant Monitoring Station
NWS – National Weather Service
RAWS – Wildland Fire Remote Automated Weather Stations
SLAMS – State and Local Air Monitoring Station
TAPI $PM_{2.5}$ - Teledyne Advanced Pollution Instrumentation $Beta^{Plus}$ particulate monitor
WRCC – Western Regional Climate Center

2.1 Site descriptions

The Truckee Meadows area, defined by Hydrographic Area 87 (HA 87, ~500 km^2, Fig. 1), includes the Reno/Sparks metropolitan area (population of ~$3.0x10^5$ in 2014) and part of unincorporated Washoe County (www.census.gov, 2017). One valley site was located at the Nevada Agricultural Experiment Station Greenhouse Facility located at the Valley Road field labs and Greenhouse complex of the University of Nevada, Reno, USA (UNRG, Table 1). UNRG is located ~0.03 km north of Interstate-80 (I-80) and 1.5 km west of Interstate-580 (I-580/U.S. Route 395). In addition to local highway pollution, regional transport from San Francisco, CA, USA, and long-range transport of air masses have previously been observed at UNRG in 2014 from June to November (Pierce et al, 2017). See Pierce and Gustin (2017) for more detail on this measurement site.

Washoe County Air Quality Management (WCAQ) operates the second valley site (site ID: 32-031-0016 Reno3, 301A State St. Reno, NV, USA, Table 1) as part of the regulatory monitoring network (U.S. EPA Air Quality System). The WCAQ site is located ~1.2 km south of I-80, ~1.4 km south of UNRG, and 2.1 km west of I-580 in a mixed residential and commercial neighborhood.

The Peavine Peak measurement site (PEAV, Table 1) is located at the summit, above tree line, ~15 km east of the Sierra Nevada Mountain range and ~12 km northwest of downtown Reno, NV, USA at the border of the Truckee Meadows area. The site is accessed by a dirt road from the southwest. Traffic in the area consists mainly of service vehicles to the relay station located at the peak, off-road recreational vehicles, and non-motorized traffic. More detail on this site can be found in Gustin et al. (2015) and Pierce and Gustin (2017). The PEAV site is generally above the PBLH in winter and below the PBLH in the summer. Due to its location, PEAV experiences free tropospheric air as well as upslope flow of air and pollutants in the afternoon from the Reno/Sparks metropolitan area when convective mixing increases the depth of the mixed layer above PEAV (Pierce et al, 2017). Long-range transport was observed at PEAV, June to November 2014 (Pierce et al, 2017). PEAV and UNRG were setup as part of the Nevada Rural Ozone Initiative (NVROI, Gustin et al, 2015; Pierce et al, 2017).

All three sites experience regional (urban areas and wildfires in surrounding states) and long-range (trans-Pacific) transport of pollution (Pierce et al, 2017). The valley sites experience local urban sources of pollutants from the Reno/Sparks metropolitan area and experience thermal circulation creating up- and downslope flows

that can mix tropospheric and stratospheric air down to the valley (Gustin et al, 2015; Pierce et al, 2017).

2.2 Particulate monitors

The Teledyne Advanced Pollution Instrumentation (TAPI) Beta^{Plus} particulate monitor (Model 602, San Diego, CA, USA) measures particulate matter < 2.5 µm in aerodynamic diameter ($PM_{2.5}$) through two separate inlets. Mass concentration is measured using beta attenuation. At 24 h the TAPI 602 Beta^{Plus} has a detection limit of 0.3 µg m^{-3} (TAPI, 2012). Lead (Pb) concentrations and isotopic composition were also measured using this instrument and were used to asses long-range transport in this study (for more detail see Pierce & Gustin, 2017; Pierce et al, 2017). One TAPI was located at Peavine Peak and one was located at UNRG in the Reno/Sparks metropolitan area in the Truckee Meadows.

Washoe County Air Quality Management (WCAQ), following regulations for monitoring criteria pollutants set by the U.S. EPA, operated a Beta Attenuation Monitor (BAM-1020, MetOne Instruments, Grants Pass, OR, USA) during this time in the Reno/Sparks metropolitan area in Truckee Meadows. The relative uncertainty of $PM_{2.5}$ concentrations is ~ ±0.1µg m^{-3} per hour (EPA, 2017a). Previous studies have shown that $PM_{2.5}$ measured at WCAQ and UNRG are positively correlated (r^2 = 0.84, p-value < 0.01) and have significantly similar (ANOVA one-way p-value < 0.05) concentrations (Pierce & Gustin, 2017). Hourly data was used to average to 24 h. Data were used if > 50% of the data were available.

2.3 Aerosol optical properties

The Cimel sun photometer (CE-318), the standard instrument used in the AErosol RObotic NETwork (AERONET), measures direct solar and sky irradiance at nine wavelengths (Holben et al, 1998). AERONET retrieves columnar aerosol optical properties through direct-Sun and almucantar scans at three levels of data. This study used hourly average data retrieved from direct-Sun scan at level 1 (raw data) for periods during smoke plumes and level 2 (quality assurance) for non-smoke plume periods using algorithms from Loría-Salazar et al. (2016) to retain τ_{ext}. Retaining level 1 data is necessary during smoke plumes because level 2 data will remove periods of smoke due to the similarity of the data to cloud periods in the current version 2 of the AERONET algorithm. Hourly data was used with no restriction on available data in a 1 h sample period. τ_{ext} (440 nm) and fine and coarse mode aerosol fractions (500 nm), retrieved from AERONET, were used. The relative uncertainty of τ_{ext} from AERONET is estimated to be in the range of ~ ±0.01 and ~ ±0.02 (Eck, 2010; Eck et al, 1999). Ångström Extinction Exponent (AEE, 440-870 nm) was also collected from AERONET and is used as a qualitative indicator of particle size: AEE ~ 1 or less is indicative of coarse mode aerosols (dust and sea salt) while AEE close to or > 2 is indicative of fine mode aerosols from biomass burning or urban pollution (Eck et al, 1999). Periods when AEE was > 1.8 were flagged as fire periods (Loría-Salazar et al, 2016).

A dual wavelength Photoacoustic and Integrated Nephelometer (PIN) was used to measure β_{ext} (surface-level aerosol light scattering [β_{sca}] + absorption [β_{abs}]) at 405 nm. Hourly averages of β_{ext} were used. The relative uncertainty of the scattering and absorption observations are 15% and 5% respectively (Lewis et al, 2008). The Cimel and

PIN are collocated on top of a four-story building at the University of Nevada, Reno (UNR) campus.

2.4 Gaseous data

At UNRG, O_3 was measured with a Thermo 49i (Thermo Fisher Scientific, Inc. Franklin, MA, USA) every 15 min with a reported detection limit of 0.5 ppbv. WCAQ operated a TAPI 400E with a 1 h average time and a reported detection limit of 5 ppbv. Ozone at PEAV was measured every 15 min using a TAPI T400E UV absorption O_3 trace level analyzer with a reported detection limit of 0.6 ppbv. Ozone measurements were used for hourly averages, 24 h averages, maximum (max) daily 1 h O_3, and max daily 8 h averages (MDA8). Data were used if > 50% of the data were available.

Other instruments operated at UNRG included Thermo Fisher Scientific (Waltham, MA, USA) gas analyzers for CO (48i), NO_x and NO (42i), and SO_2 (43i). PEAV had a Thermo gas analyzer for CO (48i). All gas analyzers at UNRG and PEAV were mounted in a climate-controlled shelter; sample air was pulled in through a single Teflon tube and split to supply ambient sample air to the analyzer. CO, NO_x and NO, and SO_2 were collected from the U.S. EPA Air Quality Station (AQS) WCAQ site. Data were used if > 50% of the data were available.

2.5 Meteorological data

One-hour meteorological data (temperature, RH, wind speed, pressure) were collected from the Western Regional Climate Center (WRCC) site, located ~0.2 km north of UNRG in the same Greenhouse complex, and from the WCAQ site. Meteorological

data collected at PEAV included 5 min temperature and RH (hmp45c Campbell Scientific, ± 0.2 ºC and ± 2% RH), 5 min wind speed (RM Young 05305 ± 0.2 m s-1), and 5 min barometric pressure (Vaisala PTB110, ±0.3 hPa at 20 °C). The 5 min data were averaged for 1 h and 24 h values. Temperature and pressure data were collected from the Nevada Agricultural Experiment Station Farm Facilities, Reno, NV, USA (FARM, WRCC) and Galena, NV, USA (GALE, WRCC) for use in vertical temperature difference and in the surface layer of the heat deficit calculations discussed in sect. 3.1. Data were used if > 50% of the data were available. Meteorological data were also collected from atmospheric balloon soundings released by the National Weather Service (NWS) at 04:00 PST and 16:00 PST, discussed further in sect. 3.2.

3. Data analysis

3.1 Atmospheric stability

Temperature data from GALE and the FARM were used to calculate the difference in temperature between a site at higher elevation and a site at the valley floor ($\Delta T = T_{GALE} - T_{FARM}$, dz = 792 m) to characterize temperature inversions in the Truckee Meadows valley, similar to Chen et al. (2012).

Valley heat deficit was calculated following Whiteman et al. (1999; 2014) as

$$HD(z) = c_p \int_{h_0}^{h} \rho(z)[\theta_h - \theta(z)]dz \text{ [J m}^{-2}\text{]} \quad (1)$$

where c_p = the specific heat of air at constant pressure (1005 J Kg^{-1} K^{-1}), z = height above valley floor, h_0 = valley floor (1342 m), h = height of surrounding

mountain ridge above valley floor (2134 m), $\rho(z)$ = density of air at height z, θ_h = potential temperature at ridge height, and $\theta(z)$ potential temperature at height z. Heat deficit was calculated twice a day at 04:00 PST and 16:00 PST using balloon soundings released from the NWS and supplemented with data from the valley floor (FARM, Table 1) for the lowest height layer. The morning and afternoon total heat deficit values were averaged for a daily average heat deficit.

Heat deficit (HD) has previously been used as a measure of atmospheric stability in valleys to characterize cold air pools (Chemel et al, 2016; Green et al, 2015; Whiteman et al, 1999). Valley heat deficit is the energy required to mix a layer of air from the valley floor to the potential temperature (θ) at a ridge line (Whiteman et al, 1999). Generally, higher heat deficit values are associated with stable atmospheric boundary layers, and therefore more energy is required to mix the air in the valley.

3.2 Vertical structure

Balloon soundings released at 04:00 and 16:00 PST were used to estimate the PBLH. The vertical potential temperature gradient method to find the inversion layer was used during periods of high convective mixing (Stull, 1988). The height at which virtual potential temperature exceeds the surface temperature by 1.5 K was used for periods with low convective mixing (Holzworth, 1964; Seibert et al, 2000).

β_{ext} from the PIN was used with τ_{ext} from AERONET to calculate Apparent Optical Height (AOH, eq. 1).

$$AOH\ (440, 405) = \frac{\tau_{ext}(440\ nm)}{\beta_{ext}(405\ nm)} \quad (2)$$

AOH is a measure of the maximum depth that aerosol pollution resides in the atmosphere (Loría-Salazar, 2014). AOH was compared to PBLH to determine if $PM_{2.5}$ was confined within or was present above the PBL. If AOH and PBLH were not similar, than it was assumed that conditions in the column did not reflect conditions at the surface.

3.3 Statistical analysis

3.3.1 Spatial gradients

Statistical testing using ANOVA (one-way) was applied to determine statistically significant differences in the means of atmospheric pollutant concentrations observed at the three measurement sites to aid in investigating the spatial gradients for each pollutant. Statistical tests were considered significant at $\alpha < 0.05$.

3.3.2 Quadrant method

The quadrant method was developed as a data exploration tool to understand the relationship between τ_{ext} and surface $PM_{2.5}$ observations. τ_{ext} and surface $PM_{2.5}$ were separated into four quadrants using threshold values for τ_{ext} and $PM_{2.5}$ to identify clean and polluted periods. When AERONET τ_{ext} and surface $PM_{2.5}$ are visualized on a scatter plot the quadrants are as follows: quadrant 1 (Q1) is the lower left quadrant with low τ_{ext} and $PM_{2.5}$; quadrant 2 (Q2) is the upper left quadrant with high $PM_{2.5}$ at the surface but not in the column; quadrant 3 (Q3) is the upper right quadrant with high τ_{ext} and $PM_{2.5}$; and quadrant 4 (Q4) is the lower right quadrant with low $PM_{2.5}$ at the surface but not in the column. Quadrant 1 and Q3 had a positive association between τ_{ext} and surface $PM_{2.5}$.

In Q2 and Q4, there was vertical heterogeneity of aerosol concentrations and therefore no association between surface τ_{ext} and $PM_{2.5}$ observations.

Hourly and 24 h $PM_{2.5}$ concentrations from WCAQ and 24 h data from UNRG were used. To increase the sample size (from n = 139 to n = 356) and improve the statistical robustness for the quadrant method analysis all 24 h data available from both the UNRG and WCAQ sites were used for statistical testing with Tukey's simultaneous 95% confidence intervals. These two sites were close together (~1.4 km) and generally experienced similar aerosol sources and physical processes during the sampling period, based on preliminary ANOVA testing (data not shown here).

Threshold values for 1 h WCAQ data were 25 μg m^{-3} (WHO 24 h standard) and 0.2 τ_{ext} (at 440 nm) following Loría-Salazar et al. (2017). For 24 h data, threshold values were the 75^{th} percentile values for 24 h τ_{ext} retrievals and $PM_{2.5}$ concentrations. Values above the 75^{th} percentile were considered reasonably polluted values specific to the sites. Values lower than the 50^{th} percentile may not indicate polluted periods, while values greater than the 75^{th} percentile would indicate heavily polluted periods, but may not identify pollution present in filamentous layers aloft. Each τ_{ext} and $PM_{2.5}$ pair had corresponding meteorological and aerosol data measured at each site. These additional data were selected for statistical analysis, and included meteorological variables (RH, temperature, wind speed), aerosol optical properties (AEE, fine and coarse mode fraction aerosols), vertical structure (PBLH, AOH), measures of stability (ΔT, heat deficit), and O_3 concentrations (24 h average, max 1 h, MDA8). Variables that were not available in 1 h temporal resolution (PBLH, heat deficit, max 1 h, MDA8) were not used in the comparison between 1 h and 24 h WCAQ data. Other variables used to aid in

identification of atmospheric pollution sources and processes in the quadrants, but not used in the statistical analysis, included fire flags identified using AERONET data, presence of temperature inversions, and presence of strong temperature inversions following Chen et al. (2012).

ANOVA one-way statistical analysis was used to characterize statistically significant differences in the means of meteorological variables, aerosol optical properties, vertical structure, stability measures, and ozone concentrations in the quadrants. Tukey's simultaneous 95% confidence intervals were used to determine if the difference between the means of a variable in two quadrants was statistically significant (e.g. the mean of all the wind speed data points associated with the τ_{ext} and $PM_{2.5}$ points classified in Q1 compared to the mean of all the wind speed data points associated with the τ_{ext} and $PM_{2.5}$ points classified in Q2). Confidence intervals were calculated, for each pair of quadrants (e.g. Q1 vs Q2) for each variable, to quantify statistically significant differences in the variable means. If the confidence interval did not span zero, then the difference between the mean of the variables in Q1 and the mean of the variables in Q2 was determined to be statistically significant. The differences in the means of the meteorological variables, aerosol optical properties, vertical structure, stability measures, and ozone concentrations associated with the τ_{ext} and $PM_{2.5}$, separated into each quadrant, could then be used to identify the atmospheric sources and processes related to a positive association between τ_{ext} and $PM_{2.5}$ and periods when there was vertical heterogeneity and therefore no association between τ_{ext} and $PM_{2.5}$.

Hourly and 24 h data from WCAQ were both separated into quadrants and compared qualitatively to determine if the quadrant method could be applied to 24 h data.

Regulatory monitoring networks often use 24 h $PM_{2.5}$ measurements due to resource and access constraints and use of the quadrant method for 24 h $PM_{2.5}$ data could increase the use of this method for rural sites that only have 24 h measurements. Statistically different means between quadrants, based on the Tukey pairwise comparison, were noted and the means were qualitatively labeled as low, moderate, or high compared to the means of that variable in other quadrants that were statistically significant. Qualitative labeling of the statistical results was used to compare the overall results in each quadrant between 1 h and 24 h WCAQ data to identify large discrepancies (low vs. high labels) between the two datasets that would indicate that 24 h data was not suitable for use in the quadrant method.

The statistical results for each quadrant of the 24 h data from UNRG and WCAQ were then analyzed to identify differences in variable means between quadrants to determine the different sources and physical processes affecting the relationship between τ_{ext} and $PM_{2.5}$ in each quadrant. Results from this study and from Loría-Salazar et al. (2017) were compared because Reno is an inland site in the Western USA, and it was previously used in Loría-Salazar et al. (2017). Where available, data from PEAV were used to compare the concentrations of atmospheric pollutants at a higher elevation site to the concentrations at the valley sites.

4. Results and Discussion

4.1 Atmospheric stability

Valley heat deficit, used as a measure of the bulk stability of the Truckee Meadows valley, had a seasonal cycle. Total heat deficit (total, 1342 m to 2134 m), heat

deficit in the surface layer (surface, 1342 m to 1516 m, SI Fig. 1a and 1b), and morning heat deficit had higher values in winter and fall, lower values in summer, and the lowest values in spring (SI Table 4). Afternoon heat deficit had the highest values in winter, the lowest values in fall, and similar values in spring and summer (SI Table 4). High heat deficit in winter indicates higher stability and therefore less mixing, which is expected in winter due to lower solar radiation and temperatures. Morning heat deficit (SI Fig. 1c) was higher than the afternoon heat deficit (SI Fig. 1d) 99% of the days during the sample period (SI Fig. 1e), indicating higher stability in the morning compared to the afternoon, in agreement with daily periods of low and high convective mixing associated with solar radiation.

The difference in temperature (ΔT) between GALE and the FARM, used to characterize temperature inversions in the Truckee Meadows valley, was high in the fall and low in the spring (fall > winter > summer > spring, SI Table 4). Green at al. (2015) found that ΔT and heat deficit were positively correlated ($r^2 = 0.48$) in winter in Reno. In the current study, heat deficit was positively correlated with ΔT for all data ($r^2 = 0.57$, p-value < 0.05, SI Fig. 2a), 24 h average heat deficit and ΔT ($r^2 = 0.40$, p-value < 0.05, SI Fig. 2b), and morning heat deficit and ΔT ($r^2 = 0.58$, p-value < 0.05, SI Fig. 2c), but not for afternoon heat deficit and ΔT ($r^2 = 0.055$, p-value < 0.05, SI Fig. 2d). Heat deficit and ΔT were positively correlated for all seasons except summer (SI Fig. 3). These results indicate that ΔT and heat deficit were correlated and either could be used as measures of atmospheric stability outside of summer months.

Heat deficit and $PM_{2.5}$ concentrations were also previously shown to be positively correlated in winter (r^2 = 0.53 to 0.59, Green et al, 2015). The relationship between daily average heat deficit and $PM_{2.5}$ concentrations (r^2 = 0.49, p-value < 0.05, SI Fig. 6) in Reno in the winter compares well to the previous work. Daily average heat deficit was not well correlated with average $PM_{2.5}$ concentrations, unless days with fires were removed (SI Fig. 4 and 5). Days with fire flags, determined using AEE, were only available when the Cimel was operating, therefore some days during fires may not have been removed, due to missing Cimel data. However, removing data with available fire flags improved the positive correlation between total 24 h average heat deficit (r^2 = 0.29, p-value < 0.05), morning heat deficit (r^2 = 0.24, p-value < 0.05), and afternoon heat deficit (r^2 = 0.26, p-value < 0.05) with $PM_{2.5}$ (SI Fig. 5). Heat deficit and $PM_{2.5}$ were positively correlated for all seasons except summer (SI Fig. 6). A similar improvement of ΔT and $PM_{2.5}$ correlation occurred when fire data were removed (data not shown). This indicates that measures of stability were useful for understanding $PM_{2.5}$ concentrations during certain conditions, but were not useful during conditions influenced by other factors, such as wildfire emissions. A period of elevated heat deficit that occurred in January 2015 is discussed in sect. 4.3.4.

4.2 Vertical structure

PBLH was high in the summer (median: 2.5 km) and low in the winter (median: 0.75 km) with spring and fall median values of 1.7 km and 1.9 km, respectively. As expected, PBLH was only correlated with heat deficit (r^2 = 0.21, p-value < 0.05) and

WCAQ $PM_{2.5}$ (r^2 = 0.11, p-value < 0.05) in the winter when there was less convective mixing, higher stability, and enhanced $PM_{2.5}$ at the surface (SI Fig. 10, 11, 12, and 13). Calculated AOH was higher in the summer (median: 3.8 km) than in the fall (median: 2.4 km). There were only three data points for spring and no winter data available due to lack of Cimel data during instrument calibration (SI Table 5 and SI Fig. 7). High values of PBLH and AOH in the summer were expected due to higher convective mixing and aerosols present aloft. However, PBLH and AOH were not well correlated (r^2 = 0.029, SI Fig. 8 and 9). Because AOH is a measure of the maximum depth that aerosol pollution resides in the atmosphere based on columnar and surface extinction, it will not necessarily be related to PBLH or atmospheric stability. Secondary aerosol formation and lofting of pollutants into the free atmosphere over the Sierra Nevada Mountains affect AOH independently of the PBLH (Loria-Salazar et al, 2014)

4.3 Statistical analysis

4.3.1 Spatial gradients

Ozone (1 h average and MDA8) increased significantly (ANOVA p-value < 0.01, Table 2) in concentration further from the highways (UNRG < WCAQ < PEAV). For June 2014 to October 2015, the valley sites (UNRG and WCAQ) did not have significantly different max 1 h O_3 concentrations (p-value = 0.07). June to November 2014, max 1 h O_3 concentrations at the two sites furthest from the highways (WCAQ and PEAV) were not significantly different (ANOVA p-value > 0.05), but both were significantly higher than UNRG (ANOVA p-value < 0.01, for both). The formation of O_3 from photochemical reactions between VOCs and NO_x explains the higher concentration

at WCAQ, which is further from the highways, compared to UNRG. In Truckee Meadows, on-road mobile emissions, dominated by truck emissions, were the largest sources of NO_x (68% of total emissions) in 2011 (Washoe County, 2012). The highways were a dominant source of NO_x emissions, where photochemical reactions were the main source of O_3 at the valley sites. Ozone at PEAV is not necessarily dependent on distance from the highways as the site experiences limited photochemical production of O_3 during the day and is influenced by stratospheric mixing of O_3 and long-range transport (Pierce et al, 2017).

$PM_{2.5}$ at the valley sites was not significantly different, while PEAV was significantly lower than both valley sites (ANOVA p-value < 0.01, for both, Table 2). Distance to the highway will affect primary $PM_{2.5}$ concentrations. However, non-point sources account for 87% of $PM_{2.5}$ emissions in Truckee Meadows and will affect $PM_{2.5}$ concentrations independently of distance to highways, as will secondary formation of $PM_{2.5}$ (Washoe County, 2012). Primary $PM_{2.5}$ emissions will be higher closer to highways, while secondary formation with be enhanced further from highways. Miscellaneous area sources, which include wildfires, were the main non-point source of $PM_{2.5}$, and have been shown to degrade air quality in the area (EPA, 2017b; Loría-Salazar et al, 2017; Miller et al, 2015; Pierce et al, 2017).

CO was significantly lower in concentration (ANOVA p-value < 0.01, Table 2) further from the highways (UNRG > WCAQ > PEAV). This is not surprising, as on-road mobile emissions from passenger cars and trucks were the largest sources (44% of total emissions) of CO. Non-road mobile sources including non-road vehicles, non-road engines, and railroads, emit another 27% of total CO emissions, and non-point sources

(e.g. wildfires) of CO account for 28% of total emissions (Washoe County, 2012). CO can then undergo chemical reactions leading to O_3 formation.

NO_x, NO, and SO_2 were only measured at the valley sites. UNRG had significantly higher concentrations of NO_x and NO than WCAQ (ANOVA p-value < 0.01, Table 2). On-road mobile emissions, dominated by truck emissions, were the largest sources of NO_x (68% of total emissions), while non-road mobile sources accounted for another 20% of total NO_x emissions (Washoe County, 2012). NO_x can then also contribute to O_3 formation. Based on the dominant sources of CO and NO_x, concentrations were influenced by proximity to the highways at the two valley sites, with higher concentrations at UNRG.

WCAQ had significantly higher SO_2 than UNRG (ANOVA p-value < 0.01, Table 2). Non-point emissions (external and internal stationary fuel combustion and miscellaneous area sources, such as wildfires) were the largest sources of SO_2 (76% of total emissions) in Truckee Meadows (Washoe County, 2012). Proximity to sources of SO_2, such as highways and point sources, will affect SO_2 concentrations; however, non-point sources will have a larger contribution.

To compare our roadway gradients of pollutants to previous results, background normalization is calculated by dividing the near-road concentrations by a concentration far enough from the highways to be considered background. Karner et al. (2010) found that CO, NO_x, NO returned to background concentrations between 0.16 and 0.57 km from a highway, while Riley et al. (2014) found that NO_x returned to background concentrations by ~0.30 km from a highway. Based on these findings the median concentration of hourly WCAQ data was used as the background concentration since it is

located 1.2 and 2.1 km from the highways. Hourly data from days classified in Q1 had average enhancements of CO, NO_x, and NO at UNRG by 1.6, 2.9, and 8.3 times WCAQ compared to 21, 1.8, 3.3, respectively, in Karner et al. (2010) and 3.5 times for NO_x in Riley et al. (2014). O_3 and SO_2 were on average 0.72 and 0.52 times less at UNRG than at WCAQ. Karner et al. (2010) and Riley et al. (2014) had similar results (~0.5 and 0.7, respectively) for O_3 but did not report values for SO_2. Both studies had measurements closer to the highway or calculated the edge-of-highway values, which may account for the differences in this study (e.g., UNRG is 0.03 km from the highway), due to the rapid decrease of some pollutants, such as CO, with distance from the highway (Karner et al, 2010). Differences in the gradients may also be due to the volume and type of traffic on the highways.

Variable	Site comparison (x-y)	Slope	p-value	r	ANOVA p-value	Higher	Jun-Nov 2014
O_3 (1 h)	UNRG-WCAQ	0.79	<0.01	0.85	<0.01	WCAQ	
	UNRG-PEAV	0.12	<0.01	0.31	<0.01	PEAV	
	WCAQ-PEAV	0.21	<0.01	0.49	<0.01	PEAV	
O_3 (max 1 h)	UNRG-WCAQ	0.64	<0.01	0.69	0.07		<0.01 WCAQ
	UNRG-PEAV	0.26	<0.01	0.48	<0.01	PEAV	
	WCAQ-PEAV	0.49	<0.01	0.79	<0.01	PEAV	0.35
O_3 (MDA8)	UNRG-WCAQ	0.68	<0.01	0.72	<0.01	WCAQ	
	UNRG-PEAV	0.23	<0.01	0.48	<0.01	PEAV	
	WCAQ-PEAV	0.42	<0.01	0.77	<0.01	PEAV	
CO (1 h)	UNRG-WCAQ	0.75	<0.01	0.84	<0.01	UNRG	
	UNRG-PEAV	0.026	<0.01	0.09	<0.01	UNRG	
	WCAQ-PEAV	0.035	<0.01	0.10	<0.01	WCAQ	
$PM_{2.5}$ (24 h)	UNRG-WCAQ	0.90	<0.01	0.91	>0.05		
	UNRG-PEAV	0.60	<0.01	0.69	<0.01	UNRG	
	WCAQ-PEAV	0.61	<0.01	0.77	<0.01	WCAQ	
NO_x (1 h)	UNRG-WCAQ	0.72	<0.01	0.80	<0.01	UNRG	
NO (1 h)	UNRG-WCAQ	0.66	<0.01	0.81	<0.01	UNRG	
SO_2 (1 h)	UNRG-WCAQ	1.2	<0.01	0.72	<0.01	WCAQ	

Table 2: Slope, p-value of linear regression, correlation coefficient (r), one-way ANOVA p-values for each site comparison, and the site that has higher values for all data available. The last column indicates differences in ANOVA p-values and the site that is higher for June to November 2014.

4.3.2 Evaluation of the quadrant method using 24 h data

Because the quadrant method was developed for 1 h data, the method was applied to both 1 h and 24 h data at WCAQ to determine if the method could be used with 24 h data. It is expected that the statistical quadrant method will provide more robust results using the hourly data with more data points. However, at many locations throughout the USA only 24 h $PM_{2.5}$ data is available, including UNRG and PEAV. Using 24 h data required selecting new threshold values for τ_{ext} and $PM_{2.5}$ based on 75^{th} percentile values at the site to identify site specific clean and polluted periods (SI Tables 1, 2, and 3). Statistical results identified in each quadrant will therefore change depending on the site τ_{ext} and $PM_{2.5}$ values, and the variables selected for the ANOVA statistical testing. Statistically significant differences, based on Tukey pairwise comparison, between the means of variables in different quadrants were labeled as low, moderate, and high based on the mean values (Fig. 2). This was done to investigate how the results in each quadrant compared and not to compare the absolute means in each quadrant, as the absolute means will differ between 1 h and 24 h data (see SI Table 6 for absolute values).

Differences in the means of the variables in each quadrant generally identified similar sources and physical processes for the 1 h and 24 h datasets (Fig. 2). Quadrant 1 contained a majority of the data points for 1 h and 24 h data. Quadrant 2 had the highest percentage of temperature inversions, while Q3 had the highest percentage of days with fire flags for both datasets. Aerosol modes were similar between the 1 h and 24 h data, except Q4, which had some coarse mode aerosols in the 24 h data, but was dominated by fine mode aerosols in the 1 h data. There were differences in mean RH in Q1 and Q4 for the 1 h data, but mean RH was not significantly different in these two quadrants for the

24 h data. There were also differences in mean wind speed for Q1, where there was high mean wind speed for the 24 h data and moderate mean wind speed for the 1 h data in Q1. There was a difference in the mean ΔT for Q3, where there was moderate mean ΔT for the 24 h data and low mean ΔT for 1 h data. Mean wind speed was not significantly different in Q3 or Q4 for the 24 h data but was statistically different for the 1 h data. In Q4, mean ΔT was low for the 24 h data and moderate for the 1 h data and mean temperatures and O_3 concentrations were moderate in the 24 h data and high in the 1 h data.

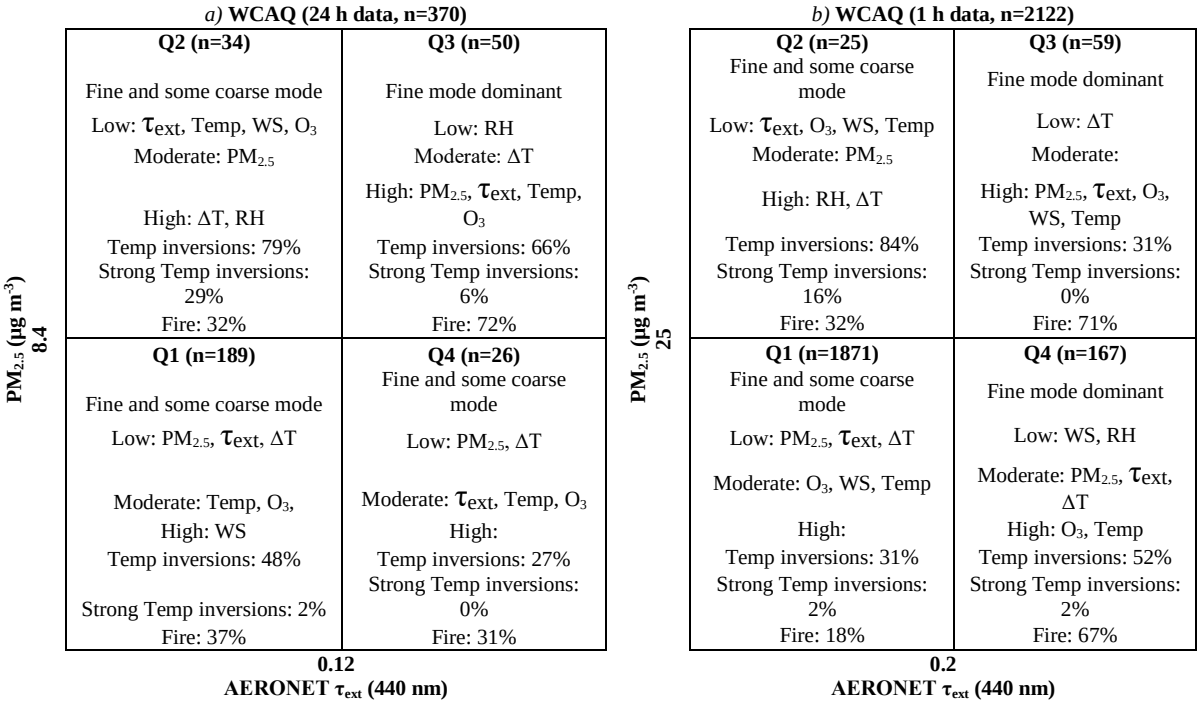

Figure 2: Significant meteorological variables, aerosol optical properties, vertical structure, atmospheric stability measures, and ozone (O_3) concentrations for a) 24 h data and b) 1 h data at WCAQ in each quadrant (Q1-Q4).

If there were large discrepancies (e.g. low vs. high means) between observed differences in the variable means when comparing the quadrants for 1 h vs 24 h, then the

quadrant method for 24 h data identified different sources and physical processes compared to the 1 h data and may indicate issues using the method for 24 h data. Other differences in variable means occurred when variable means considered significantly different between two quadrants for the 1 h data were not significantly different between the same two quadrants for the 24 h data, this difference between 1 h and 24 h quadrants did not change the overall source or physical process identified for those quadrants.

Differences between means for 1 h and 24 h data were expected due to the nature of the τ_{ext} retrievals only occurring during daylight hours, removing nighttime $PM_{2.5}$ measurements from the 1 h ANOVA testing, while 24 h $PM_{2.5}$ samples will include day- and nighttime concentrations. VanCuren et al. (2005) found that nighttime fumigation is an important source of free tropospheric air to surface monitoring sites at high elevation and often contains Asian aerosols. This nighttime fumigation would be lost in the 1 h data but retained in the 24 h $PM_{2.5}$ measurements. Additionally, discreet transport events may occur on shorter time scales than 24 h due to filamentous layers of pollution aloft (Fine et al, 2015; Lin et al, 2012; Stohl et al, 2003).

However, due to the similarities in the results of the statistical analysis between the 1 h and 24 h quadrants, the quadrant method was used for 24 h data.

4.3.3 Quadrant method results for 24 h combined UNRG and WCAQ data

The 75th percentile thresholds for all 24 h data from UNRG and WCAQ were 0.12 for τ_{ext} and 8.8 μg m^{-3} for $PM_{2.5}$. For days with quadrant classification, UNRG had 138 days and WCAQ had 218 days available. There were 129 days with quadrant classification at both sites between June 2014 and October 2015. There were 19 days in

which UNRG and WCAQ were classified in different quadrants. On 9 of those days, UNRG had higher $PM_{2.5}$ concentrations; the other 10 days WCAQ had higher concentrations, indicating that one site was not consistently higher than the other.

There was no winter data due to calibration of the Cimel, and very few data points in spring due to cloud cover. There was a positive correlation between τ_{ext} and $PM_{2.5}$ for all data ($r^2 = 0.35$, p-value < 0.01, Fig. 3) and good correlation between τ_{ext} and $PM_{2.5}$ ($r^2 = 0.65$, p-value < 0.01, SI Fig. 14) in the summer. Although there was higher positive correlation between τ_{ext} and $PM_{2.5}$ for the 24 h data at these sites compared to the hourly data in Loría-Salazar et al. (2017), there were still periods that were not explained by a linear relationship (Fig. 3 and SI Fig. 14).

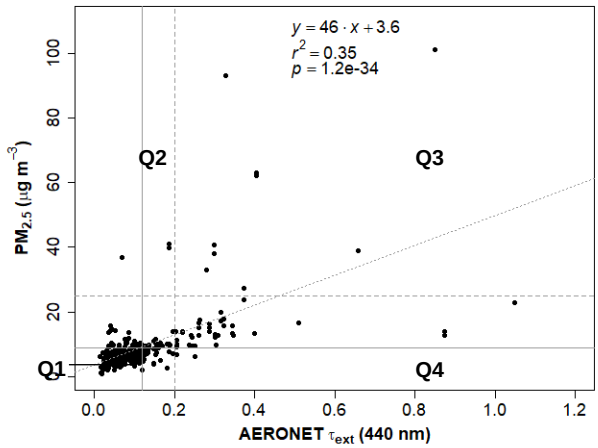

Figure 3: Scatter plot of all AERONET τ_{ext} and $PM_{2.5}$ (µg m^{-3}) 24 h data available from UNRG and WCAQ. Solid grey lines indicate τ_{ext}: 0.12 and $PM_{2.5}$: 8.8 µg m^{-3}, dashed grey lines indicate τ_{ext}: 0.2 and $PM_{2.5}$: 25 µg m^{-3}, dotted grey line is the linear fit line.

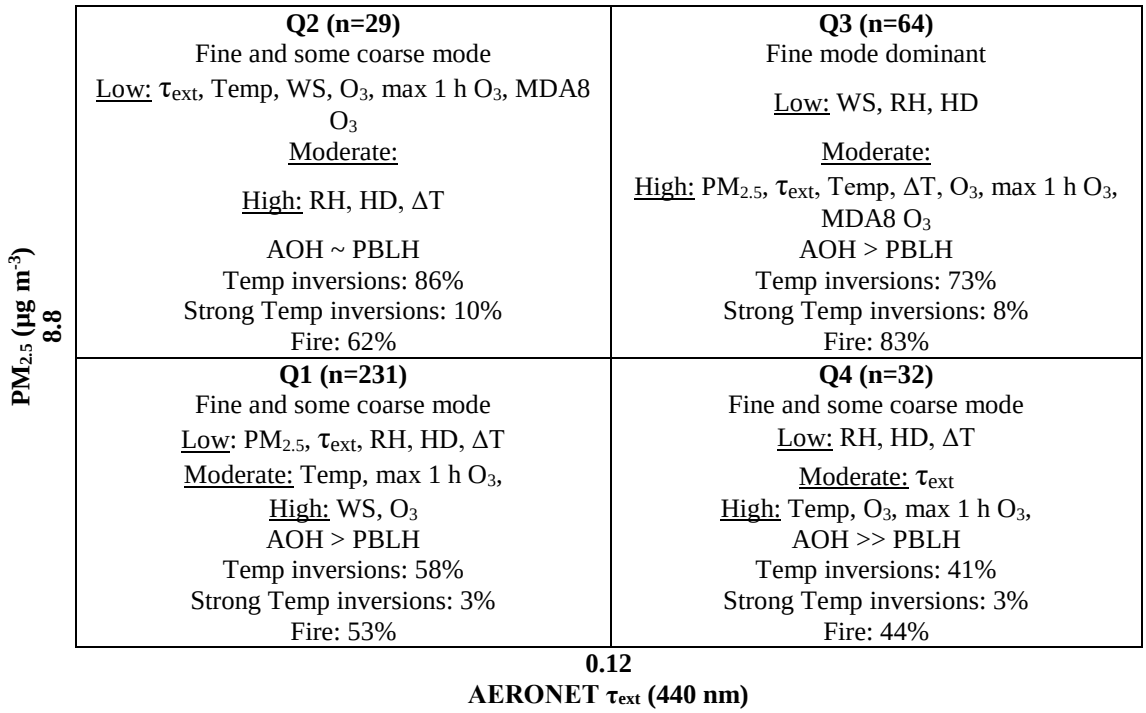

Figure 4: Significant meteorological variables, aerosol optical properties, vertical structure, atmospheric stability measures, and ozone (O_3) concentrations for all 24 h data from UNRG and WCAQ in each quadrant (Q1-Q4).

Quadrants 1, 2, and 4 had similar AEE and fine mode with some coarse mode fraction aerosols (SI Table 7). There were differences between Q1 and Q4 in the means of wind speed, temperature, and max 1 h O_3. There were also differences in PBLH and AOH between Q1 and Q4. The low measures of atmospheric stability (heat deficit and ΔT), high wind speed, and high O_3 but moderate max 1 h and MDA8 O_3 in Q1 indicated unstable conditions and a well-mixed PBL with low τ_{ext} and $PM_{2.5}$ concentrations. The differences in the means of PBLH and AOH in Q4 indicated more aerosols higher in the column than the PBLH. High mean max 1 h O_3 in Q4 but similar 24 h average mean O_3 to Q1 also indicated short-term increases in pollutants occurring in Q4 and a PBL that was not well mixed. Quadrant 2 had high measures of atmospheric stability (heat deficit and ΔT), low temperatures, low O_3, and aerosols confined within the PBLH

(AOH~PBLH, SI Table 7 and 8), indicating a stable atmosphere and local pollutants accumulating at the surface leading to reduction in O_3 through titration with NO. The highest AEE and fine mode fraction aerosols dominated in Q3, along with high O_3, max 1 h O_3 and MDA8 O_3, and a high percentage of days with fires, indicated aerosols from fires affected this quadrant (Fig. 4 and 5).

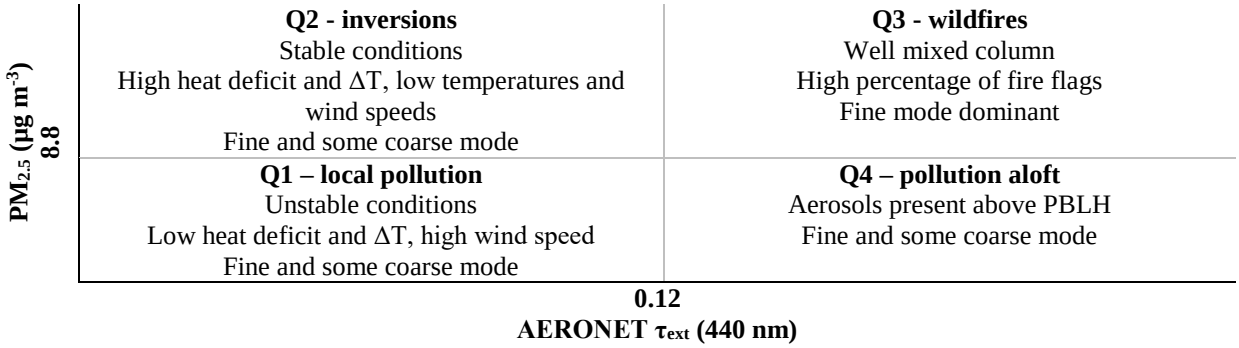

Figure 5: Summary of conditions in each quadrant at the two valley sites, UNRG and WCAQ.

There were differences in the statistically significant means of certain variables and aerosols modes between the quadrants identified in Loría-Salazar et al. (2017) for inland sites in the Western USA and the quadrants identified in this study. Differences in means are expected between sites and sample periods. However, because the current study used data from Reno, NV, USA, which is also a site used in the previous study, the differences are worth noting. Q1, Q2, and Q4 all had higher fine mode fraction aerosols compared to the previous study. Q1 and Q2 also had higher values of AEE than the previous study. Q3 in the previous study had higher RH, used as an indicator of wildfire plumes (Parmar et al, 2008), however in this study, Q3 had RH similar to Q1 and Q4, which were all significantly less than Q2, making the wildfire determination less distinct in this study.

Differences in aerosol fraction are important because coarse mode fraction aerosols were used as evidence for local pollutants for Q1 and Q2 in the previous study. The similarity in fine mode fraction between Q1, Q2, and Q4 in the current study indicates aerosol optical properties were less useful in understanding the processes affecting the variables in those quadrants for the 24 h data. Gustin et al. (2015) found that valley structure, i.e. size of the valley, height of surrounding topography, and distance to surrounding topography impacts air quality due to the differences in surface area for deposition and in convective mixing. Inland sites in Loría-Salazar et al. (2017) included Reno and Frenchman Flat, NV, and Fresno, CA. Frenchman flat (940 m asl) and Fresno (94 m asl) are both lower in elevation than Reno (1341 m asl), therefore both sites will experience different convective mixing and influence from entrainment of pollutants aloft. Fresno (population: $5.0x10^5$), located in the southern half of the Central Valley (47,000 km^2) of California, west of the Sierra Nevada Mountains and is not considered part of the intermountain west. Fresno is influenced by high population density and the agricultural industry that dominates the area (www.census.gov, 2017). The lower elevation and large valley size, high population density, and agricultural sources of atmospheric pollutants would lead to differences in convective mixing and in the fine and coarse mode fraction aerosols present, compared to Truckee Meadows.

The Frenchman Flat hydrographic area is 1200 km^2, more than twice the size of the Truckee Meadows hydrographic area, lower in elevation, located on a dry riverbed with topographic surroundings lower in elevation than Reno (NV, 2017). Frenchman Flat is part of the Nevada National Security Site and does not have a permanent population, and would therefore have limited local sources of fine urban aerosols. The surface $PM_{2.5}$

measurements are from the Las Vegas, NV U.S. EPA AQS. The Las Vegas U.S. EPA AQS site is located on the northwest border of the Las Vegas metropolitan area (population: ~2 mill), 71 km southeast of the AERONET τ_{ext} observed in Frenchman Flat (www.census.gov, 2017). Using τ_{ext} observations from Frenchman Flat and $PM_{2.5}$ concentrations near Las Vegas for the quadrant method in this area, likely would have different statistical results than collocated observations of τ_{ext} and $PM_{2.5}$ due to the difference in urban and non-urban pollutants. Both Frenchman Flat and Fresno are likely impacted by coarse mode fraction aerosols due to locations in a dry lakebed and agricultural area. These two sites may have skewed the aerosol mode fraction toward higher levels of coarse mode fraction aerosols in the previous study than was observed in Reno for this study.

4.3.4 Analysis of quadrant method results

Individual quadrants for the 24 h UNRG and WCAQ data were analyzed to understand the statistical results for each classified quadrant. All data in Q1 was analyzed together. Case studies were analyzed for Q2 and Q3. Days that classified in Q4 and that had data from PEAV were analyzed. Days with high input of trans-Pacific pollutants, but were not necessarily classified in Q4 were also analyzed. Data from PEAV, surface and 500 mb weather maps, the MODIS visible product, and Naval Research Laboratory Aerosol Analysis and Prediction System (NRL NAAPS) aerosol surfaces were used to corroborate quadrant classification.

Quadrant 1 (Q1): unstable conditions and mixing of local pollutants

Quadrant 1 contained the majority of data points (n=231, 65%) for 24 h data. Median $PM_{2.5}$ concentration for Q1 data in the valley (5.9 µg m^{-3}) was lower than the median concentration (6.7 µg m^{-3}) for the sample period (SI Table 2 and 7). The median $PM_{2.5}$ concentration (3.8 µg m^{-3}) at PEAV, for days (n=62) classified as Q1 in the valley, was lower than the median $PM_{2.5}$ concentration (4.5 µg m^{-3}) at PEAV, June to November 2014 (SI Table 9). τ_{ext} was similar to Q2 but AOH was higher in Q1. Because Q1 contained a majority of the data points, characterized by low measures of atmospheric stability, it was analyzed in bulk as the quadrant representative of the base state of the measurement sites.

For days classified in Q1, pollutant concentrations were higher and the ranges of the diel patterns (Fig. 6) were larger for CO (174 to 458 ppbv), NO_x (14 to 54 ppbv), and NO (1.7 to 29 ppbv) at UNRG compared to WCAQ (CO: 145 to 309 ppbv, NO_x: 5.6 to 32 ppbv, and NO: 1.4 to 15 ppbv). Ozone (8.2 to 44 ppbv) and SO_2 (0.061 to 0.38 ppbv) concentrations were lower at UNRG compared to WCAQ (O_3: 21 to 53ppbv, SO_2: 0.16 to 0.51 ppbv). Morning peaks in concentrations coincided with rush hour traffic. CO, NO, and SO_2 peaked at 07:00 PST and then dropped below nighttime levels until 21:00 PST when concentrations returned to nighttime levels at both sites, except for SO_2 at WCAQ, which remained elevated above nighttime levels until 21:00 PST. The morning peak in SO_2 at both sites indicates that vehicles were a source of SO_2; however, the elevated concentration throughout the day at WCAQ indicated another source of SO_2 was also present. Major point sources of SO_2 in Truckee Meadows include the Reno-Tahoe International Airport located ~5.1 km southeast of UNRG and ~4.3 km southeast of

WCAQ. Major non-point sources include commercial and industrial fuel combustion and wildfires. NO_x concentrations at UNRG were 54 ppb from 06:00 to 07:00 PST but were lower during this time at WCAQ (30 to 32 ppb) indicative of on-road sources dominating NO_x emissions. Ozone concentrations were lowest at both sites at 05:00 PST and peaked between 13:00 and 14:00 PST. This pattern is similar to that measured previously in Reno, suggested to be due to mixing from the free troposphere (Gustin et al, 2015; Gustin et al, 2013; Pierce et al, 2017). AERONET τ_{ext} had a small peak at 07:00 PST, a minimum at 14:00 PST and maximum peak (0.074) at 18:00 PST (τ_{ext} was only available at UNR and during daylight hours 06:00 to 19:00 PST). The maximum peak was later than seen in June (16:00 PST) and July (14:00 PST) of 2012 at this site (Loría-Salazar, 2014) and was attributed to secondary aerosol formation. $PM_{2.5}$ started to increase at 05:00 PST, peaked at 09:00 PST (9.5 μg m^{-3}), and then decreased until 19:00 PST (hourly $PM_{2.5}$ was only available at WCAQ, Fig. 6). This is similar to findings in Loría-Salazar (Loría-Salazar, 2014) that showed primary pollutants at the surface in the morning and secondary aerosol formation present in the atmospheric column in the afternoon, indicating no association between τ_{ext} and $PM_{2.5}$ in the afternoons.

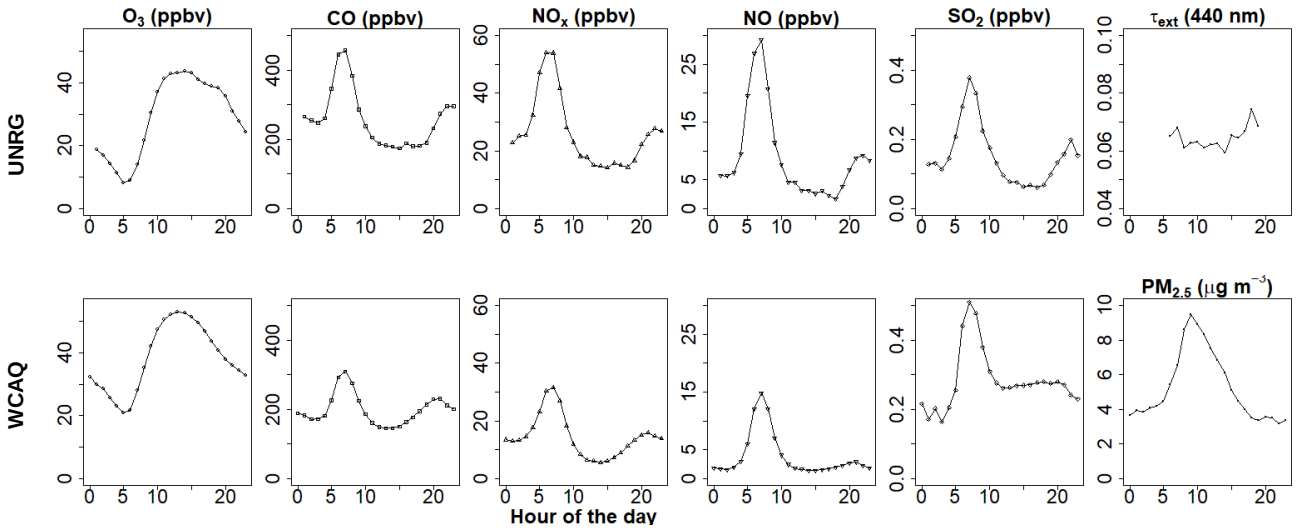

Figure 6: Average ozone (O_3, ppbv), carbon monoxide (CO, ppbv), oxides of nitrogen (NO_x, ppbv), nitrogen monoxide (NO, ppbv), sulfur dioxide (SO_2, ppbv), AERONET aerosol optical depth (τ_{ext}, at 440 nm), and particulate matter ($PM_{2.5}$, µg m^{-3}) for each hour of the day (PST) of the days classified in Q1 at UNRG and WCAQ.

Quadrant 2 (Q2): Stable conditions, shallow PBLH, and local pollutants

Quadrant 2 had the least amount of available data (n=29, 8%) due to a combination of missing Cimel data during the winter, cloudy conditions, and the extent of the sample period. The median $PM_{2.5}$ concentration for Q2 (10 µg m^{-3}) was higher than the median concentration for the sample period (6.7 µg m^{-3}) while the median concentration at PEAV (1.9 µg m^{-3}), for available days (n=8) where the valley was classified as Q2, was less than the median concentration (4.5 µg m^{-3}) at PEAV, June to November 2014. Similar τ_{ext} and lower AOH than Q1 and lower $PM_{2.5}$ concentrations at PEAV support the confinement of aerosols within the PBLH in the valley. A case study in January 2015 was analyzed as a representative of a cold pool event, though the Cimel was not operating at this time.

From January 1 to January 9, 2015, total average heat deficit was > 4 MJ m^{-2}, except on January 4 (3.6 MJ m^{-2}). Total morning heat deficit was > 5 MJ m^{-2} from

January 2 to 9. January 2 to 5 and January 8 and 9 had maximum ΔT > 5 °C and minimum ΔT > -2 °C and would be considered strong temperature inversion periods following criteria from Chen et al. (2012). Although these days were not categorized into quadrants, due to missing Cimel data, it is clear that it was an extended period of a stable atmospheric boundary layer in which pollutants accumulated and a cold air pool was present.

Elevated $PM_{2.5}$ concentrations above the 8.8 µg m^{-3} threshold occurred during this time; $PM_{2.5}$ reached 26 µg m^{-3} on January 2 at UNRG. There were no $PM_{2.5}$ data at UNRG for January 7 to 9. At UNRG, 24 h average CO reached over 1000 ppbv, NOx was over 100 pbbv and NO was over 80 ppbv. O_3 at UNRG, dropped to < 2 ppbv by the end of the 9 days while max 1 h O_3 dropped below 10 ppbv and MDA8 O_3 dropped to 5 ppbv or below. Ozone concentrations were depressed due to the accumulation of NO_x and NO causing NO_x titration and removal of O_3 through reaction with NO. Wind speeds were > 1 m s^{-1} before and after this period and < 0.5 m s^{-1} during. Temperatures started at -7 °C, and gradually rose to 7 °C by the end of the period. RH increased from 66% to 76% and pressure was elevated, starting to drop the last day of the period as air in the valley began to mix. PBLH was less than 1 km on all days except on January 4 (1.5 km). WCAQ had almost identical patterns, the only differences were that max $PM_{2.5}$ was 22 µg m^{-3}, January 6 had higher wind speeds (1.1 m s^{-1}), and RH ranged from 58% to 69%. There were no $PM_{2.5}$, CO, or meteorological measurements at PEAV during this time. O_3 at PEAV was similar to the median monthly concentrations for 24 h average O_3 (38 ppb), max 1 h O_3 (43 ppb), and MDA8 O_3 (41 ppb) for January 2015. PEAV did not experience

a change in O_3 concentrations and remained above the PBLH for the entire period, except on January 4.

An inverted trough of low pressure was present along the coast of California (SI Fig. 15a) until January 4 when a high-pressure area was present over Northern California and the trough was less pronounced (SI Fig. 15b). High pressure remained over most of Nevada for this period. Strong winds aloft started out east northeasterly on December 31, 2014 due to cyclonic flow aloft centered over southern California (SI Fig. 16a), which dissipated by January 4. The winds shifted northerly (SI Fig. 16b), northwesterly (SI Fig. 16c), westerly and weakened (SI Fig. 16d), until January 9 when they become southerly (SI Fig. 16e) and pollutant levels began to decrease and heat deficit and ΔT decreased. This analysis demonstrated the usefulness of the measures of stability in the quadrant method for understanding processes affecting atmospheric pollutants during periods when τ_{ext} and $PM_{2.5}$ were not associated.

Quadrant 3 (Q3): transport and mixing of smoke plumes

Quadrant 3 had the highest median τ_{ext} (0.26), $PM_{2.5}$ concentration (13 μg m^{-3}, n=64, 18% of data), AEE (1.8), and fine mode fraction aerosols (0.92) and the highest percentage of days with fires (83%) identified by the AERONET data. Median $PM_{2.5}$ concentration for days available at PEAV (n=17) during days classified as Q3 for the valley also had the highest median concentration (11 μg m^{-3}). The similarity between the valley and PEAV supports a well-mixed column, while high AEE and percentage of days with fires indicates wildfire aerosols were dominant in this quadrant. One day in September 2014 classified in Q3 was further analyzed.

On September 19, 2014, the two valley sites were classified as Q3. The King Fire burned 390 km^2 in El Dorado County, CA, ~100 km southwest of Reno, NV, from September 13 to October 31, 2014 (CA, 2017). The smoke plume from this fire can be seen in the MODIS visible images (SI Fig. 17a and 17b), when the plume was transported downwind to Reno.

In the valley (SI Table 10), τ_{ext} (0.85 to 0.37), coarse mode fraction, PBLH (3.2 to 1.6 km), and heat deficit decreased from the day before while fine mode fraction, ΔT, AOH (0.83 to 3.7 km), and AEE (1.83 to 1.96) increased. AOH was << PBLH on September 18 and >> PBLH on September 19. There was a fire flag from the AERONET data during this time. At UNRG (SI Table 10), wind speed, O_3, max 1 h O_3, MDA8 O_3, CO, and SO_2 decreased from the previous day, while pressure, NO_x, and NO increased. Temperature and RH were similar to the previous day. $PM_{2.5}$ was 23.7 μg m^{-3}, higher than the 75th percentile (9.4 μg m^{-3}) for this site (there was no $PM_{2.5}$ data for 2 days prior).

At WCAQ (SI Table 10), wind speed, O_3, max 1 h O_3, MDA8 O_3, CO, and SO_2 decreased from the day before, while NO_x and NO increased, and temperature and RH were similar. $PM_{2.5}$ was 27 μg m^{-3}, a decrease from 101 μg m^{-3} the previous day, both higher than the 75th percentile (8.4 μg m^{-3}) for this site. No hourly or daily pressure measurements are reported for WCAQ.

At PEAV, RH, wind speed, CO, O_3, max 1 h O_3, and MDA8 O_3 decreased from the previous day while temperature and pressure increased. $PM_{2.5}$ was 6.7 μg m^{-3}, higher than the 75th percentile (6.0 μg m^{-3}) for this site. No $PM_{2.5}$ data was measured for 6 days prior and no NO_x measurements occurred at PEAV.

On September 18 and 19, low-pressure systems resided off the coast of California (SI Fig. 18a, 18b, and 18c). Winds at the surface shifted from southwesterly on September 18 to northeasterly on September 19, to northeasterly and southeasterly on September 20. Winds at 500 mb shifted from prevailing westerly flows to south and easterly flows (SI Fig. 19a, 19b, 19c, and 19d). This shift in wind direction briefly directed smoke to the west, away from the Truckee Meadows area (SI Fig. 17c). This shift is also seen in the NRL NAAPS smoke surface (SI Fig. 20a, 20b, and 20c), particularly on September 19 (SI Fig. 20b, 10:00 PST)

For this case, all three sites had similar behavior for variables measured at all three sites, except temperature and RH, which were different between PEAV and the valley sites. Decreases in CO across all three sites and of $PM_{2.5}$ at WCAQ indicated that the smoke plume had less impact on the measurement sites on September 19 compared to previous days. The decrease in RH at PEAV that did not occur at either valley site may indicate that PEAV was intercepting drier free tropospheric air. AOH increased from 0.83 km to 3.6 km while PBLH decreased from 3.2 to 1.6 km from September 18 to 19 indicating that the height of aerosols in the atmospheric column was within the PBLH on September 18 and that aerosols were present above the PBLH on September 19 (SI Table 8). PEAV was likely experiencing residual smoke in the early morning (SI Fig. 17c and SI Fig. 20a) that was pushed further west as the day continued (SI Fig. 17d and SI Fig. 20b and 20c). Although PEAV had a lower $PM_{2.5}$ concentration than the two valley sites, the concentration was higher than the 75^{th} percentile for the site. This day supports the identification of Q3 influenced by wildfire plumes. Changing conditions when smoke

plumes are transported aloft and are not confined to the surface may present difficulties in quadrant classification (see Q4).

Quadrant 4 (Q4): Pollution aloft

The median $PM_{2.5}$ concentration (7.1 μg m^{-3}, n = 32, 9% of data) for Q4 was similar to the median concentration (6.7 μg m^{-3}) for the sample period. The median concentration (4.3 μg m^{-3}) for days (n=7) available at PEAV when the valley was classified as Q4 was similar to the median concentration (4.5 μg m^{-3}) for the PEAV sample period. Due to cloud cover and short sample period, the lack of data during spring hinders a full assessment of Q4. In spring, we would expect to see an increase in pollution aloft due to increased frontal activity and long-range transport (Cooper et al, 2010; Fiore et al, 2014; Jacob et al, 1999; Langford et al, 2015; Lin et al, 2012; Vingarzan, 2004). Data from a previous study (Pierce et al, 2017) was used to identify days with moderate to high trans-Pacific input based on Pb isotopic ratios.

There were 9 days from June to November 2014 in which one of the valley sites was classified in Q4 (Table 3). Days in June, July, and the beginning of August had clouds causing some daylight hours (<50%) to be lost to cloud cover, affecting available retrievals of τ_{ext} and therefore classification on those days. On August 20 and 21, UNRG was classified in Q3 while WCAQ was classified in Q4. August 20 had some clouds in the area (SI Fig. 21a and 21b) and winds aloft from the west that strengthened on August 21 and shifted to the northwest (SI Fig. 22). Both days were likely impacted by smoke from the Happy Camp Complex Fire from Northern California, ~400 km northwest of Reno, NV that burned 543 km^2 from August 14 to October 31, making it the largest fire

of 2014, in California (SI Fig. 21, CA, 2017). PEAV $PM_{2.5}$ concentrations were above the monthly median on August 21 (no $PM_{2.5}$ measurements on August 20 at PEAV). The mixing of smoke aloft increased $PM_{2.5}$ at PEAV but had lower influence at the surface, increasing $PM_{2.5}$ concentrations just to the threshold value (8.8 μg m^{-3}). Smoke present aloft, instead of at the surface as observed in Loría-Salazar (2017), likely made quadrant classification on this day difficult.

On September 12, both valley sites were classified in Q4. PEAV had $PM_{2.5}$ concentrations below the monthly median. PBLH was higher than PEAV but there were no AOH observations. Data from Pierce et al. (2017) indicate some trans-Pacific influence on this day. The NRL NAAPS images show smoke coverage from California, USA (SI Fig. 23). Smoke plumes traveling aloft from regional wildfires will increase τ_{ext} in some cases mixing with trans-Pacific aerosols.

		2014								
		Jun. 2	**Jul. 6**	**Jul. 10**	**Jul. 31**	**Aug. 11**	**Aug. 20**	**Aug. 21**	**Aug. 28**	**Sep. 12**
UNRG	**Quadrant**	NA	Q4	NA	Q4	NA	Q3	Q3	Q3	Q4
	$PM_{2.5}$	NA	5.6	NA	8.5	NA	9.9	8.8	11	7.7
WCAQ	**Quadrant**	Q4	Q4	Q4	Q3	Q4	Q4	Q4	Q4	Q4
	$PM_{2.5}$	8.7	7.8	7.2	9.8	7.2	7.3	6.9	8.4	6.0
PEAV	**$PM_{2.5}$**	NA	4.9	4.1	3.1	4.3	NA	6.9	6.0	3.9
τ_{ext}		0.14	0.13	0.13	0.16	0.13	0.16	0.12	0.15	0.12
PBLH		1.6	3.8	3.6	4.1	1.7	3.4	2.3	3.5	3.7
AOH		4.1	5.6	4.7	3.2	NA	4.4	3.4	2.7	NA

Table 3: Days with at least one valley site classified in quadrant 4 (Q4) from June to November 2014.

Several days in 2014 experienced moderate to high levels of trans-Pacific influence based on Pb isotope ratios from Pierce et al. (2017), but were not classified in Q4. Table 4 lists the days that had Pb isotope measurements with a percentage of Pb

attributable to Eurasia above the 50th and 75th percentile values for Eurasian Pb samples available at UNRG. For days that classified as Q1 and had measurements at PEAV (June 6, July 25, and October 9, 2014), the PBLH was higher than PEAV. AOH was at or above PBLH on July 6 and October 9 (AOH was not available for July 25). June 6 and October 9 had similar $PM_{2.5}$ concentrations at all three sites, while July 25 had $PM_{2.5}$ concentrations at PEAV below the 25th percentile values for the site. The height of the PBLH, indicative of high convective mixing may have entrained pollutants transported in filamentous layers in the free troposphere that contributed to Eurasian Pb influence but did not increase $PM_{2.5}$ consistently through the column, complicating quadrant classification on these days.

For days that classified in Q3 (August 7 and September 22, 2014), it is likely that $PM_{2.5}$ from fires was much greater, at all sites, than aerosols at the surface or aloft. For days with no τ_{ext} observations and therefore no quadrant classification we can only speculate on a quadrant, September 26 and 27, 2014 had low $PM_{2.5}$ concentrations and therefore could only be classified in Q1 or Q4. The $PM_{2.5}$ concentration at PEAV on September 27 was below the 25th percentile concentration for this sample period. October 17, 2014 quadrants for UNRG and WCAQ would have been different based on $PM_{2.5}$ concentrations above the 8.8 μg m^{-3} threshold at UNRG and below the threshold at WCAQ. The sources and physical processes identified in Q4 were difficult to reconcile with measurements in the valley and at the high elevation site.

>50th percentile Eurasian Pb		2014 June 6	July 25	August 7	September 22	September 26	2015 June 8	September 2
UNRG	Quadrant	Q1	Q1	Q3	Q3	NA	Q1	Q2
	$PM_{2.5}$	8.7	5.7	18	63	1.9	4.6	10
WCAQ	Quadrant	Q1	Q1	Q3	Q3	NA	Q1	Q2
	$PM_{2.5}$	7.8	5.2	16	62	5.3	6.3	11
PEAV	$PM_{2.5}$	7.1	1.3	15	42	NA	NA	NA
τ_{ext}		0.099	0.052	0.32	0.40	NA	0.074	0.083
PBLH		3.2	2.6	1.8	2.6	1.1	0.98	2.9
AOH		4.2	NA	NA	1.4	NA	4.7	1.8

>75th percentile Eurasian Pb		2014 June 12	September 27	October 9	October 17	2015 June 9
UNRG	Quadrant	Q1	NA	Q1	NA	Q1
	$PM_{2.5}$	8.4	2.7	4.9	10	7.0
WCAQ	Quadrant	Q1	NA	Q1	NA	Q1
	$PM_{2.5}$	6.3	4.3	2.6	8.3	7.1
PEAV	$PM_{2.5}$	NA	1.7	3.4	5.6	NA
τ_{ext}		0.063	NA	0.036	NA	0.082
PBLH		1.9	0.92	2.2	0.31	1.7
AOH		3.6	NA	2.3	3.9	1.5

Table 4: Days with > 50th percentile and > 75th percentile values for Eurasian lead (Pb) indicating days with high trans-Pacific influence.

5. Conclusions

The purpose of this study was to investigate the horizontal and vertical pollution gradients affecting three sites in Reno, NV, USA. Horizontal gradients of criteria air pollutants were characterized to determine the impact of different air pollution sources in the Truckee Meadows Valley. The quadrant method was then applied to 24 h τ_{ext} and $PM_{2.5}$ observations using meteorological variables, aerosol optical properties, vertical structure of the atmosphere, measures of atmospheric stability, and ozone concentrations to identify four specific conditions affecting the relationship between columnar and surface aerosol concentrations.

The site observations (Table 2) indicated that sites further from the highways had statistically lower concentrations of primary pollutants and higher concentrations of secondary pollutants and pollutants from non-point sources. This horizontal gradient is important for understanding exposure to near-road pollutants. The U.S. EPA monitors

near-road pollutants (CO and $PM_{2.5}$) in a limited capacity in cities with > 500,000 people (Batterman, 2013; EPA, 2016); however, smaller metropolitan areas such as Reno, NV, USA will also experience significant pollutant gradients near heavily traveled roads. Diel patterns for Q1 data show that pollutants from the morning commute (Fig. 6) affect both valley sites.

Similarities in the results of the statistical analysis for the quadrants for 1 h vs 24 h data at WCAQ (Table 3) support using the quadrant method for 24 h data, with several limitations. First, retrievals of AERONET τ_{ext} was not possible at all three sites, necessitating the use of τ_{ext} from UNR for the two valley sites to perform columnar versus surface comparisons. Second, retrievals of τ_{ext} only occur during daylight hours and comparing a daily τ_{ext} average to 24 h $PM_{2.5}$ measurements may make quadrant classification for 24 h data less accurate than for 1 h data, this is particularly important for days with partial cloud cover. Third, use of 24 h data reduces the number of data points and therefore reduces the power of the statistical testing, longer sample periods are necessary. Fourth, retrieval of τ_{ext} only occurs during clear sky periods, which excludes a large amount of winter and spring data, particularly in the Western USA. Interference from clouds may also cause issues with hourly data, if a 1 h period does not have enough data available it may not be representative of the conditions in that hour. Hourly data used for the quadrant method in future studies, like the 24 h data in this study, should have a restriction on the data used if a certain percentage of the data is not available.

Evaluating the results of the statistical analysis of the quadrants, using valley and peak sample sites in Reno, NV, USA indicated that the quadrant method is applicable for understanding τ_{ext} and $PM_{2.5}$ relationships for 24 h data. Use of the quadrant method for

24 h $PM_{2.5}$ data could improve the application of this method over a larger spatial extent in rural and remote areas, such as National Parks and Wilderness Areas where conditions influencing atmospheric pollution are not well quantified (Fine et al, 2015a; Mioduszewski et al, 2011). Use of the quadrant method to characterize concentrations of gases (e.g. O_3), based on the relationship between columnar and surface aerosol observations was also demonstrated.

The quadrant method, used for all available 24 h data from UNRG and WCAQ, identified four quadrants with different sources and physical processes. Quadrant 1 contained a majority of the data, had low measures of atmospheric stability, and was dominated by local sources of pollution in a well-mixed PBL. Quadrant 2 had the highest measures of atmospheric stability and temperature inversions. The use of measures of atmospheric stability in the quadrant method for understanding processes affecting atmospheric pollutants during periods when τ_{ext} and $PM_{2.5}$ were not associated was demonstrated. Quadrant 3 had the highest $PM_{2.5}$, AEE, fire flags, and was the only quadrant dominated by fine mode aerosols. Measurements at PEAV supported the conclusion that wildfire plumes influenced this quadrant. Quadrant 4 had low measures of atmospheric stability and aerosols higher in the atmospheric column than the PBLH, indicating pollution aloft. Because spring data was minimal, a time when an increase in pollution aloft due to frontal activity and long-range transport, data from a previous study was used to identify periods of trans-Pacific input. The sources and processes identified in Q4 were difficult to reconcile with measurements in the valley and at the high elevation site, particularly without enough data. It may be necessary to identify another variable for future studies that would better characterize pollution aloft.

The mix of complex terrain, long-range transport, and wildfires can make quadrant classification for specific events difficult to resolve. Q1 and Q4 results are confounded by the fact that during summer and fall, when convective mixing is high, there is a semi-continuous contribution of trans-Pacific pollution (VanCuren, 2003; VanCuren et al, 2005), but in low enough concentrations or present in filamentous air masses, that it may not be easily distinguishable from local pollutants. Wildfire plumes traveling aloft will also be difficult to separate between Q3 and Q4. Differences in the quadrant results between the current and previous study, with a site in common, highlight the importance of topography, local sources, and the locations of the τ_{ext} instrument in relation to the location of the $PM_{2.5}$ instrument. Ideally, τ_{ext} and surface $PM_{2.5}$ observations should be collocated to characterize the specific processes affecting observations at a site.

Using τ_{ext} and surface $PM_{2.5}$ observations, aids in performing statistical investigations of the atmospheric processes affecting the transport of aerosols in complex terrain. The 24 h data threshold values for τ_{ext} and $PM_{2.5}$ need to be site specific to identify clean or polluted periods and the sources and physical processes affecting different sites, particularly in diverse topographic surroundings. Future studies should focus on sites in the intermountain west with different elevations and during different fire regimes. A better understanding of these relationships will help to improve the use of satellite τ_{ext} retrievals for estimating surface $PM_{2.5}$ conditions over large spatial scales. Furthermore, identifying measurement periods affected by specific processes, such as wildfires and temperature inversions, will aid regulatory agencies in identifying controllable and non-controllable pollution events.

Acknowledgments:

We acknowledge the Nevada Division of Environmental Protection (NDEP), the UNR College of Agriculture, Biotechnology, and Natural Resources, and a USDA-HATCH grant (NIFA Accession# NEV05295) for supporting this project. Balloon sounding data is available from Atmospheric Soundings Wyoming Weather Web. Thank you to Dr. Rebekka Fine for initial research on the TAPI Beta^{Plus} particulate measurement systems for use in this project; to Matthieu Miller for site support, data collection, and processing; to Dave Metts for allowing access to and support at the Peavine Peak site; and to Kristien King for assistance with data processing.

References:

Batterman, S. (2013) The Near-Road Ambient Monitoring Network and Exposure Estimates for Health Studies. *EM (Pittsburgh, Pa.)*, 2013(7), 24-30.
Bergin, M. H., Schwartz, S. E., Halthore, R. N., Ogren, J. A. & Hlavka, D. L. (2000) Comparison of aerosol optical depth inferred from surface measurements with that determined by Sun photometry for cloud-free conditions at a continental U.S. site. *Journal of Geophysical Research: Atmospheres*, 105(D5), 6807-6816.
CA, S. o. C. G. (2017) *2014 Large Fires List*, 2017. Available online: http://cdfdata.fire.ca.gov/incidents/incidents_statsevents#2014 [Accessed.
Campbell, J. R., Welton, E. J., Spinhirne, J. D., Ji, Q., Tsay, S.-C., Piketh, S. J., Barenbrug, M. & Holben, B. N. (2003) Micropulse lidar observations of tropospheric aerosols over northeastern South Africa during the ARREX and SAFARI 2000 dry season experiments. *Journal of Geophysical Research: Atmospheres*, 108(D13), n/a-n/a.
Chemel, C., Arduini, G., Staquet, C., Largeron, Y., Legain, D., Tzanos, D. & Paci, A. (2016) Valley heat deficit as a bulk measure of wintertime particulate air pollution in the Arve River Valley. *Atmospheric Environment*, 128, 208-215.
Chen, L. W. A., Watson, J. G., Chow, J. C., Green, M. C., Inouye, D. & Dick, K. (2012) Wintertime particulate pollution episodes in an urban valley of the Western US: a case study. *Atmos. Chem. Phys.*, 12(21), 10051-10064.
Colvile, R. N., Hutchinson, E. J., Mindell, J. S. & Warren, R. F. (2001) The transport sector as a source of air pollution. *Atmospheric Environment*, 35(9), 1537-1565.
Cooper, O., R., Parrish, D., D., Stohl, A., Trainer, M., Nedelec, P. & Thouret, V. C., J. P. Oltmans, S. J. Johnson, B. J. Tarasick, D. Leblanc, T. McDermid, I. S. Jaffe, D. Gao, R. Stith, J. Ryerson, T. Aikin, K. Campos, T. Weinheimer, A. Avery, M. A. (2010) Increasing springtime ozone mixing ratios in the free troposphere over western North America. *Nature*, 463(7279), 344-348.
Corbin, K. C., Kreidenweis, S. M. & Vonder Haar, T. H. (2002) Comparison of aerosol properties derived from Sun photometer data and ground-based chemical measurements. *Geophysical Research Letters*, 29(10), 1-1-1-3.
Crosbie, E., Sorooshian, A., Monfared, N. A., Shingler, T. & Esmaili, O. (2014) A Multi-Year Aerosol Characterization for the Greater Tehran Area Using Satellite, Surface, and Modeling Data. *Atmosphere*, 5(2), 178-197.
Eck, T. F. (2010) AERONET—An internationally federated network, *aerosol observability workshop*. Monterey, CA, USA.
Eck, T. F., Holben, B. N., Reid, J. S., Dubovik, O., Smirnov, A., O'Neill, N. T., Slutsker, I. & Kinne, S. (1999) Wavelength dependence of the optical depth of biomass burning, urban, and desert dust aerosols. *Journal of Geophysical Research: Atmospheres*, 104(D24), 31333-31349.
Engel-Cox, J. A., Holloman, C. H., Coutant, B. W. & Hoff, R. M. (2004) Qualitative and quantitative evaluation of MODIS satellite sensor data for regional and urban scale air quality. *Atmospheric Environment*, 38(16), 2495-2509.
EPA (2016) *Near-road NO2 Monitoring*, 2016. Available online: https://www3.epa.gov/ttnamti1/nearroad.html [Accessed.
EPA, U. (2017a) *AirData PM2.5 Continuous Monitor Comparability Assessments*, 2017a. Available online: http://www.epa.gov/airquality/airdata/ad_rep_frmvfem.html [Accessed.
EPA, U. S. E. P. A. (2017b) *Exceptional events documents ozone - Washoe, NV*, 2017b. Available online: https://www.epa.gov/air-quality-analysis/exceptional-events-documents-ozone-washoe-nv [Accessed.

Fernando, H. J. S. (2010) Fluid Dynamics of Urban Atmospheres in Complex Terrain. *Annual Review of Fluid Mechanics*, 42(1), 365-389.
Fine, R., Miller, M. B., Yates, E. L., Iraci, L. T. & Gustin, M. S. (2015) Investigating the influence of long-range transport on surface O3 in Nevada, USA, using observations from multiple measurement platforms. *Science of The Total Environment*, 530–531(0), 493-504.
Fiore, A. M., Oberman, J. T., Lin, M. Y., Zhang, L., Clifton, O. E., Jacob, D. J., Naik, V., Horowitz, L. W., Pinto, J. P. & Milly, G. P. (2014) Estimating North American background ozone in U.S. surface air with two independent global models: Variability, uncertainties, and recommendations. *Atmospheric Environment*, 96(0), 284-300.
Green, M. C., Chow, J. C., Watson, J. G., Dick, K. & Inouye, D. (2015) Effects of Snow Cover and Atmospheric Stability on Winter PM2.5 Concentrations in Western U.S. Valleys. *Journal of Applied Meteorology and Climatology*, 54(6), 1191-1201.
Gupta, P., Christopher, S. A., Wang, J., Gehrig, R., Lee, Y. & Kumar, N. (2006) Satellite remote sensing of particulate matter and air quality assessment over global cities. *Atmospheric Environment*, 40(30), 5880-5892.
Gustin, M. S., Fine, R., Miller, M., Jaffe, D. & Burley, J. (2015) The Nevada Rural Ozone Initiative (NVROI): Insights to understanding air pollution in complex terrain. *Science of The Total Environment*, 530–531(0), 455-470.
Gustin, M. S., Huang, J., Miller, M. B., Peterson, C., Jaffe, D. A., Ambrose, J., Finley, B. D., Lyman, S. N., Call, K., Talbot, R., Feddersen, D., Mao, H. & Lindberg, S. E. (2013) Do We Understand What the Mercury Speciation Instruments Are Actually Measuring? Results of RAMIX. *Environmental Science & Technology*, 47(13), 7295-7306.
Hao H., Chang H. H., Holmes H.A., Mulholland J. A., Klein M., Darrow L. A. & J.., S. M. (2016) Air pollution and preterm birth in the U.S. state of Georgia (2002–2006): associations with concentrations of 11 ambient air pollutants estimated by combining Community Multiscale Air Quality Model (CMAQ) simulations with stationary monitor measurements. *Environmental Health Perspectives*, 124(6), 875–880.
HEI, H. E. I. (2010) *Traffic-related air pollution: A Critical review of the literature on emissions, exposure, and health effects*.Boston, MA.
Holben, B. N., Eck, T. F., Slutsker, I., Tanré, D., Buis, J. P., Setzer, A., Vermote, E., Reagan, J. A., Kaufman, Y. J., Nakajima, T., Lavenu, F., Jankowiak, I. & Smirnov, A. (1998) AERONET—A Federated Instrument Network and Data Archive for Aerosol Characterization. *Remote Sensing of Environment*, 66(1), 1-16.
Holzworth, G. C. (1964) Estimates of mean maximum mixing depths in the contiguous United States. *Monthly Weather Review*, 92(5), 235-242.
Jacob, D. J., Logan, J. A. & Murti, P. P. (1999) Effect of rising Asian emissions on surface ozone in the United States. *Geophysical Research Letters*, 26(14), 2175-2178.
Karner, A. A., Eisinger, D. S. & Niemeier, D. A. (2010) Near-Roadway Air Quality: Synthesizing the Findings from Real-World Data. *Environmental Science & Technology*, 44(14), 5334-5344.
Langford, A. O., Senff, C. J., Alvarez Ii, R. J., Brioude, J., Cooper, O. R., Holloway, J. S., Lin, M. Y., Marchbanks, R. D., Pierce, R. B., Sandberg, S. P., Weickmann, A. M. & Williams, E. J. (2015) An overview of the 2013 Las Vegas Ozone Study (LVOS): Impact of stratospheric intrusions and long-range transport on surface air quality. *Atmospheric Environment*, 109(0), 305-322.
Lee, H. J., Chatfield, R. B. & Strawa, A. W. (2016) Enhancing the Applicability of Satellite Remote Sensing for PM2.5 Estimation Using MODIS Deep Blue AOD and Land Use Regression in California, United States. *Environmental Science & Technology*, 50(12), 6546-6555.

Levy, R. C., Mattoo, S., Munchak, L. A., Remer, L. A., Sayer, A. M., Patadia, F. & Hsu, N. C. (2013) The Collection 6 MODIS aerosol products over land and ocean. *Atmos. Meas. Tech.*, 6(11), 2989-3034.

Lewis, K., Arnott, W. P., Moosmüller, H. & Wold, C. E. (2008) Strong spectral variation of biomass smoke light absorption and single scattering albedo observed with a novel dual-wavelength photoacoustic instrument. *Journal of Geophysical Research: Atmospheres*, 113(D16), n/a-n/a.

Li, J., Carlson, B. E. & Lacis, A. A. (2015) How well do satellite AOD observations represent the spatial and temporal variability of PM2.5 concentration for the United States? *Atmospheric Environment*, 102, 260-273.

Lin, M., Fiore, A. M., Horowitz, L. W., Cooper, O. R., Naik, V., Holloway, J., Johnson, B. J., Middlebrook, A. M., Oltmans, S. J., Pollack, I. B., Ryerson, T. B., Warner, J. X., Wiedinmyer, C., Wilson, J. & Wyman, B. (2012) Transport of Asian ozone pollution into surface air over the western United States in spring. *Journal of Geophysical Research: Atmospheres*, 117(D21), D00V07.

Liu, Y., Paciorek, C. J. & Koutrakis, P. (2009) Estimating Regional Spatial and Temporal Variability of PM(2.5) Concentrations Using Satellite Data, Meteorology, and Land Use Information. *Environmental Health Perspectives*, 117(6), 886-892.

Loria-Salazar, M. S., Arnott, P. W. & Moosmuller, H. (2014) Accuracy of near-surface aerosol extinction determined from columnar aerosol optical depth measurements in Reno. *Journal of Geophysical Research: Atmospheres*, 119(19), 355-374.

Loría-Salazar, S. M., Holmes, H. A., Patrick Arnott, W., Barnard, J. C. & Moosmüller, H. (2016) Evaluation of MODIS columnar aerosol retrievals using AERONET in semi-arid Nevada and California, U.S.A., during the summer of 2012. *Atmospheric Environment*, 144(Supplement C), 345-360.

Loría-Salazar, S. M., Panorska, A., Arnott, W. P., Barnard, J. C., Boehmler, J. M. & Holmes, H. A. (2017) Toward understanding atmospheric physics impacting the relationship between columnar aerosol optical depth and near-surface PM2.5 mass concentrations in Nevada and California, U.S.A., during 2013. *Atmospheric Environment*, 171(Supplement C), 289-300.

Loría-Salazar, S. M. a. A. W. P. a. M. H. (2014) Accuracy of near-surface aerosol extinction determined from columnar aerosol optical depth measurements in Reno, NV, USA. *Journal of Geophysical Research: Atmospheres*, 119(19), 11,355--11,374.

McMurdie, W. L. & Houze, R. A. (2006) 8 - Weather Systems, *Atmospheric Science (Second Edition)*. San Diego: Academic Press, 313-373.

Miller, M. B., Fine, R., Pierce, A. M. & Gustin, M. S. (2015) Identifying sources of ozone to three rural locations in Nevada, USA, using ancillary gas pollutants, aerosol chemistry, and mercury. *Science of The Total Environment*, 530–531(0), 483-492.

Nguyen, T. K. V., Ghate, V. P. & Carlton, A. G. (2016) Reconciling satellite aerosol optical thickness and surface fine particle mass through aerosol liquid water. *Geophysical Research Letters*, 43(22), 11,903-11,912.

NV, S. o. N. D. o. W. R. (2017) *Appendix A-4--Nevada Hydrographic Regions, Areas, and Sub-Areas*, 2017. Available online: http://water.nv.gov/programs/planning/dictionary/appd-A4.pdf [Accessed.

Parmar, R. S., Welling, M., Andreae, M. O. & Helas, G. (2008) Water vapor release from biomass combustion. *Atmos. Chem. Phys.*, 8(20), 6147-6153.

Pierce, A. M. & Gustin, M. S. (2017) Development of a Particulate Mass Measurement System for Quantification of Ambient Reactive Mercury. *Environmental Science & Technology*, 51(1), 436-445.
Pierce, A. M., Gustin, M. S., Christensen, J. N. & Loría-Salazar, S. M. (2017) Use of multiple tools including lead isotopes to decipher sources of ozone and reactive mercury to urban and rural locations in Nevada, USA. *Science of The Total Environment*, 615(Supplement C), 1411-1427.
Riley, E. A., Banks, L., Fintzi, J., Gould, T. R., Hartin, K., Schaal, L., Davey, M., Sheppard, L., Larson, T., Yost, M. G. & Simpson, C. D. (2014) Multi-pollutant mobile platform measurements of air pollutants adjacent to a major roadway. *Atmospheric Environment*, 98(Supplement C), 492-499.
Seibert, P., Beyrich, F., Gryning, S.-E., Joffre, S., Rasmussen, A. & Tercier, P. (2000) Review and intercomparison of operational methods for the determination of the mixing height. *Atmospheric Environment*, 34(7), 1001-1027.
Silcox, G. D., Kelly, K. E., Crosman, E. T., Whiteman, C. D. & Allen, B. L. (2012) Wintertime PM2.5 concentrations during persistent, multi-day cold-air pools in a mountain valley. *Atmospheric Environment*, 46, 17-24.
Sorek-Hamer, M., Cohen, A., Levy, R. C., Ziv, B. & Broday, D. M. (2013) Classification of dust days by satellite remotely sensed aerosol products. *International Journal of Remote Sensing*, 34(8), 2672-2688.
Sorek-Hamer, M., Kloog, I., Koutrakis, P., Strawa, A. W., Chatfield, R., Cohen, A., Ridgway, W. L. & Broday, D. M. (2015) Assessment of PM2.5 concentrations over bright surfaces using MODIS satellite observations. *Remote Sensing of Environment*, 163(Supplement C), 180-185.
Stohl, A., Bonasoni, P., Cristofanelli, P., Collins, W., Feichter, J., Frank, A., Forster, C., Gerasopoulos, E., Gäggeler, H., James, P., Kentarchos, T., Kromp-Kolb, H., Krüger, B., Land, C., Meloen, J., Papayannis, A., Priller, A., Seibert, P., Sprenger, M., Roelofs, G. J., Scheel, H. E., Schnabel, C., Siegmund, P., Tobler, L., Trickl, T., Wernli, H., Wirth, V., Zanis, P. & Zerefos, C. (2003) Stratosphere-troposphere exchange: A review, and what we have learned from STACCATO. *Journal of Geophysical Research: Atmospheres*, 108(D12), 8516.
Stull, R. B. (1988) *An Introduction to Boundary Layer Meteorology*Springer Netherlands.
TAPI, T. A. P. I. (2012) Operation Manula: Model 602 BETA PLUS particle measurement system. San Diego, CA: Teledyne Advanced Pollution Instrumentation.
VanCuren, R. A. (2003) Asian aerosols in North America: Extracting the chemical composition and mass concentration of the Asian continental aerosol plume from long-term aerosol records in the western United States. *Journal of Geophysical Research: Atmospheres*, 108(D20), 4623.
VanCuren, R. A., Cliff, S. S., Perry, K. D. & Jimenez-Cruz, M. (2005) Asian continental aerosol persistence above the marine boundary layer over the eastern North Pacific: Continuous aerosol measurements from Intercontinental Transport and Chemical Transformation 2002 (ITCT 2K2). *Journal of Geophysical Research: Atmospheres*, 110(D9), D09S90.
Vingarzan, R. (2004) A review of surface ozone background levels and trends. *Atmospheric Environment*, 38(21), 3431-3442.
Washoe County, N. (2012) *2011 Periodic Emissions Inventory*.
Whiteman, C. D., Bian, X. & Zhong, S. (1999) Wintertime Evolution of the Temperature Inversion in the Colorado Plateau Basin. *Journal of Applied Meteorology*, 38(8), 1103-1117.
Whiteman, C. D., Hoch, S. W., Horel, J. D. & Charland, A. (2014) Relationship between particulate air pollution and meteorological variables in Utah's Salt Lake Valley. *Atmospheric Environment*, 94(0), 742-753.

Whiteman, C. D., Zhong, S., Shaw, W. J., Hubbe, J. M., Bian, X. & Mittelstadt, J. (2001) Cold Pools in the Columbia Basin. *Weather and Forecasting*, 16(4), 432-447.
WHO, W. H. O. (2017) *Urban Population Growth*, 2017. Available online: http://www.who.int/gho/urban_health/situation_trends/urban_population_growth_text/en/ [Accessed.
www.census.gov (2017) *USA Census,*, 2017. Available online: http://quickfacts.census.gov/qfd/states/32000.html [Accessed.

Chapter 5

Superaggregates or instrument artifact?

Ashley M. Pierce[1], S. Marcela Loría-Salazar[2], W. Patrick Arnott[2], Grant C. Edwards[3], Matthieu B. Miller[3], Mae Sexauer Gustin[1]

[1]Department of Natural Resources and Environmental Sciences, University of Nevada Reno, NV, USA 89557
[2]Atmospheric Science Program, Department of Physics, University of Nevada Reno, NV, USA 89557
[3]Department of Environmental Sciences, Faculty of Science and Engineering, Macquarie University, Sydney, New South Wales, Australia

Correspondence to: Ashley M. Pierce (ash.pie4@gmail.com)

Submitted: *Atmospheric Measurement Techniques*

Abstract. Previous studies have indicated that superaggregates, clusters of aggregates of soot primary particles, can be formed in large-scale turbulent fires. High intensity fires may also produce the right circumstances to inject plumes into the upper troposphere and lower stratosphere during pyrocumulonimbus thunderstorms, where the superaggregates can then be transported long distances. Due to lower effective densities, higher porosity, and lower aerodynamic diameters, superaggregates may be deposited past inlets designed to stop particles < 2.5 μm in aerodynamic diameter ($PM_{2.5}$). Ambient particulate matter samples were collected at Peavine Peak, NV, USA (2515 m) northwest of Reno, NV, USA from June to November 2014. The Teledyne Advanced Pollution Instrumentation (TAPI) 602 Beta^{Plus} particulate monitor was used to collect $PM_{2.5}$ on two filter types. During this time, particles > 2.5 μm in aerodynamic diameter were collected on 36 days. On preliminary analysis, it was thought that these particles were superaggregates, depositing past PM_{10} (particles < 10 μm in aerodynamic diameter) pre-impactors and $PM_{2.5}$ cyclones. However, further analysis revealed that these particles were dissimilar to superaggregates observed in previous studies. To determine if the particles were superaggregates or an instrument artifact, elemental analysis, presence of fires, high relative humidity and wind speeds, as well as the use of generators onsite were investigated. Samples with aggregates were analyzed using a scanning electron microscope for size and shape of the aggregates and energy-

dispersive x-ray spectroscopy was used for elemental analysis. It was determined that a sampling artifact associated with sample inlet setup and prolonged, high wind events were the probably reason for the observed aggregates.

1 Introduction

When primary particles collide and stick together, agglomerates or aggregates can form, creating complex structures (Kulkarni et al, 2011a). Agglomerate particles can be categorized as branched-chain or compact aggregates (Kulkarni et al, 2011a). Branched-chain particles with internal voids between branches and compact aggregates with internal voids have mass equivalent diameters that are less than the volume equivalent diameter, which implies lower densities than an equivalent ideal spherical particle (Kulkarni et al, 2011a). Soot particles are fractal-like, chain aggregates produced from incomplete combustion (Kulkarni et al, 2011a; Wang et al, 2017). Large-scale turbulent fires provide vortices where soot aggregates (~100s of monomers) can be trapped in a high particle volume fraction, creating superaggregates consisting of thousands of monomers (Chakrabarty et al, 2014; Kearney & Pierce, 2012; Kulkarni et al, 2011a). Large, turbulent fires can cause pyrocumulonimbus thunderstorm formation, which promote injection of superaggregates into the upper troposphere and lower stratosphere where they can then be transported long distances (Fromm et al, 2010; Peterson et al, 2014; Peterson, 2014). Superaggregates tend to have larger lengths and mobility diameters than smaller particles; however, they have low aerodynamic diameters (a measure of their terminal settling velocity), lower effective

densities, and are more porous, causing different behavior than primary particles or smaller aggregates (Chakrabarty et al, 2014; Kulkarni et al, 2011a).

Superaggregates were observed, from several wildfires in Chakrabarty et al. (2014) and from a laboratory fire in Kearney and Pierce (2012), with fractal dimensions (D_f) of ~2.6 and lengths of 10 to 20 μm (Chakrabarty et al, 2014; Kearney & Pierce, 2012). These superaggregates had "wispy" or "fluffy" appearances when observed using a scanning electron microscope (SEM, Chakrabarty et al, 2014; Kearney & Pierce, 2012). The elemental composition, using energy-dispersive x-ray spectroscopy (EDS), was found to be mainly carbon and oxygen (Chakrabarty et al, 2014).

Superaggregates are of concern due to the mobility of the particles. In Chakrabarty (2014), superaggregates were collected in the third stage of an aerosol impactor with a cut point of < 0.3 μm aerodynamic diameter (D_a). Measurement of superaggregates would therefore require different size conventions, beyond the widely used aerodynamic diameter, for detection and measurement (Chakrabarty et al, 2014; Marple & Olson, 2011). From a health perspective, these aerosols could also be deposited deep in the lungs of organisms (John, 2011; Kleinstreuer & Zhang, 2009). The optical properties of the superaggregates are also different, due to the complex morphology, and may contribute 90% more atmospheric warming compared to a

volume-equivalent Mie-sphere (Chakrabarty et al, 2014; Sorensen et al, 2011), requiring models to adjust estimates of climate forcing.

Ambient particulate matter (PM) samples were collected as part of a project to develop and apply a new particulate monitor configured for the measurement of atmospheric mercury (Hg) and lead (Pb) isotopes (Pierce & Gustin, 2016; Pierce et al, 2017). One Teledyne Advanced Pollution Instrumentation (TAPI) 602 Beta^{Plus} particulate monitor was located at Peavine Peak, NV, USA (PEAV, 2515 m) and another TAPI was located ~12 km southeast in Reno, NV, USA (UNRG, 1367 m), to collect particles < 2.5 µm in aerodynamic diameter ($PM_{2.5}$). During the sampling campaign, when instruments were deployed simultaneously at PEAV and UNRG, June to November of 2014, 36 days had particles > 2.5 µm in aerodynamic diameter on sample filters at PEAV, but these were not observed at the lower elevation site (Table 1, Fig. 1 and 2). A season of drought leading to high intensity wildfires in the Western USA (CA, 2017) resulted in numerous smoke events, and preliminary images of the filters with SEM seemed to support the hypothesis that these particles were fire-generated superaggregates (Fig. 3). The observation of aggregates that did not conform to the description of superaggregates from previous studies led us to wonder if the observed aggregates may in fact be an artifact of the instrument setup and not an ambient air phenomenon. Possible explanations for the aggregates, including elemental

composition, presence of fires and fire indicators, correlations with relative humidity (RH) and wind speed, as well as the use of generators onsite, were investigated. SEM and EDS were used to determine the shape and elemental composition. This paper presents the results of this investigation and the most probable cause for the observed aggregates.

2 Site descriptions

The Peavine Peak, NV, USA (PEAV, 2515 m asl, 39.5895 N, -119.9290 W) measurement site was located above tree line in a sage/steppe ecosystem at the summit, ~15 km east of the Sierra Nevada Mountain range and ~12 km northwest of downtown Reno, NV, USA. The measurement trailer was located within a fenced area that also contained a radio and cellular relay station. The fence restricted unauthorized visitors from approaching within ~15 m of the measurement trailer. There were weekly visits to the site for maintenance of the relay station. There is one dirt road that leads up to the site from the southwest, all other dirt roads and trails are >500 m away from the site and lower in elevation. Traffic in the area consists of off-road gas and diesel vehicles (trucks, ATVs, and dirt bikes), as well as non-motorized traffic. Back-up power diesel generators, for the relay station, were periodically operated at the site. During June to

October 2014, PEAV was, on average, within the planetary boundary layer from the valley and was influenced by upslope mixing from the valley and free tropospheric air (Pierce et al, 2017). In November 2014, the average planetary boundary layer height was below PEAV and thus, air from the free troposphere primarily influenced the site.

The lower elevation site was located near the valley floor at the University of Nevada, Reno Greenhouse complex (UNRG) at the Nevada Agricultural Experiment Station Greenhouse Facility (1367 m asl, 39.5374 N, -119.8044 W) in Reno, NV, USA near the intersection of two major highways, Interstate-80 and Interstate-580 (U.S. Route 395). UNRG and PEAV are ~1 km different in elevation.

Great Basin National Park, NV (GBNP, 2061 m asl, 39.0052 N, -114.2161 W) is located on the eastern side of Nevada. Measurements occurred from March to October 2015. The measurement trailer was collocated with a Clean Air Statuses and Trends Network (CASTNET) site.

3 Instrumentation and data sources

3.1 Particulate measurements

The TAPI was configured to measure $PM_{2.5}$ through two separate inlets each with a 10 μm pre-impactor (FAI Instrument S.R.L. Fonte Nuova, Rome) and a 2.5 μm

cyclone (VSCC-A, BGI inc. Waltham, Ma, USA) in-line to prevent particles < 2.5 μm in aerodynamic diameter from continuing in the sample stream (Fig 4). Ambient air was sampled at 16.7 Lpm for 24 h (00:00 to 00:00 PST) simultaneously through two filter mediums: 47 mm cation exchange membranes (CEM; Pall Corporation, PN: MSTGS3R, Line A), and 47 mm Teflon (Pall Corporation, PN: EW-36329-08, Line B). Particulate matter mass concentration on the filters was measured using β attenuation (Sohirripa Spagnolo, 1987). At 24 h resolution the TAPI has a detection limit of 0.3 μg m^{-3} (TAPI, 2012). CEM filters were destructively analyzed for total Hg (Pierce & Gustin, 2017), Teflon filters were used for Pb isotope (Pierce et al, 2017) and aggregate analysis. Teflon membranes are made of polytetrafluoroethylene (PTFE), a hydrophobic fluorocarbon.

Inlets were connected to the instrument by 2.1 m (CEM filter line) and 1.7 m (Teflon filter line) anodized aluminum sample tubes (2.54 cm outer diameter), supplied with the instrument, that passed into the temperature-controlled trailer to the TAPI housed inside (Fig. 4). Inside the temperature-controlled trailer, the sample lines connected to condensation water traps on each line to collect any water droplets that formed on the inside of the sample tubes due to condensation. Just below the condensation water traps were sample line heaters (Fig. 4). The sample line heaters on each line were set to only heat the line if the RH in the sample air stream exceeded 40%

RH and would stop heating once the RH reached 30%. A CEM reference filter was also used automatically throughout the sample process to account for humidity effects on the sample filters (TAPI, 2012).

The pressure drop across the CEM filters was higher than the pressure drop across the Teflon filters due to difference in material. The higher-pressure drop on the CEM filters (Pierce & Gustin, 2017; TAPI, 2012) necessitated a different sample line inlet nozzle (located where the sample line enters the TAPI measurement box, Fig. 4), tested and adjusted by Teledyne before the instruments were operated. The inlet nozzle was therefore a different size (smaller in diameter) for the CEM sample line (0.75 cm diameter) compared to the Teflon sample line (1.9 cm diameter) and may have caused different flow dynamics for the CEM sample line. Constrictions in sample air flow causes gases in the sample stream to increase in velocity and focus in the center of the tube, this dynamic causes increased particle deposition (Kulkarni et al, 2011b). The different inlet nozzle sizes required a different β sample area (CEM: 4.7 cm^2 β sample area, Teflon: 12 cm^2 β sample area), or the area of the filter used for β attenuation. The filters were supported in different filter cartridges for the CEM and Teflon filters due to the difference in β sample area. Filters were automatically loaded and unloaded, and then held in an unloader tube until collection every 1 to 2 weeks. Sample inlets were

cleaned monthly, following instructions from the instrument manual, and pumps were rebuilt every 6 to 8 months.

Calibration of the operating flow rate regulation system, β source span checks, and pneumatic circuit leak tests automatically occurred at the start of each sampling period for both sample lines. There were three days during the sample period in October 2014 when data validation was not passing after the automatic tests were performed. These days are discussed in sect. 4.5. On 25 days, of 158 in the sample period, there were warnings related to pump valve, span tests, leak tests, or internal cooling fan failure. These warnings cleared and the sample passed data validation for the day. Six days with warnings occurred on days with aggregates. Four days, June 13, 16, 19, and September 16, were pneumatic leak test warnings; 2 days, September 18 and 23, were pump valve warnings. Aggregates on the June warning days occurred only on the CEM inlet, aggregates on the September warning days occurred on both inlets.

3.2 Shape, size, and elemental composition

Teflon filters were analyzed at Macquarie University in Sydney, Australia using a scanning electron microscope (SEM, JEOL USA Inc. model: 6480 LA, Peabody, MA, USA) for size, shape, and elemental composition. Preliminary SEM analysis was performed with backscattered electron imaging on un-coated filter segments in low

vacuum to avoid charging and breakdown of the aggregates. Elemental analysis using energy-dispersive x-ray spectroscopy (EDS) was also performed with backscattered electron imaging in low vacuum mode. A second SEM analysis with secondary electron imaging, using a different filter segment from the initial SEM, was performed with gold coating, to prevent charging during analysis in high vacuum. The second SEM analysis was a more in depth exploration of the morphology of the aggregates.

3.3 Fire indicators using aerosol optical properties

Aerosol Optical Depth (AOD, 440 nm) and Ångström Extinction Exponent (AEE, 440-870 nm) were collected from a Cimel (CE-318) sun photometer used in the AErosol RObotic NETwork, located at the University of Nevada, Reno (UNR) campus on top of a four-story building (Loría-Salazar et al, 2017; Loría-Salazar, 2014). One hour data were collected and averaged for 24 h. AOD is a measure of the columnar aerosol loading and when compared with surface $PM_{2.5}$ measurements can aid in identifying periods of wildfires (Loría-Salazar et al, 2017). AEE is used as a qualitative indicator of particle size; AEE ~ 1 is indicative of coarse mode aerosols (i.e. dust and sea salt) while AEE $\geq$ 2 is indicative of fine mode aerosols from biomass burning or urban pollution (Eck et al., 1999). Data with AEE >1.8 were flagged as fire periods (Loría-Salazar et al, 2016).

3.4 Meteorological data

At PEAV, RH was measured by an HMP45c model Campbell Scientific RH monitor (± 0.2 ºC and ± 2% RH), wind speed was measured by an RM Young 05305 wind vane (± 0.2 m s^{-1}). Wind speed at UNRG was collected from the Western Regional Climate Center. Wind speed at GBNP was collected from the CASTNET site. Hourly meteorological data was used for 1 h max values and 2 h averages.

3.5 Generator use

From October 20 (Monday) to October 24 (Friday), multiple diesel generators were operated at PEAV while maintenance was occurring on the power lines at the relay station. A back-up power, diesel generator was also located on site and was operated periodically throughout the sample period. The back-up generator was located ~10 m southeast and around the corner of the relay station building from the measurement trailer. Exact timing of back-up generator use is not available.

4 Results

4.1 Particulate measurements

Of the 36 days with aggregates > 2.5 µm in aerodynamic diameter at the PEAV site, aggregates were observed on both inlets 22 days, the other 14 days, aggregates were observed on one inlet (Table 1). All single inlet days, except for one, occurred on the CEM inlet. This may be due to the higher-pressure drop across the CEM filter and higher flow constriction causing different flow dynamics for the CEM sample line. Aggregates, when observed only on a single inlet, had light loading, only two of the 14 single inlet days exceeded the 75^{th} percentile concentration (7.1 µg m^{-3}) for the sample period and both of those days had visually high $PM_{2.5}$ loading, a fire flag, and minimal aggregates. Presence of aggregates in some cases were associated with high $PM_{2.5}$ concentrations, 20 days of the 36 had concentrations >7.1 µg m^{-3}; however, due to aerosols from fires, this was not always related to aggregate loading.

This instrument was located at the lower elevation site (UNRG) with another TAPI instrument, before and after it was located at PEAV. Correlation between this instrument and the TAPI instrument located at UNRG was high before ($r^2 = 0.8$, $p < 0.05$, $n = 6$) and after ($r^2 = 0.88$, $p < 0.05$, $n = 71$) it was located at PEAV, indicating that the two instruments were operating similarly (Pierce & Gustin, 2017). Furthermore,

no aggregates were observed when the TAPI was moved to GBNP from March to October 2015, where the instrument was also impacted by fire plumes (Pierce & Gustin, 2017).

Black aggregates occurred on filters on days when inlets were cleaned and on days before and after cleaning (Fig. 2). Black particles were not observed in the PM_{10} pre-impactor or $PM_{2.5}$ cyclone inlets during routine inlet cleaning; brown dust particulates were observed (Fig. 5). During a thorough cleaning on October 3, 2014, after aggregates had been observed for multiple days in September, black particulate matter was noticed in the condensation water traps (Fig. 6). After cleaning the condensation water traps and reassembling the inlets, aggregates were again observed on multiple days in October.

4.2 Shape, size, and elemental composition

During the second, in depth look at the aggregates using the SEM, it became apparent that the aggregates were not predominantly "fluffy" (Fig. 3) like those observed in Chakrabarty et al. (2014) or Kearney and Pierce (2012), but more compact and did not resemble chain-aggregates (Fig. 7, Table 1). On eight of the 12 filters analyzed on the SEM, aggregates that were fluffy could be located; however, they were outnumbered by compact aggregates such as those in Fig. 7 and Fig. 8. The fluffy

aggregates observed were 10 to 20 µm in length (Fig. 3), compact aggregates observed were 10 to >100 µm in length (Fig. 7).

Blank Teflon filters were 25 to 41% carbon (C), 0 to 8% oxygen (O), and 51 to 75% fluorine (F) identified by EDS. Filter segments with $PM_{2.5}$ but no aggregates, had a range of elements including C, O, F, sodium (Na), magnesium (Mg), Al, Si, S, Cl, K, Ca, and Fe. For these segments, F (21 to 68%) and C (22 to 61%) with some O (3.4 to 19%) and small amounts of the remaining elements dominated the chemical composition. Aggregate chemical composition on the other hand consisted of C, O, F, Mg, Al, Si, S, Cl, K, Ca, and Cu, dominated by F (11 to 59 %), C (15 to 60%), O (4.6 to 38%), Al (0.19 to 42 %) and small amounts of the remaining elements (Table 3).

4.3 Fire indicators using aerosol optical properties

There was a drought in the Western USA from 2012 to 2016 that contributed to dry conditions and many wildfires throughout 2014 (CA, 2017). There were ~52 fires that exceeded 1 km^2 of burned area in California and ~63 fires that exceeded 4 km^2 of burned area in Oregon and Washington in 2014. There were two large fires during the measurement campaign. The first and largest in California for 2014, the Happy Camp Complex Fire, located in northern California, ~400 km northwest of PEAV, burned 543 km^2 from August 14 to October 31 (CA, 2017). The King Fire burned 390 km^2 in El

Dorado County, California, ~100 km southwest of PEAV from September 13 to October 9, 2014 (CA, 2017). Several fire plumes throughout the measurement campaign affected PEAV (Pierce et al, 2017), and aggregates occurred more frequently in September 2014 when the fire plume from the King Fire was heavily impacting the area (Fig. 2).

Aerosol Optical Depth (AOD, at 440 nm), a measure of the columnar aerosol loading, was positively correlated with $PM_{2.5}$ at PEAV for all data ($r^2 = 0.33$, $p < 0.05$, Fig. 9a) and higher if only days with aggregates are used ($r^2 = 0.49$, $p < 0.05$, Fig. 9b). If aggregate days were removed, the correlation increased to 0.58 for all data. The positive correlation for AOD and $PM_{2.5}$ for aggregates days was influenced by one point with AOD > 0.8 (highest AOD observed for the entire sample period) that occurred on September 18, when smoke from the King Fire was heavily influencing the sites (Fig. 9b). When that point is removed the correlation decreased to 0.36.

AEE was used here as a general indicator of particle size to identify biomass burning in the region (Fig. 10). For 31 aggregate days with AEE available, 24 days occur during days with fires (Fig. 10b). Of 158 days during the sample period with data from the Cimel, 120 days had fire flags. There was no correlation between AEE and all $PM_{2.5}$ nor between AEE and days with aggregates.

4.4 Meteorological data

Ambient RH was measured at PEAV, as well as inside the instrument box of the TAPI during sample collection and sample analysis with β attenuation (Fig. 11). Same day RH was not correlated with $PM_{2.5}$ for all data or days with aggregates for any of the RH measurements (outside RH, internal TAPI RH during sample collection, and internal TAPI RH during sample analysis). The in-line heaters did not turn on during this time, as RH during sampling (Fig. 11c and 11d) did not exceed 40% RH. RH also did not exceed 40% during sample analysis with β attenuation (Fig. 11e and 11f). It is possible that the RH effect on hygroscopic growth of particles was lagged and same day RH would therefore not be an effective measure. However, lagging the RH by 1, 2, and 5 days did not improve the correlation with aggregate days.

Higher wind speeds were observed at PEAV (median: 2.5 m s^{-1}, range: 0.0 to 36 m s^{-1}) relative to UNRG (median: 1.4 m s^{-1}, range: 0.0 to 9.6 m s^{-1}). PEAV also had higher wind speeds than GBNP (median: 2.4 m s^{-1}, range: 0.0 to 13 m s^{-1}) where the TAPI was later located during the fire season of 2015 with no aggregates observed. Wind speed was weakly, positively correlated with $PM_{2.5}$ for all data (r^2 = 0.33, p-value < 0.05, n= 152, Fig. 12a). This correlation increased only slightly when only days with aggregates were used in the analyses (r^2 = 0.39, p-values < 0.05, n=36, Fig. 12b).

Maximum (max) 1 h wind speed was also only weakly correlated with $PM_{2.5}$ ($r^2 = 0.26$, p-value < 0.05, Fig. 12c) for all data and analyses using only days with aggregates ($r^2 = 0.25$, p-value < 0.05, Fig. 12d).

There were 49 days out of 155 at PEAV with wind speed measurements, when wind speed exceeded 10 m s^{-1} for at least one hour of the day. Twenty-seven out of 36 days with aggregates occurred on days with hourly wind speeds >10 m s^{-1} and 33 out of 36 days with aggregates occurred on days with wind speeds >5 m s^{-1}. Of the nine days with observed aggregates that did not occur on high wind days, seven days aggregates only occurred on one inlet, which always had light loading. On the 13 aggregate days labelled as medium or heavy loading (Table 1), wind speeds exceeded 20 m s^{-1} for at least one hour of the day or wind speeds exceeded 10 m s^{-1} for 10 h or longer leading up to or during that day. Five days with high wind speed occurred during the week of generator use (October 20 to 24), and it is unclear if aggregates were present due to the high loading on these filters. Of the remaining 17 days with high wind speeds, 12 days occurred either before or after an aggregate day or had only one hour of the day that exceeded 10 m s^{-1}.

4.5 Generator use

From October 20 (Monday) to October 24 (Friday), multiple generators were operated. On October 22 to 24, the data from the TAPI located at PEAV did not pass data validation due to two errors related to flow rate and pump valve. The heavy loading observed on the filters (Fig. 13a) caused the TAPI to be unable to sample through these filters for the full sample period. This loading quickly cleared from the sample line once the generators were removed (Fig. 13b). A back-up power generator was located on site and was operated periodically throughout the sample period. We do not have exact timing for generator use but most likely, the generator would have been operated on weekdays when maintenance was performed. Aggregates occurred on weekends five times (both inlets 3 days and on one inlet 2 days).

5 Discussion

Potential causes of the particles > 2.5 μm in aerodynamic diameter investigated here include presence of fires, high RH potentially causing hygroscopic growth of particulates in the sample stream, high wind events causing degradation of the Al tubing, and exhaust from generators operated on site. The large number of fires in the Western USA and days with fire flags (120 days out of 158 with data available)

throughout the measurement campaign and the increase in aggregates during September 2014 when the fire plume from the King Fire was heavily impacting the area (Fig. 2) seemed to support superaggregates generated by high intensity fires. The moderate correlation between AOD and $PM_{2.5}$ ($r^2 = 0.33$ for all data and $r^2 = 0.49$ for aggregate days, Fig. 9) indicated that high aerosol loading in the atmospheric column may influence the occurrence of aggregates. If aggregate days were removed, however, the correlation increased to 0.58 for all data. The removal of the one point with AOD > 0.8 decreased the correlation for aggregate days to 0.36. AEE, used here as a general indicator of particle size to identify biomass burning in the region (Fig. 10), demonstrated that many days with fires occur with no aggregates. Based on findings in Loría-Salazar et al. (2017), we would expect $PM_{2.5}$ and AOD to be positively correlated in certain conditions (unstable conditions in a well-mixed boundary layer and during wildfires). Given the high frequency of fires, if the aggregates were generated and transported in fire plumes, we would expect the correlation with AOD and AEE to be higher.

It is possible that high RH could promote hygroscopic growth of aerosols in ambient air or in the sample stream. Hygroscopic growth factors (diameter of a particle at a certain RH/dry diameter) are estimated for ammonium sulfate, ammonium nitrate, and sea salt aerosols, for use in the national network, IMPROVE light extinction

algorithm (Pitchford et al, 2007). Pure ammonium sulfate crystallizes at 37% RH, and it is assumed no hygroscopic growth occurs below 37% RH, based on the efflorescence or hysteresis branch of the ammonium sulfate growth curve (Clegg et al, 1998; Pitchford et al, 2007). Sea salt aerosols are assumed to have no hygroscopic growth below 47% RH and ambient organic mass particulates are assumed to have limited to no hygroscopic growth (Pitchford et al, 2007).

The Western USA generally has higher ambient organic carbonaceous mass particulates, lower mass concentration of inorganic species known to impact hygroscopic growth (sulfates and nitrates), and strong seasonal fluctuations in boundary layer RH compared to the Eastern USA (Buseck & Schwartz, 2003; Malm et al, 2011; Malm et al, 2004; Malm & Sisler, 2000; Nguyen et al, 2016). Wintertime build-up of particulate nitrate has been observed in Western USA valleys (Green et al, 2015), but PEAV would likely not be affected by this build-up due to elevation and sample period. Furthermore, Loría-Salazar et al. (2017) found no correlation between AOD measurements and RH in the boundary layer in Reno, NV for a yearlong sample period in 2013. Outside RH did at times exceed 37%; however, internal TAPI RH measurements indicated that the RH in the sample stream did not exceed 37%. Due to the higher ambient organic mass particulates in the West and RH < 37% in the sample line, it does not seem likely that this was the cause of the aggregates.

High wind speed may have caused sections of anodized Al tubing to rub together, also known as fretting corrosion (Davis, 1999; Waterhouse, 1992). Fretting is defined as small-amplitude movement that can occur between contacting surfaces, usually due to external vibration (Waterhouse, 1992). Fretting corrosion arises when dry oxidation during rubbing occurs, producing a black powder of aluminum oxide, more likely to occur when aluminum contacts aluminum (Davis, 1999). Aluminum tubing was in contact with another surface in four places: where the sample tubes connected to the base of the $PM_{2.5}$ cyclones, before and after the water condensation water traps, and where the sample tubes entered the TAPI measurement box (marked in red, Fig. 4). On several occasions during site visits, it was noticed that the PM_{10} and $PM_{2.5}$ inlets were in different positions from the last site visit, indicating that high wind speeds had caused the inlets to rotate on the sample tubes. The observation of a black powder in the condensation water traps (Fig. 6) and not in the PM_{10} pre-impactor (Fig. 5) or $PM_{2.5}$ cyclone supports the generation of aggregates in the sample line after the inlets and before the condensation water traps. The increase of Al and O in the aggregate samples indicated that the anodized coating on the sample lines was possibly undergoing fretting corrosion. Anodized Al coatings are ~80% aluminium oxide, ~18% aluminium sulfate, and ~2% water.

The samples from October 20 (Monday) to October 24 (Friday), when multiple generators were running at PEAV indicate that aggregates may have been caused by generator exhaust, due to the similarity of the filter at the end of the period to other aggregate filters. Smits et al. (2012) measured generator exhaust emissions at different loadings for a small-scale generator using a low-sulfur fuel. Diesel generators emit nitrogen oxides (NOx), volatile organic compounds (VOCs), carbon monoxide (CO), and PM (Smits et al, 2012). Elements found in the generator exhaust included potassium (K), calcium (Ca), titanium (Ti), strontium (Sr), chromium (Cr), iron (Fe), nickel (Ni), manganese (Mn), copper (Cu), zinc (Zn), lead (Pb), sulfur (S), and chlorine (Cl). Elements that were not detected included silicon (Si), vanadium (V), selenium (Se), cadmium (Cd), antimony (Sb), and aluminum (Al). SEM from Smits et al. (c.f. Fig. 4 of Smits et al, 2012) look similar to the SEM we have collected in this study, however, the absence of Al in Smits et al. (2012) differs from our findings (Table 2 and 3). Aluminum was assumed to be a tracer for environmental atmospheric samples in Smits et al. (2012), filters with ambient $PM_{2.5}$ from PEAV are consistent with this assumption with small amounts of Al (Table 2). Aggregate samples however had much higher Al (Table 3), indicating these samples were not background environmental $PM_{2.5}$. Aluminum is not a common additive to diesel fuel or lubricating oil. Aggregates on

weekends, when it is unlikely that maintenance was occurring, and the large percentage of Al present indicated that generator exhaust was likely not the cause of the aggregates.

6 Conclusions

During the sampling campaign at PEAV from June to November 2014, the presence of fires and fire indicators, high RH, high wind speeds, and use of generators onsite were investigated to understand the presence of ambient particles that exceeded 2.5 µm in aerodynamic diameter on 36 measurement days. Particles > 2.5 µm in aerodynamic diameter were not observed on samples from the same days at the lower elevation site, from the TAPI before and after it was deployed at PEAV, nor when it was moved to another high elevation site, GBNP impacted by fires in 2015. RH and AEE were not correlated with aggregate measurements, indicating RH and indicators of fire did not predict aggregate formation. The presence of aerosols in the column (AOD) was correlated with $PM_{2.5}$, however, the positive correlation was heavily influenced by one data point and AOD did not fully explain the presence of aggregates. Linear regression may not be adequate to identify the cause due to mass concentration of the filters being a combination of $PM_{2.5}$ and aggregate mass. Generator use at the site could be the source of the aggregates and would be an interesting area of further

research if particulates from the exhaust were able to deposit past the PM_{10} pre-impactor and $PM_{2.5}$ cyclones, however chemical composition did not support generator exhaust as the source of aggregates.

High concentrations of Al and O observed in the EDS elemental analysis suggested that the anodized Al sample tube coating contributed aggregates to the samples. Fretting corrosion, occurring where two sections of Al tubing were rubbing together, caused by prolonged, high wind events at PEAV seems to be the most likely explanation of the observed aggregates. Aluminum tubing was in contact with another surface in four places: the base of the PM_{10} pre-impactor, before and after the condensation water trap, and where the sample tubes enter the TAPI measurement box (marked in red in Fig 4). The observation of black particles in the condensation water traps (Fig. 6) but not on the PM_{10} pre-impactor plates (Fig. 5) or in the $PM_{2.5}$ cyclones also supports fretting corrosion occurring in the sample line downstream of the PM_{10} pre-impactor plates and the $PM_{2.5}$ cyclones. More experiments to test this theory are needed to understand the specific conditions promoting fretting corrosion.

In other particulate monitors, such as the Beta Attenuation Monitor (BAM-1020), used in regulatory networks, filter tape is automatically advanced, without post-processing. The BAM uses a similar inlet setup to the TAPI. At sites with high wind speeds, if there are sections of Al tubing susceptible to fretting corrosion, a similar

situation could occur and go unnoticed and potentially impact measured $PM_{2.5}$ concentrations. The observations presented suggest inlet configuration is important to consider for sites with high wind events.

Acknowledgments

We acknowledge the Nevada Division of Environmental Protection (NDEP), the UNR College of Biotechnology and Natural Resources, and a USDA-HATCH grant (NIFA Accession# NEV05295) for supporting this project. We would like to acknowledge help from Sue Lindsey and Katrina Macsween at Macquarie University in Sydney, New South Wales, Australia for assistance with and use of the scanning electron microscope. Thank you to Dave Metts of High Sierra Communications for allowing access to and support at the Peavine Peak site. Thank you to Kristien King for assistance with data processing.

References

Buseck, P. R. & Schwartz, S. E. (2003) 4.04 - Tropospheric Aerosols, in Holland, H. D. & Turekian, K. K. (eds), *Treatise on Geochemistry*. Oxford: Pergamon, 91-142.

CA, S. o. C. G. (2017) *2014 Large Fires List*, 2017. Available online: http://cdfdata.fire.ca.gov/incidents/incidents_statsevents#2014 [Accessed.

Chakrabarty, R. K., Beres, N. D., Moosmuller, H., China, S., Mazzoleni, C., Dubey, M. K., Liu, L. & Mishchenko, M. I. (2014) Soot superaggregates from flaming wildfires and their direct radiative forcing. *Sci. Rep.*, 4.

Clegg, S. L., Brimblecombe, P. & Wexler, A. S. (1998) Thermodynamic Model of the System H+−NH4+−SO42-−NO3-−H2O at Tropospheric Temperatures. *The Journal of Physical Chemistry A*, 102(12), 2137-2154.

Davis, J. R. (1999) *Corrosion of Aluminum and Aluminum Alloys*A S M International.

Fromm, M., Lindsey, D. T., Servranckx, R., Yue, G., Trickl, T., Sica, R., Doucet, P. & Godin-Beekmann, S. (2010) The Untold Story of Pyrocumulonimbus. *Bulletin of the American Meteorological Society*, 91(9), 1193-1209.

Green, M. C., Chow, J. C., Watson, J. G., Dick, K. & Inouye, D. (2015) Effects of Snow Cover and Atmospheric Stability on Winter PM2.5 Concentrations in Western U.S. Valleys. *Journal of Applied Meteorology and Climatology*, 54(6), 1191-1201.

John, W. (2011) Size Distribution Characteristics of Aerosols, *Aerosol Measurement*John Wiley & Sons, Inc., 41-54.

Kearney, S. P. & Pierce, F. (2012) Evidence of soot superaggregates in a turbulent pool fire. *Combustion and Flame*, 159(10), 3191-3198.

Kleinstreuer, C. & Zhang, Z. (2009) Airflow and Particle Transport in the Human Respiratory System. *Annual Review of Fluid Mechanics*, 42(1), 301-334.

Kulkarni, P., Baron, P. A., Sorenson, C. M. & Harper, M. (2011a) Nonspherical Particle Measurement: Shape Factor, Fractals, and Fibers, *Aerosol Measurement*John Wiley & Sons, Inc., 507-547.

Kulkarni, P., Baron, P. A. & Willeke, K. (2011b) Fundamentals of Single Particle Transport, *Aerosol Measurement*John Wiley & Sons, Inc., 15-30.

Loría-Salazar, S. M., Holmes, H. A., Patrick Arnott, W., Barnard, J. C. & Moosmüller, H. (2016) Evaluation of MODIS columnar aerosol retrievals using AERONET in semi-arid Nevada and California, U.S.A., during the summer of 2012. *Atmospheric Environment*, 144(Supplement C), 345-360.

Loría-Salazar, S. M., Panorska, A., Arnott, W. P., Barnard, J. C., Boehmler, J. a. M. & Holmes, H. A. (2017) Toward Understanding Atmospheric Physics Impacting the Relationship between Columnar Aerosol Optical Depth and Near-Surface PM2.5 Mass

Concentrations in Nevada and California, U.S.A., During 2013. *Atmospheric Environment*.

Loría-Salazar, S. M. a. A. W. P. a. M. H. (2014) Accuracy of near-surface aerosol extinction determined from columnar aerosol optical depth measurements in Reno, NV, USA. *Journal of Geophysical Research: Atmospheres*, 119(19), 11,355--11,374.

Malm, W. C., Schichtel, B. A. & Pitchford, M. L. (2011) Uncertainties in PM2.5 gravimetric and speciation measurements and what we can learn from them. *J Air Waste Manag Assoc*, 61(11), 1131-49.

Malm, W. C., Schichtel, B. A., Pitchford, M. L., Ashbaugh, L. L. & Eldred, R. A. (2004) Spatial and monthly trends in speciated fine particle concentration in the United States. *Journal of Geophysical Research: Atmospheres*, 109(D3), D03306.

Malm, W. C. & Sisler, J. F. (2000) Spatial patterns of major aerosol species and selected heavy metals in the United States. *Fuel Processing Technology*, 65–66(0), 473-501.

Marple, V. A. & Olson, B. A. (2011) Sampling and Measurement Using Inertial, Gravitational, Centrifugal, and Thermal Techniques, *Aerosol Measurement*John Wiley & Sons, Inc., 129-151.

Nguyen, T. K. V., Ghate, V. P. & Carlton, A. G. (2016) Reconciling satellite aerosol optical thickness and surface fine particle mass through aerosol liquid water. *Geophysical Research Letters*, 43(22), 11,903-11,912.

Peterson, D. A., Hyer, E. J., Campbell, J. R., Fromm, M. D., Hair, J. W., Butler, C. F. & Fenn, M. A. (2014) The 2013 Rim Fire: Implications for Predicting Extreme Fire Spread, Pyroconvection, and Smoke Emissions. *Bulletin of the American Meteorological Society*, 96(2), 229-247.

Peterson, D. a. H. E. a. W. J. (2014) Quantifying the potential for high-altitude smoke injection in the North American boreal forest using the standard MODIS fire products and subpixel-based methods. *Journal of Geophysical Research: Atmospheres*, 119(6), 3401--3419.

Pierce, A. M. & Gustin, M. S. (2016) Development of a Particulate Mass Measurement System for Quantification of Ambient Reactive Mercury. *Environmental Science & Technology*.

Pierce, A. M. & Gustin, M. S. (2017) Development of a Particulate Mass Measurement System for Quantification of Ambient Reactive Mercury. *Environmental Science & Technology*, 51(1), 436-445.

Pierce, A. M., Gustin, M. S., Christensen, J. N. & Loría-Salazar, S. M. (2017) Use of multiple tools including lead isotopes to decipher sources of ozone and reactive mercury to urban and rural locations in Nevada, USA. *Science of the Total Environment*.

Pitchford, M., Maim, W., Schichtel, B., Kumar, N., Lowenthal, D. & Hand, J. (2007) Revised algorithm for estimating light extinction from IMPROVE particle speciation data. *J Air Waste Manag Assoc*, 57(11), 1326-36.
Smits, M., Vanpachtenbeke, F., Horemans, B., De Wael, K., Hauchecorne, B., Van Langenhove, H., Demeestere, K. & Lenaerts, S. (2012) Effect of Operating and Sampling Conditions on the Exhaust Gas Composition of Small-Scale Power Generators. *PLOS ONE*, 7(3), e32825.
Sohirripa Spagnolo, G. (1987) Automatic instrument for aerosol samples using the beta-particle attenuation. *Journal of Aerosol Science*, 18(6), 899-902.
Sorensen, C. M., Gebhart, J., O'Hern, T. J. & Rader, D. J. (2011) Optical Measurement Techniques: Fundamentals and Applications, *Aerosol Measurement*John Wiley & Sons, Inc., 269-312.
TAPI, T. A. P. I. (2012) Operation Manula: Model 602 BETA PLUS particle measurement system. San Diego, CA: Teledyne Advanced Pollution Instrumentation.
Wang, Y., Liu, F., He, C., Bi, L., Cheng, T., Wang, Z., Zhang, H., Zhang, X., Shi, Z. & Li, W. (2017) Fractal Dimensions and Mixing Structures of Soot Particles during Atmospheric Processing. *Environmental Science & Technology Letters*.
Waterhouse, R. B. (1992) Fretting fatigue. *International Materials Reviews*, 37(1), 77-98.

Figures

(a) 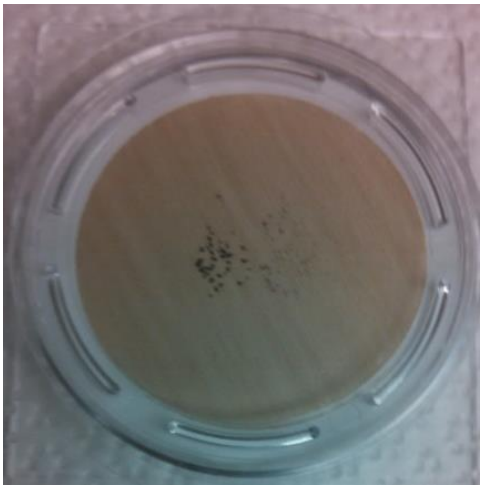 **(b)** 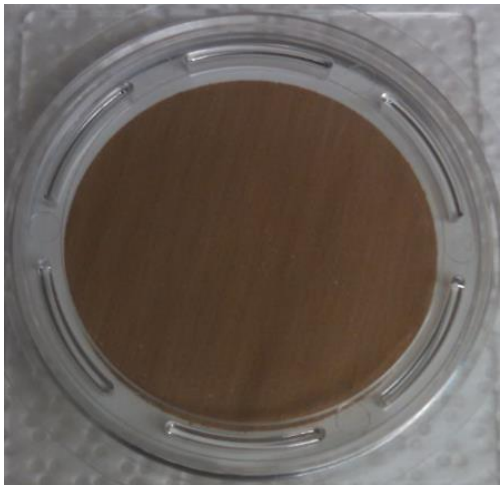

Figure 1: Filter (a) is from the higher elevation, rural site (PEAV) and filter (b) is from the lower elevation, urban site (UNRG) on September 16, 2014. Aggregates were observed at PEAV but not at UNRG.

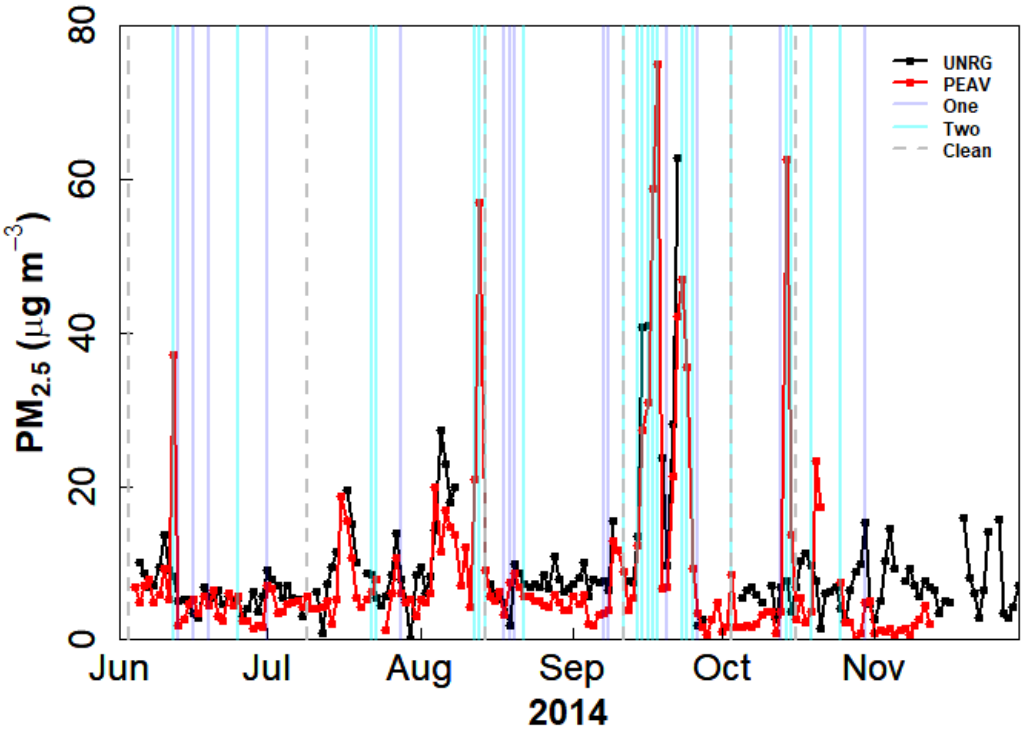

4

Figure 2: $PM_{2.5}$ (µg m^{-3}) at PEAV (red) and UNRG (black) for June to November 2014. Vertical dark blue lines are days with aggregates on one inlet, vertical light blue lines are days with aggregates on two inlets, dashed grey lines are days when the inlets were cleaned.

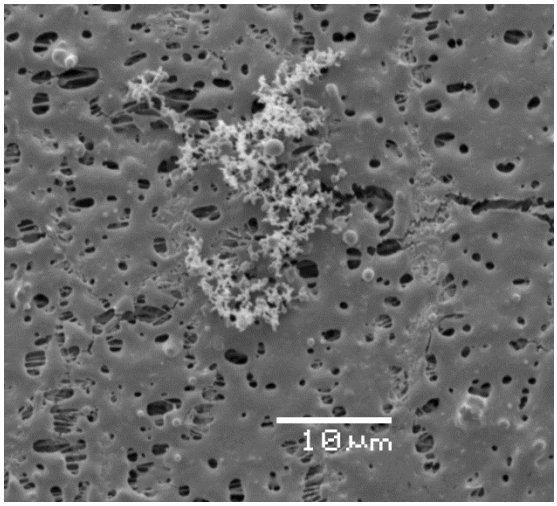

Figure 3: SEM (uncoated, backscattered electron imaging, low vacuum) image of an aggregate on a Teflon filter from the higher elevation, rural site (PEAV) on September 18, 2014.

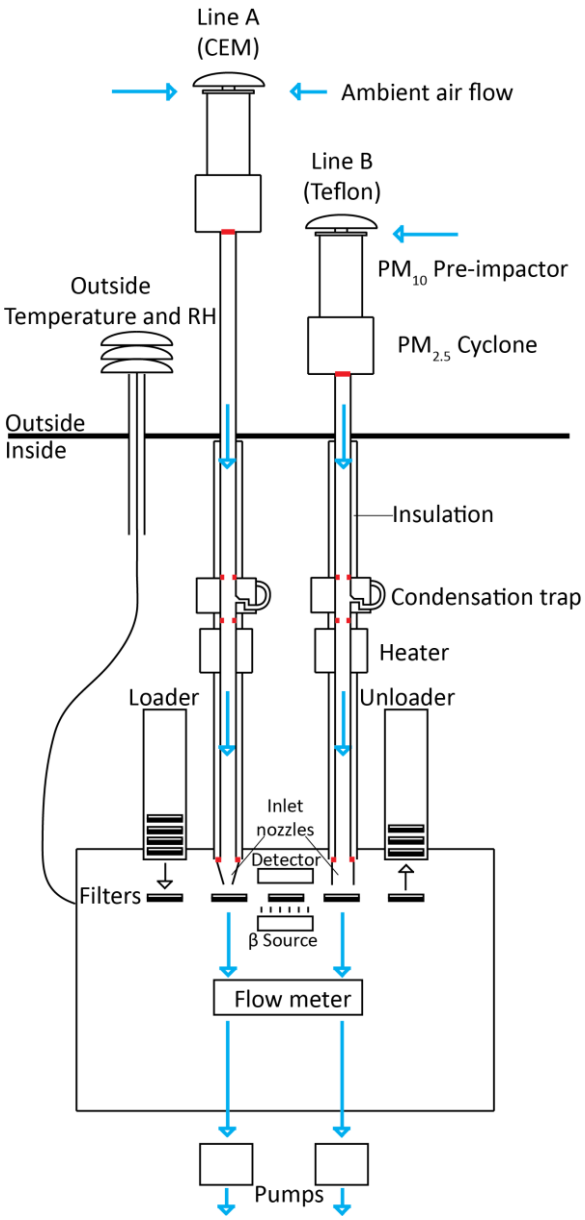

Figure 4: Diagram of Teledyne Advanced Pollution Instrumentation (TAPI) 602 Beta^{Plus} particulate monitor (modified from Pierce & Gustin, 2017). Blue indicates the airflow through the instrument. Red indicates where aluminum tubing is in contact with another surface: the base of the $PM_{2.5}$ cyclones, before and after the condensation water traps, and where the sample tubes entered the TAPI measurement box above the inlet nozzles.

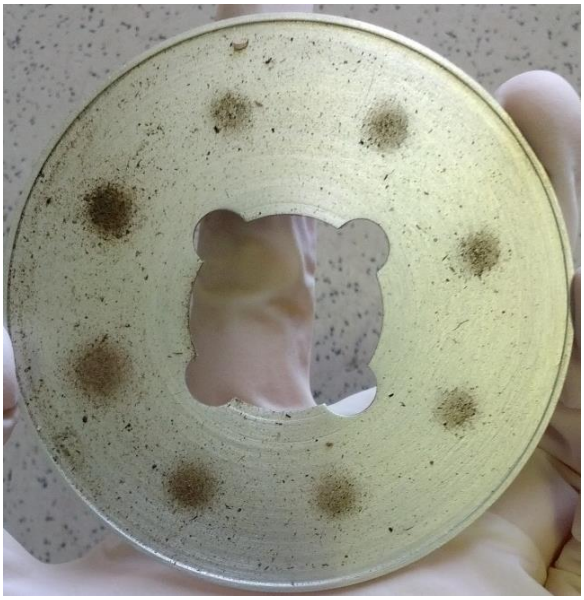

Figure 5: PM_{10} pre-impactor plate from the CEM inlet (Line A, Fig. 4) during a routine cleaning after a high wind event.

Figure 6: Condensation water trap during a cleaning on October 3, 2014. Black powder was visible in the condensation water trap. The black around the outside of the trap is insulating foam.

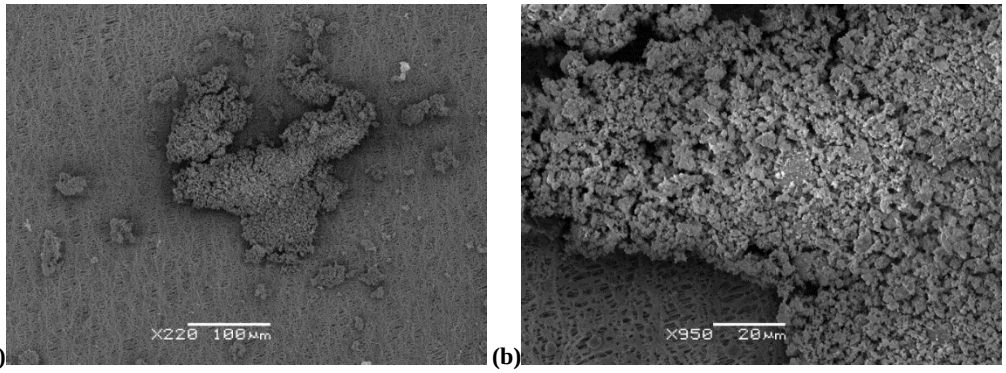

(a) (b)

Figure 7: SEM images of aggregates (gold-coated, secondary electron imaging, high vacuum) for (a) September 16, 2014 (b) higher magnification of same aggregate.

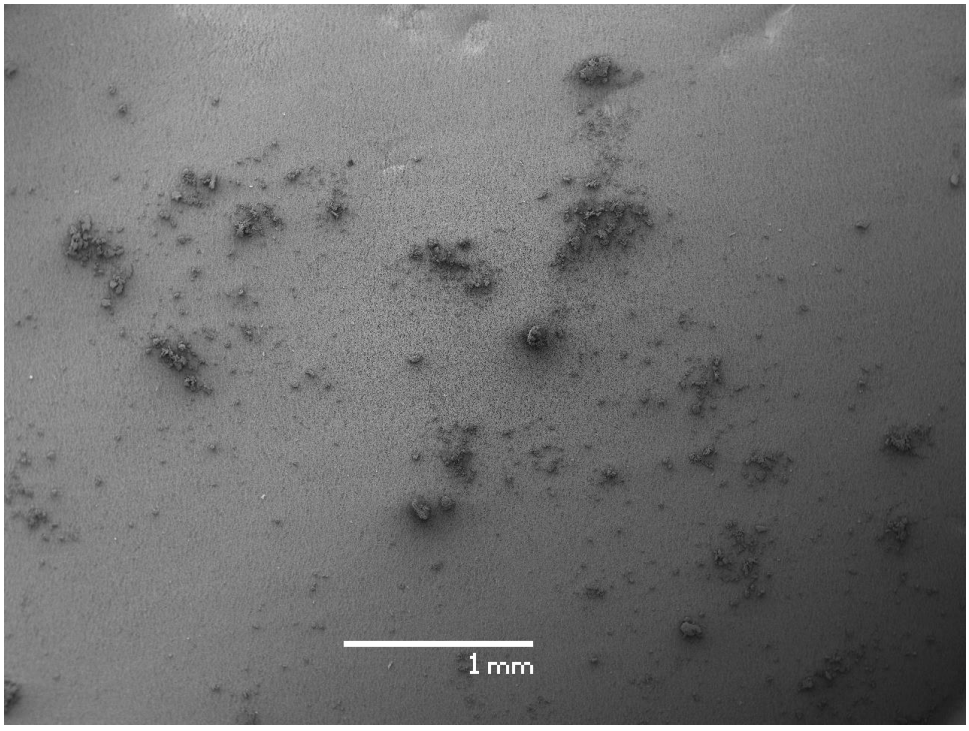

Figure 8: SEM image (uncoated, backscattered electron imaging, low vacuum) of aggregates on September 16, 2014.

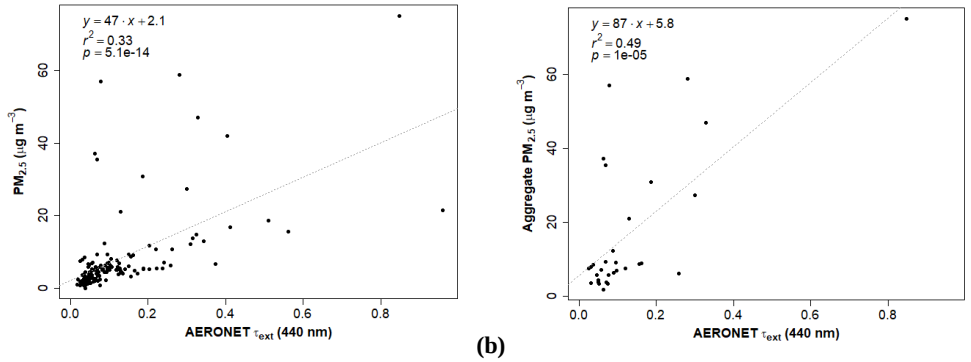

(a) **(b)**

Figure 9: Aerosol Optical Depth (AOD, τ_{ext}) from the Cimel sun photometer located in the valley plotted against $PM_{2.5}$ (µg m^{-3}) at PEAV for (a) all data and (b) days with aggregates.

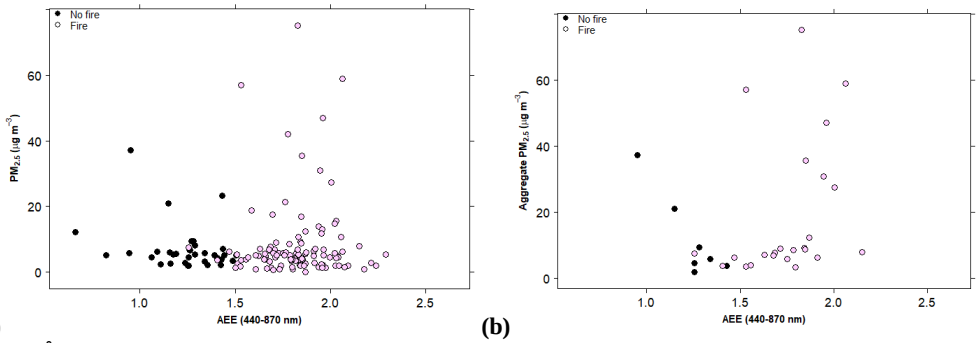

(a) **(b)**

Figure 10: Ångström Extinction Exponent (AEE) from the Cimel sun photometer located in the valley plotted against $PM_{2.5}$ (µg m^{-3}) at PEAV grouped by days with (open points) and without (filled points) fires for (a) all data and (b) days with aggregates.

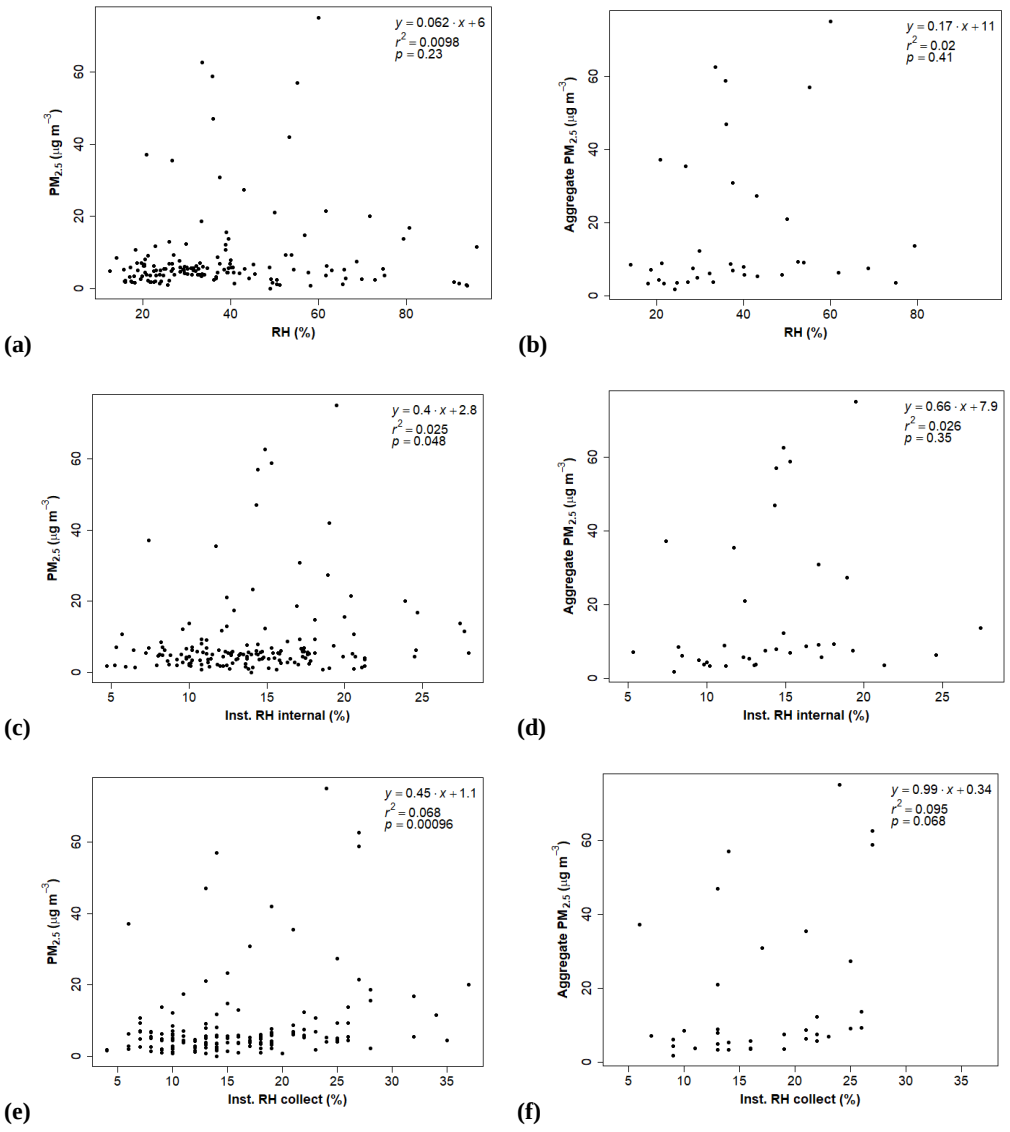

Figure 11: Relative Humidity (%) and $PM_{2.5}$ (µg m^{-3}) measured June to November 2014 for (a) ambient RH for all data, (b) ambient RH on aggregate days, (c) average instrument RH during sampling for all data, (d) average instrument RH during sampling for days with aggregates, (e) average instrument RH during β-attenuation collection for all data, and (f) average instrument RH during β-attenuation collection for days with aggregates.

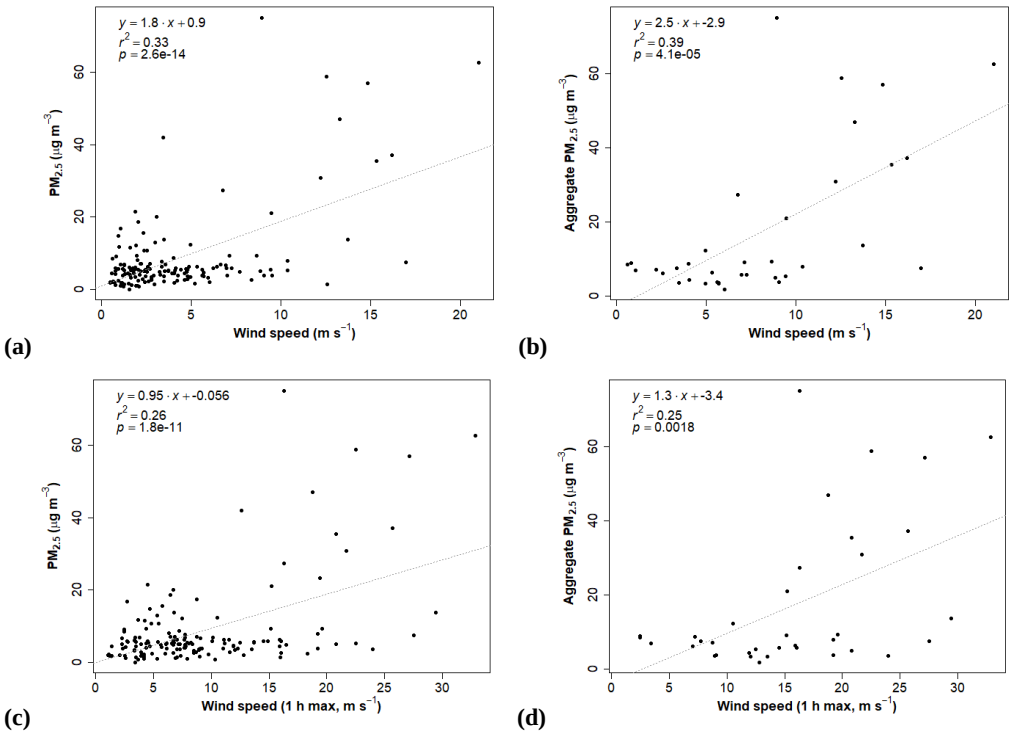

Figure 12: Wind speed (m s^{-1}) and $PM_{2.5}$ (µg m^{-3}) at PEAV for (a) all data and (b) days with aggregates and for maximum 1 h wind speed for (c) all data and (d) days with aggregates.

(a) 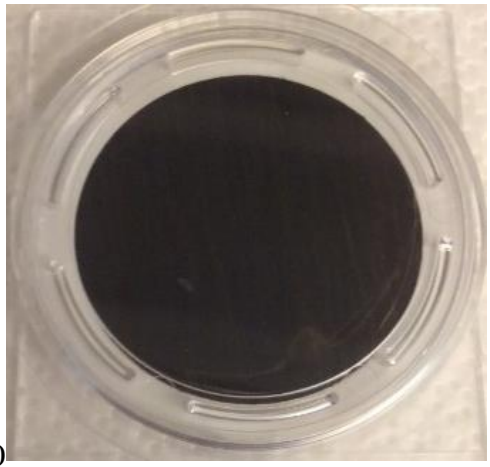 **(b)** 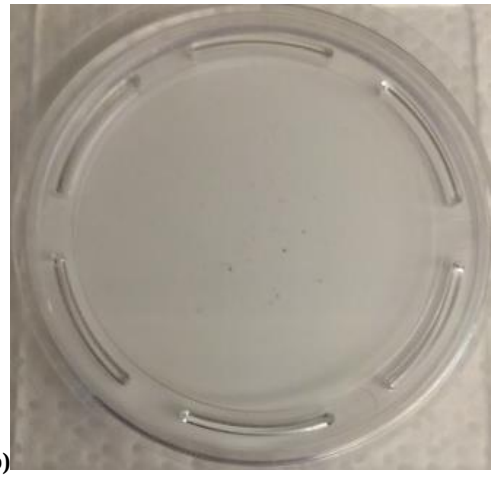

Figure 13: Teflon filters from (a) October 21, 2014 during multiple generators running at PEAV and (b) October 25, 2014 the day after multiple generators were running at PEAV.

Tables

Filter	Inlet	Visual loading	Mass concentration >7.1 µg m^{-3}	Fire?	SEM/ EDS?	Description	Wind speed >20 m s^{-1} or >10 m s^{-1} for >10 hours
12-Jun	Both	Medium to heavy	✓				>20 m s^{-1}
13-Jun	CEM	Light					
16-Jun	CEM	Light					
19-Jun	CEM	Light					
25-Jun	Both	Light to medium			✓	Compact, some fluffy	>10 h
1-Jul	CEM	Light		✓			
22-Jul	Both	Light		✓			
23-Jul	Both	Light to medium	✓	✓	✓	Compact, some fluffy	>10 h
28-Jul	Teflon	Light		✓	✓	Compact, some more diffuse	
12-Aug	Both	Medium	✓		✓	Compact and some larger structures	>10 h
13-Aug	Both	Medium to heavy	✓	✓			>20m s^{-1}
14-Aug	Both	Light	✓	✓			
18-Aug	CEM	Light		✓			
19-Aug	CEM	Light	✓	✓			
20-Aug	CEM	Light	✓	✓			
22-Aug	Both	Light		✓	✓	Compact and fluffy	
7-Sep	CEM	Light		✓			
8-Sep	CEM	Light		✓			
11-Sep	Both	Light	✓	✓	✓	Compact, some fluffy	
14-Sep	Both	Light	✓	✓			
15-Sep	Both	Light	✓	✓	✓	Compact and fluffy	
16-Sep	Both	Medium	✓	✓	✓	Compact	>10h, >20m s^{-1}
17-Sep	Both	Medium	✓	✓			>10h, >20m s^{-1}
18-Sep	Both	Light	✓	✓	✓	Compact, some fluffy	>10h
20-Sep	CEM	Light		✓			
23-Sep	Both	Light to medium	✓	✓	✓	Compact, some fluffy, some spores/pollen	>10h
24-Sep	Both	Medium to heavy	✓	✓			>10h, >20m s^{-1}
25-Sep	Both	Light to medium	✓		✓	Compact, some fluffy	>10h
26-Sep	CEM	Light		NA			
3-Oct	Both	Light		✓			

13-Oct	CEM	Light		✓			
14-Oct	Both	Heavy	✓	NA	✓	Compact, disperse	>10h, >20m s^{-1}
15-Oct	Both	Medium	✓	NA			>10h, >20m s^{-1}
19-Oct	Both	Light					
25-Oct	Both	Light to medium	✓	✓			>10h, >20m s^{-1}
30-Oct	CEM	Light		NA			>20m s^{-1}

Table 1: Days at PEAV in 2014 with visible aggregates on filters, the inlet with aggregates, and the loading on the filters, whether mass concentration exceeded 75th percentile value for the sample period (7.1 µg m^{-3}), presence of fire flag, SEM and EDS analysis, subjective description of the shape, and whether wind speed exceeded 20 m s^{-1} for at least one hour of the sample day or wind speed exceeded 10 m s^{-1} for 10 h or longer leading up to or during the sample day.

		Composition filter with $PM_{2.5}$ not aggregates (range, %)											
Filter	**Inlet**	**C**	**O**	**F**	**Na**	**Mg**	**Al**	**Si**	**S**	**Cl**	**K**	**Ca**	**Fe**
Blank		25-41	0-8	51-75									
25-Jun	Both	27-29	4.5-5.0	65			2.0-2.2	0.15					
28-Jul	Teflon	29-30	3.4-11	50-67	6.5	0.79	0.54-2.2		0.18-0.65	0.0-0.19	0.28	0.31	
12-Aug	Both	24-38	3.6-8.7	56-68			0.31-3.5		0.21-0.64				
22-Aug	Both	24-37	4.6-10	58-60			0.19-6.0	0.0-0.14	0.13-0.29				
11-Sep	Both	29-39	4.7-8.7	54-65		0.0-0.14	0.26-3.1	0.12-0.60					
15-Sep	Both	44-55	7.1-10	34-46		0.0-0.14	0.0-1.4		0.21-0.75		0.0-0.46	0.0-0.79	
16-Sep	Both	35-48	13-14	35-46			2.9-5.1		0.33-0.55		0.0-0.27		
18-Sep	Both	52-53	19	21-25			2.4-4.8	0.0-2.1	0.37-0.57		0.0-0.58		
23-Sep	Both	45-61	12-16	23-40			1.0-5.2		0.0-0.25		0.18-0.19		
25-Sep	Both	34-29	4.7-16	49-65		0.0-0.34	1.5-5.6	0.0-2.1	0.0-0.30		0.0-0.62		0.0-3.2
14-Oct	Both	22-26	14-18	45-53			8.4-10	0.26-0.35	0.31-0.42				

Table 2: Elemental composition of sections of Teflon with particulate matter.

		Composition of aggregates (range, %)										
Filter	**Inlet**	**C**	**O**	**F**	**Mg**	**Al**	**Si**	**S**	**Cl**	**K**	**Ca**	**Cu**
Blank		25-41	0-8	51-75								
25-Jun	Both	17-22	17-29	33-43		18-21		0.0-0.24	0.0-0.23			
23-Jul	Both	18-28	5.2-25	37-58	0.0-0.32	8.3-26	0.0-3.3	0.0-0.42	0.0-0.16	0.0-0.89		
28-Jul	Teflon	20-28	8.1-22	39-43		14-25		0.19-0.33	0.0-0.92			
12-Aug	Both	16-26	12-34	36-52	0.0-0.36	6.0-17		1.0-3.5			0.0-0.23	
22-Aug	Both	16-37	4.6-28	29-59		0.19-29		0.13-0.32	0.0-0.29			
11-Sep	Both	16-20	17-31	31-38	0.0-0.29	17-28	0.0-0.37	0.0-0.26	0.22-0.52			
15-Sep	Both	29-34	18-26	29-32		15-16		0.19-0.26		0.0-0.22		
16-Sep	Both	20-46	11-34	15-46	0.0-0.24	2.2-42	0.0-0.23	0.0-0.63		0.0-0.25		
18-Sep	Both	36-60	15-38	11-30	0.0-0.13	1.7-16		0.18-0.55	0.0-0.38	0.0-0.13		
23-Sep	Both	34-45	13-31	16-41		1.8-23		0.0-0.26	0.0-0.24			
25-Sep	Both	18-21	21-25	39-47		11-17		0.0-0.15	0.0-0.44			
14-Oct	Both	15-21	22-37	24-29		22-32	0.0-0.37	0.26-0.97				0.0-0.76

Table 3: Elemental composition of sections of Teflon with visible aggregates.

Chapter 6

Summary, Conclusions, and Recommendations

1. Summary

This research was directed at further refining and supporting conclusions presented in the initial stage of the Nevada Rural Ozone Initiative (NVROI): 1) Ozone (O_3) concentrations measured at rural sites in Nevada approach the National Ambient Air Quality Standard (NAAQS) for O_3 regardless of the lack of large sources in the State; 2) industrialization in Eurasia and the observed trans-Pacific pollution will continue to be a source of atmospheric pollutants in this area; 3) understanding discreet pollution events in complex terrain requires a suite of measurements; and 4) monitoring sites in rural Nevada, used for tracking regional air quality trends, should be sustained. Several research gaps were also addressed: 1) improved methods for measuring ambient reactive mercury (RM) are needed due to the underestimation of RM measurements from the commercially available analytical instrument; and 2) additional measurements and effective methods for identifying sources and source regions of air masses intercepted in rural Nevada and other parts of the Western USA are needed.

The goal of this research was to identify sources affecting the concentration of atmospheric pollutants in Nevada, specifically particulate matter < 2.5 µm in aerodynamic diameter ($PM_{2.5}$), ozone (O_3), and RM, using lead (Pb) isotopic ratios and a suite of measurements, including gaseous data, meteorological data, and aerosol optical properties. Statistical and back trajectory analyses were also used. The four research objectives were directed at developing and deploying a new method for quantifying RM, applying the data collected with this method to identify sources of atmospheric

pollutants, source regions, and atmospheric processes using Pb isotope data and a statistical method, and investigating data anomalies observed during the sample campaign.

2. Summary, conclusions, and recommendations for the specific research objectives

2.1 Research objective 1

The first research objective was to develop a method to quantify $PM_{2.5}$ on two filter materials that allowed for post-processing of filter samples for RM concentrations, Pb concentrations, and Pb isotopic ratios using the Teledyne Advanced Pollution Instrumentation (TAPI) model 602 $Beta^{Plus}$ particulate monitor. $PM_{2.5}$ concentrations measured with the TAPI were statistically similar to those obtained from $PM_{2.5}$ Federal Reference and Federal Equivalent Methods (FRM and FEM), when located at two different measurement sites, indicating reliable measurements of $PM_{2.5}$ by the TAPI, as configured for this study. Simultaneous measurements at high and low elevation sites showed that $PM_{2.5}$ concentrations were higher at the lower elevation site located next to two highways in Reno, NV, USA than at the two higher elevation sites located on the west (Peavine Peak) and east side (Great Basin National Park) of Nevada. RM was statistically higher at Great Basin National Park on the east side of Nevada and statistically similar between the Reno and Peavine Peak sites.

The TAPI allowed for finer temporal resolution (24 h) of RM measurements at a higher sample flow (16.7 Lpm) than measurements using the same cation exchange membranes (CEM) from the University of Nevada, Reno Reactive Mercury Active System (UNRRMAS) with a two-week sample period at lower sample flow (1 Lpm).

However, the TAPI consistently underestimated RM compared to the two-week UNRRMAS measurements. These differences are not surprising, due to inlet differences and sample flow. However, this instrument also measured higher RM in the summer, lower RM concentrations in the winter/spring, and similar RM concentrations in the fall/early winter compared to measurements from the commercially available instrument (Tekran), with known differences in RM collection efficiency and known interferences. The seasonal difference corresponded to similar behavior in atmospheric water vapor, which was high in the summer, low in the winter/spring, and intermediate in the fall/early winter. Increases in RM retention on filter surfaces with increasing water vapor and decreases in breakthrough indicate that water vapor affects ambient RM measurements on these filters. This finding is consistent with previous studies indicating that water vapor increases retention of RM on CEM (Huang and Gustin, 2015; Huang et al., 2013; Peterson et al., 2012).

A statistically significant relationship was found for 24 h versus two-week UNRRMAS filter measurements; however, differences in RM concentrations collected at low flow for longer sample periods and high flow for shorter sample periods need to be resolved in order to apply the filter material for shorter temporal resolution sampling. Preliminary tests using a newly developed calibrator system to address breakthrough and long-term sampling on the CEM were performed. CEM filters pre-loaded with RM, using the calibrator system, had higher concentrations after two weeks of ambient sampling than would be expected based on the initial concentration of RM loaded on to the filters and the concentration of ambient RM collected over the two week period. This discrepancy indicated that filters exposed to high concentrations of RM might collect

more RM over time than would be expected. Filters loaded with RM that were held in jars for two weeks did not have statistically different RM concentrations after two weeks, indicating that RM was not gained or lost in this time. Breakthrough was not consistent in ambient air for either filter method (24 h and two week). Inconsistent breakthrough and increased RM on two-week atmospheric samples that did not occur on samples held in jars indicated that other atmospheric constituents might affect measurements.

Several improvements to this research objective include adding another TAPI, longer sampling periods, more tests of the CEM, heated inlets, and better collocation of the TAPI instruments. Access to three TAPIs would have been beneficial for both initial testing and deployment for longer sample periods at all three sites (UNR Greenhouse, Peavine Peak, and Great Basin National Park). Running all three TAPIs collocated in the same sample trailer at the start of the experiment for several months would have allowed for a better comparison between the instruments to determine if RM concentrations were statistically similar between instruments. This would also allow for continued testing of the 24 h vs multiple day measurements on the TAPI.

Tests of the CEM surface chemistry would include use of a permeation system and the calibrator system used to load CEM filters. The permeation system would be used for laboratory tests, some of which have been started under a new National Science Foundation grant. These tests would include permeating different RM compounds (e.g. $HgCl_2$, $HgBr_2$, HgO) in dry clean air through two filters inline. This requires a setup with two sample lines, one with the CEM filters, and the other with a pyrolyzer inline to convert RM to GEM for analysis on a Tekran 2537 to determine permeation rate through the filters. GOM collection efficiency on the CEM has only been determined for passive

samplers (Lyman et al., 2009) and should be determined for active systems at 1 Lpm and higher flow rates. This will also address breakthrough of different compounds for periods relevant to sample collection (24 h to two weeks). Previous breakthrough tests were performed using the calibrator and only occurred for 20 to 40 s followed by a 130 to 160 s flush. Further testing using this setup would include permeations of Hg compounds with varying water vapor contents and different gaseous constituents at varying concentrations in zero air to determine CEM behavior in controlled environments with known variables.

Field-tests would include repeating the CEM tests already performed to increase sample size and therefore statistical analysis of the differences in RM concentrations. This would include use of the calibrator system to load filters to repeat long-term behavior and RM retention tests on filters loaded with RM and then held in jars or with ambient air drawn through.

To test the differences in concentrations between 24 h samples and 3 day or two week samples an inlet system like the UNRRMAS should be setup and run for 24 h samples at 16.7 Lpm collocated with a TAPI and the UNRRMAS. This would allow for collection of samples without a PM inlet at 16.7 Lpm with a second filter inline to collect breakthrough. Comparing these 24 h measurements to the two week UNRRMAS samples would confirm if the inlet was the main difference between TAPI and UNRRMAS measurements. If 24 h measurements from the modified UNRRMAS setup at 16.7 Lpm averaged to two weeks were still lower than the UNRRMAS this would indicate that the higher flow rate of the TAPI setup is likely altering RM retention on the CEM. Ambient tests could then be performed at varying sample lengths, flow rates, and CEM filter sizes to determine the relationship between sample length, flow rate, and RM retention.

To reduce loss of RM to the TAPI inlet, it would be necessary to heat the inlet. The Tekran sample line is heated to 50 °C, however several studies have indicated that 100 °C is more efficient at reducing losses to inlets (Huang et al., 2013; McClure et al., 2014). Heating the inlet could lead to loss of volatile $PM_{2.5}$ (Deary et al., 2016). This would require either determining calibration factors to apply to heated line $PM_{2.5}$ measurements to correct for loss of volatile species, or reconfiguring the TAPI to use Teflon reference filters to measure $PM_{2.5}$ mass concentrations on the unheated Teflon line.

The UNRRMAS currently has no inlet in front of the filters. It is possible that the TAPI, with a $PM_{2.5}$ inlet, would measure different RM concentrations from UNRRMAS even if loss of RM to the sample line was minimized. The UNRRMAS filters have visible particles on the surface of the filters and are therefore, collecting particulate matter, and likely some PBM. It is assumed that the UNRRMAS collects mainly GOM based on comparison with a Tekran system in ambient and laboratory air (Huang et al., 2013), however, this has not been empirically tested. To test this a Teflon filter could be installed in front of the UNRRMAS that would theoretically collect particulate matter and, therefore, PBM but not GOM. If there were differences in RM concentrations on the UNRRMAS CEM with and without a Teflon filter in front, the difference could theoretically be attributed to PBM. Care would need to be taken in addressing the difference in airflow the Teflon filter would create.

These improvements and further tests would address several of the deficiencies reported for this research objective. Several of these improvements would also benefit the second and third research objective.

2.2 Research objective 2

The second research objective was to use the Pb isotope data from the TAPI, in addition to a suite of other measurements, to identify sources of RM and elevated O_3 to Nevada. At the two higher elevation rural sites, Peavine Peak and Great Basin National Park, RM was negatively correlated with indicators of trans-Pacific sources, suggesting that RM was removed from air masses due to deposition or conversion to elemental Hg before reaching the sample sites. Positive correlations between RM and O_3, indicated formation of RM from photo-oxidation of GEM in dry upper altitude air. The positive correlations with regional indicators also indicated that regional sources of oxidants facilitated production of RM.

Peavine Peak and Great Basin National Park also had higher concentrations of O_3 and smaller daily ranges in concentration than the lower elevation, urban site, indicating access to free tropospheric air and limited photochemical production during the day. Back trajectory analyses and Pb isotopic composition indicated that trans-Pacific air masses influenced the Western USA in spring through fall of 2014 and 2015. Sources of atmospheric pollutants to the measurement sites included regional urban centers and wildfires, and long-range transport of urban and wildfire emissions from Eurasia, enhancing O_3 concentrations at the surface, at times approaching or exceeding the NAAQS. Regional sources (e.g. San Francisco, CA; marine boundary layer) to the high elevation site in western Nevada, Peavine Peak, differed from regional sources (e.g. Los Angeles, CA; Las Vegas, NV) to the high elevation site in eastern Nevada, Great Basin National Park.

Ozone was elevated following low-pressure systems with associated cold fronts, due to subsidence of cold air following the front. High-pressure systems and cyclonic flow aloft also facilitated subsidence of air with elevated O_3. The high convective mixing in summer caused entrainment of free tropospheric air. Differences between the two sites on either side of the State indicate that multiple measurement sites are needed to characterize pollution events in Nevada.

Objective two would also benefit from longer sample periods and three TAPI instruments located at each measurement site, allowing for Pearson correlations at the three sites on a seasonal basis. O_3 concentrations have strong seasonal variation and correlations using seasonal data would have provided a clearer association between O_3 concentrations and sources.

Comparing measurements of O_3 from this study to longer-term measurements would have been helpful in determining if any changes in air quality trends had occurred. The initial years of O_3 measurements by the NVROI were documented in Fine et al. (2015a; 2015b), Gustin et al. (2015), and Miller et al. (2015), while O_3 and Pb measurements were documented in Christensen et al. (2015). Although most NVROI monitoring sites had been taken off line, O_3 measurements from the Great Basin National Park CASTNET site are available for characterizing long-term trends in O_3 to assess how the measurements from this study compared.

Instead of choosing specific events for Pb isotope analysis, having Pb isotopes for longer, directed periods, for several months or for the whole sample period at all three sites would have aided in tracking air masses as they moved across Nevada and influenced the specific events identified in this objective. Choosing specific events for Pb

isotope analysis instead of having continuous samples hindered the ability to illustrate the progression of air masses across the State. More Pb isotope data would have also been useful in the Pearson correlations and would have reduced the bias towards O_3 events inherent in analyzing limited samples.

Determining whether O_3 was contributed from the O_3 rich stratosphere or was transported in the troposphere would aid in further identifying sources of O_3 to the measurement sites. Stratospheric O_3 contributions to the troposphere cannot be directly measured and are poorly constrained in atmospheric models due to the episodic nature and limited measurements to characterize events (Lin et al., 2012; Zhang et al., 2011). However, integrating tropospheric O_3 measurements from satellites, aircraft, lidar, and ozonesondes with surface measurements and model outputs (e.g. GFDL AM3) would aid in improving vertical resolution and spatial coverage of O_3 concentrations and chemistry.

Isentropic Potential Vorticity (IPV) from the National Oceanic and Atmospheric Administration (NOAA) product, TOAST (Total Ozone Analysis using Solar Backscatter Ultrviolet Version 2 [SBUV/2] and Advanced Tiros-N Operational Vertical Sounder [TOVS]) has been used to characterize stratospheric intrusions (Sullivan et al., 2015). The stratosphere has higher potential vorticity than the troposphere due to the static stability of the stratosphere, and can therefore be used, along with low dew points and high O_3 concentrations, to identify stratospheric intrusions (Wallace and Hobbs, 2006).

Other measurements that would aid in identifying stratospheric intrusions include oxygen isotope measurements in CO_2 and beryllium. Isotopic composition of the oxygen in CO_2 is different when formed in the upper atmosphere with O_3 and O_2 photochemistry and can therefore be distinguished from the isotopic composition of oxygen in CO_2

formed via biogenic and atmospheric processes at the surface (Liang and Mahata, 2015). Beryllium (^{7}Be) is mainly produced above the tropopause and is therefore a good tracer of stratospheric air (Elbern et al., 1997). O_3/CO ratios have also previously been used to identify upper troposphere/lower stratosphere influence (slope of -1.3 O_3/CO with little influence from Asian long-range transport) and would aid in distinguishing between stratospheric input and long-range input or a mix of the two, based on the slope. This ratio would have been useful to asses in this study as O_3 and CO were measured at all three measurement sites (Ambrose et al., 2011; Stohl et al., 2000).

Total O_3 products from NOAA's Global Ozone Monitoring Experiment 2 (GOME2) of Geostationary Operational Environmental Satellite (GOES) would be helpful in identifying high O_3 events in upper levels of the atmosphere and could also be used to characterize subsidence of stratospheric O_3. Longitudinal cross section data from the Real-Time Air Quality Modelling-system (RAQMS) for high O_3 events would also aid in understanding entrainment and subsidence of air masses across Nevada.

Measurements of reactive nitrogen oxides (NO_y = NO_x + nitric acid [HNO_3] + nitrate radical [NO_3] + nitrous acid [HONO] + peroxyacetyl nitrate [PAN] + other organic nitrogen compounds), hydroxyl radicals (OH), and volatile organic compounds (VOCs) would aid in understanding the atmospheric chemistry occurring at each measurement site. The ratio of NO_x to NO_y is indicative of the oxidant formation that has occurred in an air mass and therefore the relative age (NRC, 1991). Larger NO_x to NO_y ratios would indicate local sources. OH measurements would also be a good indication of the reactions occurring and the oxidizing capacity of the atmosphere. VOC concentration and species measurements would aid in identifying anthropogenic (mobile and stationary)

and biogenic sources of VOCs and the contribution to O_3 production based on reactivity of the VOCs present.

These improvements and added measurements would enhance source and source region identification in this research objective and would aid in better quantification of O_3 enhancements during discreet events. Development of instruments that are low cost and easy to deploy, will continue to be necessary to understand sources of atmospheric pollutants in underrepresented rural sites.

2.3 Research objective 3

The third objective was to apply a statistical method to data collected by the TAPI to better understand the sources and physical processes affecting horizontal and vertical heterogeneity of atmospheric pollutants at adjacent valley and peak measurement sites in Reno, NV, USA. Air pollution gradients were observed between the two sites in the Reno valley and at higher elevation, Peavine Peak. The two valley sites, located ~1.4 km apart, had statistically different concentration of O_3, carbon monoxide (CO), oxides of nitrogen (NO_x), nitrogen oxide (NO), and sulfur dioxide (SO_2). CO, NO_x, and NO were enhanced close to the highways due to mobile sources, while O_3 and SO_2 were influenced by mobile sources but were also enhanced further from the highway due to chemical reactions and non-point sources. Peavine Peak, ~12 km away and ~1.2 km higher in elevation than the valley sites, had higher concentrations of O_3, and lower concentrations of CO and $PM_{2.5}$. Ozone at Peavine Peak was not necessarily dependent on distance from the highways as the site experienced limited photochemical production of O_3 during the day and was influenced by stratospheric mixing of O_3. Lower concentrations of CO and

$PM_{2.5}$ at Peavine Peak were indicative of distance from sources (highways and non-point) in the valley. Horizontal gradients of pollutants, different distances from high volume highways, will affect exposure to pollutants in metropolitan areas with <500,000 people, such as Reno, NV, USA, and are therefore important to monitor.

Major sources and physical processes affecting vertical gradients in Reno, NV, USA identified using the quadrant method were: 1) unstable conditions leading to a well-mixed boundary layer and mixing of local pollutants; 2) stable atmospheric conditions with accumulation of local pollutants; 3) transport and mixing of smoke plumes; and 4) transport of pollution aloft. Use of the 24 h surface measurements with columnar measurements, aided in performing statistical investigations of the sources and atmospheric processes affecting the transport of aerosols in complex terrain. Applying the quadrant method to 24 h $PM_{2.5}$ data increases the applicability of the method for rural and remote sites that often only have 24 h samples. Comparison to a previous study demonstrated the importance of site location of the ground-based, columnar aerosol optical depth and surface $PM_{2.5}$ measurement instruments for use in the quadrant method.

Complex terrain, long-range transport, and wildfires made it difficult to reconcile columnar and surface measurements for specific events. Difficulties arose when trans-Pacific transport was present, due to the semi-continuous contribution of trans-Pacific pollution throughout the year (VanCuren, 2003; VanCuren et al., 2005), but in low concentrations or present in filamentous air masses, that were not easily distinguishable from local pollutants. Wildfire plumes transported aloft mixing with long-range pollution transported aloft will also present problems for separating influence specific to wildfires and to long-range sources.

Further testing of the quadrant method, across the Western USA, is necessary to characterize sources and atmospheric processes affecting the relationship between columnar and surface observations. Future studies should focus on inland sites in the Western USA, with different elevations, and during different fire regimes. Application of the quadrant method for other atmospheric pollutants, using a paired valley and peak site, would also be useful in identifying processes that affect other pollutants. Similarly to the aerosol column retrievals, column and surface observations of gases could be used to identify processes affecting the distribution of these gases, for example, column retrievals of O_3 and surface measurements. Column O_3 is retrieved from satellites (e.g. Total Ozone Mapping Spectrometer [TOMS], GOME2) and from ground-based instruments (e.g. Dobson spectrophotometers) much like aerosol optical depth (Cracknell and Varotsos, 2012). O_3 variability in stratospheric air due to latitude and longitude can be subtracted from total column O_3, allowing for quantification of tropospheric O_3 (Cracknell and Varotsos, 2012; Hudson et al., 1995; McKenzie et al., 1991). Differences in tropospheric O_3 and surface O_3 observations can then be used in a similar manner as columnar and surface aerosol optical depth observations in the quadrant method. O_3 confined to the surface would indicate anthropogenic and biogenic sources, O_3 aloft but not observed at the surface would indicate long-range transport and stratospheric input. Diel patterns of hourly O_3 concentrations could also be used with ground-based columnar O_3 retrievals to identify discreet pollution events that differ from daily processes. Measurement issues over bright surfaces and clouds would have to be taken into account for satellite column O_3 retrievals (Fishman and Larsen, 1987; Hudson et al., 1995).

Measurements of the O_3 vertical profile at each site would also aid in understanding the vertical distribution of column O_3. These measurements include ozonesondes, instruments mounted on aircraft, or ground based measurements such as a Dobson or Brewer spectrophotometer that measures the ratio of zenith sky radiance during sunrise and sunset at two wavelengths that strongly and weakly absorb O_3 to determine O_3 concentrations at different heights (Cracknell and Varotsos, 2012).

A major limitation of this study was the missing winter and spring data, therefore this objective would have also benefitted from longer sample periods when the Cimel was not out for calibration, with the TAPI located at Peavine Peak for the entire sample period. Aerosol optical depth measurements at each measurement site would be necessary to fully evaluate the statistical results for each site. Applying the quadrant method to 24 h data from more sites across the Western USA would have increased the use of the quadrant method and allowed for further evaluation of the statistical results. For horizontal gradients, a transect of measurement sites from the highways along the prevailing wind direction would have provided a clearer measure of the gradients of pollutants (Karner et al., 2010; Riley et al., 2014).

Adding a variable to use in the quadrant method for distinguishing stratospheric and long-range inputs is necessary to better characterize data in the fourth quadrant (pollution aloft). This variable could be O_3/CO ratios, which would be readily available at many sites, or any of the measurements discussed in the recommendations for objective two.

It will also be necessary to develop a method for determining relationships between columnar and surface observations during nighttime and cloudy periods when

aerosol optical depth measurements are not available but sources and physical processes continue to affect measurement sites. Use of the quadrant method to identify different sources and processes at a site may also be used to identify periods when a site is impacted by an exceptional event, such as plumes from a wildfire.

2.4 Research objective 4

The fourth objective was to investigate possible sources of anomalous particulate matter collected at one of the sample sites during the sample period. The anomalous samples would either indicate that particles that behaved differently from ideal spherical particles were observed at this site or that the TAPI setup introduced an artifact to the samples.

The presence of fires and fire indicators, high relative humidity, high wind speeds, use of diesel generators onsite, and elemental composition were investigated to understand the presence of ambient particles > 2.5 μm in aerodynamic diameter on 36 measurement days from June to November 2014. High concentrations of certain elements (aluminum and oxygen) on the aggregate samples indicated that sections of aluminum sample tubing may have been rubbing together, due to prolonged, high wind speed events, causing particles of aluminum to form within the sample line and deposit on the sample filters. Other methods for measuring particulate matter, used as FEM, have similar inlet designs. Not all of these methods post-process the sample filters and therefore do not observe sample filter surfaces on a regular basis. At sites with high wind speeds, it is possible that a similar situation could be observed and would artificially

increase particulate matter concentrations. More experiments are needed to test this conclusion.

It would be useful to collocate multiple particulate monitors (TAPI, FEM, FRM) at the Peavine Peak site, and other sites with high wind events, to determine if this phenomena could be replicated and observed using other instruments. This would require accurate measurements of wind speed and direction, which were challenging during this sample period due to high wind speeds and constraints on location of wind vanes at Peavine Peak.

To determine if generator exhaust was the cause of aggregates, generator filters could be analyzed using scanning electron spectroscopy and energy dispersive x-ray spectroscopy to determine morphology and elemental composition of the samples collected during generator use. It would also be useful to have information on the generators used at the site (i.e. days that generators were in use, type of generator, fuel used, lubricating oil used, etc.) Fractal properties of the aggregates would also be useful in quantifying differences in the morphology of the aggregates.

The results from this objective highlight the need to carefully pick site locations and to assess samples collected with a suite of other measurements to identify any issues that may arise.

3. General conclusions and recommendations

Since the current research began, the operation of the monitoring sites across Nevada has ended. Particulate matter is only monitored in the major urban centers and at three non-urban sites, while O_3 is only monitored in the major urban centers and at two

non-urban sites in northern and eastern Nevada. However, monitoring across rural areas of the Western USA will continue to be essential for improving the understanding of the complex processes affecting atmospheric pollutants. Limited measurement sites across Nevada or the Western USA will not be sufficient for understanding sources and atmospheric processes affecting atmospheric pollutant concentrations in this large mountainous state. This is illustrated by the differences in regional sources to the west and east side of the State and the effects of frontal activity. Ozone concentrations will continue to approach or exceed the NAAQS across rural Nevada, and likely other parts of Western USA; however, regional or global sources of pollution are not reasonably controllable by the State. As industrialization and human population continue to grow both in the USA and globally, it is important to have measurements of atmospheric pollutants and an understanding of the processes affecting pollutants as sources increase and change. Rural Nevada intercepts regional and long-range transport, but has few local sources and is therefore an ideal area for measuring changes in regional air quality.

A novel method for tracing sources of pollution was developed and deployed. The TAPI is useful in targeted campaigns but may be too complex and expensive to deploy for monitoring at finer spatial scales. In addition, possible instrument artifacts may occur at sites with prolonged, high wind events. Diversifying measurement methods of RM aided in understanding spatial and temporal differences in concentrations and identified areas of further research. The addition of Pb isotope data from the $PM_{2.5}$ samples and use of back trajectory analyses improved the understanding of source regions affecting air pollution in Nevada. Refining our understanding of the relationship between columnar and surface measurements improved identification of atmospheric processes and sources

of pollutants. The results of this research could aid in identifying exceptional events, and could increase spatial coverage of surface measurements in rural areas, if used to improve estimates of surface concentrations of pollutants and therefore health exposures from satellite measurements. Due to lack of atmospheric boundaries and the chemistry that can occur downwind of a source, particularly in complex terrain, development and use of versatile and robust measurement platforms is necessary to identify sources and conditions affecting air pollution.

References:

Ambrose JL, Reidmiller DR, Jaffe DA. Causes of high O3 in the lower free troposphere over the Pacific Northwest as observed at the Mt. Bachelor Observatory. Atmospheric Environment 2011; 45: 5302-5315.

Christensen JN, Weiss-Penzias P, Fine R, McDade CE, Trzepla K, Brown ST, et al. Unraveling the sources of ground level ozone in the Intermountain Western United States using Pb isotopes. Science of The Total Environment 2015; 530–531: 519-525.

Cracknell AP, Varotsos CA. Remote Sensing and Atmospheric Ozone: Springer, 2012.

Deary ME, Bainbridge SJ, Kerr A, McAllister A, Shrimpton T. Practicalities of mapping PM(10) and PM(2.5) concentrations on city-wide scales using a portable particulate monitor. Air Quality, Atmosphere, & Health 2016; 9: 923-930.

Elbern H, Kowol J, Sládkovic R, Ebel A. Deep stratospheric intrusions: a statistical assessment with model guided analyses. Atmospheric Environment 1997; 31: 3207-3226.

Fine R, Miller MB, Burley J, Jaffe DA, Pierce RB, Lin M, et al. Variability and sources of surface ozone at rural sites in Nevada, USA: Results from two years of the Nevada Rural Ozone Initiative. Science of The Total Environment 2015a; 530–531: 471-482.

Fine R, Miller MB, Yates EL, Iraci LT, Gustin MS. Investigating the influence of long-range transport on surface O3 in Nevada, USA, using observations from multiple measurement platforms. Science of The Total Environment 2015b; 530–531: 493-504.

Fishman J, Larsen JC. Distribution of total ozone and stratospheric ozone in the tropics: Implications for the distribution of tropospheric ozone. Journal of Geophysical Research: Atmospheres 1987; 92: 6627-6634.

Gustin MS, Fine R, Miller M, Jaffe D, Burley J. The Nevada Rural Ozone Initiative (NVROI): Insights to understanding air pollution in complex terrain. Science of The Total Environment 2015; 530–531: 455-470.

Huang J, Gustin MS. Uncertainties of Gaseous Oxidized Mercury Measurements Using KCl-Coated Denuders, Cation-Exchange Membranes, and Nylon Membranes: Humidity Influences. Environmental Science & Technology 2015; 49: 6102-6108.

Huang J, Miller MB, Weiss-Penzias P, Gustin MS. Comparison of Gaseous Oxidized Hg Measured by KCl-Coated Denuders, and Nylon and Cation Exchange Membranes. Environmental Science & Technology 2013; 47: 7307-7316.

Hudson RD, Kim J-H, Thompson AM. On the derivation of tropospheric column ozone from radiances measured by the total ozone mapping spectrometer. Journal of Geophysical Research: Atmospheres 1995; 100: 11137-11145.

Karner AA, Eisinger DS, Niemeier DA. Near-Roadway Air Quality: Synthesizing the Findings from Real-World Data. Environmental Science & Technology 2010; 44: 5334-5344.

Liang M-C, Mahata S. Oxygen anomaly in near surface carbon dioxide reveals deep stratospheric intrusion. Scientific Reports 2015; 5: 11352.

Lin M, Fiore AM, Cooper OR, Horowitz LW, Langford AO, Levy H, et al. Springtime high surface ozone events over the western United States: Quantifying the role of stratospheric intrusions. Journal of Geophysical Research: Atmospheres 2012; 117: n/a-n/a.

Lyman SN, Gustin MS, Prestbo EM, Kilner PI, Edgerton E, Hartsell B. Testing and Application of Surrogate Surfaces for Understanding Potential Gaseous Oxidized Mercury Dry Deposition. Environmental Science & Technology 2009; 43: 6235-6241.

McClure CD, Jaffe DA, Edgerton ES. Evaluation of the KCl Denuder Method for Gaseous Oxidized Mercury using HgBr2 at an In-Service AMNet Site. Environmental Science & Technology 2014; 48: 11437-11444.

McKenzie RL, Johnston PV, McElroy CT, Kerr JB, Solomon S. Altitude distributions of stratospheric constituents from ground-based measurements at twilight. Journal of Geophysical Research: Atmospheres 1991; 96: 15499-15511.

Miller MB, Fine R, Pierce AM, Gustin MS. Identifying sources of ozone to three rural locations in Nevada, USA, using ancillary gas pollutants, aerosol chemistry, and mercury. Science of The Total Environment 2015; 530–531: 483-492.

NRC NRC. Rethinking the Ozone Problem in Urban and Regional Air Pollution. Washington, DC: The National Academies Press, 1991.

Peterson C, Alishahi M, Gustin MS. Testing the use of passive sampling systems for understanding air mercury concentrations and dry deposition across Florida, USA. Science of The Total Environment 2012; 424: 297-307.

Riley EA, Banks L, Fintzi J, Gould TR, Hartin K, Schaal L, et al. Multi-pollutant mobile platform measurements of air pollutants adjacent to a major roadway. Atmospheric Environment 2014; 98: 492-499.

Stohl A, Spichtinger-Rakowsky N, Bonasoni P, Feldmann H, Memmesheimer M, Scheel HE, et al. The influence of stratospheric intrusions on alpine ozone concentrations. Atmospheric Environment 2000; 34: 1323-1354.

Sullivan JT, McGee TJ, Thompson AM, Pierce RB, Sumnicht GK, Twigg LW, et al. Characterizing the lifetime and occurrence of stratospheric-tropospheric exchange events in the rocky mountain region using high-resolution ozone measurements. Journal of Geophysical Research: Atmospheres 2015; 120: 12410-12424.

VanCuren RA. Asian aerosols in North America: Extracting the chemical composition and mass concentration of the Asian continental aerosol plume from long-term aerosol records in the western United States. Journal of Geophysical Research: Atmospheres 2003; 108: 4623.

VanCuren RA, Cliff SS, Perry KD, Jimenez-Cruz M. Asian continental aerosol persistence above the marine boundary layer over the eastern North Pacific: Continuous aerosol measurements from Intercontinental Transport and Chemical Transformation 2002 (ITCT 2K2). Journal of Geophysical Research: Atmospheres 2005; 110: D09S90.

Wallace JM, Hobbs PV. 7 - Atmospheric Dynamics. Atmospheric Science (Second Edition). Academic Press, San Diego, 2006, pp. 271-311.

Zhang L, Jacob DJ, Downey NV, Wood DA, Blewitt D, Carouge CC, et al. Improved estimate of the policy-relevant background ozone in the United States using the GEOS-Chem global model with 1/2° × 2/3° horizontal resolution over North America. Atmospheric Environment 2011; 45: 6769-6776.

Appendix A

Supplemental Information

Development of a particulate mass measurement system for quantification of ambient reactive mercury

Ashley M. Pierce*, Mae Sexauer Gustin

Department of Natural Resources and Environmental Sciences, University of Nevada, Reno 1664 N. Virginia St. Reno, NV, USA 89557
*Corresponding Author: Ashley M. Pierce, ash.pie4@gmail.com, phone: (775) 784-4020, fax: (775) 784-4583
25 pages, 3 Tables, and 19 Figures.

Published: *Environmental Science & Technology* (Web: 2016, Print: 2017)

Site Description

Nevada is located between 120º and 114 º W longitude, and 35 º and 42 º N latitude with and a mean elevation of 1676 m[1]. The main industries in Nevada include entertainment and tourism, mining (mainly gold and silver as well as other metals and minerals), and cattle ranching. Large pollution point sources consist of mines and energy generating facilities (three coal-fired and one gas-fired); smaller sources consist of mobile (e.g. transportation), line (e.g. highways and railways) and point sources (e.g. industrial). Nevada has few large sources of air pollution and generally clean, dry air. The State generally rises in baseline elevation from south and west (~600 m in southwest, ~1240 m in northwest) to northeast and east (~1800 m in east), with more than 200 mountain ranges that run north-to-south and peaks that reach close to 4000 m in some ranges. Prevailing winds from the west bring moist air up over the Sierra Mountains, where the air then cools and condenses, causing most of the moisture to precipitate out. Air moving into Nevada warms and sinks with little moisture (i.e. the rain shadow effect), which results in mainly desert and steppes in the lower elevations across the State with forests in the higher elevations[1]. High solar radiance across much of Nevada results in rapid surface heating, low annual precipitation and therefore large ranges of low and high daily temperatures[1]. Average annual precipitation varies across the State: less than 13 cm in the south, ~46 cm in the northeast and ~102 cm in the west with heavy snowfall occurring in the northern mountains[1]. Given these conditions there is high convective mixing across the State that brings free tropospheric air to valley floors[2].

The population estimate for Nevada in 2015 was 2.89 million people, with about 15 people per km^2 compared to about 149 people per km^2 in California[3]. The State has

two counties, Clark and Washoe County, containing ~87% of the population with the rest of the population spread across the state[3].

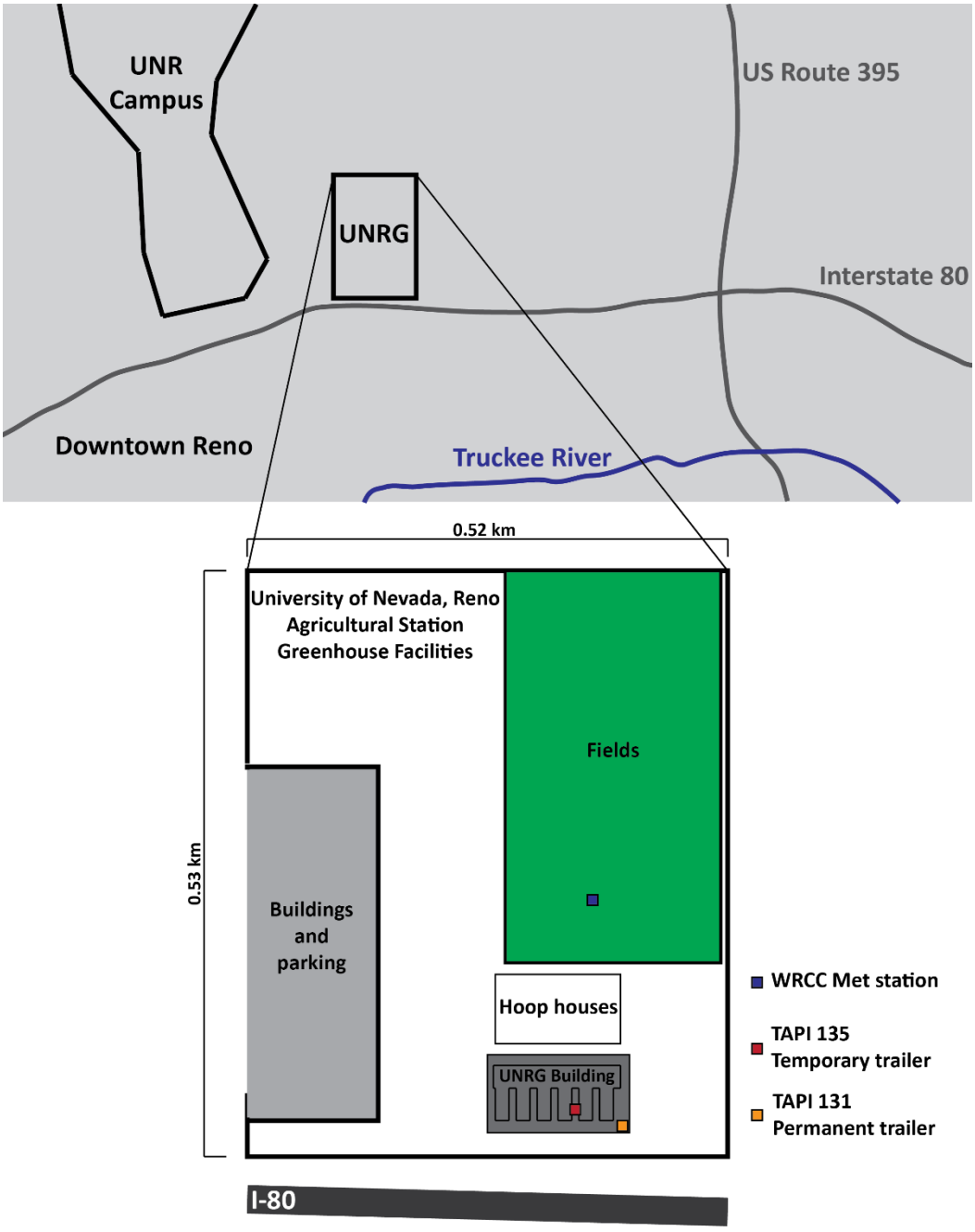

Figure SI 1: Diagram of University of Nevada, Reno Agricultural Station Greenhouse Facilities showing position next to Interstate 80 and U.S. Route 395 and location of the WRCC meteorological station (blue box), the TAPI 131 permanent trailer (yellow box), and the TAPI 135 temporary trailer (red box).

Methods:

TAPI

β particles (^{14}C source, half-life: 5,730 yr.) were passed through a filter and measured, sample was then collected on the filter, and β rays are again passed through the filter. The decrease in β particles due to the absorption by the deposited particles was used to calculate the mass of particles deposited to the filter material. The number of β particles passing through absorbing matter decreases almost exponentially related to the mass collected on the filter. Equation SI 1, similar to Beer's Law, relates the β-particle flux and the mass thickness of the filter and PM, which was then used to calculate the particulate mass concentration in air.

$$I = I_o \cdot e^{-ux} \qquad \text{Eq. SI 1}$$

Where I = Beta counts through the filter with particulates

I_o = Beta counts through the filter without particulates (blank)

u = Beta absorption constant

x = Density of absorbing matter

UNRRMAS

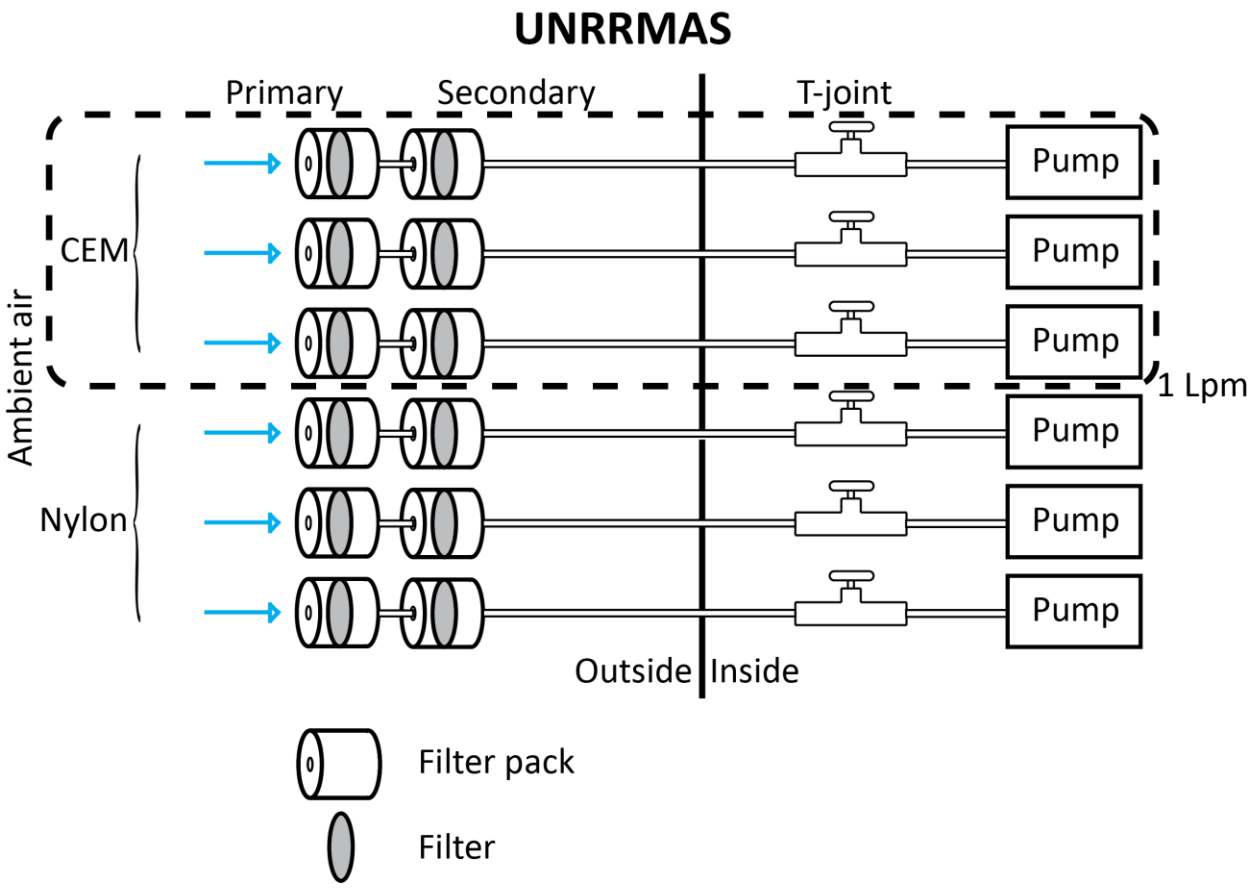

Figure SI 2: Diagram of the UNRRMAS system. Dashed black line indicates the measurements used in this study.

Total Hg analysis of CEM

Individual filters were placed in 125 mL soda-lime glass jars that were then filled with 100 mL of 1% Optima hydrogen chloride (HCl) and MilliQ (18MΩ) water. Bromine monochloride (BrCl) solution was added to the samples to make a 2% by volume solution. Samples, calibration blanks, and standards then digest for at least 12 but less than 24 h. Prior to analyses, hydroxylamine (NH_2OH) was added to an equivalent of 0.2% of the volume and allowed to react for at least 5 min to remove any halogens before analysis. Hg(II) forms in the solution were reduced to GEM using stannous chloride

($SnCl_2$) and purged from the liquid using a phase separator and ultrahigh purity argon gas. GEM was then collected on gold traps, thermally desorbed, and measured by CVAFS. Reported detection limit for the Tekran 2600 is 0.2 ng L^{-1}. The calibration curve was made using four calibration blanks followed by five standards (1, 5, 10, 25, 100 ng l^{-1}). At least four calibration standards must pass within ±5% to create a calibration curve. Ongoing Precision Recovery (OPR) samples were analyzed every ten samples and two of every ten samples were duplicates to ensure the instrument was running reliably. OPRs had to pass within ±10% in order to continue analysis.

CEM tests

The UNRG had 22 instances of breakthrough out of 149 samples that were >40%, of those 22, seven were greater than 50%. Of these 22 instances, 15 occurred during a period when a new operator of the system was starting. PEAV had no breakthrough greater than 40%; this site was started later (June 2014) than the UNRG (December 2013) and only had 29 samples.

Meteorological data

Specific humidity calculation:

$$e_s(T) = e_{s0}\exp\left[\left(\frac{L_v(T)}{R_v}\right)\left(\frac{1}{T_0}-\frac{1}{T}\right)\right] \qquad \text{Eq. SI 2a, b, c, d}$$

$$RH = \frac{e}{e_s}$$

$$w = \frac{eR_d}{R_v(p-e)}$$

$$q = \frac{w}{w+1}$$

$e_s(T)$: saturation vapor pressure (Pa)

e_{s0} : saturation vapor pressure at T_0 (Pa)

e : actual vapor pressure (Pa)

T_0 : reference temperature (273.16 K)

T : temperature (K)

$L_v(T)$: specific enthalpy of vaporization (J kg^{-1})

R_v : specific gas constant for water vapor (J kg^{-1} K^{-1})

R_d : specific gas constant for dry air (J kg^{-1} K^{-1})

RH : relative humidity as a fraction (0 to 1)

w : mass mixing ratio of water vapor to dry air (dimensionless)

p : pressure (Pa)

q : specific humidity (mass mixing ratio of water vapor to total air, dimensionless, kg kg^{-1})

Results and Discussion

Table SI 1: Descriptive statistics for $PM_{2.5}$ data at each site, indicating data is not normally distributed.

$PM_{2.5}$	WCAQ Galletti	WCAQ Reno	UNRG TAPI 131 PM	UNRG TAPI 135 PM	PEAV TAPI PM	GBNP TAPI PM	GBNP IMPROVE	GBNP EBAM
Median (µg m^{-3})	6.4	6.6	6.7	7.7	5	3.8	2.6	3
Mean (µg m^{-3})	9.4	8.4	7.7	9.2	8.3	4.4	3.3	3.4
Standard error of mean (µg m^{-3})	0.5	0.3	0.3	0.6	0.9	0.2	0.4	0.1
Confidence interval of mean (0.95) (µg m^{-3})	1.0	0.6	0.6	1.1	1.8	0.4	0.7	0.2
Variance (µg m^{-3})^2	106.1	63.1	31.1	37.9	135.7	8.7	9.1	3.6
Std deviation (µg m^{-3})	10.3	7.9	5.6	6.2	11.6	2.9	3.0	1.9
Variation coefficient	1.1	0.9	0.7	0.7	1.4	0.7	0.9	0.6
Skewness	4.1	5.6	4.5	1.5	3.4	3.2	3.6	2.0
Kurtosis	25.7	48.8	31.9	2.4	12.9	13.7	14.6	6.4
Shapiro-Wilk (S-W) test of normality	0.6	0.6	0.6	0.9	0.5	0.7	0.6	0.8
S-W probability	5.23E-28	3.13E-38	1.11E-27	1.61E-08	4.49E-20	8.90E-18	3.13E-13	2.01E-19

Table SI 2: Descriptive statistics for RM data from TAPIs at UNRG, PEAV, GBNP, indicating data is not normally distributed.

RM	UNRG TAPI 131 RM	UNRG TAPI 135 RM	PEAV TAPI RM	GBNP TAPI RM
Median (pg m^{-3})	22.18	13.22	35.69	37.87
Mean (pg m^{-3})	29.80	14.11	42.76	44.89
Standard error of mean (pg m^{-3})	1.26	0.73	2.13	2.49
Confidence interval of mean (0.95) (pg m^{-3})	2.48	1.46	4.20	4.92
Variance (pg m^{-3})^2	577.17	56.65	728.02	1088.22
Std deviation (pg m^{-3})	24.02	7.53	26.98	32.99
Variation coefficient	0.81	0.53	0.63	0.73
Skewness	1.10	0.70	1.12	0.62
Kurtosis	0.83	0.21	1.38	-0.63
Shapiro-Wilk (S-W) test of normality	0.90	0.96	0.92	0.92
S-W probability	4.94E-15	0.0053	1.20E-07	4.37E-08

Table SI 3: Descriptive statistics for Tekran Hg data at each site, indicating data is not normally distributed.

Hg	Tekran GOM	Tekran PBM	Tekran RM
Median (pg m^{-3})	12.8	9.2	23.5
Mean (pg m^{-3})	16.6	12.5	29.1
Standard error of mean (pg m^{-3})	0.7	0.8	1.3
Confidence interval of mean (0.95) (pg m^{-3})	1.4	1.6	2.5
Variance (pg m^{-3})^2	147.7	204.0	499.3
Std deviation (pg m^{-3})	12.2	14.3	22.4
Variation coefficient	0.7	1.1	0.8
Skewness	1.0	2.9	1.6
Kurtosis	0.5	12.0	3.6
Shapiro-Wilk (S-W) test of normality	0.9	0.7	0.9
S-W probability	0.0	0.0	0.0

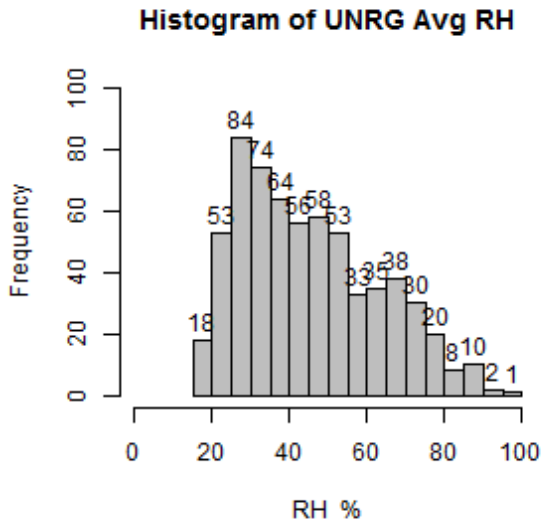

Figure SI 3: Histogram of average ambient relative humidity at UNRG

Tests of the TAPI reconfiguration for $PM_{2.5}$ measurements

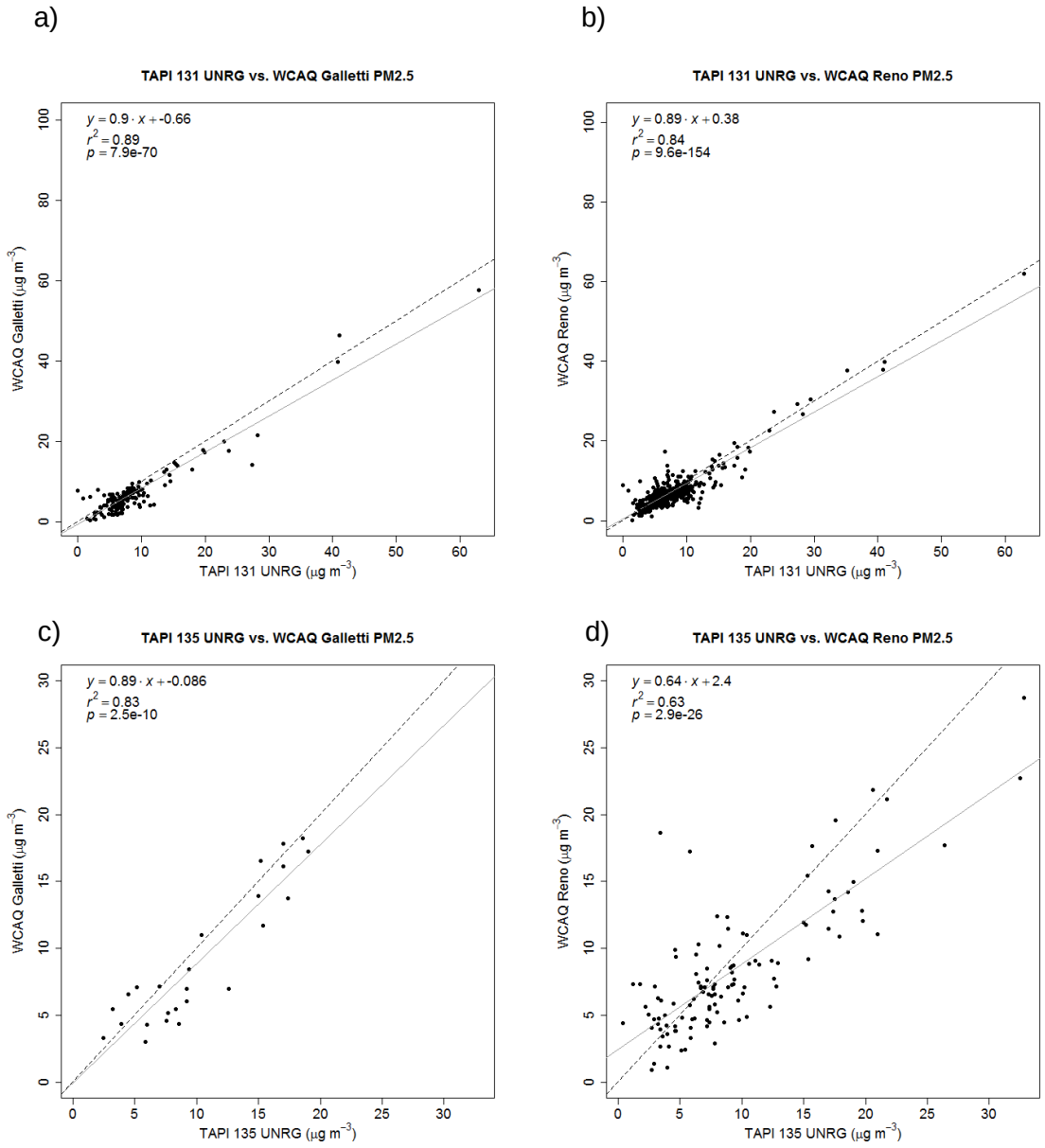

Figure SI 4: a) Regression between $PM_{2.5}$ concentration data from TAPI 131 at UNRG and the BAM-1020 at the WCAQ Galletti site, which went offline in November 2014. b) Regression between $PM_{2.5}$ concentration data from TAPI 131 at UNRG and the BAM-1020 at the WCAQ Reno site. c) Regression between $PM_{2.5}$ concentration data from TAPI 135 at UNRG and the BAM-1020 at the WCAQ Galletti site. d) Regression between $PM_{2.5}$ concentration data from TAPI 135 at UNRG and the BAM-1020 at the WCAQ Reno site. Grey line is the regression, black dashed line is the 1:1 line.

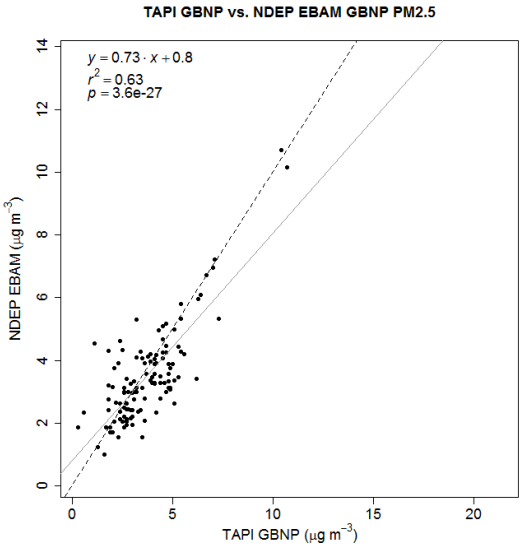

Figure SI 5: Regression for GBNP TAPI 135 and an EBAM run by NDEP at Great Basin National Park. Grey line is the regression, black dashed line is the 1:1 line.

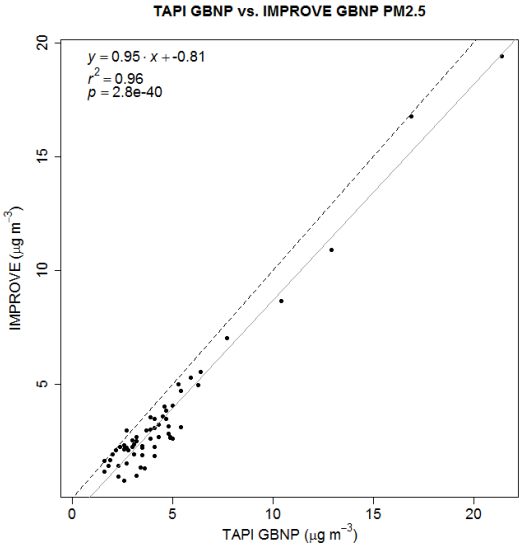

Figure SI 6: Regression for TAPI 135 and FRM IMPROVE site at Great Basin National Park. Grey line is the regression, black dashed line is the 1:1 line.

Comparison of the UNRG TAPI $PM_{2.5}$ and RM data

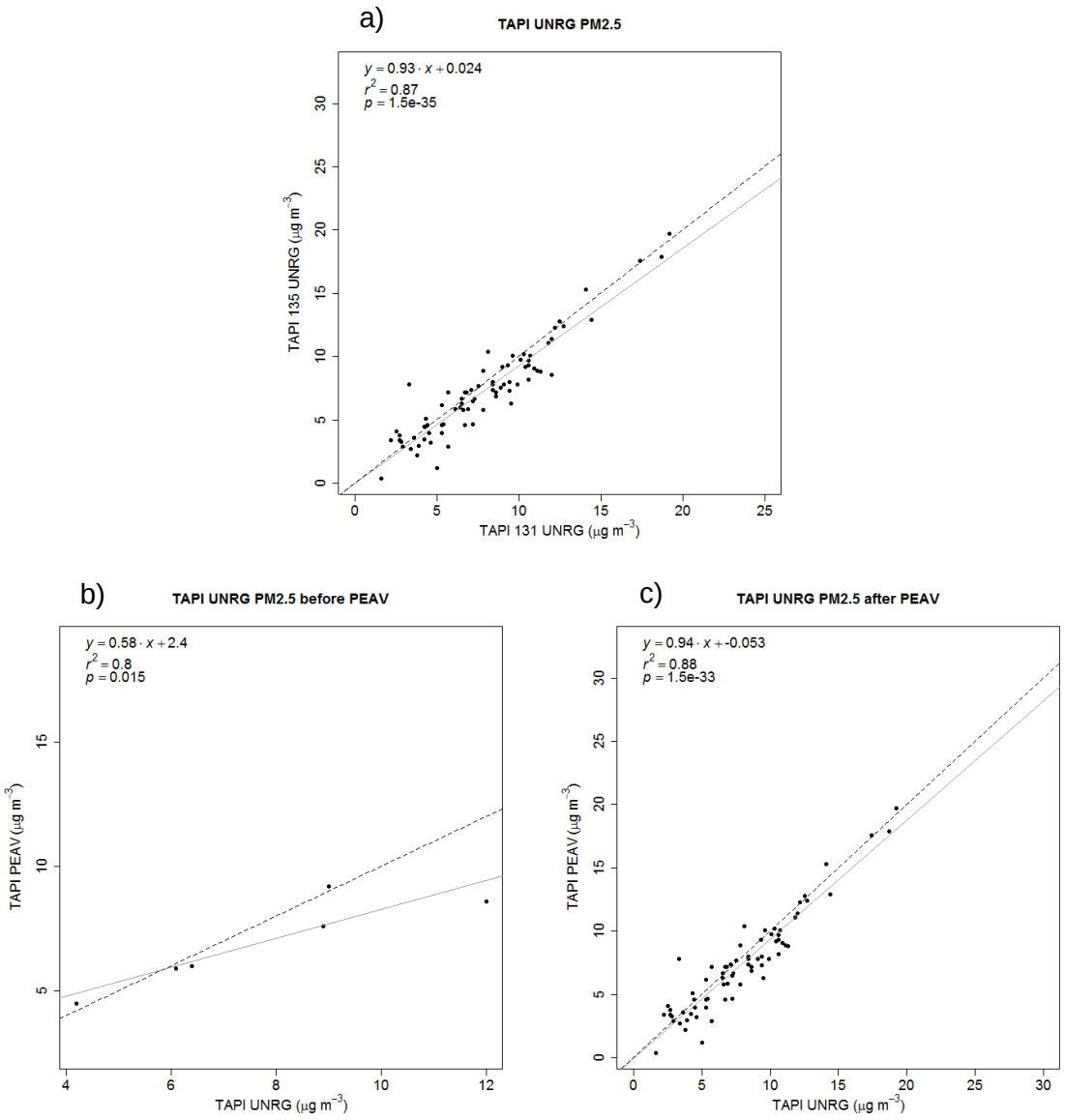

Figure SI 7: a) regression between both TAPI instruments located at UNRG in April 2014 b) from November 2014 to March 2015 c) and all data from both periods together. Grey line is the regression, black dashed line is the 1:1 line.

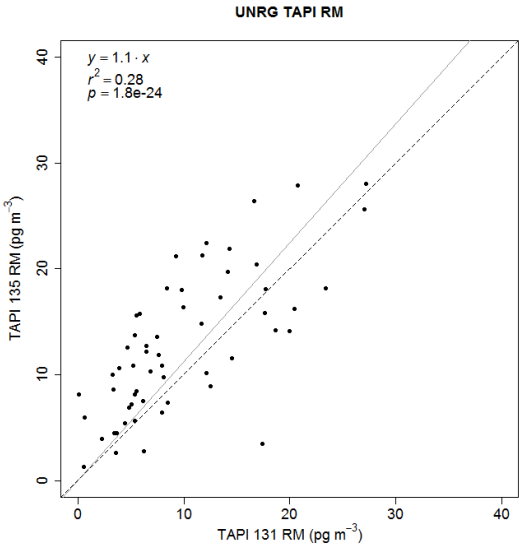

Figure SI 8: Linear regression of TAPI 131 and TAPI 135 when located at UNRG. Grey line is the regression with a forced zero intercept, black dashed line is the 1:1 line.

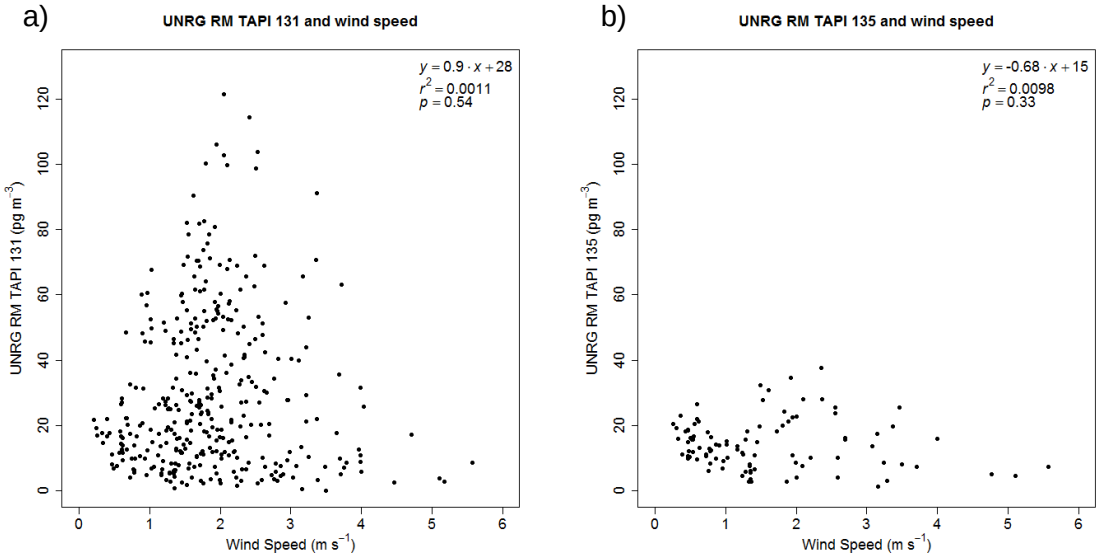

Figure SI 9: Wind speed at UNRG during a) TAPI 131 RM measurements and b) TAPI 135 measurements.

a)

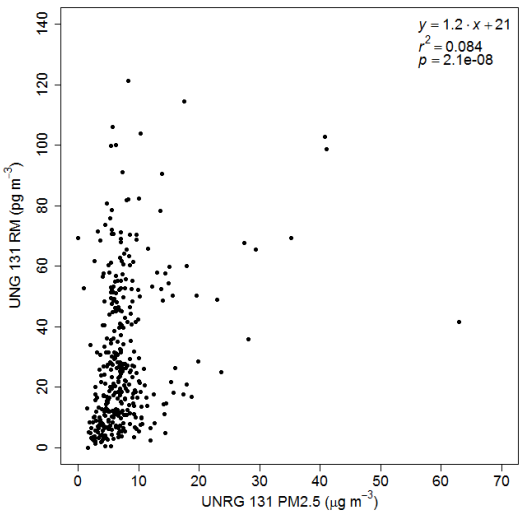
All data UNRG 131 PM2.5 and RM
y = 1.2 · x + 21
r2 = 0.084
p = 2.1e-08
UNG 131 RM (pg m-3)
UNRG 131 PM2.5 (µg m-3)
0
20
40
60
80
100
120
140
0
10
20
30
40
50
60
70

b)

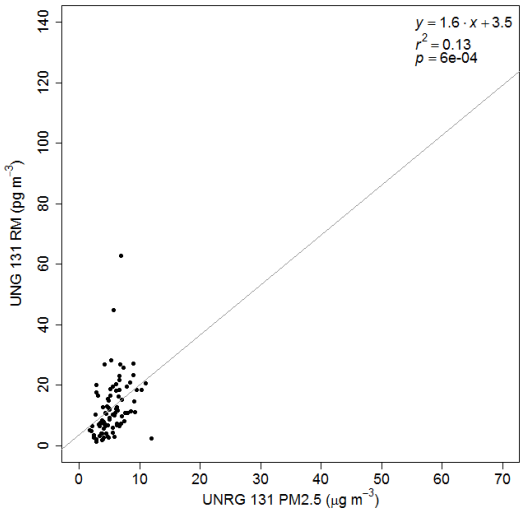
Spring UNRG 131 PM2.5 and RM
y = 1.6 · x + 3.5
r2 = 0.13
p = 6e-04
UNG 131 RM (pg m-3)
UNRG 131 PM2.5 (µg m-3)
0
20
40
60
80
100
120
140
0
10
20
30
40
50
60
70

c)

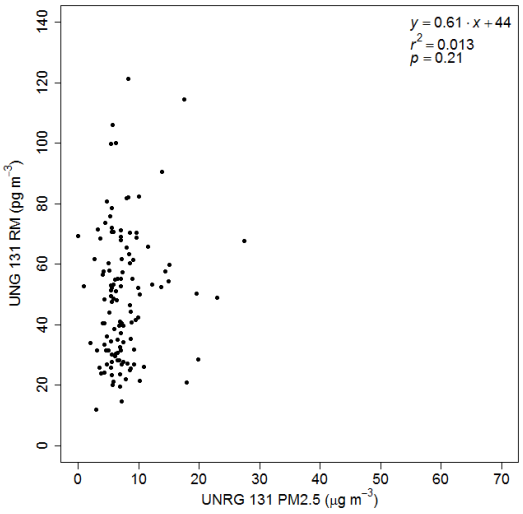
Summer UNRG 131 PM2.5 and RM
y = 0.61 · x + 44
r2 = 0.013
p = 0.21
UNG 131 RM (pg m-3)
UNRG 131 PM2.5 (µg m-3)
0
20
40
60
80
100
120
140
0
10
20
30
40
50
60
70

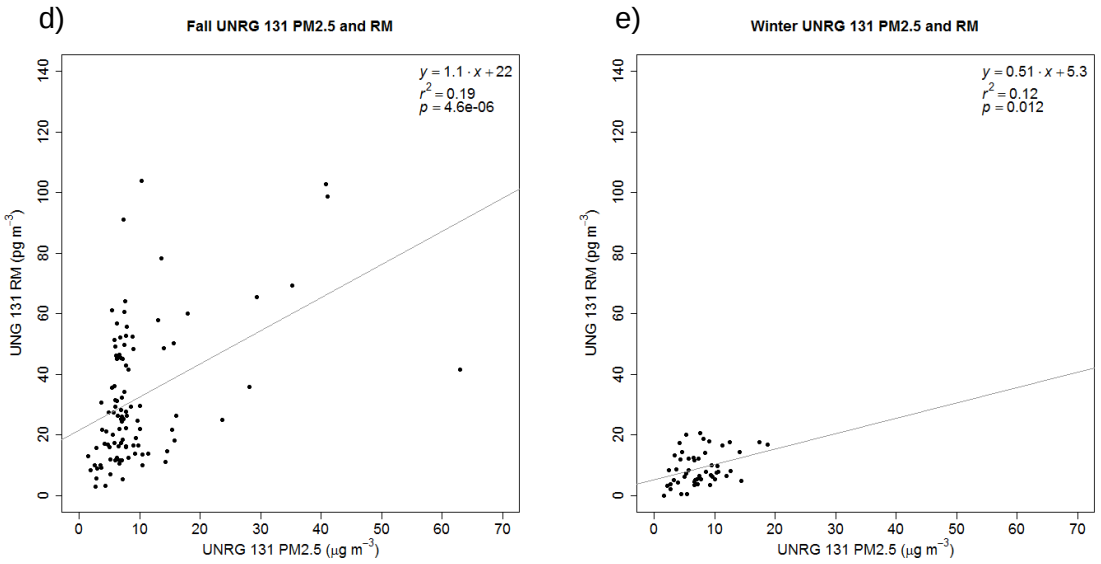

Figure SI 10: $PM_{2.5}$ and RM at UNRG for TAPI 131 a) all data, b) spring data (2014, 2015), c) summer data (2014, 2015), d) fall data (2014, 2015), and e) winter data (2014).

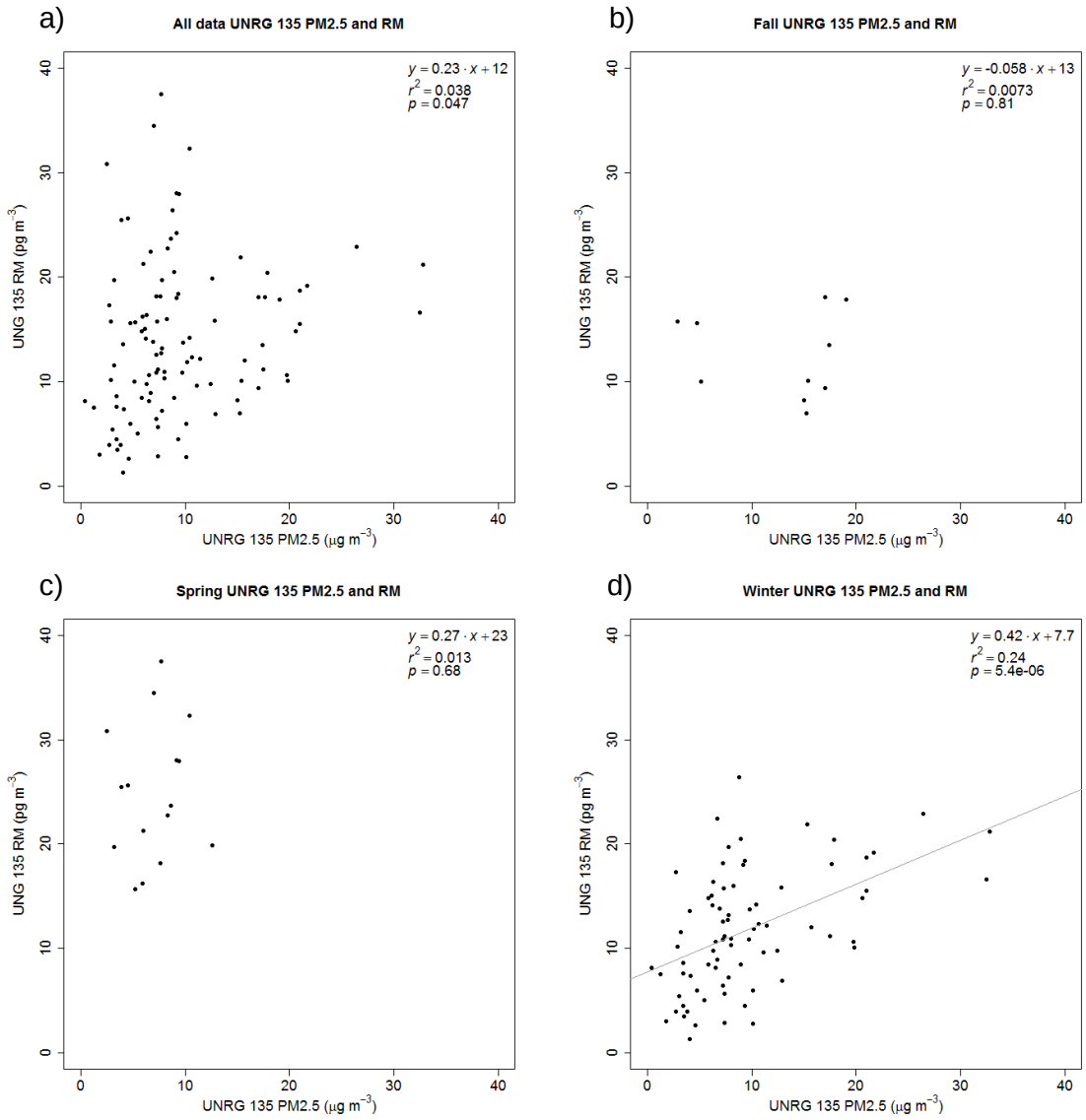

Figure SI 11: $PM_{2.5}$ and RM at UNRG for TAPI 135 a) all data, b) fall data (2013), c) spring data (2014), d) winter data (2014).

Comparison of the PEAV TAPI $PM_{2.5}$ and RM data

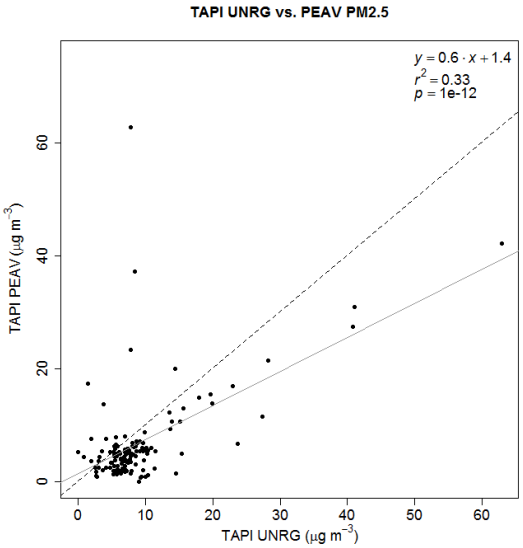

Figure SI 12: Linear regression for UNRG (TAPI 131) and Peavine Peak $PM_{2.5}$ data June to November 2014. Grey line is the regression, black dashed line is the 1:1 line.

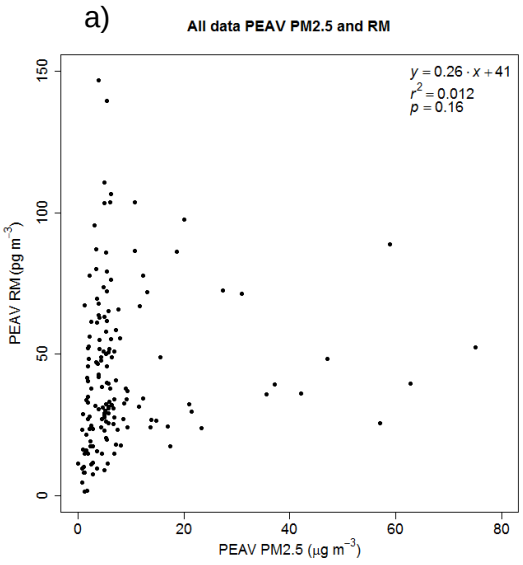

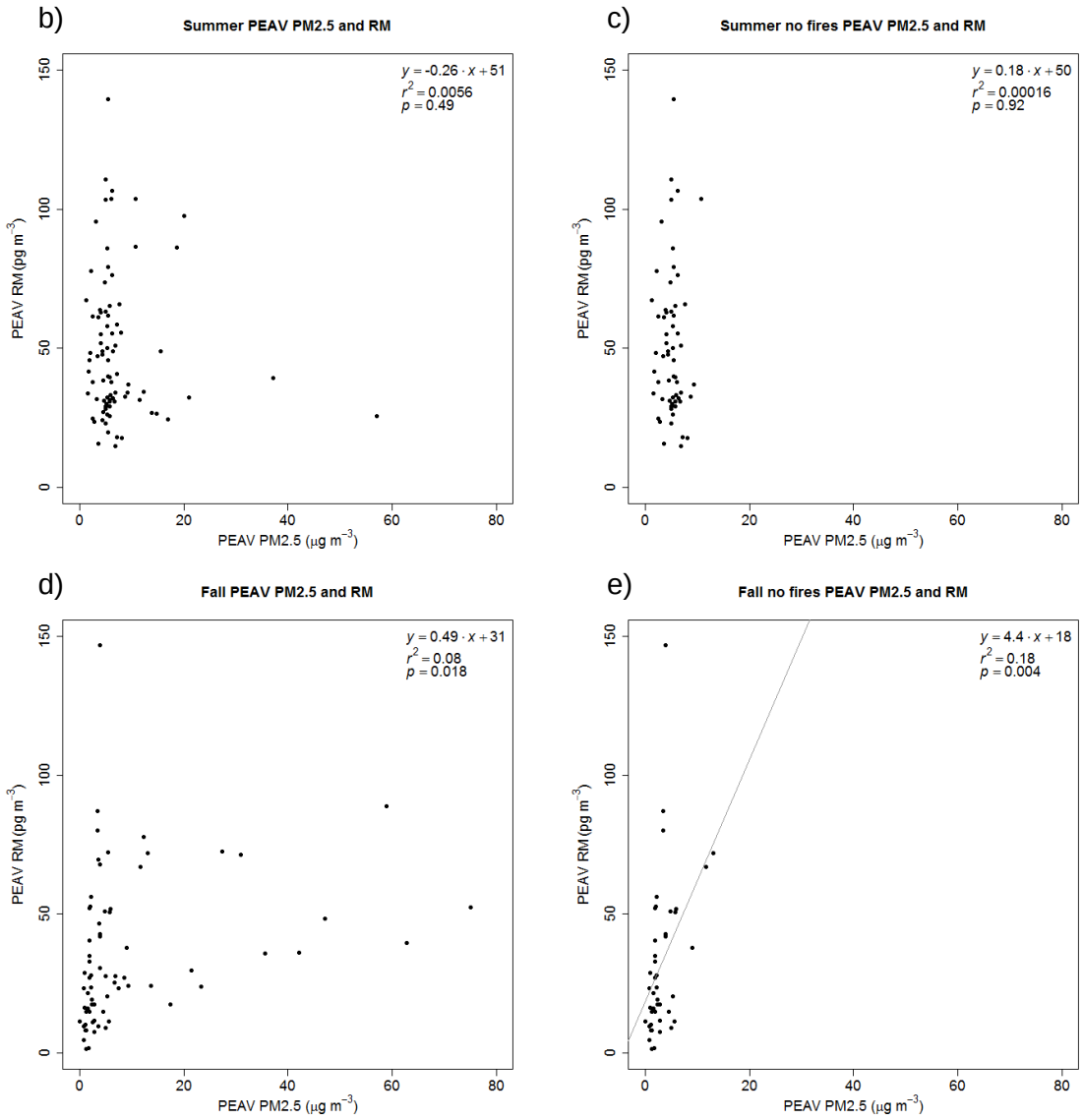

Figure SI 13: $PM_{2.5}$ and RM at PEAV a) all data, b) summer data (2014), c) summer data with no fire data (2014), d) fall data(2014), e) fall data with no fire data (2014).

Comparison of the GBNP TAPI $PM_{2.5}$ and RM data

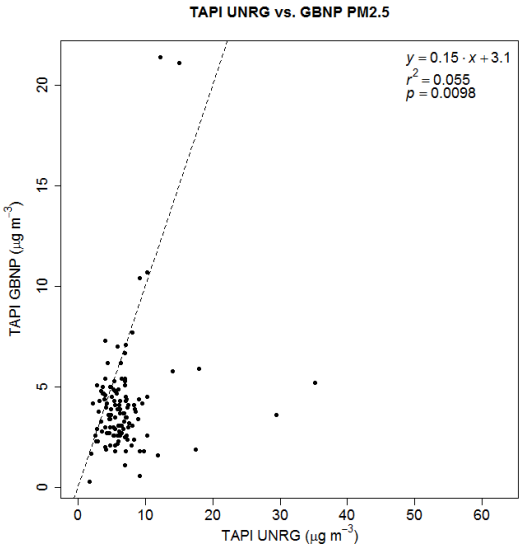

Figure SI 14: Scatter plot for UNRG TAPI and GBNP TAPI data March to October 2015. Black dashed line is the 1:1 line.

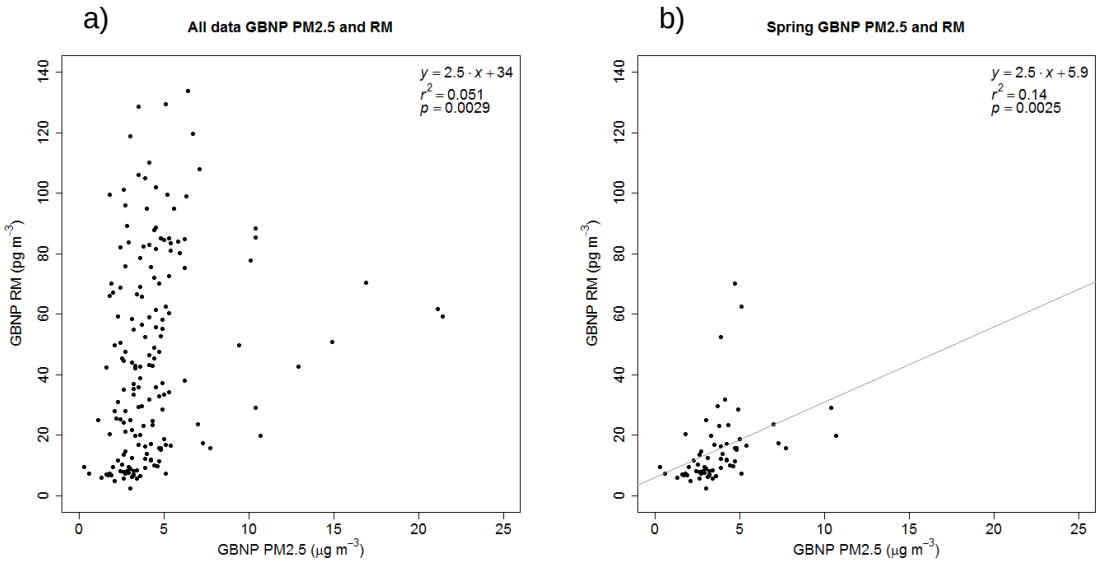

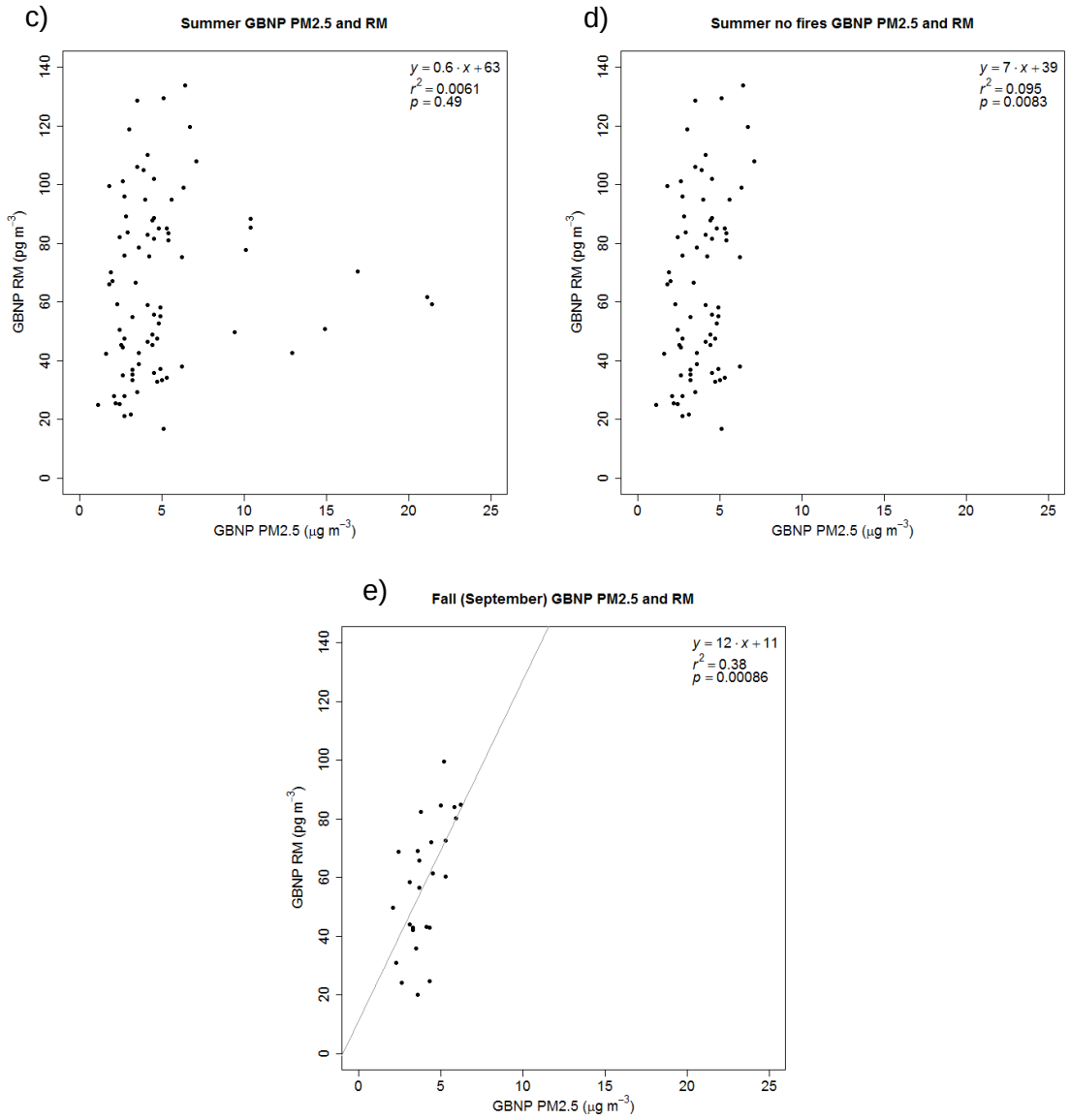

Figure SI 15: $PM_{2.5}$ and RM at GBNP a) all data, b) spring data (2015), c) summer data (2015) d) summer data without fire points in August, e) fall data (2015).

CEM tests

Inlet testing to determine loss of RM to TAPI inlet

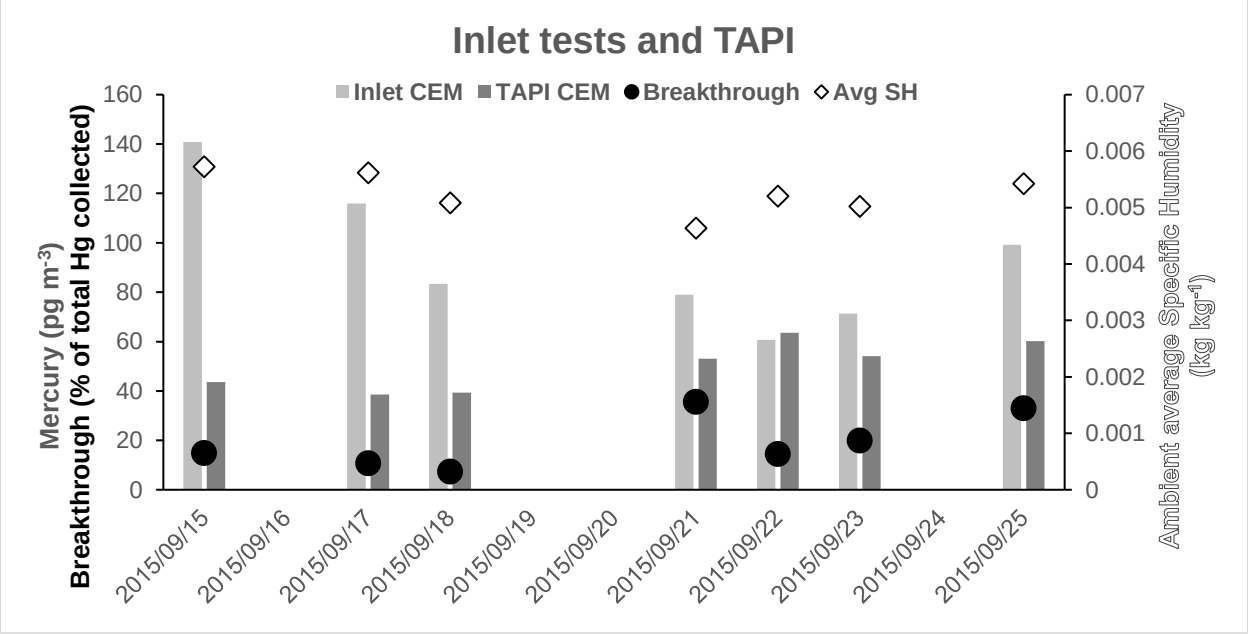

Figure SI 16: Inlet tests in light grey (average of three inlets) were run using three filter packs that contained two inline CEM filters deployed adjacent to the TAPI inlet. Filter pack inlets consisted of a 2.5 cm length pulled, ambient air through the filter packs at 16.7 Lpm, and were collected on the same time scale as the TAPI (dark grey, 24 h). Black circles indicate breakthrough on the inlet tests as percent of total RM collected and white diamonds indicate the average ambient specific humidity (SH).

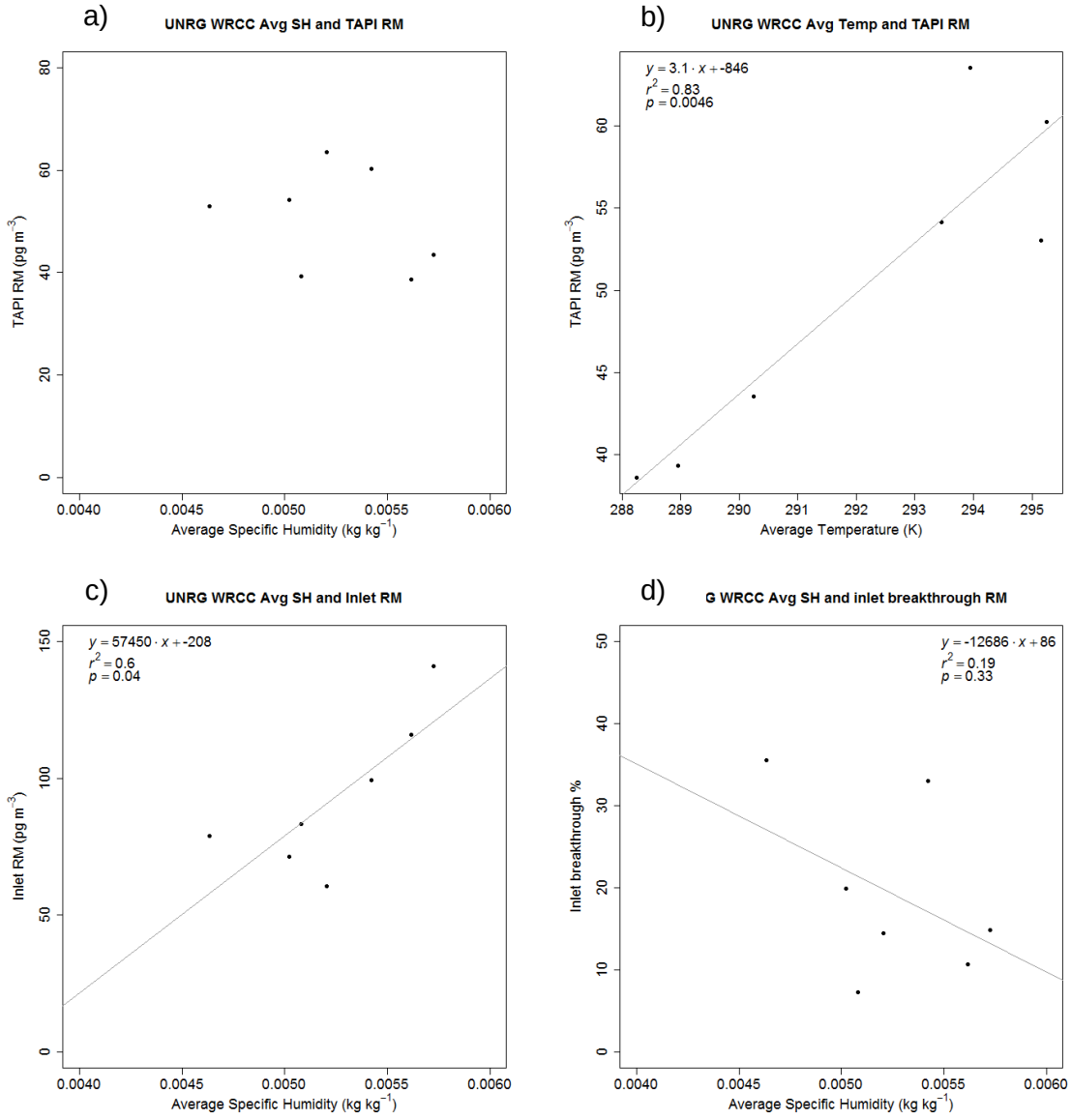

Figure SI 17: a) Average specific humidity (kg kg^{-1}) from WRCC and total RM from the TAPI at UNRG. b) Average outside temperature (K) from WRCC and total RM from the TAPI at UNRG. c) Average specific humidity and total RM from both filters from inlet setup. d) Average specific humidity and breakthrough percent of total RM from inlet setup.

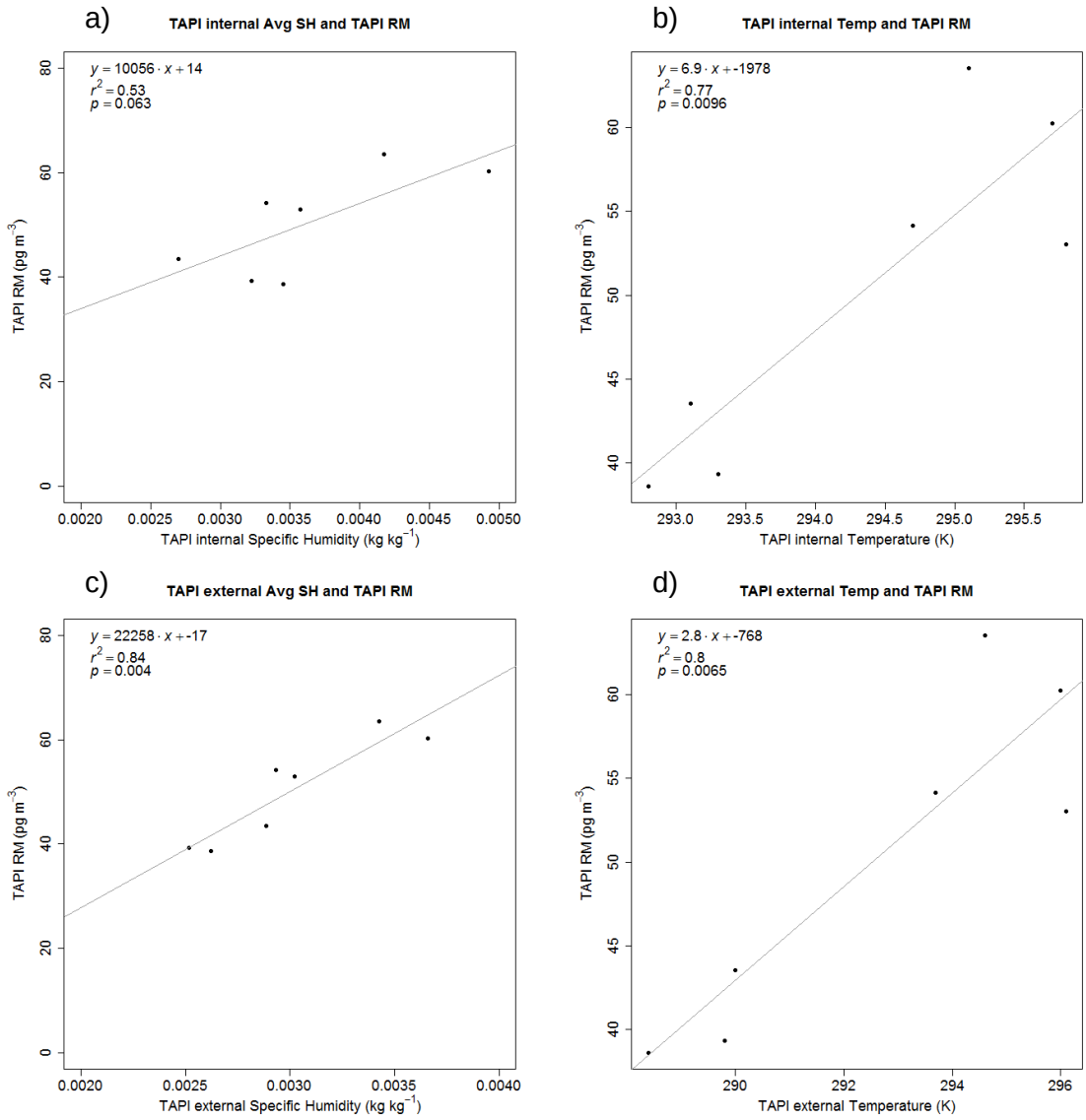

Figure SI 18: a) Average internal TAPI specific humidity and total RM from the TAPI at UNRG. b) Average internal TAPI temperature (K) and total RM from the TAPI at UNRG. c) Average external TAPI specific humidity and total RM from the TAPI at UNRG. d) Average external TAPI temperature (K) and total RM from the TAPI at UNRG.

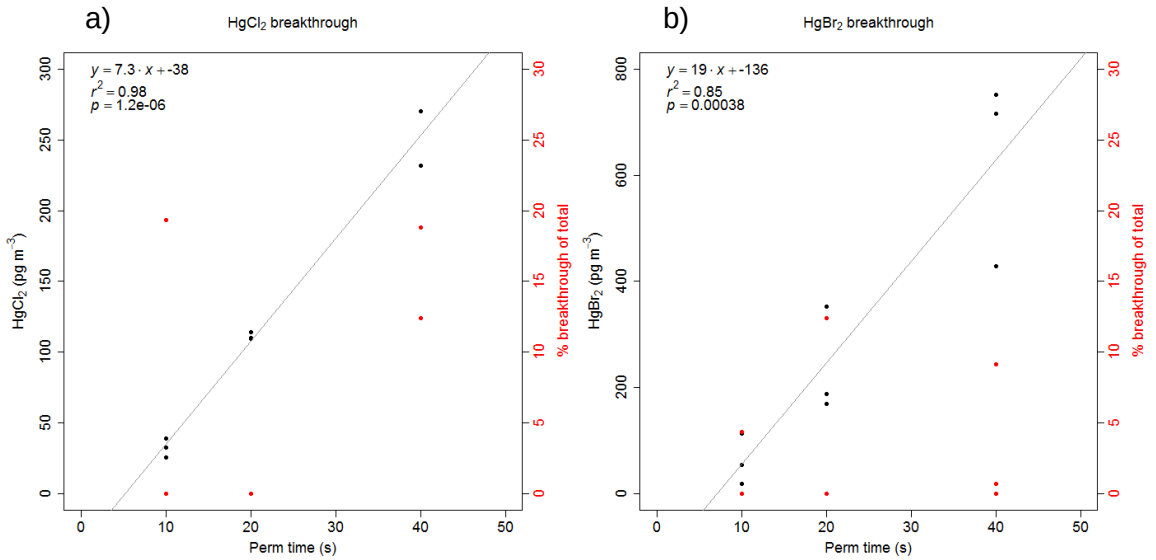

Figure SI 19: Percent breakthrough of total RM collected on two inline filters for three different permeation times (10, 20, and 30 sec) for a) $HgCl_2$ and b) $HgBr_2$

References

1. WRCC, W. R. C. C. Climate of Nevada. (2016),
2. Gustin, M. S.; Fine, R.; Miller, M.; Jaffe, D.; Burley, J., The Nevada Rural Ozone Initiative (NVROI): Insights to understanding air pollution in complex terrain. *Science of The Total Environment* **2015,** *530–531*, (0), 455-470.
3. www.census.gov Nevada. http://quickfacts.census.gov/qfd/states/32000.html (September 18, 2004),

Appendix B

Supplemental Information

Use of multiple tools including lead isotopes to decipher sources of ozone and reactive mercury to urban and rural locations in Nevada, USA

Ashley M. Pierce[a,*], Mae S. Gustin[a,*], John N. Christensen[b], S. Marcela Loría-Salazar[c]

*Corresponding author: ash.pie4@gmail.com; mgustin@cabnr.unr.edu

[a]Department of Natural Resources and Environmental Sciences, University of Nevada Reno, NV, USA 89557

[b] Energy Geosciences Division, Lawrence Berkeley National Laboratory, Berkeley, CA, USA 94720

[c]Atmospheric Science Program, Department of Physics, University of Nevada, Reno, Nevada, USA 89557

Published: *Science of the Total Environment* (Web: 2017, Print: 2018)

Methods:

Teledyne Advanced Pollution Instrumentation (TAPI) Beta^{Plus} Particulate Monitor

Automatic pneumatic circuit leak tests, beta source span checks, and calibration of the operating flow rate regulation system occurred at the start of each sampling period for both sample lines. Sample pumps were rebuilt every 6-8 months and sample inlets were cleaned monthly, following instructions from the manufacturer. Filters were held in cartridges specific to the TAPI 602 Beta^{Plus} and loaded into the TAPI. Filters were unloaded and held in the instrument unloader until collection every one to two weeks. Filters were then extracted using clean tweezers, into jars (CEM) and Petri dishes (Teflon) and stored in a freezer (-22 ºC) until further analysis.

Lead isotope analysis

Pb was leached from Teflon filters in clean Savillex vials using 6N HCl, sealed, and heated at 90 °C for 4 h. Filters were rinsed with 6N HCl and removed from the vials. Sample liquid collected in the vials was then evaporated at 100 °C and transferred to smaller Savillex vials to evaporate completely. Samples were then re-dissolved with concentrated HNO_3 and evaporated again at 100 °C. 0.5N HBr was added to the samples and the samples were centrifuged. Samples were then loaded onto fresh AGI –X8 resin for standard ion exchange chemistry using 0.5N HBr to rinse and 6N HCl to strip Pb from the resin. Pb stripped from resin in 6N HCl was collected in Savillex sample vials and evaporated at 100 °C. Samples were then re-dissolved in 0.3N HNO_3. Samples were spiked with thallium (5:1 ratio of Pb to Tl) with known isotopic composition (^{205}Tl:^{203}Tl) to adjust for instrumental mass fractionation of Pb during analysis with multi-collector

inductively coupled plasma mass spectrometry (MC-ICPMS; Neptune, Thermo Scientific, Ewing et al., 2010). Samples were introduced using a desolvation nebulization system (an Apex IR with ACM, by ESI). The MC-ICPMS instrument settings were optimized for ^{208}Pb before sampling. Pb standards (NBS981) were evaluated for procedural recovery at the start and end of each sample set.

Mercury

Individual CEM filters were placed in 125 mL soda-lime glass jars with PTFE-lined polypropylene caps and digested in 100 mL of 1% Optima hydrogen chloride (HCl) and MilliQ (18MΩ) water. Bromine monochloride (BrCl) solution was added to the samples to make a 2% by volume solution. Samples, calibration blanks, and standards digest for 24 h. Hydroxylamine (NH_2OH) was added to an equivalent of 0.1% of the volume and reacted for at least 5 min to remove any halogens before analysis. Any RM in the solution was then reduced using stannous chloride ($SnCl_2$) and removed from the liquid using a phase separator and ultra-high purity argon. The calibration curve was made using at least seven calibration blanks followed by five standards (1, 5, 10, 25, 100 ng l^{-1}). GEM was then collected on gold traps, thermally desorbed, and measured by cold vapor atomic fluorescence spectroscopy (CVAFS).

Hybrid Single Particle Lagrangian Integrated Trajectory Model (HYSPLIT)

Table 1: Trajectory residence time (TRT) source boxes.

Source box	Latitude	Longitude	Area (km^2)	Height (km)
Northern Eurasia (N. Eurasia)	78 to 45	30 to 180	28801728	10
East Asia (E. Asia)	45 to 20	100 to 150	12931786	10
San Francisco, CA* (SF)	39 to 37	-123 to -121	38971	1 (>3)
Las Angeles, CA* (LA)	35 to 32.5	-120 to -117	77098	1
Las Vegas, NV* (LV)	37 to 35	-116 to -114	40010	1

*Following (Fine et al., 2015; Wright et al., 2014)

Results:

Table 2: Corrected and blank subtracted Pb isotopic ratios, calculated Δ208 Pb and % Asian Pb, and uncertainties (uncert). Expected 208/207 ratios are calculated using the slope of the California array (Fig 1 and 2 in manuscript) and measured 206/207 ratios and used to calculate the Δ208 Pb and % Asian Pb following Ewing et al. (2010).

Site	Date	206/207	uncert	208/207	uncert	expected 208/207	Δ208 Pb	uncert of Δ208Pb	% Asian Pb	uncert of % Asian Pb
GBNP	03/27/2015	1.1543	5.34E-05	2.4381	9.26E-05	2.4220	16.15	0.11	64.61	0.43
	03/31/2015	1.1566	4.19E-05	2.4334	6.81E-05	2.4239	9.51	0.08	38.03	0.32
	05/23/2015	1.1591	5.72E-05	2.4363	1.10E-04	2.4259	10.43	0.12	41.72	0.50
	06/08/2015	1.1582	4.49E-05	2.4403	6.95E-05	2.4252	15.12	0.08	60.49	0.33
	06/09/2015	1.1584	4.50E-05	2.4405	7.26E-05	2.4253	15.16	0.09	60.62	0.34
	06/14/2015	1.1531	5.55E-05	2.4316	9.33E-05	2.4210	10.66	0.11	42.62	0.43
	06/17/2015	1.1556	4.41E-05	2.4327	7.13E-05	2.4231	9.62	0.08	38.48	0.34
	06/18/2015	1.1471	4.71E-05	2.4261	7.21E-05	2.4161	10.08	0.09	40.30	0.34
	06/22/2015	1.1612	5.05E-05	2.4359	7.94E-05	2.4277	8.23	0.09	32.91	0.38
	06/24/2015	1.1666	4.58E-05	2.4362	7.74E-05	2.4321	4.12	0.09	16.47	0.36
	06/26/2015	1.1617	4.57E-05	2.4355	7.64E-05	2.4280	7.46	0.09	29.83	0.36
	07/05/2015	1.1486	8.85E-05	2.4227	2.09E-04	2.4173	5.44	0.23	21.76	0.91
	07/14/2015	1.1659	8.55E-05	2.4332	2.09E-04	2.4315	1.67	0.23	6.68	0.90
	07/17/2015	1.1504	9.77E-05	2.4231	2.62E-04	2.4188	4.25	0.28	17.00	1.12
	07/20/2015	1.1615	9.18E-05	2.4362	2.15E-04	2.4279	8.34	0.23	33.36	0.94
	07/25/2015	1.1531	8.50E-05	2.4274	2.18E-04	2.4210	6.44	0.23	25.76	0.94
	08/11/2015	1.1750	1.16E-04	2.4442	2.33E-04	2.4389	5.32	0.26	21.27	1.04
	08/20/2015	1.1611	7.53E-05	2.4336	1.40E-04	2.4276	6.06	0.16	24.25	0.64
	08/21/2015	1.1643	1.03E-04	2.4333	2.98E-04	2.4302	3.17	0.32	12.68	1.26
	08/26/2015	1.1629	8.37E-05	2.4344	1.63E-04	2.4290	5.40	0.18	21.62	0.73
	09/03/2015	1.2010	4.10E-05	2.4533	1.23E-04	2.4603	-6.99	0.13	-27.97	0.52

	09/05/2015	1.1635	8.22E-05	2.4355	1.83E-04	2.4295	6.04	0.20	24.15	0.80
	09/10/2015	1.1541	7.48E-05	2.4403	1.27E-04	2.4218	18.46	0.15	73.85	0.59
PEAV	06/06/2014	1.1374	2.81E-05	2.4171	8.87E-05	2.4081	8.96	0.09	35.84	0.37
	06/12/2014	1.1551	2.58E-05	2.4329	6.14E-05	2.4226	10.25	0.07	41.00	0.27
	06/17/2014	1.1360	7.13E-05	2.4127	1.53E-04	2.4070	5.70	0.17	22.81	0.67
	06/22/2014	1.1379	1.15E-04	2.4152	2.61E-04	2.4085	6.69	0.29	26.75	1.14
	06/26/2014	1.1568	5.35E-05	2.4305	9.55E-05	2.4240	6.47	0.11	25.89	0.44
	06/28/2014	1.1405	4.39E-05	2.4186	7.64E-05	2.4107	7.92	0.09	31.68	0.35
	07/06/2014	1.1400	4.25E-05	2.4156	7.10E-05	2.4103	5.33	0.08	21.33	0.33
	07/15/2014	1.1385	4.75E-05	2.4130	9.93E-05	2.4090	4.06	0.11	16.25	0.44
	07/22/2014	1.1303	4.15E-05	2.4036	7.09E-05	2.4023	1.29	0.08	5.17	0.33
	07/25/2014	1.1299	2.95E-05	2.4065	6.05E-05	2.4020	4.50	0.07	17.98	0.27
	07/26/2014	1.1508	3.09E-05	2.4192	5.04E-05	2.4191	0.13	0.06	0.51	0.24
	08/07/2014	1.1377	4.06E-05	2.4126	7.87E-05	2.4083	4.26	0.09	17.06	0.35
	09/06/2014	1.1411	4.41E-05	2.4137	7.05E-05	2.4111	2.58	0.08	10.32	0.33
	09/22/2014	1.1636	2.55E-05	2.4334	5.56E-05	2.4296	3.86	0.06	15.44	0.24
	09/24/2014	1.1514	2.78E-05	2.4242	5.87E-05	2.4196	4.60	0.06	18.39	0.26
	09/27/2014	1.1581	4.55E-05	2.4395	8.09E-05	2.4250	14.43	0.09	57.71	0.37
	10/09/2014	1.1481	3.35E-05	2.4233	6.57E-05	2.4169	6.35	0.07	25.39	0.30
	10/15/2014	1.1563	2.62E-05	2.4343	5.54E-05	2.4236	10.65	0.06	42.62	0.24
	10/17/2014	1.1521	2.57E-05	2.4334	5.24E-05	2.4202	13.20	0.06	52.82	0.23
UNRG	04/14/2014	1.1507	2.51E-05	2.4263	4.43E-05	2.4191	7.26	0.05	29.05	0.20
	04/14/2014	1.1515	2.12E-05	2.4271	4.11E-05	2.4197	7.38	0.05	29.54	0.18
	04/17/2014	1.1527	3.17E-05	2.4328	5.77E-05	2.4207	12.11	0.07	48.43	0.26
	04/17/2014	1.1519	2.31E-05	2.4322	5.17E-05	2.4200	12.25	0.06	48.99	0.23
	06/06/2014	1.1436	2.35E-05	2.4217	5.74E-05	2.4132	8.46	0.06	33.86	0.25
	06/12/2014	1.1520	2.42E-05	2.4318	5.30E-05	2.4201	11.72	0.06	46.87	0.23
	06/17/2014	1.1615	3.60E-05	2.4290	6.35E-05	2.4279	1.13	0.07	4.53	0.29
	06/22/2014	1.1315	3.04E-05	2.4065	5.68E-05	2.4033	3.16	0.06	12.66	0.26
	06/26/2014	1.1470	5.46E-05	2.4211	9.65E-05	2.4160	5.19	0.11	20.77	0.44
	06/28/2014	1.1411	4.21E-05	2.4135	6.39E-05	2.4111	2.36	0.08	9.45	0.31
	07/06/2014	1.1334	3.78E-05	2.4099	6.58E-05	2.4048	5.08	0.08	20.32	0.30
	07/15/2014	1.1391	4.47E-05	2.4140	7.12E-05	2.4095	4.57	0.08	18.28	0.34
	07/22/2014	1.1430	2.22E-05	2.4143	5.61E-05	2.4127	1.65	0.06	6.62	0.24
	07/25/2014	1.1434	2.17E-05	2.4221	4.93E-05	2.4130	9.07	0.05	36.29	0.22
	07/26/2014	1.1227	2.85E-05	2.3955	6.44E-05	2.3961	-0.61	0.07	-2.42	0.28
	08/07/2014	1.1414	2.87E-05	2.4177	6.01E-05	2.4114	6.33	0.07	25.31	0.27
	09/06/2014	1.1369	3.25E-05	2.4087	4.72E-05	2.4077	1.02	0.06	4.06	0.23
	09/22/2014	1.1609	2.81E-05	2.4336	4.77E-05	2.4273	6.23	0.06	24.91	0.22
	09/26/2014	1.1553	2.69E-05	2.4302	6.02E-05	2.4228	7.40	0.07	29.60	0.26
	09/27/2014	1.1485	2.82E-05	2.4279	5.26E-05	2.4172	10.60	0.06	42.42	0.24

10/09/2014	1.1502	2.51E-05	2.4296	5.20E-05	2.4186	11.08	0.06	44.31	0.23
10/15/2014	1.1580	3.25E-05	2.4303	7.29E-05	2.4250	5.26	0.08	21.03	0.32
10/17/2014	1.1552	2.74E-05	2.4384	5.24E-05	2.4227	15.68	0.06	62.72	0.24
02/21/2015	1.1672	4.24E-05	2.4351	7.31E-05	2.4325	2.57	0.08	10.30	0.34
02/21/2015	1.1650	4.40E-05	2.4343	8.58E-05	2.4308	3.53	0.10	14.14	0.39
03/28/2015	1.1540	4.11E-05	2.4379	8.54E-05	2.4217	16.21	0.09	64.86	0.38
03/31/2015	1.1607	4.30E-05	2.4397	8.01E-05	2.4272	12.48	0.09	49.94	0.36
05/28/2015	1.1447	4.24E-05	2.4276	6.90E-05	2.4141	13.53	0.08	54.13	0.32
06/08/2015	1.1536	4.46E-05	2.4313	7.52E-05	2.4214	9.90	0.09	39.60	0.35
06/09/2015	1.1520	4.51E-05	2.4386	6.62E-05	2.4201	18.56	0.08	74.25	0.32
07/15/2015	1.1696	9.73E-05	2.4404	2.67E-04	2.4345	5.91	0.28	23.63	1.14
08/19/2015	1.1557	1.22E-04	2.4260	4.45E-04	2.4231	2.87	0.46	11.48	1.85
08/20/2015	1.1561	8.66E-05	2.4282	2.21E-04	2.4235	4.77	0.24	19.06	0.95
08/29/2015	1.1505	8.51E-05	2.4211	2.07E-04	2.4189	2.26	0.22	9.03	0.90
08/31/2015	1.1903	9.61E-05	2.4557	2.60E-04	2.4515	4.18	0.28	16.73	1.11
09/02/2015	1.1892	7.61E-05	2.4568	1.71E-04	2.4506	6.22	0.19	24.90	0.75

PEAV 2014:

Figure 1: Diel pattern of O_3 and CO at PEAV averaged over the sample period for each hour for a) same y-axis scale as UNRG (Fig. 2 and 3 below) and b) y-axis scaled for PEAV data.

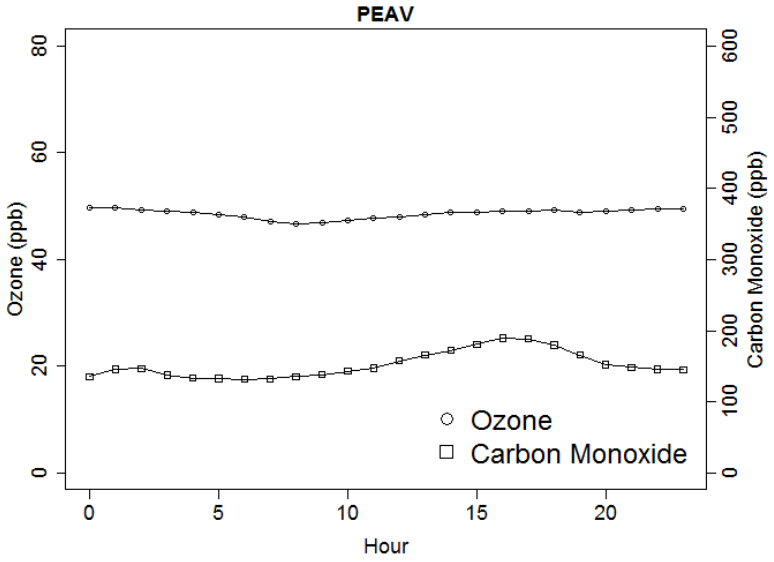

a)

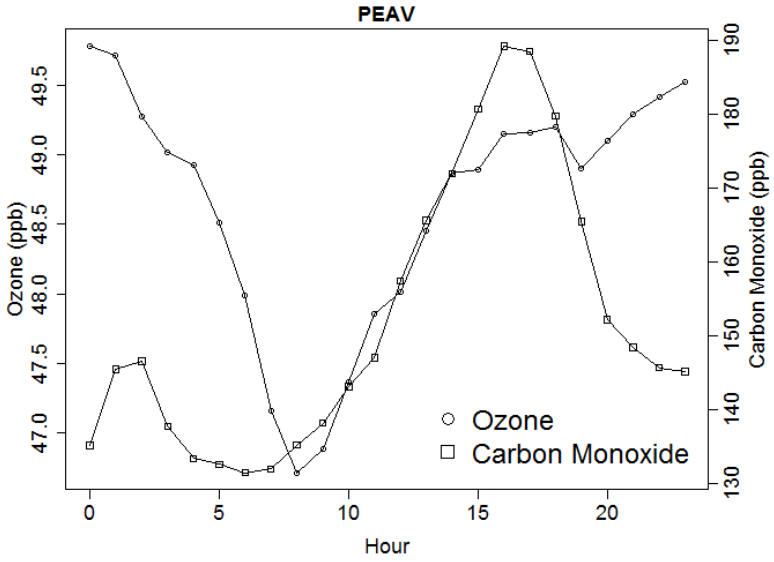

b)

Pearson Correlation for site data:

*Table 3: Pearson correlations for $PM_{2.5}$ and gas data at PEAV in 2014. Italic data indicates significance level p<0.1, **bold italic data** indicates significance level p<0.05, grey data indicates <50% of available data.*

PEAV	$PM_{2.5}$	RM	O_3	Max 1 h O_3	MDA8 O_3	CO
O_3	0.09	***0.22***		***0.87***	***0.88***	0.15
Max 1 h O_3	***0.18***	***0.21***	***0.87***		***0.92***	***0.24***
MDA8 O_3	0.07	*0.15*	***0.88***	***0.92***		0.15
RM	0.11		***0.22***	***0.21***	*0.15*	0.09

CO – carbon monoxide
Max 1 h O_3 – maximum 1 h O_3
MDA8 O_3 – maximum daily average (8 h O_3)
NO – nitrogen oxide
NOx – nitrogen oxide compounds
O_3 – ozone
PEAV – Peavine Peak, Reno, NV, USA
$PM_{2.5}$ – particulate matter <2.5 µm in diameter
RM – reactive mercury
SO_2 – sulfur dioxide

*Table 4: Pearson correlations for meteorological data at PEAV in 2014. Italic data indicates significance level p<0.1, **bold italic data** indicates significance level p<0.05.*

PEAV	Temp	RH	Wind speed	Pressure	ABLH
O_3	***0.48***	***-0.42***	-0.04	0.16	***0.25***
Max 1 h O_3	***0.45***	***-0.41***	0.05	0.11	***0.33***
MDA8 O_3	***0.43***	***-0.42***	0.01	0.11	***0.25***
RM	***0.63***	***-0.41***	-0.08	***0.51***	***0.48***

ABLH – atmospheric boundary layer height
Max 1 h O_3 – maximum 1 h O_3
MDA8 O_3 – maximum daily average (8 h) O_3
O_3 – ozone
PEAV – Peavine Peak, Reno, NV, USA
RH – relative humidity
RM – reactive mercury
Temp – temperature

Table 5: Pearson correlations for source box trajectory residence time (TRT) analysis for PEAV in 2014. Italic data indicates significance level p<0.1, ***bold italic data*** *indicates significance level p<0.05.*

PEAV	N. Eurasia					E. Asia					SF		LA	LV
	<1 km	**<2 km**	**<3 km**	**Total**	**>3 km**	**<1 km**	**<2 km**	**<3 km**	**Total**	**>3 km**	**<1 km**	**>3 km**	**<1 km**	**<1 km**
O_3	*-0.15*	*-0.16*	***-0.19***	0.02	0.07	0.05	0.02	0.01	-0.01	-0.02	***0.31***	0.14	-0.12	*-0.16*
Max 1 h O_3	-0.10	-0.12	-0.14	0.07	0.11	0.07	0.04	0.05	0.06	0.05	***0.24***	0.11	***-0.21***	*-0.16*
MDA8 O_3	-0.14	*-0.15*	*-0.17*	0.10	*0.15*	0.10	0.07	0.08	0.11	0.10	***0.21***	0.09	***-0.18***	-0.14
RM	*-0.15*	***-0.19***	***-0.24***	***-0.29***	***-0.27***	-0.08	-0.08	-0.08	-0.05	-0.02	0.00	***0.33***	-0.11	-0.12

LA – Las Angeles, CA, USA
LV – Las Vegas, NV, USA
Max 1 h O_3 – maximum 1 h O_3
MDA8 O_3 – maximum daily average (8 h) O_3
O_3 – ozone
PEAV – Peavine Peak, Reno, NV, USA
RM – reactive mercury
SF – San Francisco, CA, USA

Table 6: Positive and negative correlations for PEAV 2014. Bold + indicate α<0.05, italic + indicate α<0.1, while large — indicate α<0.05, small - indicate α<0.1.

PEAV 2014		Positive					Negative				
		$PM_{2.5}$	**O_3**	**Max 1 h O_3**	**MDA8 O_3**	**RM**	**$PM_{2.5}$**	**O_3**	**Max 1 h O_3**	**MDA8 O_3**	**RM**
Filter	**$PM_{2.5}$**			**+**							
	RM		**+**	**+**	*+*						
Gas	**CO**	**+**		**+**							
Meteorological	**Temp**		**+**	**+**	**+**	**+**					
	RH							**—**	**—**	**—**	**—**
	Wind speed	**+**									
	Pressure					**+**					
	Dew point	**+**								-	
	ABLH		**+**	**+**	**+**	**+**					
N. Eurasia	**<3 km**							**—**		-	**—**
	Total						-				**—**
	>3 km				*+*		-				**—**
SF	**<1 km**		**+**	**+**	**+**						
	>3 km					**+**					
LA	**<1 km**	**+**							**—**	**—**	
LV	**<1 km**							-	-		

ABLH – atmospheric boundary layer height
CO – carbon monoxide
LA – Los Angeles, CA, USA
LV – Las Vegas, NV, USA
Max 1 h O_3 – maximum 1 h average of each day averaged by site
MDA8 O_3 – maximum daily average (8 h) for each day averaged by site
O_3 – ozone
PEAV – Peavine Peak, Reno, NV, USA
$PM_{2.5}$ – particulate matter <2.5 µm in diameter
RH – relative humidity
RM – reactive Hg
SF – San Francisco, CA, USA

PEAV 2014 (Pb days):

Mean O_3 concentration for the Pb sample days were higher at PEAV (50±10, range 34 to 69 ppb, n=19) than UNRG (30±10, range 12 to 49 ppb, n=14) and WCAQ (40±10, range 22 to 60 ppb, n=19). Ozone (daily average, Max 1 h, MDA8) was positively correlated with temperature, total Pb mass (MDA8 p<0.1), and with <3 km and total trajectories from San Francisco. MDA8 O_3 was positively correlated with <3 km

trajectories from Northern Eurasia ($p<0.1$). Ozone (daily average, Max 1 h, MDA8) was negatively correlated with RH.

Reactive mercury was positively correlated with temperature, pressure, ABLH, and trajectories arriving >3 km above San Francisco and Las Vegas. RM was negatively correlated with RH, percent Asian Pb, and total trajectories from East Asia.

Table 7: Statistics for days with Pb samples at PEAV June to November 2014, a) filter samples and b) O_3.

a)

PEAV 2014	Pb mass (ng)	Δ208Pb	% Asian Pb	Total Pb (ng m^{-3})	Asian Pb (ng m^{-3})	RM (pg m^{-3})	$PM_{2.5}$ (ug m^{-3})	ng Pb ug^{-1} $PM_{2.5}$
Min	3.24	0.1286	0.51	0.1346	0.0025	1.86	1.30	0.0103
Mean	8.26	6.3809	26	0.3436	0.0897	52.14	10.46	0.0703
Median	7.65	5.7018	23	0.3183	0.0651	37.86	5.40	0.0661
Max	17.23	14.4269	58	0.7165	0.3784	139.65	42.10	0.1714
StDev	3.71	3.7829	15	0.1542	0.0893	35.88	12.94	0.0471
Count	19	19	19	19	19	19	19	19

b)

PEAV	AvgO3	MaxHrO3	MDA8O3
Min	33.83	42.05	39.05
Mean	50.20	58.84	55.65
Median	51.38	58.90	55.93
Max	68.72	78.03	77.55
Stdev	10.35	10.32	11.30
Count	19	19	19

Pearson Correlation for Pb days:

*Table 8: Pearson correlations for $PM_{2.5}$ and gas data on days with Pb samples at PEAV in 2014. Italic data indicates significance level p<0.1, **bold italic data** indicates significance level p<0.05, grey data indicates <50% of available data.*

PEAV	$PM_{2.5}$	RM	O_3	Max 1 h O_3	MDA8 O_3	CO
O_3	0.30	0.16				0.25
Max 1 h O_3	0.23	0.11				0.28
MDA8 O_3	0.23	0.20				0.32
RM	-0.19		0.16	0.11	0.20	-0.09
Total Pb	***0.52***	-0.03	***0.54***	***0.46***	*0.40*	0.39
Asian Pb	0.24	-0.37	0.16	0.12	0.06	0.01
%Asian Pb	-0.04	***-0.57***	-0.24	-0.23	-0.25	-0.25

CO – carbon monoxide
Max 1 h O_3 – maximum 1 h O_3
MDA8 O_3 – maximum daily average (8 h) O_3
NO – nitrogen oxide
NO_x – nitrogen oxide compounds
O_3 – ozone
PEAV – Peavine Peak, Reno, NV, USA
$PM_{2.5}$ – particulate matter <2.5 µm in diameter
RM – reactive mercury
SO_2 – sulfur dioxide.

*Table 9: Pearson correlations for meteorological data on days with Pb samples at PEAV in 2014. Italic data indicates significance level p<0.1, **bold italic data** indicates significance level p<0.05.*

PEAV	Temp	RH	Wind speed	Pressure	ABLH
O_3	***0.54***	***-0.64***	0.19	0.31	-0.03
Max 1 h O_3	***0.52***	***-0.62***	0.07	0.28	0.04
MDA8 O_3	***0.60***	***-0.64***	0.07	0.39	0.04
RM	***0.75***	***-0.57***	-0.30	***0.72***	***0.64***
Total Pb	0.23	-0.36	0.24	0.09	-0.19
Asian Pb	-0.26	-0.08	0.31	*-0.48*	***-0.52***
%Asian Pb	***-0.65***	0.32	0.26	***-0.68***	***-0.63***

ABLH – atmospheric boundary layer height
Max 1 h O_3 – maximum 1 h O_3
MDA8 O_3 – maximum daily average (8 h) O_3
O_3 – ozone
PEAV – Peavine Peak, Reno, NV, USA
RH – relative humidity
RM – reactive mercury
Temp – temperature

Table 10: Pearson correlations for source box trajectory residence time (TRT) analysis on days with Pb samples for PEAV in 2014. Italic data indicates significance level p<0.1, ***bold italic data*** *indicates significance level p<0.05.*

PEAV	N. Eurasia			E. Asia			SF		LA	LV
	<3 km	Total	>3 km	<3 km	Total	>3 km	<1 km	>3 km	<1 km	<1 km
O_3	-0.34	0.20	0.33	0.08	0.22	0.25	0.20	0.35	-0.19	0.04
Max 1 h O_3	-0.25	0.25	0.36	0.09	0.27	0.30	0.21	0.28	-0.22	0.08
MDA8 O_3	*-0.40*	0.15	0.29	0.00	0.20	0.28	0.21	0.28	-0.21	0.07
RM	-0.31	-0.37	-0.32	-0.38	***-0.50***	*-0.40*	-0.17	***0.51***	-0.14	-0.09
Total Pb	-0.22	-0.06	0.00	***0.58***	0.25	-0.09	-0.04	0.18	0.02	0.27
Asian Pb	0.00	0.21	0.23	***0.79***	***0.55***	0.17	0.19	-0.29	-0.09	-0.03
%Asian Pb	0.13	0.34	0.34	***0.50***	***0.61***	***0.47***	0.24	***-0.48***	-0.05	-0.15

LA – Las Angeles, CA, USA
LV – Las Vegas, NV, USA
Max 1 h O_3 – maximum 1 h O_3
MDA8 O_3 – maximum daily average (8 h) O_3
O_3 – ozone
PEAV – Peavine Peak, Reno, NV, USA
RM – reactive mercury
SF – San Francisco, CA, USA

Table 11: Positive and negative correlations for 19 days with Pb samples at PEAV 2014. Bold + indicate α<0.05, italic + indicate α<0.1, while large — indicate α<0.05, small - indicate α<0.1.

PEAV Pb 2014		Positive						Negative					
		$^{206}Pb/^{207}Pb$	$^{208}Pb/^{207}Pb$	% Asian Pb	total Pb mass	Asian Pb mass	ng Pb/ug PM	$^{206}Pb/^{207}Pb$	$^{208}Pb/^{207}Pb$	% Asian Pb	total Pb mass	Asian Pb mass	ng Pb/ug PM
Filter	$PM_{2.5}$	**+**	*+*		**+**								**—**
	RM								**—**	**—**			
Gas	O_3				**+**								
	Max 1 h O_3				**+**								
	MDA8 O_3				*+*								
Met	Temp							**—**	**—**	**—**			
	RH		*+*										
	Wind speed	**+**	**+**										-
	Pressure								**—**	**—**		-	
	Dew point												-
	ABLH							**—**	**—**	**—**		**—**	
N. Eurasia	Total						**+**						
	>3 km						**+**						
E. Asia	<3 km			**+**	**+**	**+**							
	Total			**+**		**+**	*+*						
	>3 km			**+**			*+*						
SF	<1 km						*+*						
	>3 km									**—**			
LA	<1 km												-
LV	<1 km	*+*											

ABLH – atmospheric boundary layer height
LA – Los Angeles, CA, USA
LV – Las Vegas, NV, USA
Max 1 h O_3 – maximum 1 h average of each day averaged by site
MDA8 O_3 – maximum daily average (8 h) for each day averaged by site
O_3 – ozone
PEAV – Peavine Peak, Reno, NV, USA
$PM_{2.5}$ – particulate matter <2.5 μm in diameter
RH – relative humidity
RM – reactive Hg
SF – San Francisco, CA, USA

UNRG 2014:

Figure 2: Diel pattern of O_3, CO, and NO_x at UNRG 2015 averaged over the sample period for each hour.

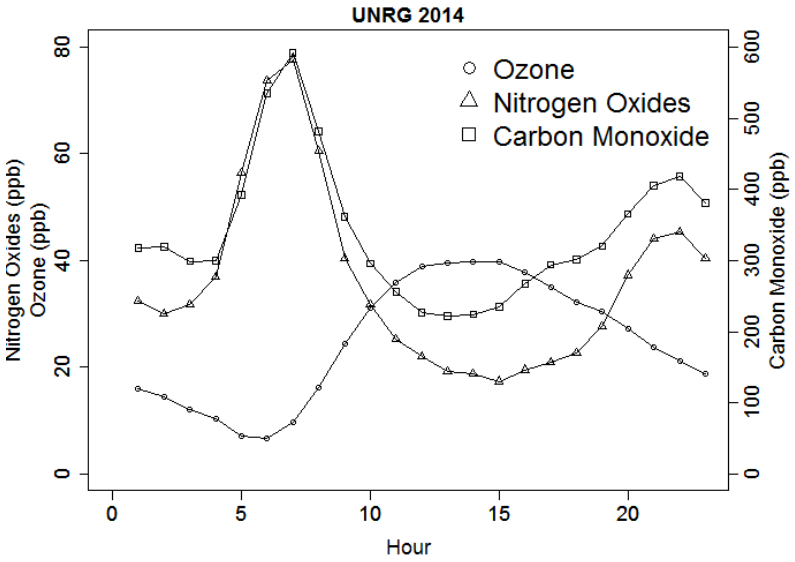

UNRG 2015:

Figure 3: Diel pattern of O_3, CO, and NO_x at UNRG 2015 averaged over the sample period for each hour for a) March to October 2015 and b) June to October 2015 (similar time of year as UNRG 2014).

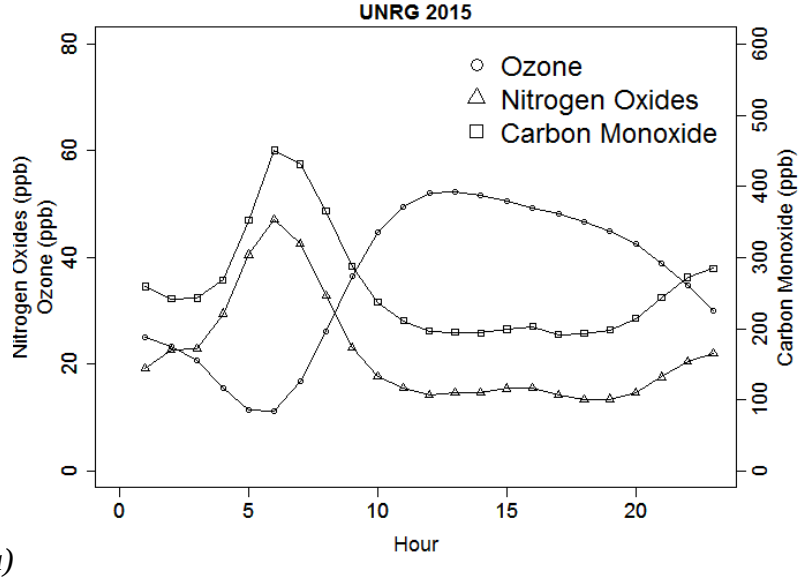

a)

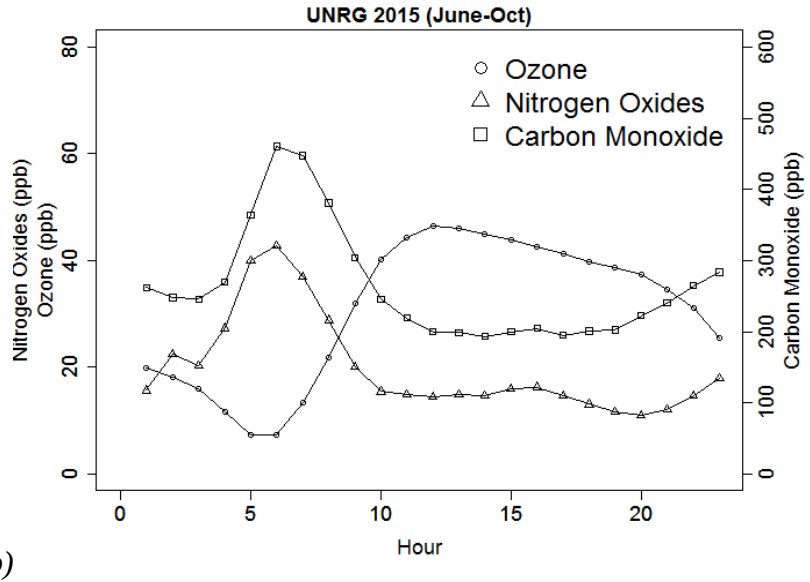

b)

UNRG 2014:

*Table 12: Pearson correlations for $PM_{2.5}$ and gas data at UNRG in 2014. Italic data indicates significance level p<0.1, **bold italic data** indicates significance level p<0.05, grey data indicates <50% of available data.*

UNRG 2014	$PM_{2.5}$	RM	O_3	Max 1 h O_3	MDA8 O_3	CO	SO_2	NO_x	NO
O_3	-0.02	*-0.21*		***0.84***	***0.86***	-0.13	0.09	*-0.66*	-0.16
Max 1 h O_3	0.07	***-0.29***	***0.84***		***0.98***	0.14	***0.33***	-0.20	***0.23***
MDA8 O_3	0.03	***-0.30***	***0.86***	***0.98***		0.07	***0.27***	*-0.23*	***0.21***
RM	***0.20***		*-0.21*	***-0.29***	***-0.30***	-0.07	-0.16	-0.09	***-0.42***

CO – carbon monoxide
Max 1 h O_3 – maximum 1 h O_3
MDA8 O_3 – maximum daily average (8 h) O_3
NO – nitrogen oxide
NO_x – nitrogen oxide compounds
O_3 – ozone
$PM_{2.5}$ – particulate matter <2.5 µm in diameter
RM – reactive mercury
SO_2 – sulfur dioxide
UNRG – University of Nevada, Reno Greenhouse facility, USA

*Table 13: Pearson correlations for meteorological data at UNRG in 2014. Italic data indicates significance level p<0.1, **bold italic data** indicates significance level p<0.05.*

UNRG 2014	Temp	RH	Wind speed	Pressure	ABLH	Solar radiation	Precipitation
O_3	0.07	***-0.42***	***0.37***	***-0.43***	0.12	*0.18*	***-0.27***
Max 1 h O_3	-0.14	***-0.36***	-0.03	-0.15	0.00	0.08	***-0.27***
MDA8 O_3	-0.11	***-0.39***	0.00	*-0.18*	0.04	0.14	***-0.31***
RM	***0.63***	-0.14	0.07	0.01	***0.36***	0.09	0.13

ABLH – atmospheric boundary layer height.
Max 1 h O_3 – maximum 1 h O_3
MDA8 O_3 – maximum daily average (8 h) O_3
O_3 – ozone
RH – relative humidity
RM – reactive mercury
Temp – temperature
UNRG – University of Nevada, Reno Greenhouse facility, USA

Table 14: Pearson correlations for source box trajectory residence time (TRT) analysis for UNRG in 2014. Italic data indicates significance level p<0.1, ***bold italic data*** *indicates significance level p<0.05.*

UNRG 2014	N. Eurasia					E. Asia					SF		LA	LV
	<1 km	**<2 km**	**<3 km**	**Total**	**>3 km**	**<1 km**	**<2 km**	**<3 km**	**Total**	**>3 km**	**<1 km**	**>3 km**	**<1 km**	**<1 km**
O_3	0.15	***0.23***	***0.23***	***0.34***	***0.33***	***0.22***	***0.24***	***0.26***	***0.30***	***0.26***	***0.25***	***-0.21***	***-0.22***	0.01
Max 1 h O_3	*0.17*	***0.21***	***0.21***	***0.33***	***0.33***	***0.23***	***0.26***	***0.28***	***0.33***	***0.28***	0.00	***-0.20***	***-0.27***	0.04
MDA8 O_3	*0.19*	***0.22***	***0.22***	***0.35***	***0.35***	***0.25***	***0.27***	***0.29***	***0.34***	***0.29***	0.02	***-0.22***	***-0.28***	0.03
RM	***-0.23***	***-0.30***	***-0.35***	***-0.36***	***-0.31***	-0.13	*-0.18*	***-0.22***	***-0.22***	***-0.20***	0.14	***0.28***	0.04	-0.02

LA – Las Angeles, CA, USA
LV – Las Vegas, NV, USA
Max 1 h O_3 – maximum 1 h O_3
MDA8 O_3 – maximum daily average (8 h) O_3
O_3 – ozone
RM – reactive mercury
SF – San Francisco, CA, USA
UNRG – University of Nevada, Reno Greenhouse facility, USA

Table 15: Positive and negative correlations for UNRG 2014. Bold + indicate α<0.05, italic + indicate α<0.1, while large — indicate α<0.05, and small - indicate α<0.1. Grey data indicate <50% of the data was available.

UNRG 2014		Positive					Negative				
		$PM_{2.5}$	O_3	Max 1 h O_3	MDA8 O_3	RM	$PM_{2.5}$	O_3	Max 1 h O_3	MDA8 O_3	RM
Filter	$PM_{2.5}$					+					
	RM	+						-	—	—	
Gas	O_3										-
	Max 1 h O_3										—
	MDA8 O_3										—
	CO	+									
	SO2	+		+	+						
	NOx							—		-	
	NO			+	+						—
Meteorological	Temp					+					
	RH	+						—	—	—	
	Wind speed		+				-				
	Pressure							—		-	
	ABLH					+					
	Solar radiation		+				—				
	Precipitation	+						—	—	—	
N. Eurasia	<3 km		+	+	+		-				—
	Total		+	+	+		—				—
	>3 km		+	+	+		—				—
E. Asia	<3 km		+	+	+						—
	Total		+	+	+						—
	>3 km		+	+	+						—
SF	<1 km		+								
	>3 km					+		—	—	—	
LA	<1 km	+						—	—	—	
LV	<1 km	+									

ABLH – atmospheric boundary layer height
CO – carbon monoxide
LA – Los Angeles, CA, USA
LV – Las Vegas, NV, USA
Max 1 h O_3 – maximum 1 h average of each day averaged by site
MDA8 O_3 – maximum daily average (8 h) for each day averaged by site
O_3 – ozone
$PM_{2.5}$ – particulate matter <2.5 µm in diameter
RH – relative humidity
RM – reactive Hg
SF – San Francisco, CA, USA
UNRG – University of Nevada, Reno, Greenhouse, USA

UNRG 2014 (Pb days):

Ozone (daily average) was positively correlated with <1 and <2 km trajectories ($p<0.1$) and <3, total, and >3 km trajectories from Northern Eurasia. Max 1 h O_3 and MDA O_3 were positively correlated with total and >3 km trajectories from Northern Eurasia.

RM was positively correlated with solar radiation, temperature, Tekran GOM, ABLH ($p<0.1$), <1 km trajectories from San Francisco ($p<0.1$), <2, <3 km and total trajectories from San Francisco. RM was negatively correlated with RH, and <3 km ($p<0.1$) and total trajectories fro, Northern Eurasia ($p<0.1$), and <1 km trajectories ($p<0.1$) from East Asia. Tekran GEM was positively correlated with <1, <2 km trajectories and <3 km ($p<0.1$) trajectories from East Asia and negatively correlated with <1 and <2 km trajectories from San Francisco. Tekran GOM was positively correlated with <1, <2, <3, and total trajectories from San Francisco and Tekram RM was positively correlated with <1 ($p<0.1$) and <2 km trajectories from San Francisco.

Table 16: Statistics for days with Pb samples at UNRG June to November 2014, a) filter samples and b) O_3.

a)

UNRG 2014	Pb mass (ng)	Δ208Pb	% Asian Pb	Total Pb (ng m^{-3})	Asian Pb (ng m^{-3})	RM (pg m^{-3})	$PM_{2.5}$ (ug m^{-3})	ng Pb ug^{-1} $PM_{2.5}$
Min	4.81	-0.6053	-2.4	0.2000	-0.0240	8.38	1.90	0.0147
Mean	18.19	6.0737	24	0.7563	0.2385	44.82	9.80	0.1130
Median	14.53	5.2564	21	0.6043	0.1073	41.92	6.40	0.1105
Max	73.92	15.6809	63	3.0738	1.9280	105.99	62.90	0.2956
StDev	14.63	4.2644	17	0.6084	0.4296	26.12	13.41	0.0652
Count	19	19	19	19	19	18	19	19

b)

UNRG 2014	AvgO3	MaxHrO3	MDA8O3	WCAQ AvgO3	WCAQ MaxHrO3	WCAQ MDA8O3
Min	12.24	23.59	19.16	22.05	43.00	37.38
Mean	29.83	47.87	42.53	40.16	58.84	53.37
Median	31.30	46.52	41.43	40.83	59.00	56.25
Max	48.82	71.76	63.19	59.88	85.00	73.00
Stdev	10.03	12.86	11.75	9.64	11.73	11.58
Count	14	14	14	19	19	19

Pearson Correlation for Pb days:

*Table 17: Pearson correlations for $PM_{2.5}$ and gas data on days with Pb samples at UNRG in 2014. Italic data indicates significance level p<0.1, **bold italic data** indicates significance level p<0.05, grey data indicates <50% of available data.*

UNRG 2014	$PM_{2.5}$	RM	O_3	Max 1 h O_3	MDA8 O_3	CO	SO_2	NO_x	NO
O_3	0.03	-0.18				-0.04	0.03	-0.60	-0.29
Max 1 h O_3	0.32	-0.18				*0.73*	0.40	0.36	0.18
MDA8 O_3	0.27	-0.17				*0.68*	0.41	0.46	0.19
RM	0.05		-0.18	-0.18	-0.17	-0.09	-0.33	0.04	-0.38
Total Pb	0.06	-0.23	-0.13	0.24	0.22	0.53	0.39	***0.85***	***0.88***
Asian Pb	-0.01	-0.28	-0.14	0.17	0.17	0.43	0.36	***0.77***	***0.88***
%Asian Pb	-0.03	-0.18	-0.21	-0.02	-0.01	0.20	0.28	0.41	***0.64***

CO – carbon monoxide
Max 1 h O_3 – maximum 1 h O_3
MDA8 O_3 – maximum daily average (8 h) O_3
NO – nitrogen oxide
NO_x – nitrogen oxide compounds
O_3 – ozone
$PM_{2.5}$ – particulate matter <2.5 µm in diameter
RM – reactive mercury
SO_2 – sulfur dioxide
UNRG – University of Nevada, Reno Greenhouse facility, USA

*Table 18: Pearson correlations for meteorological data on days with Pb samples at UNRG in 2014. Italic data indicates significance level p<0.1, **bold italic data** indicates significance level p<0.05.*

UNRG 2014	Temp	RH	Wind speed	Pressure	ABLH	Solar radiation	Precipitation
O_3	-0.26	-0.11	0.29	-0.39	-0.12	-0.09	0.13
Max 1 h O_3	-0.16	-0.21	-0.10	-0.05	-0.05	-0.09	-0.04
MDA8 O_3	-0.15	-0.28	-0.06	-0.12	0.02	-0.03	-0.09
RM	***0.77***	***-0.54***	-0.02	-0.05	*0.41*	***0.51***	-0.12
Total Pb	-0.25	-0.05	-0.18	-0.16	-0.27	-0.17	-0.19
Asian Pb	-0.35	0.10	-0.11	-0.23	*-0.40*	-0.29	-0.09
%Asian Pb	***-0.43***	0.23	-0.03	-0.32	***-0.50***	*-0.40*	0.21

ABLH – atmospheric boundary layer height.
Max 1 h O_3 – maximum 1 h O_3
MDA8 O_3 – maximum daily average (8 h) O_3
O_3 – ozone
RH – relative humidity
RM – reactive mercury
Temp – temperature
UNRG – University of Nevada, Reno Greenhouse facility, USA

*Table 19: Pearson correlations for source box trajectory residence time (TRT) analysis on days with Pb samples for UNRG in 2014. Italic data indicates significance level p<0.1, **bold italic data** indicates significance level p<0.05.*

UNRG 2014	N. Eurasia			E. Asia			SF		LA	LV
	<3 km	Total	>3 km	<3 km	Total	>3 km	<1 km	>3 km	<1 km	<1 km
O_3	***0.54***	***0.75***	***0.72***	0.11	0.43	0.45	0.37	-0.18	-0.06	0.15
Max 1 h O_3	0.30	***0.61***	***0.61***	0.34	0.38	0.31	0.26	-0.13	-0.07	0.36
MDA8 O_3	0.34	***0.61***	***0.60***	0.33	0.40	0.33	0.30	-0.23	-0.16	0.33
RM	*-0.36*	*-0.38*	-0.32	-0.26	-0.28	-0.29	*0.37*	0.33	0.04	0.03
Total Pb	-0.15	0.13	0.18	***0.67***	***0.48***	*0.38*	-0.17	-0.09	-0.10	0.01
Asian Pb	-0.13	0.10	0.14	***0.63***	***0.44***	0.34	-0.07	-0.23	-0.10	-0.03
%Asian Pb	-0.31	-0.17	-0.11	***0.46***	*0.38*	0.33	-0.09	*-0.37*	-0.15	0.01

LA – Las Angeles, CA, USA
LV – Las Vegas, NV, USA
Max 1 h O_3 – maximum 1 h O_3
MDA8 O_3 – maximum daily average (8 h) O_3
O_3 – ozone
RM – reactive mercury
SF – San Francisco, CA, USA
UNRG – University of Nevada, Reno Greenhouse facility, USA

Table 20: Positive and negative correlations for 19 days with Pb samples at UNRG 2014. Bold + indicate α<0.05, italic + indicate α<0.1, while large — indicate α<0.05, small - indicate α<0.1. Grey data indicate <50% of the data was available.

UNRG Pb 2014		Positive						Negative					
		$^{206}Pb/^{207}Pb$	$^{208}Pb/^{207}Pb$	%Asian Pb	total Pb mass	Asian Pb mass	ng Pb/ug PM	$^{206}Pb/^{207}Pb$	$^{208}Pb/^{207}Pb$	%Asian Pb	total Pb mass	Asian Pb mass	ng Pb/ug PM
Filter	**RM**							**—**	**—**				
Gas	**NOx**				+	+							
	NO		**+**	**+**	**+**	**+**	**+**						
Meteorological	**Temp**							**—**	**—**	**—**			**—**
	RH	**+**	**+**										
	Pressure												-
	ABLH							**—**	**—**	**—**		-	
	Solar radiation							**—**	**—**	-			
E. Asia	**<3 km**		***+***	**+**	**+**	**+**	**+**						
	Total			***+***	**+**	**+**	**+**						
	>3 km				***+***		**+**						
SF	**>3 km**							**—**	**—**	-			

ABLH – atmospheric boundary layer height
RH – relative humidity
RM – reactive Hg
SF – San Francisco, CA, USA
UNRG – University of Nevada, Reno, Greenhouse, USA

GBNP 2015:

Figure 4: Diel pattern of O_3, CO, and NO_x at GBNP averaged over the sample period for each hour for a) same y-axis scale as UNRG (Fig. 2 and 3) and b) y-axis scaled for GBNP data. There was only 3 months of CO data during this time.

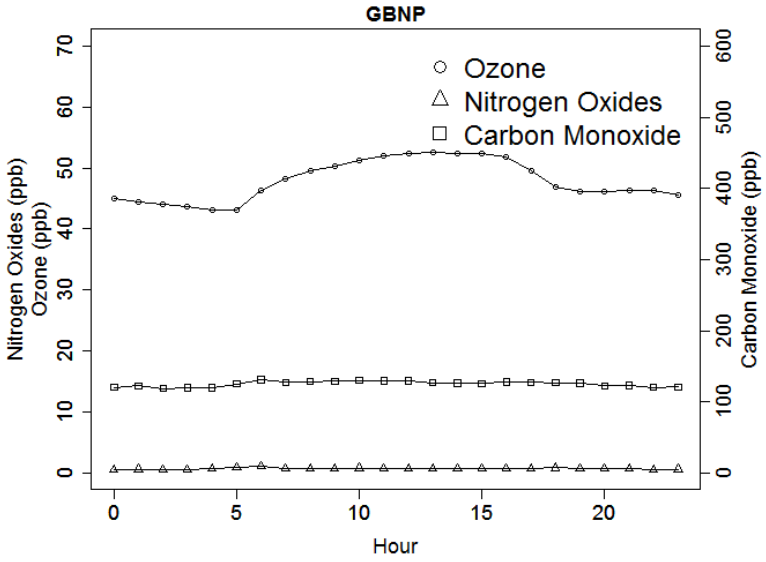

a)

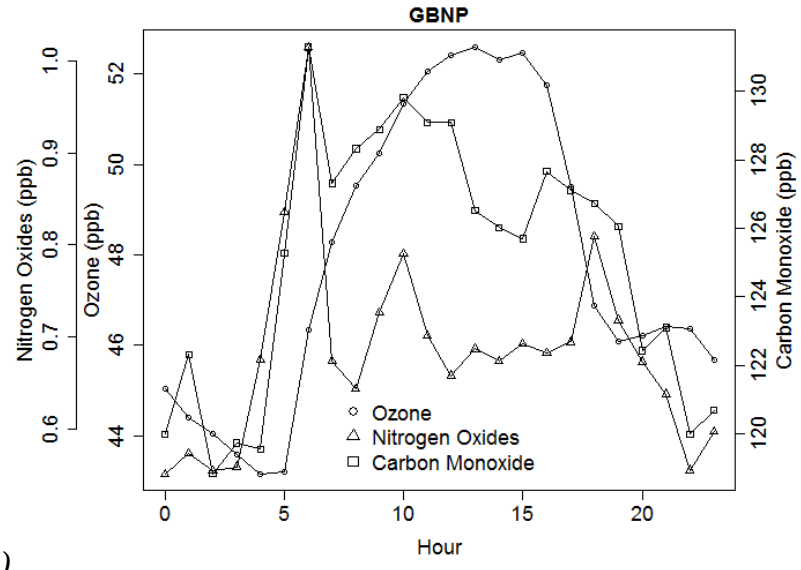

b)

Pearson Correlation for site data:

*Table 21: Pearson correlations for $PM_{2.5}$ and gas data at GBNP in 2015. Italic data indicates significance level p<0.1, **bold italic data** indicates significance level p<0.05, grey data indicates <50% of available data.*

GBNP	$PM_{2.5}$	RM	O_3	Max 1 h O_3	MDA8 O_3	CO	NO_x	NO	NO_y
O_3	***0.25***	***0.30***		***0.90***	***0.94***	***0.57***	***-0.39***	*-0.16*	0.06
Max 1 h O_3	***0.22***	***0.25***	***0.90***		***0.96***	***0.56***	***-0.27***	-0.08	***0.28***
MDA8 O_3	***0.24***	***0.25***	***0.94***	***0.96***		***0.59***	***-0.29***	-0.11	***0.21***
RM	***0.23***		***0.30***	***0.25***	***0.25***	-0.05	***-0.24***	-0.12	***-0.52***

CO – carbon monoxide
GBNP – Great Basin National Park, NV, USA
Max 1 h O_3 – maximum 1 h O_3
MDA8 O_3 – maximum daily average (8 h)
NO – nitrogen oxide
NO_x – nitrogen oxide compounds
NO_y – total reactive nitrogen
O_3 – ozone
$PM_{2.5}$ – particulate matter <2.5 µm in diameter
RM – reactive Hg

*Table 22: Pearson correlations for meteorological data at GBNP in 2015. Italic data indicates significance level p<0.1, **bold italic data** indicates significance level p<0.05, grey data indicates <50% of available data.*

GBNP	Temp	RH	Wind speed	Solar radiation	Precipitation
O_3	***0.27***	***-0.47***	***0.27***	***0.44***	***-0.19***
Max 1 h O_3	***0.18***	***-0.28***	0.14	***0.42***	-0.11
MDA8 O_3	***0.19***	***-0.32***	*0.16*	***0.40***	*-0.15*
RM	***0.80***	***-0.55***	0.14	***0.38***	*-0.14*

ABLH – atmospheric boundary layer height.
GBNP – Great Basin National Park, NV, USA
Max 1 h O_3 – maximum 1 h O_3
MDA8 O_3 – maximum daily average (8 h)
O_3 – ozone
RH – relative humidity
RM – reactive mercury
Temp – temperature

Table 23: Pearson correlations for source box trajectory residence time (TRT) analysis for GBNP in 2015. Italic data indicates significance level p<0.1, ***bold italic data*** *indicates significance level p<0.05.*

GBNP	N. Eurasia					E. Asia					SF		LA	LV
	<1 km	<2 km	<3 km	Total	>3 km	<1 km	<2 km	<3 km	Total	>3 km	<1 km	>3 km	<1 km	<1 km
O_3	-0.02	0.03	0.06	***0.25***	***0.28***	0.09	0.09	0.08	0.14	*0.15*	0.12	***0.20***	0.06	0.02
Max 1 h O_3	-0.06	-0.01	0.02	***0.28***	***0.32***	0.08	0.09	0.08	***0.19***	***0.21***	0.10	***0.17***	0.10	-0.01
MDA8 O_3	-0.05	0.00	0.03	***0.24***	***0.28***	0.08	0.08	0.07	0.14	*0.15*	0.08	*0.15*	0.08	0.00
RM	***-0.28***	***-0.28***	***-0.29***	***-0.33***	***-0.31***	***-0.25***	***-0.21***	***-0.19***	***-0.32***	***-0.34***	0.06	0.02	***0.34***	***0.24***

GBNP – Great Basin National Park, NV, USA
LA – Las Angeles, CA, USA
LV – Las Vegas, NV, USA
Max 1 h O_3 – maximum 1 h O_3
MDA8 O_3 – maximum daily average (8 h)
O_3 – ozone
RM – reactive mercury
SF – San Francisco, CA, USA

Table 24: Positive and negative correlations for GBNP 2015. Bold + indicate α<0.05, italic + indicate α<0.1, while large — indicate α<0.05, and small - indicate α<0.1. Grey data indicate <50% of the data was available.

GBNP 2015		Positive					Negative				
		$PM_{2.5}$	O_3	Max 1 h O_3	MDA8 O_3	RM	$PM_{2.5}$	O_3	Max 1 h O_3	MDA8 O_3	RM
Filter	$PM_{2.5}$		**+**	**+**	**+**	**+**					
	RM	**+**	**+**	**+**	**+**						
Gas	O_3	**+**				**+**					
	Max 1 h O_3	**+**				**+**					
	MDA8 O_3	**+**				**+**					
	CO		**+**	**+**	**+**						
	NOx	**+**						**—**	**—**	**—**	**—**
	NO							-			
	NOy			*+*	*+*						*—*
Meteorological	Temp	**+**	**+**	**+**	**+**	**+**					
	RH						**—**	**—**	**—**	**—**	**—**
	Wind speed		**+**		*+*						
	Solar radiation		**+**	**+**	**+**	**+**					
	Precipitation							**—**		-	-
N. Eurasia	<3 km										**—**
	Total	*+*	**+**	**+**	**+**						**—**
	>3 km	**+**	**+**	**+**	**+**						**—**
E. Asia	<3 km										**—**
	Total			**+**							**—**
	>3 km		*+*	**+**	*+*						**—**
SF	>3 km	**+**	**+**	**+**	*+*						
LA	<1 km					**+**					
LV	<1 km					**+**					

Table 25: Positive and negative correlations for spring GBNP 2015. Bold + indicate α<0.05, italic + indicate α<0.1, while large — indicate α<0.05, and small - indicate α<0.1. Grey data indicate <50% of the data was available.

		Positive								Negative							
GBNP Spring 2015		$PM_{2.5}$	O_3	Max 1 h O_3	MDA8 O_3	CAST O_3	CASTMax 1 h O_3	CASTMDA8 O_3	RM	$PM_{2.5}$	O_3	Max 1 h O_3	MDA8 O_3	CAST O_3	CASTMax 1 h O_3	CAST MDA8 O_3	RM
Filter	$PM_{2.5}$		+	+	+	+	+	+	+								
	RM	+	+	+	+	+	+	+									
Gas	O_3	+		+	+	+	+	+	+								
	Max 1 h O_3	+	+		+	+	+	+	+								
	MDA8 O_3	+	+	+		+	+	+	+								
	CO																-
	NO																-
	NOy										—	—	—	—	—	—	
	CAST O_3	+	+	+	+		+	+	+								
	CASTMax 1 h O_3	+	+	+	+	+		+	+								
	CASTMDA8 O_3	+	+	+	+	+	+		+								
Met	Temp	+	+	+	+	+	+	+	+								
	RH										—	—	—	—	—	—	
	Wind speed		+	+	+	+	+	+									
	Solar radiation					+	+	+	+								
	Precipitation										—		—	-			
N. Eurasia	Total																-
	>3 km																-
E. Asia	<3 km		+														
	Total		+														
SF	>3 km		+	+	+				+								
LA	<1 km					+	+	+									
LV	<1 km	+	+			+	+	+	+								

Table 26: Positive and negative correlations for summer GBNP 2015. Bold + indicate α<0.05, italic + indicate α<0.1, while large — indicate α<0.05, and small - indicate α<0.1. Grey data indicate <50% of the data was available.

GBNP Summer 2015		Positive								Negative							
		$PM_{2.5}$	O_3	Max 1 h O_3	MDA8 O_3	CAST O_3	CAST Max 1 h O_3	CASTMDA8 O_3	RM	$PM_{2.5}$	O_3	Max 1 h O_3	MDA8 O_3	CAST O_3	CASTMax 1 h O_3	CASTMDA8 O_3	RM
Filter	$PM_{2.5}$		+	+	+	+	+	+									
	RM		+	+	+	+	+	+									
Gas	O_3	+		+	+	+	+	+	+								
	Max 1 h O_3	+	+		+	+	+	+	+								
	MDA8 O_3	+	+	+		+	+	+	+								
	CO		+	+	+	+	+	+									
	NOx	+									—	—	—	—	—	—	—
	NO										—		—	-			
	NOy			+	+	+	+	+									—
	CAST O_3	+	+	+	+		+	+	+								
	CASTMax 1 h O_3	+	+	+	+	+		+	+								
	CAS MDA8 O_3	+	+	+	+	+	+		+								
Met	Temp	+	+	+	+	+	+	+	+								
	RH									-	—	—	—	—	—	—	—
	Wind speed		+														
	Solar radiation		+	+	+	+	+	+	+								
	Precipitation																—
N. Eurasia	Total	+	+	+	+	+	+	+									
	>3 km	+	+	+	+	+	+	+									
E. Asia	<3 km	+															
	Total			+	+		+	+									
	>3 km		+	+	+	+	+	+									
SF	<1 km		+			+			+								
	>3 km	+	+			+	+										
LA	<1 km								+	-							

GBNP 2015 (Pb days):

Mean O_3 concentration for the Pb sample days were higher at GBNP (52±10, range 36 to 66 ppb, n=23) than UNRG (41±11, range 19 to 61 ppb, n=10). Ozone (daily average) at GBNP was positively correlated with CO and with trajectories >3 km from San Francisco. Ozone (daily average, Max 1 h, MDA8) at GBNP was positively correlated with temperature, solar radiation, total Pb mass, total trajectories and >3 km trajectories from Northern Eurasia, and trajectories <1, <2, and <3 km from Northern Eurasia ($p<0.1$). Ozone (daily average, Max 1 h, MDA8) at GBNP was negatively correlated with NO_x, RH, and precipitation.

RM at GBNP was positively correlated with temperature, solar radiation, and trajectories <2 and <3 km, and trajectories <1 km and total trajectories ($p<0.1$) from Las Angeles. RM was negatively correlated with NO_y, RH, percent Asian Pb, total trajectories and >3 km trajectories from East Asia and >3 km trajectories from Las Vegas.

Table 27: Statistics for days with Pb samples at GBNP March to September 2015, a) filter samples and b) O_3.

a)

GBNP 2015	Pb mass (ng)	Δ208Pb	% Asian Pb	Total Pb (ng m^{-3})	Asian Pb (ng m^{-3})	Hg (pg m^{-3})	$PM_{2.5}$ (ug m^{-3})	ng Pb ug^{-1} $PM_{2.5}$
Min	2.83	-6.9914	-28	0.1178	-0.0685	6.03	1.10	0.0158
Mean	6.32	7.8315	31	0.2628	0.0813	62.03	5.04	0.0705
Median	5.89	7.4584	30	0.2451	0.0615	59.09	4.10	0.0493
Max	16.89	18.4634	74	0.7022	0.2670	133.70	21.10	0.2589
StDev	3.11	5.4259	22	0.1294	0.0712	35.89	4.09	0.0519
Count	23	23	23	23	23	23	23	23

b)

GBNP	NDEP AvgO3	NDEP MaxHrO3	NDEP MDA8O3	CAST AvgO3	CAST MaxHrO3	CAST MDA8O3
Min	35.74	43.01	40.92	34.46	39.00	38.88
Mean	51.81	61.01	57.49	50.16	58.22	54.87
Median	55.04	63.20	59.66	53.08	61.00	58.00
Max	66.21	80.85	74.10	63.67	78.00	72.38
Stdev	10.32	11.03	10.59	9.84	10.79	10.27
Count	23	23	23	23	23	23

Pearson Correlation for Pb days:

*Table 28: Pearson correlations for $PM_{2.5}$ and gas data on days with Pb samples at GBNP in 2015. Italic data indicates significance level p<0.1, **bold italic data** indicates significance level p<0.05, grey data indicates <50% of available data.*

GBNP	$PM_{2.5}$	RM	O_3	Max 1 h O_3	MDA8 O_3	CO	NO_x	NO	NO_y
O_3	0.25	0.27				***0.49***	***-0.46***	0.19	-0.27
Max 1 h O_3	0.16	0.24				0.34	***-0.46***	0.25	-0.14
MDA8 O_3	0.18	0.27				0.38	***-0.48***	0.15	-0.16
RM	0.15		0.27	0.24	0.27	-0.19	*-0.41*	-0.32	***-0.75***
Total Pb	*0.39*	0.01	***0.63***	***0.50***	***0.58***	*0.47*	-0.12	-0.19	-0.04
Asian Pb	0.03	*-0.37*	***0.49***	***0.45***	***0.48***	***0.61***	-0.21	0.23	0.37
%Asian Pb	-0.27	***-0.48***	0.02	0.04	0.03	*0.44*	-0.17	0.28	0.44

CO – carbon monoxide
GBNP – Great Basin National Park, NV, USA
Max 1 h O_3 – maximum 1 h O_3
MDA8 O_3 – maximum daily average (8 h) O_3
NO – nitrogen oxide
NO_x – nitrogen oxide compounds
NO_y – total reactive nitrogen
O_3 – ozone
$PM_{2.5}$ – particulate matter <2.5 µm in diameter
RM – reactive mercury
SO_2 – sulfur dioxide
WCAQ – Washoe County Air Quality

*Table 29: Pearson correlations for meteorological data on days with Pb samples at GBNP in 2015. Italic data indicates significance level p<0.1, **bold italic data** indicates significance level p<0.05, grey data indicates <50% of available data.*

GBNP	Temp	RH	Wind speed	Solar radiation	Precipitation
O_3	***0.54***	***-0.79***	0.52	***0.66***	***-0.53***
Max 1 h O_3	***0.45***	***-0.68***	0.49	***0.61***	***-0.52***
MDA8 O_3	***0.46***	***-0.72***	0.52	***0.62***	***-0.55***
RM	***0.71***	***-0.55***	*0.56*	***0.52***	-0.29
Total Pb	0.09	***-0.43***	0.17	0.09	-0.30
Asian Pb	-0.21	-0.21	0.10	0.04	-0.19
%Asian Pb	*-0.39*	0.11	0.04	-0.01	0.04

ABLH – atmospheric boundary layer height.
GBNP – Great Basin National Park, NV, USA
Max 1 h O_3 – maximum 1 h O_3
MDA8 O_3 – maximum daily average (8 h) O_3
O_3 – ozone
RH – relative humidity
RM – reactive mercury
Temp – temperature

Table 30: Pearson correlations for source box trajectory residence time (TRT) analysis on days with Pb samples for GBNP in 2015. Italic data indicates significance level p<0.1, ***bold italic data*** *indicates significance level p<0.05.*

GBNP	N. Eurasia			E. Asia			SF		LA	LV
	<3 km	**Total**	**>3 km**	**<3 km**	**Total**	**>3 km**	**<1 km**	**>3 km**	**<1 km**	**<1 km**
O_3	*0.42*	***0.45***	***0.43***	0.31	0.24	0.19	0.24	***0.44***	0.05	0.05
Max 1 h O_3	***0.43***	***0.53***	***0.52***	0.35	0.29	0.24	0.17	0.32	0.15	-0.02
MDA8 O_3	*0.37*	***0.44***	***0.43***	0.30	0.31	0.28	0.11	0.34	0.14	-0.05
RM	-0.07	0.03	0.05	-0.14	***-0.51***	***-0.55***	0.26	-0.01	*0.41*	0.10
Total Pb	0.04	0.10	0.11	***0.50***	***0.53***	***0.48***	0.15	***0.54***	0.14	0.25
Asian Pb	0.11	0.22	0.23	***0.53***	***0.85***	***0.84***	0.23	0.17	-0.32	-0.10
%Asian Pb	0.10	0.17	0.17	0.16	***0.56***	***0.61***	0.16	-0.14	***-0.54***	*-0.41*

GBNP – Great Basin National Park, NV, USA
LA – Las Angeles, CA, USA
LV – Las Vegas, NV, USA
Max 1 h O_3 – maximum 1 h O_3
MDA8 O_3 – maximum daily average (8 h) O_3
O_3 – ozone
RM – reactive mercury
SF – San Francisco, CA, USA

Table 31: Positive and negative correlations for 22 days with Pb samples at GBNP 2015. Bold + indicate α<0.05, italic + indicate α<0.1, while large — indicate α<0.05, small - indicate α<0.1.

GBNP Pb 2015		Positive						Negative					
		$^{206}Pb/^{207}Pb$	$^{208}Pb/^{207}Pb$	%Asian Pb	total Pb mass	Asian Pb mass	ng Pb/ug PM	$^{206}Pb/^{207}Pb$	$^{208}Pb/^{207}Pb$	%Asian Pb	total Pb mass	Asian Pb mass	ng Pb/ug PM
Filter	$PM_{2.5}$				+								—
	RM									—		-	
Gas	O_3				+	+	+						
	Max 1 h O_3				+	+							
	MDA8 O_3				+	+	+						
	CO			+	+	+	+						
	NOx	+	+										
Meteorological	Temp								-	-			
	RH										—		
	Solar radiation							-	-				
N. Eurasia	<3 km							—	-				
	Total							-					
E. Asia	<3 km				+	+							
	Total			+	+	+	+						
	>3 km			+	+	+	+						
SF	>3 km				+								
LA	<1 km	+								—			
LV	<1 km									-			

UNRG 2015:

*Table 32: Pearson correlations for $PM_{2.5}$ and gas data at UNRG in 2015. Italic data indicates significance level p<0.1, **bold italic data** indicates significance level p<0.05, grey data indicates <50% of available data.*

UNRG 2015	$PM_{2.5}$	RM	O_3	Max 1 hr O_3	MDA8 O_3	CO	NO_x	NO
O_3	*-0.15*	***-0.38***		***0.76***	***0.82***	***-0.47***	***-0.49***	***-0.83***
Max 1 h O_3	0.00	***-0.40***	***0.76***		***0.96***	0.04	0.02	***-0.40***
MDA8 O_3	-0.05	***-0.48***	***0.82***	***0.96***			-0.07	***-0.56***
RM	***0.45***		***-0.38***	***-0.40***	***-0.48***	0.12	***-0.23***	-0.06

CO – carbon monoxide
Max 1 h O_3 – maximum 1 h O_3
MDA8 O_3 – maximum daily average (8 h)
NO – nitrogen oxide
NO_x – nitrogen oxide compounds
NO_y – total reactive nitrogen
O_3 – ozone
$PM_{2.5}$ – particulate matter <2.5 µm in diameter
RM – reactive mercury
UNRG – University of Nevada, Reno Greenhouse facility, USA

Table 33: Pearson correlations for meteorological data at UNRG in 2015. Italic data indicates significance level p<0.1, ***bold italic data*** *indicates significance level p<0.05, grey data indicates <50% of available data.*

UNRG 2015	Temp	RH	Wind speed	Solar radiation	Precipitation	Pressure	ABLH
O_3	***-0.22***	-0.07	***0.58***	0.11	*-0.13*	***-0.22***	***0.31***
Max 1 h O_3	***-0.25***	***-0.17***	0.10	*0.13*	*-0.13*	0.06	***0.49***
MDA8 O_3	***-0.32***	***-0.15***	***0.17***	***0.14***	***-0.18***	0.06	***0.47***
RM	***0.77***	***-0.42***	-0.12	***0.22***	-0.10	***-0.32***	0.06

ABLH – atmospheric boundary layer height.
Max 1 h O_3 – maximum 1 h O_3
MDA8 O_3 – maximum daily average (8 h)
O_3 – ozone
RH – relative humidity
RM – reactive mercury
Temp – temperature
UNRG – University of Nevada, Reno Greenhouse facility, USA

Table 34: Pearson correlations for source box trajectory residence time (TRT) analysis for UNRG in 2015. Italic data indicates significance level p<0.1, ***bold italic data*** *indicates significance level p<0.05.*

UNRG 2015	N. Eurasia					E. Asia					SF		LA	LV
	<1 km	**<2 km**	**<3 km**	**Total**	**>3 km**	**<1 km**	**<2 km**	**<3 km**	**Total**	**>3 km**	**<1 km**	**>3 km**	**<1 km**	**<1 km**
O_3	***0.22***	***0.27***	***0.30***	***0.35***	***0.32***	0.02	0.01	0.01	-0.02	-0.04	0.04	-0.03	0.03	-0.05
Max 1 h O_3	***0.21***	***0.24***	***0.26***	***0.35***	***0.34***	***0.18***	***0.18***	***0.20***	***0.22***	***0.22***	-0.08	0.00	0.04	-0.08
MDA8 O_3	***0.26***	***0.29***	***0.32***	***0.42***	***0.40***	***0.19***	***0.19***	***0.21***	***0.24***	***0.23***	***-0.15***	-0.03	0.05	-0.08
RM	***-0.21***	***-0.18***	*-0.15*	***-0.19***	***-0.18***	***-0.35***	***-0.36***	***-0.37***	***-0.42***	***-0.42***	***0.33***	0.02	-0.01	-0.02

LA – Las Angeles, CA, USA
LV – Las Vegas, NV, USA
Max 1 h O_3 – maximum 1 h O_3
MDA8 O_3 – maximum daily average (8 h)
O_3 – ozone
RM – reactive mercury
SF – San Francisco, CA, USA
UNRG – University of Nevada, Reno Greenhouse facility, USA

Table 35: Positive and negative correlations for UNRG 2015. Bold + indicate α<0.05, italic + indicate α<0.1, while large — indicate α<0.05, and small - indicate α<0.1.

UNRG 2015		Positive					Negative				
		$PM_{2.5}$	**O_3**	**Max 1 h O_3**	**MDA8 O_3**	**RM**	**$PM_{2.5}$**	**O_3**	**Max 1 h O_3**	**MDA8 O_3**	**RM**
Filter	**$PM_{2.5}$**					**+**		-			
	RM	**+**						**—**	**—**	**—**	
Gas	**O_3**						-				**—**
	Max 1 h O_3										**—**
	MDA8 O_3										**—**
	CO	**+**						**—**			
	NOx	**+**						**—**			**—**
	NO	**+**						**—**	**—**	**—**	
Meteorological	**Temp**	**+**				**+**		**—**	**—**	**—**	
	RH						**—**		**—**	**—**	**—**
	Wind speed		**+**		**+**		**—**				
	Pressure							**—**			**—**
	ABLH		**+**	**+**	**+**						
	Solar radiation			*+*	**+**	**+**					
	Precipitation							-	-	**—**	
N. Eurasia	**<3 km**		**+**	**+**	**+**		-				-
	Total		**+**	**+**	**+**						**—**
	>3 km		**+**	**+**	**+**						**—**
E. Asia	**<3 km**			**+**	**+**						**—**
	Total			**+**	**+**						**—**
	>3 km			**+**	**+**						**—**
SF	**<1 km**					**+**				**—**	

UNRG 2015 (Pb days):

Table 36: Statistics for days with Pb samples at UNRG March to September 2015, a) filter samples and b) O_3.

a)

UNRG 2015	Pb mass (ng)	Δ208Pb	% Asian Pb	Total Pb (ng m^{-3})	Asian Pb (ng m^{-3})	Hg (pg m^{-3})	$PM_{2.5}$ (ug m^{-3})	ng Pb ug^{-1} $PM_{2.5}$
Min	8.46	2.2577	9.0	0.3517	0.0318	7.77	4.00	0.0360
Mean	36.76	8.8088	35	1.5288	0.6879	43.74	7.85	0.2489
Median	25.51	6.2240	25	1.0609	0.3389	46.50	7.00	0.1965
Max	106.62	18.5625	74	4.4337	2.8755	103.86	15.00	1.1084
StDev	29.92	5.6394	23	1.2443	0.8813	28.06	3.43	0.3008
Count	11	11	11	11	11	11	11	11

b)

UNRG 2015	AvgO3	Max HrO3	MDA8O3	WCAQ AvgO3	WCAQ MaxHrO3	WCAQ MDA8O3
Min	19.35	38.94	28.88	29.75	48.00	40.13
Mean	40.62	66.47	57.35	48.91	70.00	63.30
Median	41.13	68.32	58.59	47.63	70.00	64.00
Max	61.14	77.38	70.14	58.29	85.00	73.88
Stdev	10.52	11.65	11.71	8.25	10.09	9.92
Count	10	10	10	11	11	11

Pearson Correlation for Pb days:

*Table 37: Pearson correlations for $PM_{2.5}$ and gas data on days with Pb samples at UNRG in 2015. Italic data indicates significance level p<0.1, **bold italic data** indicates significance level p<0.05, grey data indicates <50% of available data.*

UNRG 2015	$PM_{2.5}$	RM	O_3	Max 1 hr O_3	MDA8 O_3	CO	NO_x	NO
O_3	0.23	-0.35				-0.32	*-0.64*	***-0.97***
Max 1 h O_3	0.32	-0.36				0.19	*-0.64*	***-0.99***
MDA8 O_3	0.03	*-0.54*				-0.12	*-0.60*	***-0.97***
RM	***0.61***		-0.35	-0.36	*-0.54*	0.25	*-0.55*	-0.79
Total Pb	-0.08	-0.10	0.43	0.44	*0.53*	0.11	-0.24	-0.47
Asian Pb	-0.16	-0.29	0.49	0.49	***0.58***	0.14	-0.27	-0.51
%Asian Pb	-0.16	-0.35	***0.65***	*0.54*	***0.66***	-0.21	-0.52	***-0.92***

CO – carbon monoxide
Max 1 h O_3 – maximum 1 h O_3
MDA8 O_3 – maximum daily average (8 h) O_3
NO – nitrogen oxide
NO_x – nitrogen oxide compounds
NO_y – total reactive nitrogen
O_3 – ozone
$PM_{2.5}$ – particulate matter <2.5 µm in diameter
RM – reactive mercury
SO_2 – sulfur dioxide.
UNRG – University of Nevada, Reno Greenhouse facility, USA
WCAQ – Washoe County Air Quality

Table 38: Pearson correlations for meteorological data on days with Pb samples at UNRG in 2015. Italic data indicates significance level p<0.1, ***bold italic data*** *indicates significance level p<0.05, grey data indicates <50% of available data.*

UNRG 2015	Temp	RH	Wind speed	Solar radiation	Precipitation	Pressure
O_3	0.00	-0.40	0.18	*0.53*	0.16	0.09
Max 1 h O_3	0.08	-0.47	-0.19	*0.56*	0.20	0.09
MDA8 O_3	-0.10	-0.25	-0.27	*0.54*	0.22	0.16
RM	***0.67***	-0.37	0.15	0.20	-0.06	-0.43
Total Pb	-0.12	-0.17	0.01	0.08	0.24	*0.51*
Asian Pb	-0.10	-0.05	0.00	0.07	0.41	*0.48*
%Asian Pb	0.07	0.07	-0.08	0.38	***0.57***	0.17

ABLH – atmospheric boundary layer height
Max 1 h O_3 – maximum 1 h O_3
MDA8 O_3 – maximum daily average (8 h) O_3
O_3 – ozone
RH – relative humidity
RM – reactive mercury
Temp – temperature
UNRG – University of Nevada, Reno Greenhouse facility, USA

Table 39: Pearson correlations for source box trajectory residence time (TRT) analysis on days with Pb samples for UNRG in 2015. Italic data indicates significance level p<0.1, ***bold italic data*** *indicates significance level p<0.05.*

UNRG 2015	N. Eurasia			E. Asia			SF		LA	LV
	<3 km	Total	>3 km	<3 km	Total	>3 km	<1 km	>3 km	<1 km	<1 km
O_3	-0.16	0.08	0.17	0.26	0.11	0.02	0.17	-0.20	0.07	0.12
Max 1 h O_3	-0.14	-0.01	0.04	0.09	0.00	-0.06	0.28	0.03	0.01	0.08
MDA8 O_3	-0.14	0.01	0.06	0.21	0.13	0.07	0.07	0.04	0.16	0.23
RM	***0.46***	0.20	0.10	-0.67	***-0.65***	***-0.63***	0.30	0.04	-0.01	-0.09
Total Pb	0.30	0.24	0.21	0.02	-0.10	-0.17	-0.24	0.09	0.03	-0.01
Asian Pb	-0.09	-0.12	-0.12	0.03	-0.07	-0.13	-0.23	-0.12	0.20	0.17
%Asian Pb	-0.27	-0.22	-0.19	-0.04	-0.10	-0.14	-0.32	-0.08	0.47	0.48

LA – Las Angeles, CA, USA
LV – Las Vegas, NV, USA
Max 1 h O_3 – maximum 1 h O_3
MDA8 O_3 – maximum daily average (8 h) O_3
O_3 – ozone
RM – reactive mercury
SF – San Francisco, CA, USA
UNRG – University of Nevada, Reno Greenhouse facility, USA

Table 40: Positive and negative correlations for days with Pb samples at UNRG 2015. Bold + indicate α<0.05, italic + indicate α<0.1, while large — indicate α<0.05, small - indicate α<0.1. Grey data indicate <50% of the data was available.

UNRG Pb 2015		Positive					Negative				
		$^{206}Pb/^{207}Pb$	$^{208}Pb/^{207}Pb$	%Asian Pb	total Pb mass	Asian Pb mass	$^{206}Pb/^{207}Pb$	$^{208}Pb/^{207}Pb$	%Asian Pb	total Pb mass	Asian Pb mass
Gas	O_3			**+**							
	Max 1 h O_3			*+*							
	MDA8 O_3			**+**	*+*	**+**					
	NO								—		
Met	Pressure				*+*	*+*					
	ABLH							—			
	Precipitation			**+**							
N. Eurasia	<3 km	**+**	**+**								
	Total	**+**	**+**								
	>3 km	**+**	**+**								

Figure 5: HYSPLIT 10-day back trajectories for GBNP September 3, 2015. Trajectory points are colored by altitude height (m agl). FRP points are sized based on power (MW), white circles indicate the most recent day back, light grey circles indicate an intermediate day back, and grey circles indicate the furthest day back. Black boxes indicate the five source boxes.

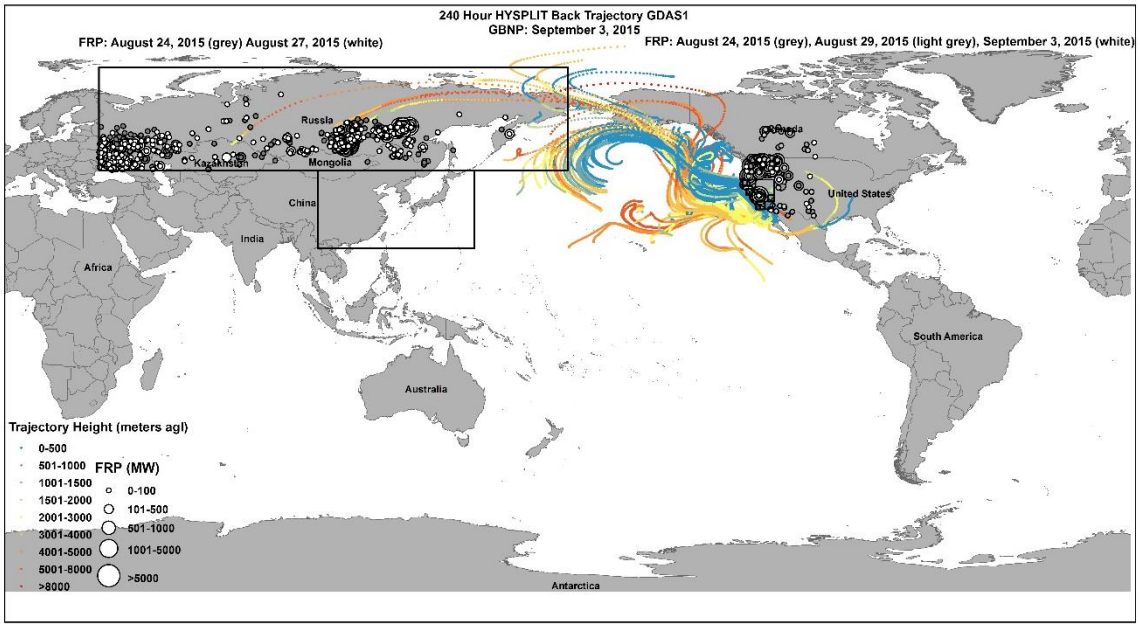

Case studies:

June 2014

Figure 6: Percent Asian Pb for specific days in June 2014 at PEAV and UNRG. The horizontal grey line indicates the 75th percentile for PEAV (36%); the horizontal black line indicates the 75th percentile for UNRG (42%).

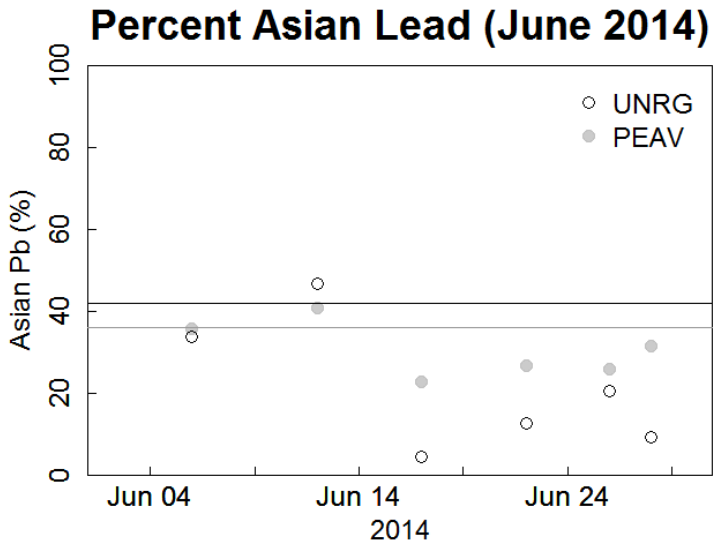

Figure 7: Surface weather maps from NOAA for a) June 6, b) 12, c) 13, and d) 17, 2014

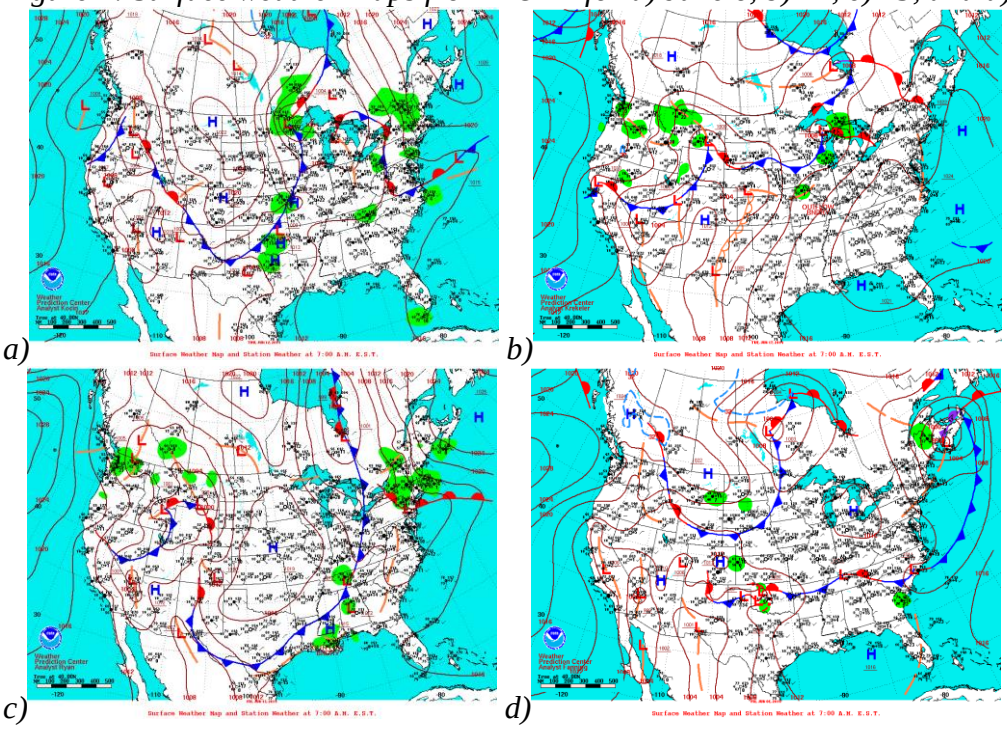

Figure 8: 500 millibar weather maps from NOAA for a) June 6, b) 12, c) 13, and d) 17, 2014

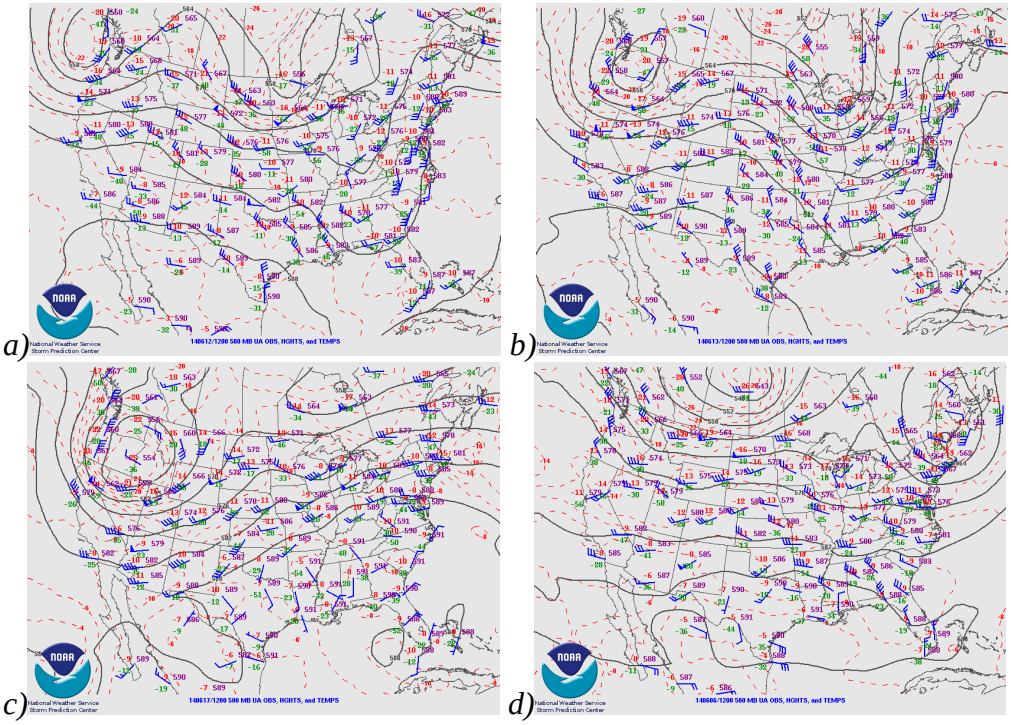

Figure 9: Peavine Peak, NV, USA, June 2014 a) time series of pollutants and RH, b) time series of CO and NO_x, and b) trajectory residence times. Dashed lines indicate the monthly median and the NAAQS for O_3. Grey shading indicates pressure systems and frontal activity.

a)

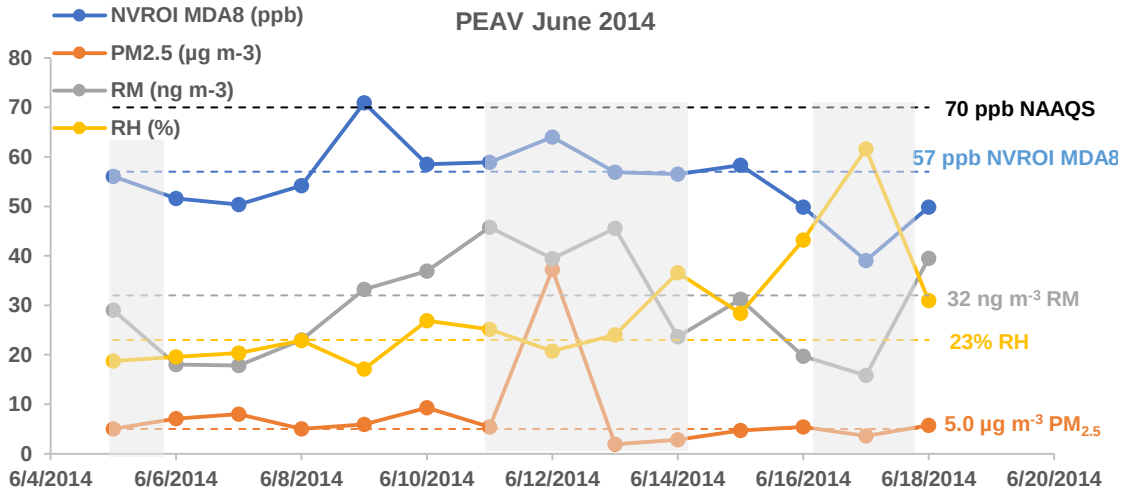

b)

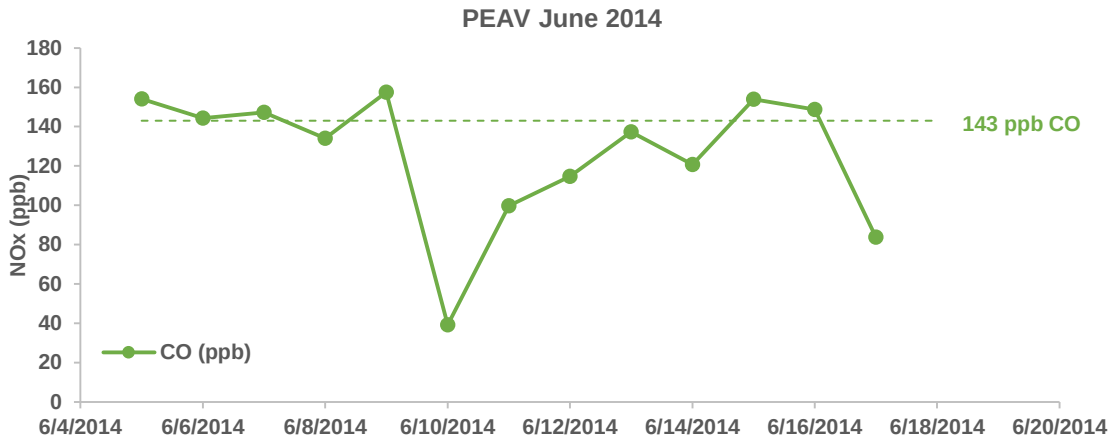
PEAV June 2014
NOx (ppb)
180
160
140
120
100
80
60
40
20
0
143 ppb CO
CO (ppb)
6/4/2014
6/6/2014
6/8/2014
6/10/2014
6/12/2014
6/14/2014
6/16/2014
6/18/2014
6/20/2014

c)

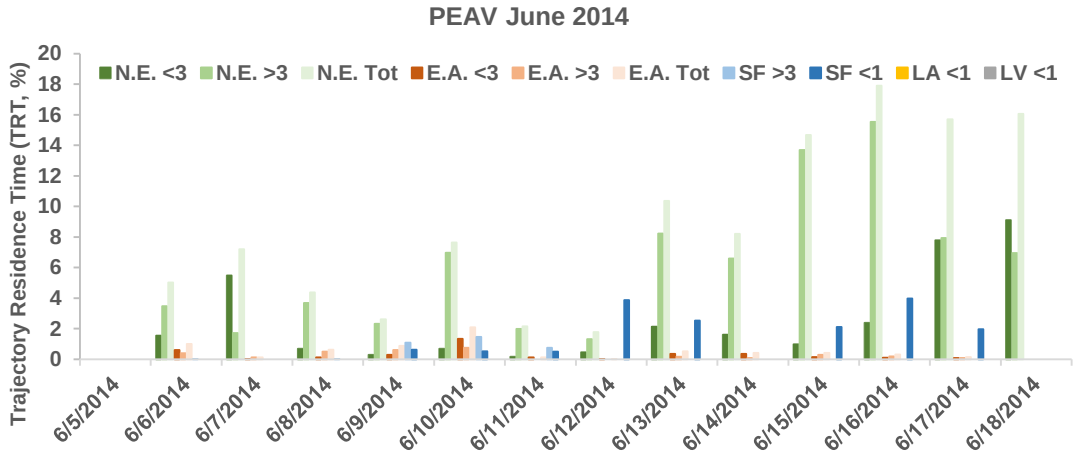
PEAV June 2014
Trajectory Residence Time (TRT, %)
20
18
16
14
12
10
8
6
4
2
0
N.E. <3
N.E. >3
N.E. Tot
E.A. <3
E.A. >3
E.A. Tot
SF >3
SF <1
LA <1
LV <1
6/5/2014
6/6/2014
6/7/2014
6/8/2014
6/9/2014
6/10/2014
6/11/2014
6/12/2014
6/13/2014
6/14/2014
6/15/2014
6/16/2014
6/17/2014
6/18/2014

Figure 10: University of Nevada, Reno Greenhouse, USA, June 2014 a) time series of pollutants and RH, b) time series of CO and NO_x, and b) trajectory residence times. Dashed lines indicate the monthly median and the NAAQS for O_3. Grey shading indicates pressure systems and frontal activity.

a)

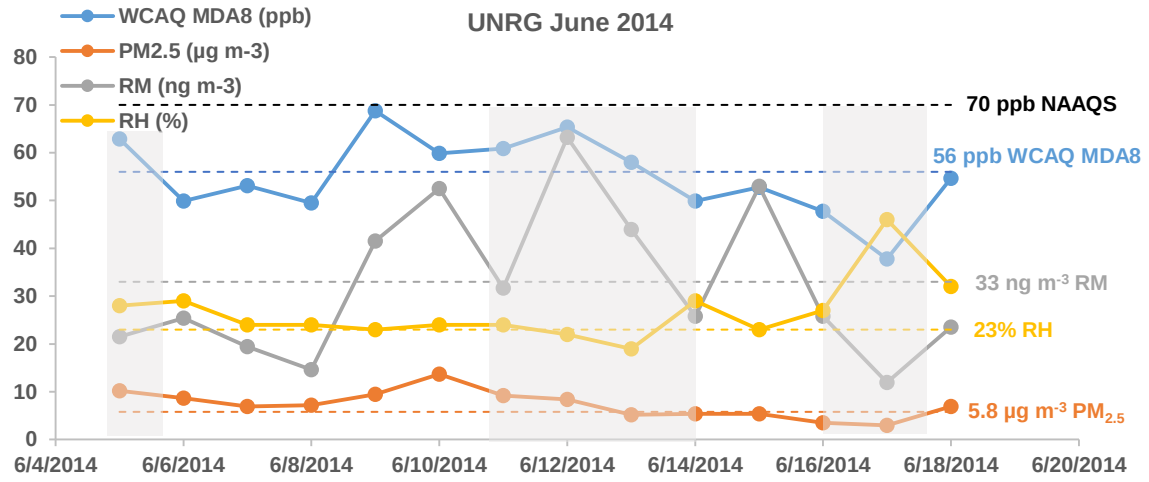

b)

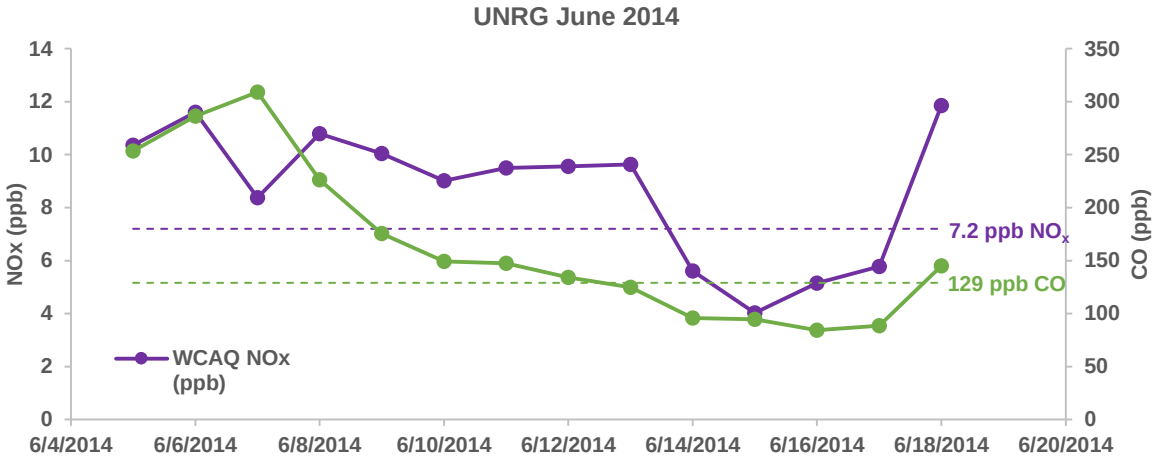

c)

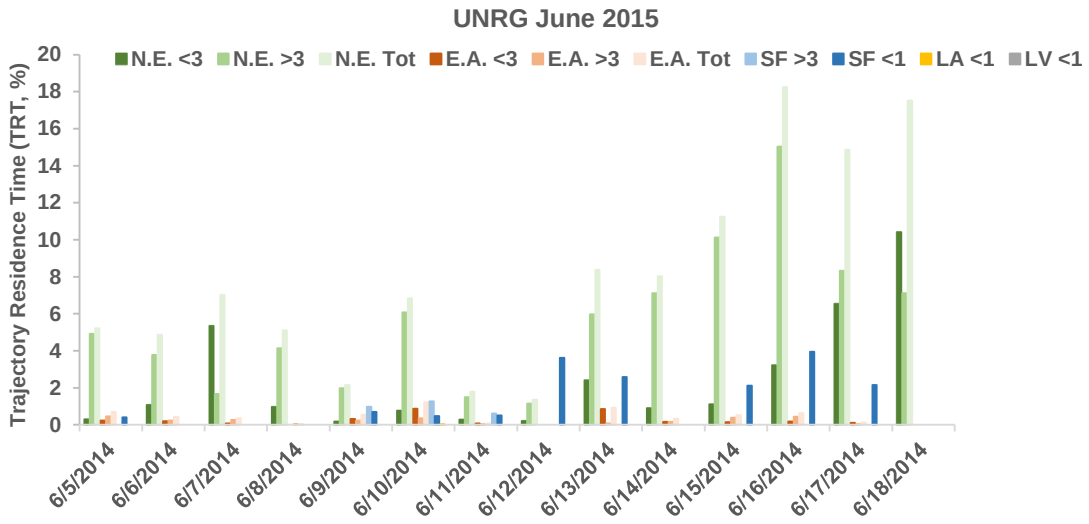

<u>September/October 2014</u>

Figure 11: Peavine Peak, Reno, NV, USA, September 2014 a) time series of pollutants and RH, b) CO and NOx time series, and c) trajectory residence times and October 2014 c) time series of pollutants and RH, d) CO and NOx time series, e) trajectory residence times. Dashed lines indicate the monthly medians and the NAAQS for O_3. Grey shading indicates frontal activity.

a)

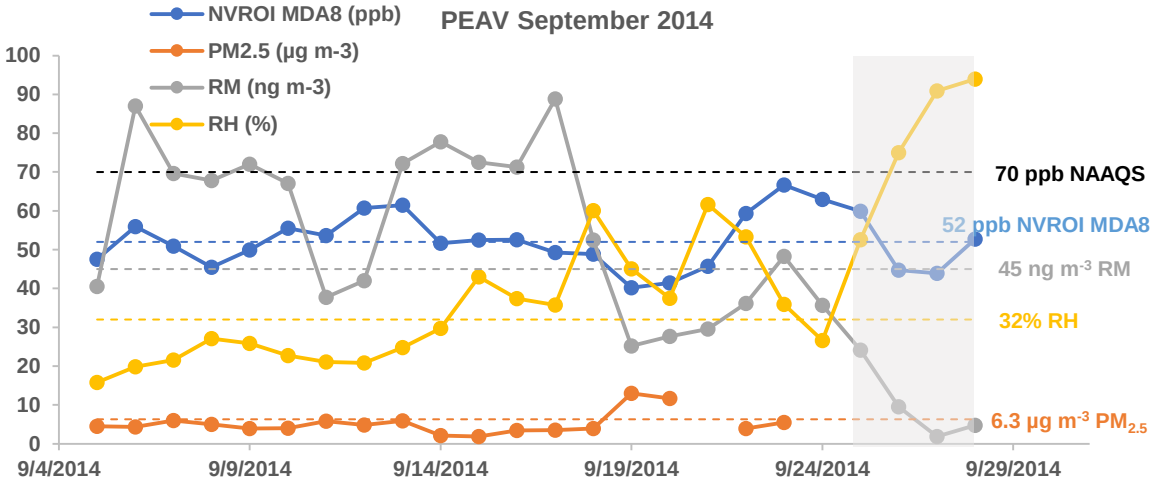

b)

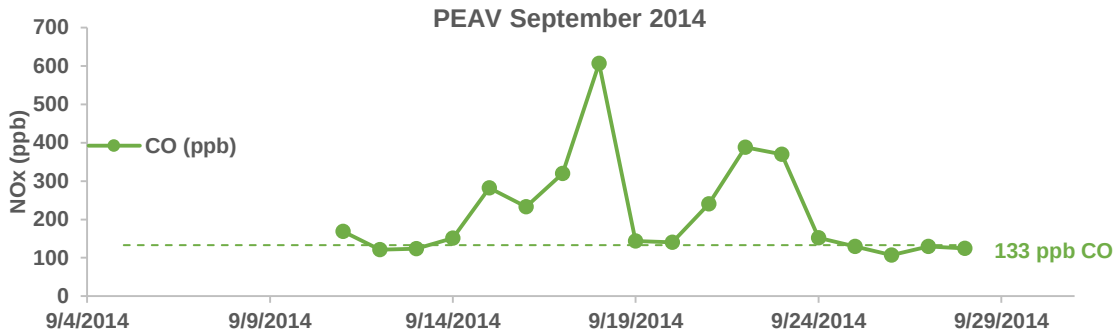
PEAV September 2014
NOx (ppb)
CO (ppb)
133 ppb CO
0
100
200
300
400
500
600
700
9/4/2014
9/9/2014
9/14/2014
9/19/2014
9/24/2014
9/29/2014

c)

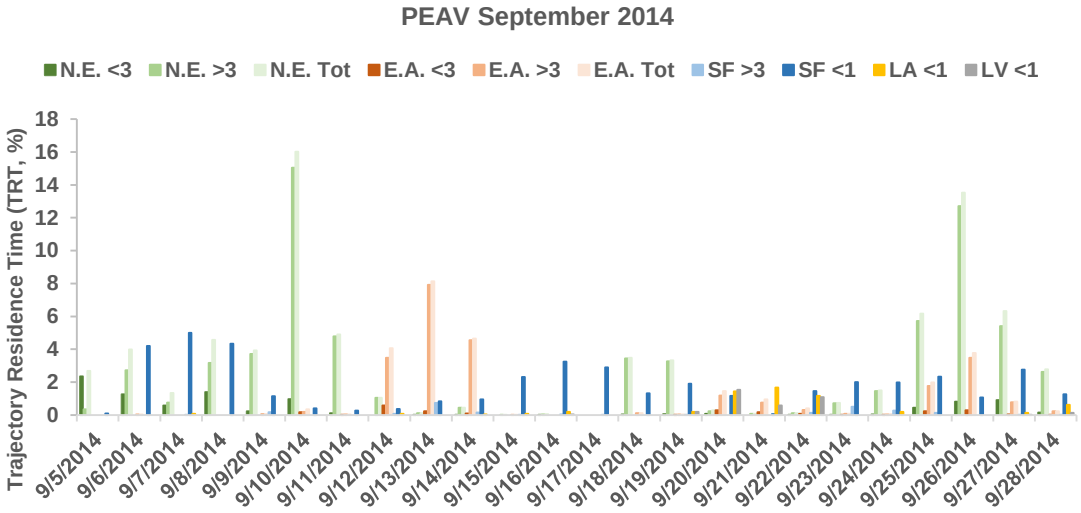
PEAV September 2014
N.E. <3
N.E. >3
N.E. Tot
E.A. <3
E.A. >3
E.A. Tot
SF >3
SF <1
LA <1
LV <1
Trajectory Residence Time (TRT, %)
0
2
4
6
8
10
12
14
16
18
9/5/2014
9/6/2014
9/7/2014
9/8/2014
9/9/2014
9/10/2014
9/11/2014
9/12/2014
9/13/2014
9/14/2014
9/15/2014
9/16/2014
9/17/2014
9/18/2014
9/19/2014
9/20/2014
9/21/2014
9/22/2014
9/23/2014
9/24/2014
9/25/2014
9/26/2014
9/27/2014
9/28/2014

d)

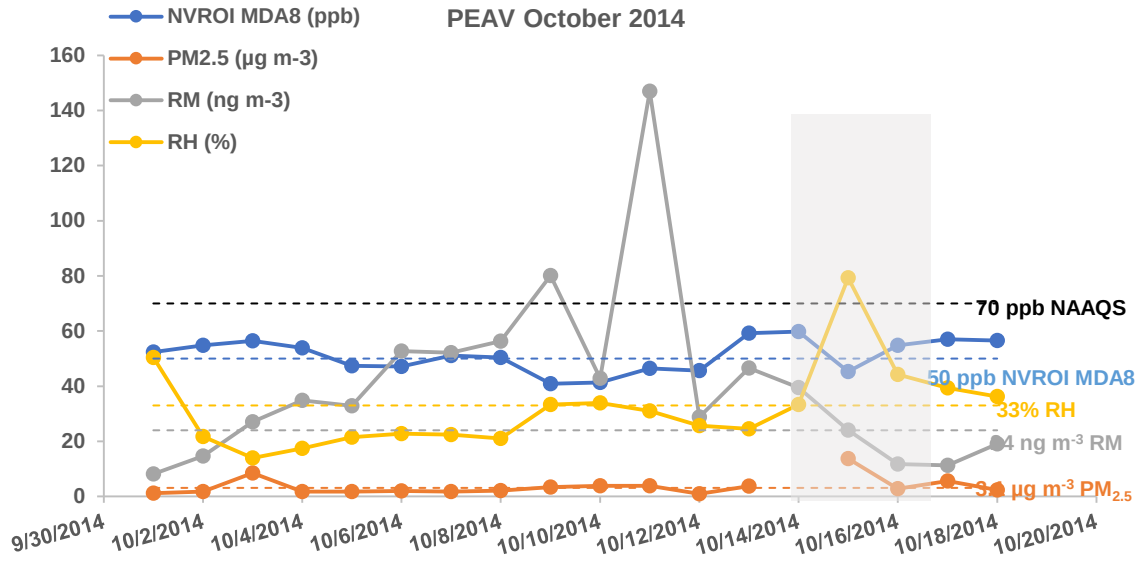
PEAV October 2014
NVROI MDA8 (ppb)
PM2.5 (µg m-3)
RM (ng m-3)
RH (%)
160
140
120
100
80
60
40
20
0
70 ppb NAAQS
50 ppb NVROI MDA8
33% RH
4 ng m-3 RM
9/30/2014
10/2/2014
10/4/2014
10/6/2014
10/8/2014
10/10/2014
10/12/2014
10/14/2014
10/16/2014
10/18/2014
10/20/2014

e)

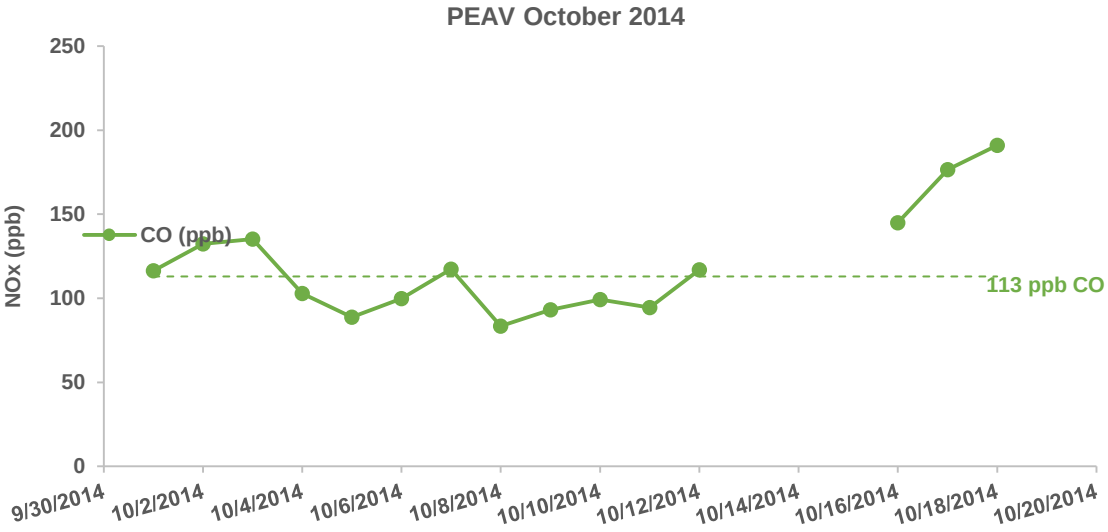
PEAV October 2014
NOx (ppb)
CO (ppb)
250
200
150
100
50
0
113 ppb CO
9/30/2014
10/2/2014
10/4/2014
10/6/2014
10/8/2014
10/10/2014
10/12/2014
10/14/2014
10/16/2014
10/18/2014
10/20/2014

f)

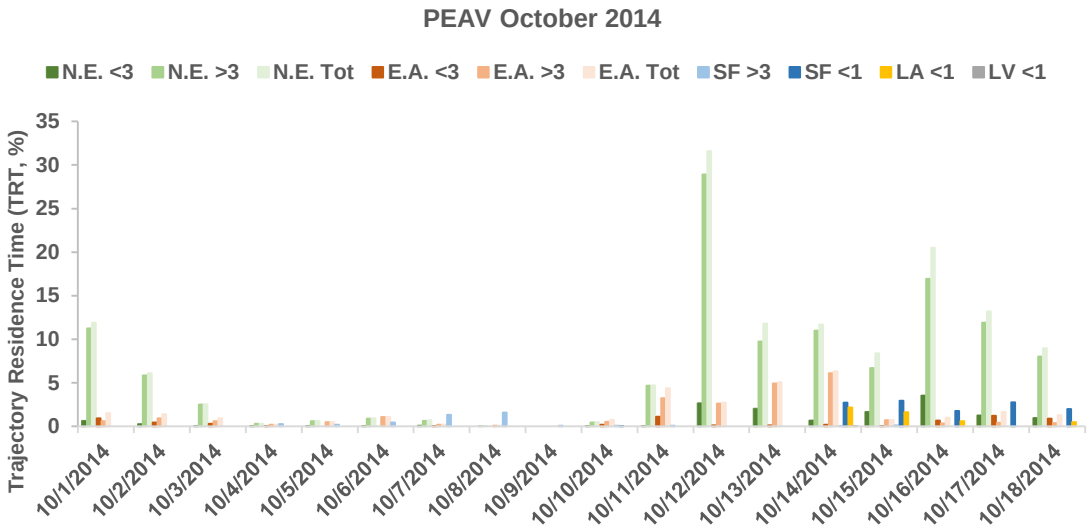

Figure 12: University of Nevada, Reno, Greenhouse, USA, September 2014 a) time series of pollutants and RH, b) CO and NOx time series, and c) trajectory residence times and October 2014 c) time series of pollutants and RH, d) CO and NOx time series, e) trajectory residence times. Dashed lines indicate the monthly medians and the NAAQS for O_3. Grey shading indicates low-pressure and frontal activity.

a)

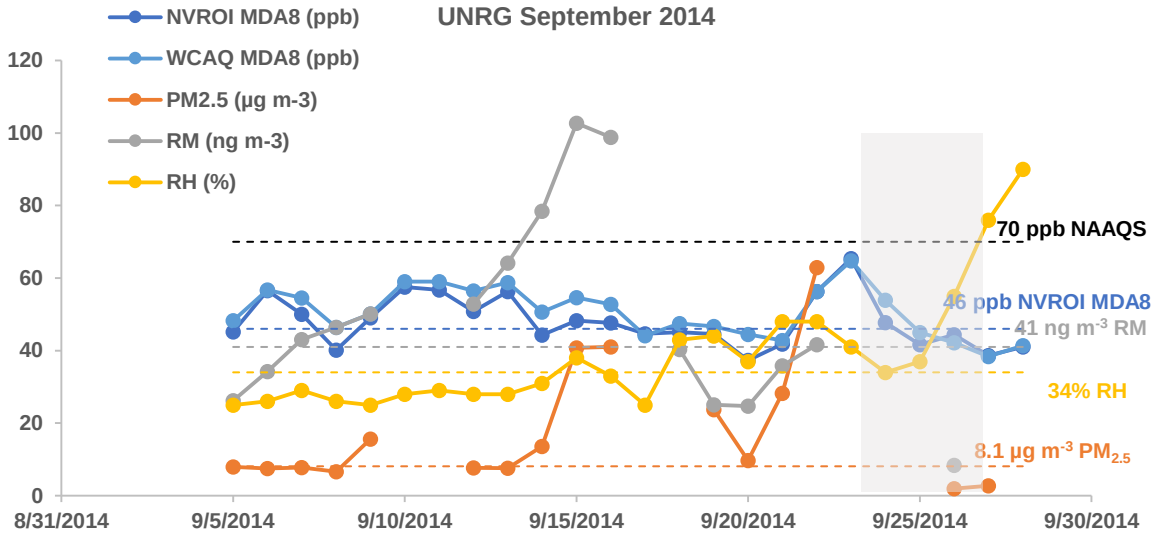

b)

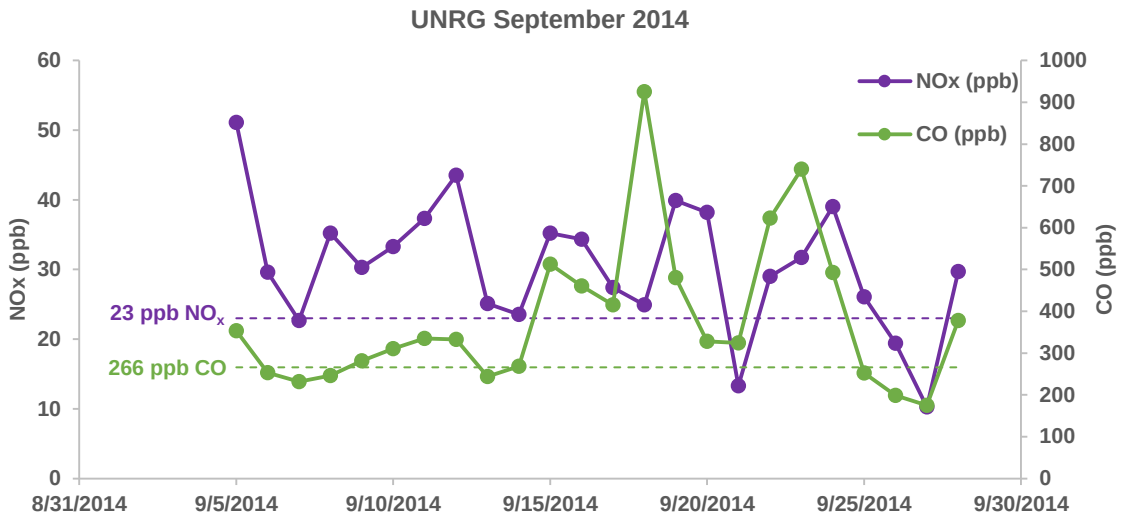
UNRG September 2014
NOx (ppb)
CO (ppb)
23 ppb NOx
266 ppb CO
60
50
40
30
20
10
0
1000
900
800
700
600
500
400
300
200
100
0
8/31/2014
9/5/2014
9/10/2014
9/15/2014
9/20/2014
9/25/2014
9/30/2014

c)

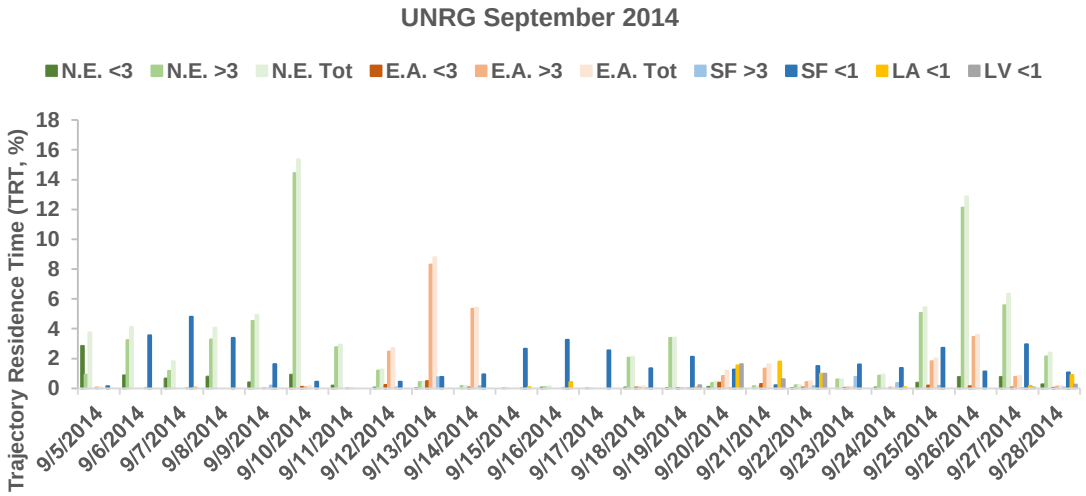
UNRG September 2014
N.E. <3
N.E. >3
N.E. Tot
E.A. <3
E.A. >3
E.A. Tot
SF >3
SF <1
LA <1
LV <1
Trajectory Residence Time (TRT, %)
18
16
14
12
10
8
6
4
2
0
9/5/2014
9/6/2014
9/7/2014
9/8/2014
9/9/2014
9/10/2014
9/11/2014
9/12/2014
9/13/2014
9/14/2014
9/15/2014
9/16/2014
9/17/2014
9/18/2014
9/19/2014
9/20/2014
9/21/2014
9/22/2014
9/23/2014
9/24/2014
9/25/2014
9/26/2014
9/27/2014
9/28/2014

d)

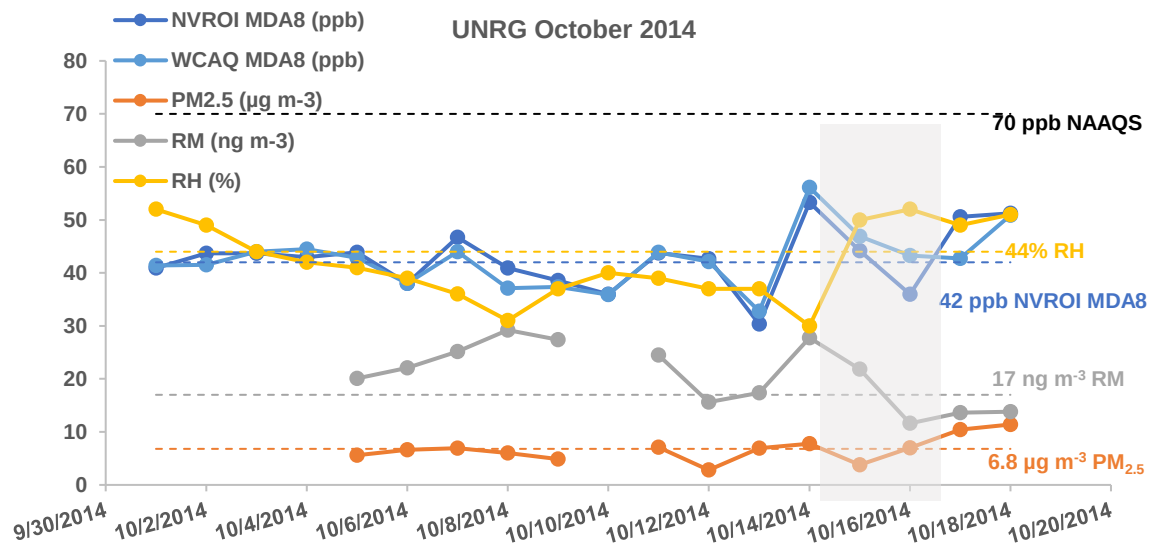
UNRG October 2014
NVROI MDA8 (ppb)
WCAQ MDA8 (ppb)
PM2.5 (µg m-3)
RM (ng m-3)
RH (%)
70 ppb NAAQS
44% RH
42 ppb NVROI MDA8
17 ng m-3 RM
6.8 µg m-3 PM2.5
80
70
60
50
40
30
20
10
0
9/30/2014
10/2/2014
10/4/2014
10/6/2014
10/8/2014
10/10/2014
10/12/2014
10/14/2014
10/16/2014
10/18/2014
10/20/2014

e)

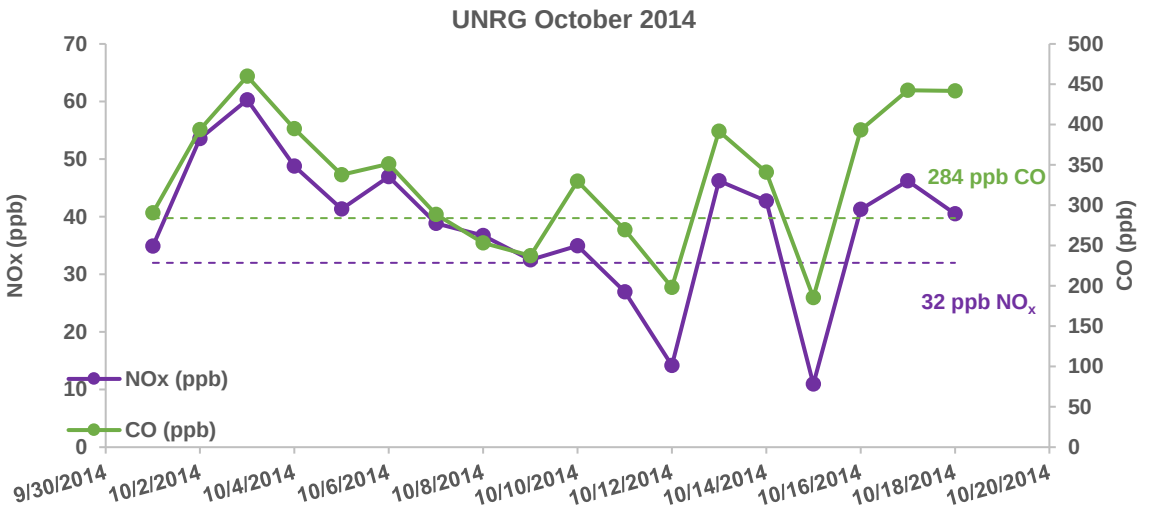
UNRG October 2014
NOx (ppb)
CO (ppb)
284 ppb CO
32 ppb NOx
70
60
50
40
30
20
10
0
500
450
400
350
300
250
200
150
100
50
0
9/30/2014
10/2/2014
10/4/2014
10/6/2014
10/8/2014
10/10/2014
10/12/2014
10/14/2014
10/16/2014
10/18/2014
10/20/2014

f)

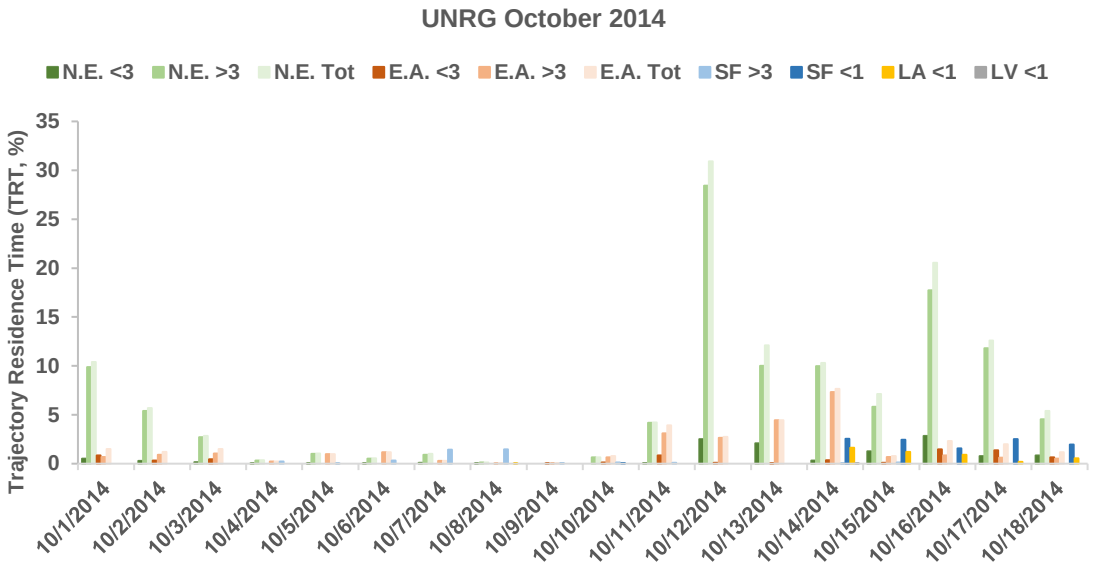

Figure 13: Naval Research Laboratory Aerosol Analysis and Prediction System (NRL NAAPS, https://www.nrlmry.navy.mil/aerosol/) smoke surface September 22 and 24, 2014.

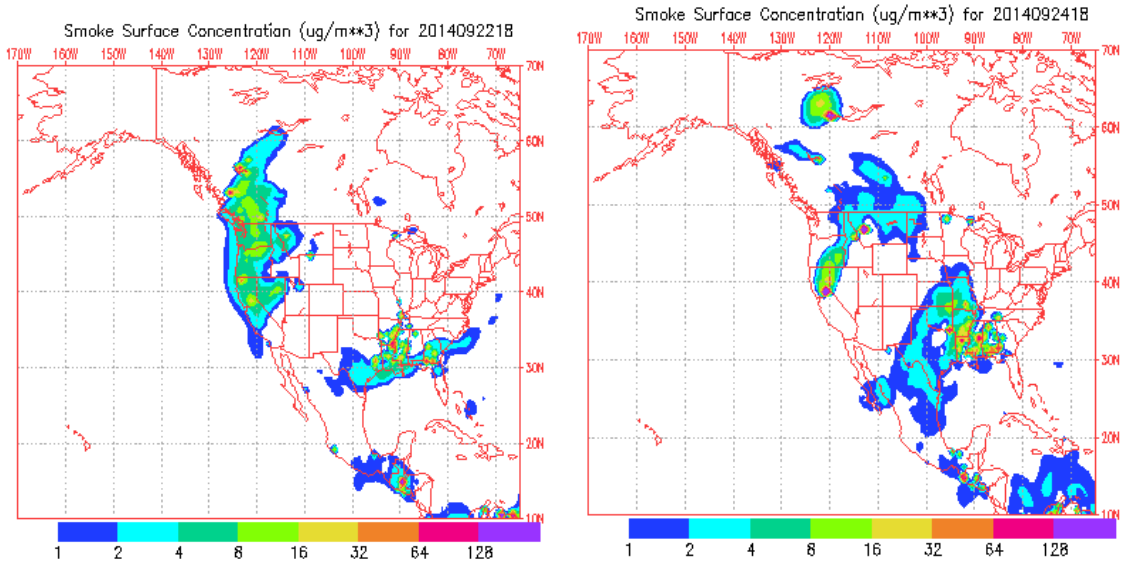

Figure 14: Percent Asian Pb for specific days in September and October 2014 at PEAV and UNRG. The horizontal grey line indicates the 75th percentile for PEAV (36%); the horizontal black line indicates the 75th percentile for UNRG (42%). Grey shading indicates the King Fire.

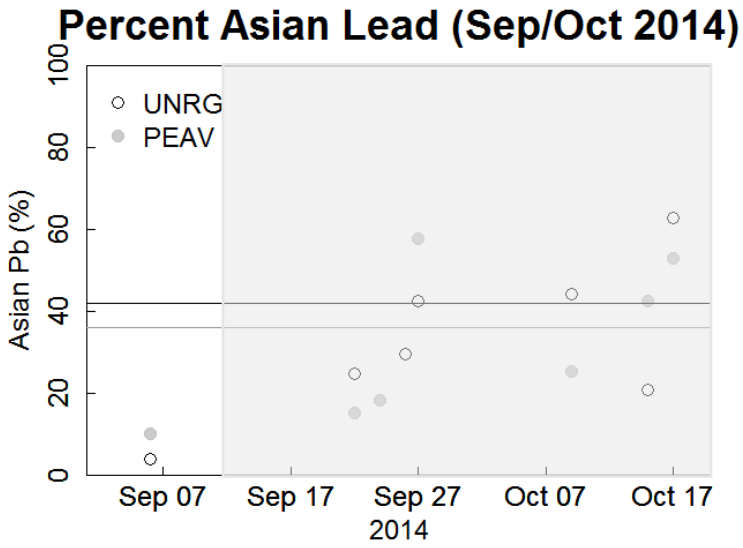

Figure 15: Surface weather maps from NOAA for October 15 (a), 16 (b), and 17 (c), 2014

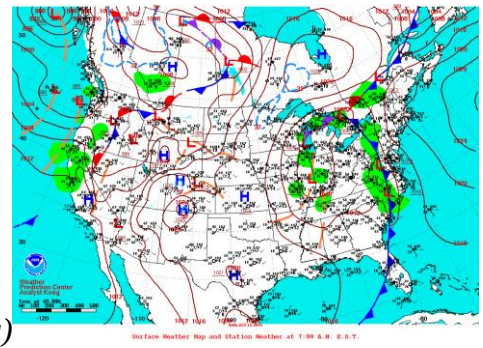

a)

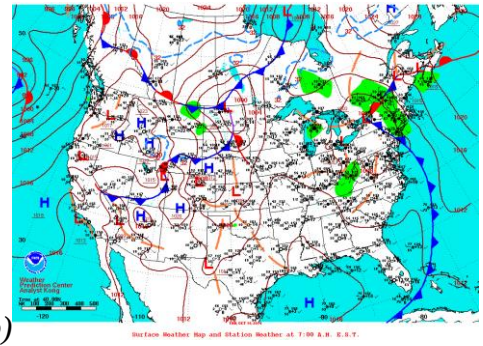

b)

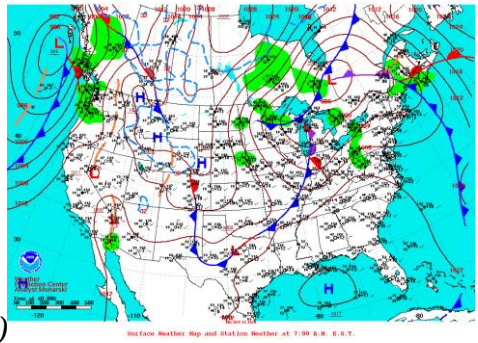

c)

March 2015:

Figure 16: Surface weather maps from NOAA for March 31 and April 1, 2015

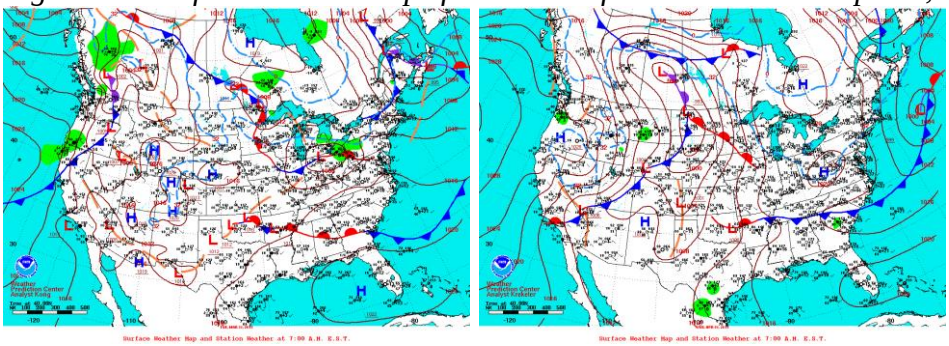

Figure 17: Great Basin National Park, NV, USA, March 2015 a) time series of pollutants and RH and b) trajectory residence times. Dashed lines indicate the monthly median and the NAAQS for O_3. Grey shading indicates frontal activity.

a)

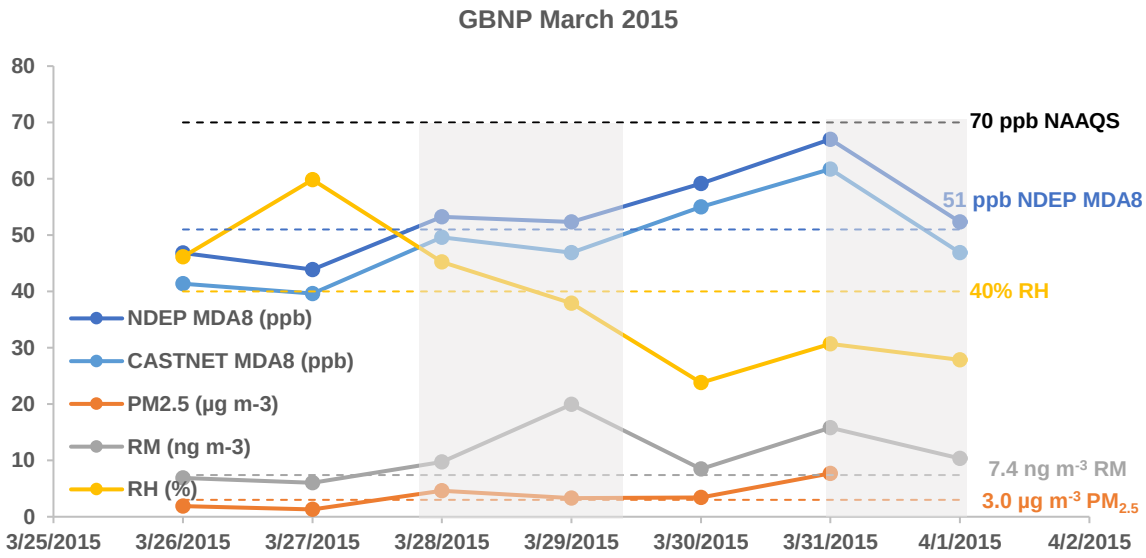

b)

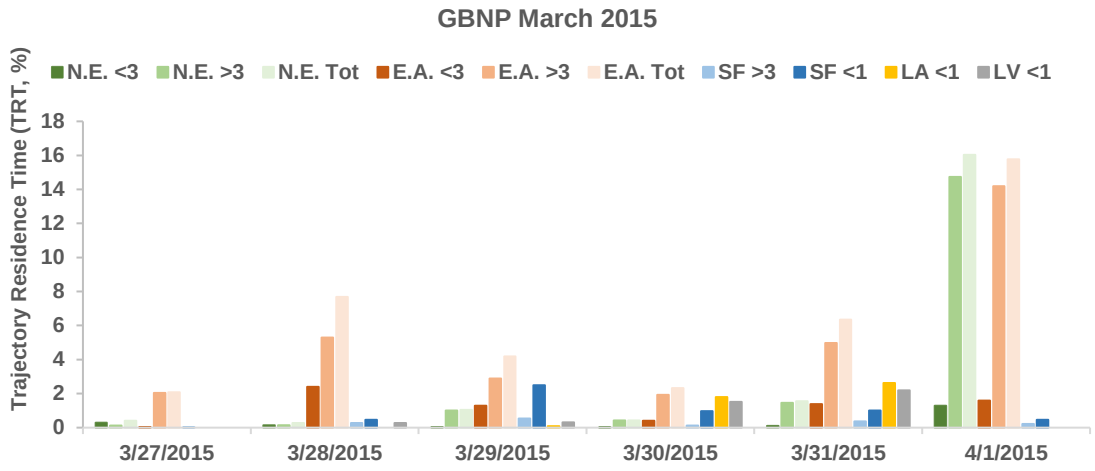

Figure 18: Percent Asian Pb for specific days in March 2015 at GBNP and UNRG. The horizontal grey line indicates the 75th percentile for GBNP (42%); the horizontal black line indicates the 75th percentile for UNRG (52%).

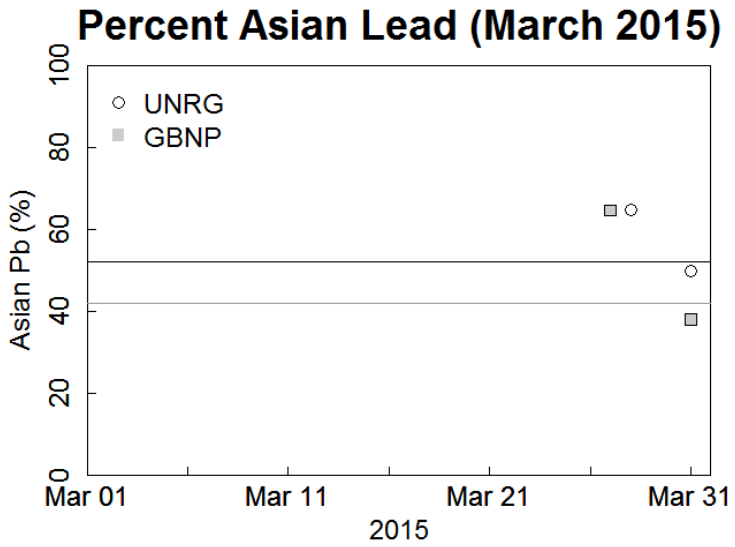

Figure 19: University of Nevada, Reno, Greenhouse, USA, March 2015 a) time series of pollutants and RH, b) time series of CO and NO_x, and b) trajectory residence times. Dashed lines indicate the monthly median and the NAAQS for O_3. Grey shading indicates frontal activity.

a)

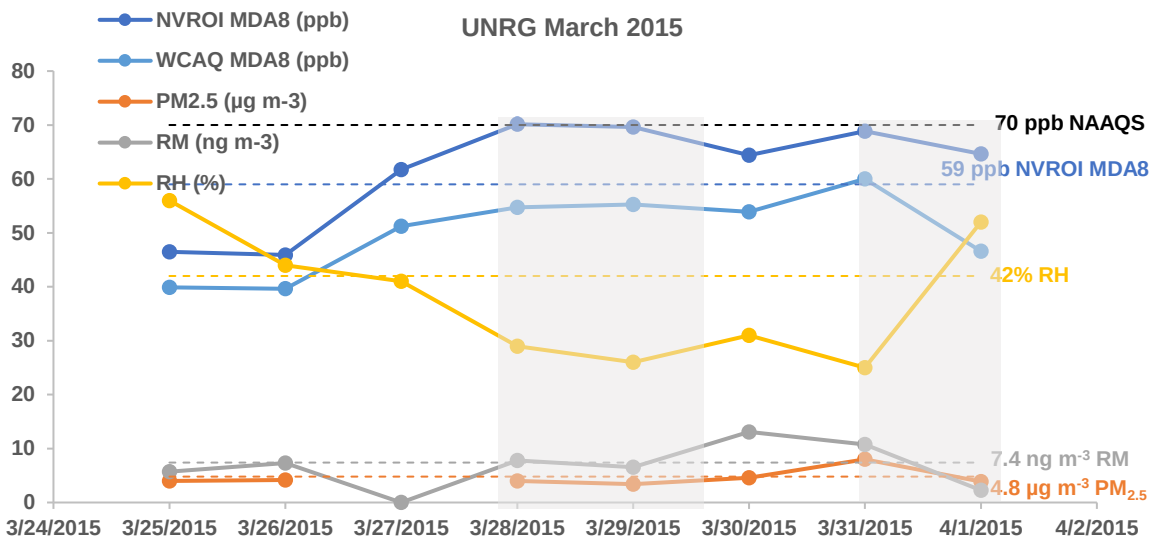
UNRG March 2015
NVROI MDA8 (ppb)
WCAQ MDA8 (ppb)
PM2.5 (µg m-3)
RM (ng m-3)
RH (%)
70 ppb NAAQS
59 ppb NVROI MDA8
42% RH
7.4 ng m-3 RM
4.8 µg m-3 PM2.5
80
70
60
50
40
30
20
10
0
3/24/2015
3/25/2015
3/26/2015
3/27/2015
3/28/2015
3/29/2015
3/30/2015
3/31/2015
4/1/2015
4/2/2015

b)

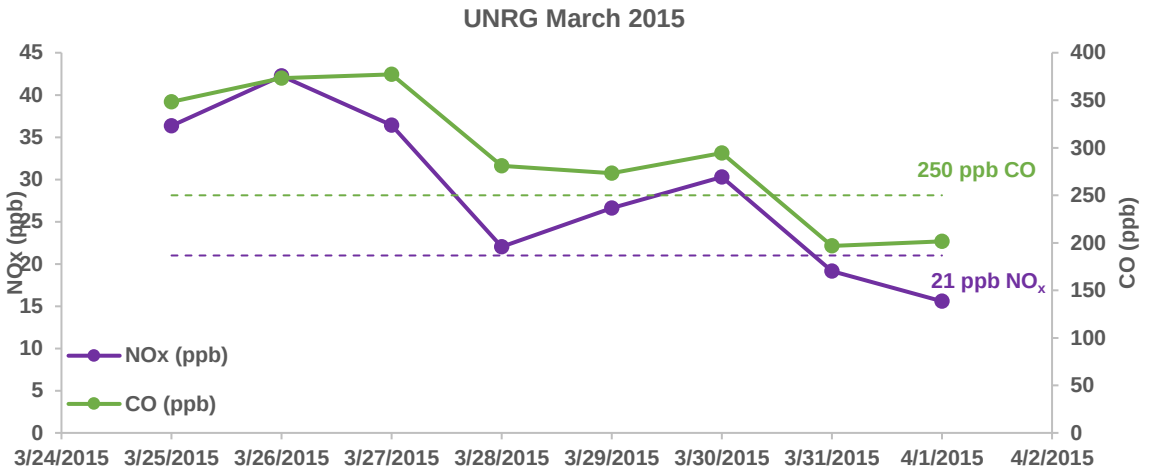
UNRG March 2015
NOx (ppb)
CO (ppb)
250 ppb CO
21 ppb NOx
NOx (ppb)
CO (ppb)
3/24/2015
3/25/2015
3/26/2015
3/27/2015
3/28/2015
3/29/2015
3/30/2015
3/31/2015
4/1/2015
4/2/2015

c)

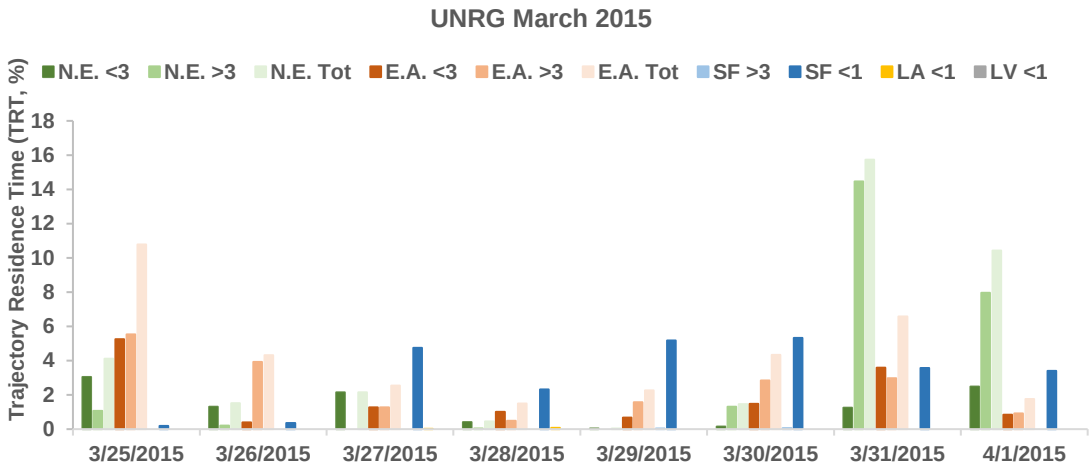
UNRG March 2015
N.E. <3
N.E. >3
N.E. Tot
E.A. <3
E.A. >3
E.A. Tot
SF >3
SF <1
LA <1
LV <1
Trajectory Residence Time (TRT, %)
3/25/2015
3/26/2015
3/27/2015
3/28/2015
3/29/2015
3/30/2015
3/31/2015
4/1/2015

Figure 20: NAAPS optical depth for March 30, 16:00 PST and March 31, 10:00 PST

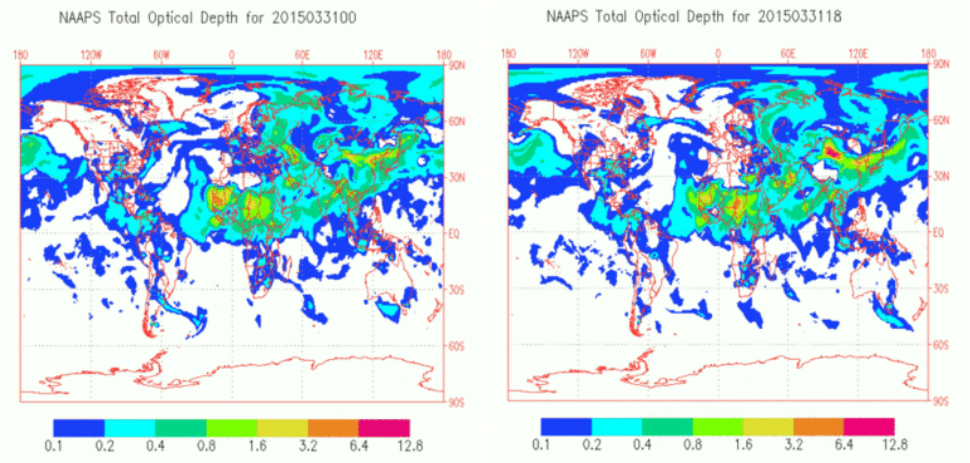

Figure 21: IMPROVE $PM_{2.5}$ chemical composition from GBNP on days with lead analysis (grey bars) compared to the monthly average (black bars). Grey graph backgrounds indicate IMPROVE data for a day near but not directly on the same day as a lead analysis, parantheses indicate day with lead analysis.

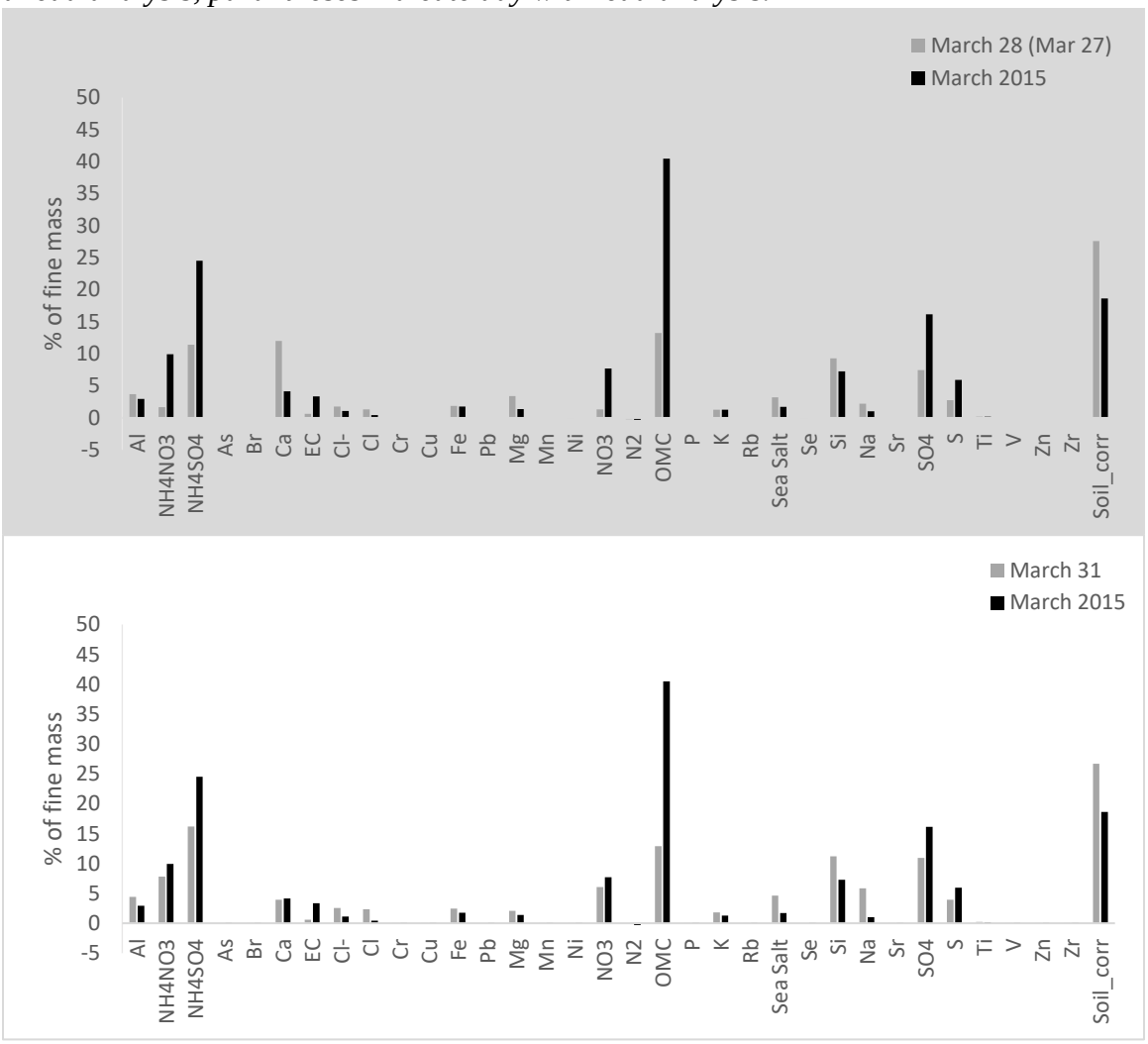

Figure 22: 1 h maximum and 8 h maximum ozone CMAQ forecasts (http://www.emc.ncep.noaa.gov/mmb/aq/prod/web/html/max_p6.html)

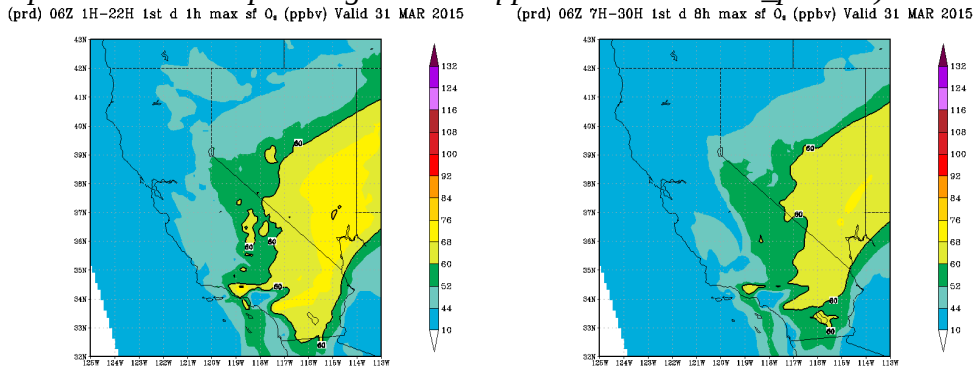

June 2015

Figure 23: Percent Asian Pb for specific days in June 2015 at GBNP and UNRG. The horizontal grey line indicates the 75th percentile for GBNP (42%); the horizontal black line indicates the 75th percentile for UNRG (52%).

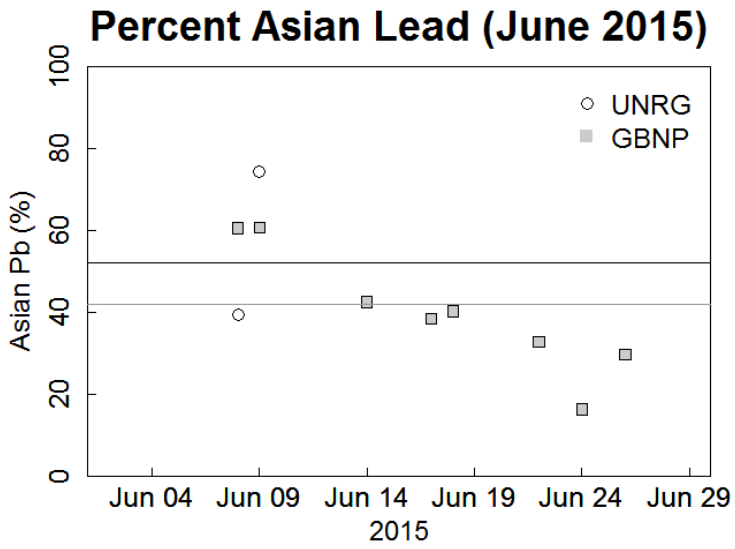

Figure 24: Great Basin National Park, NV, USA, June 2015 a) time series of pollutants and RH, b) CO and NOx time series, and c) trajectory residence times. Dashed lines indicate the monthly median and the NAAQS for O_3. Grey shading indicates high pressure.

a)

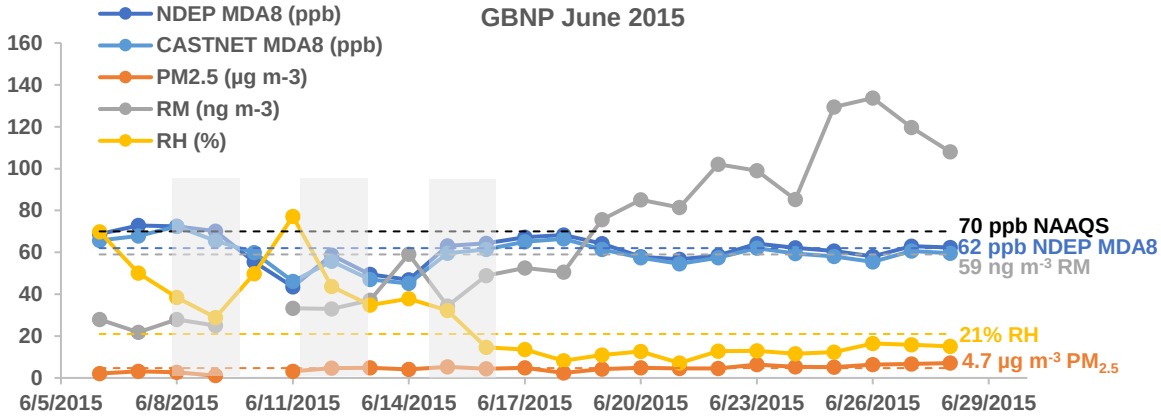

b)

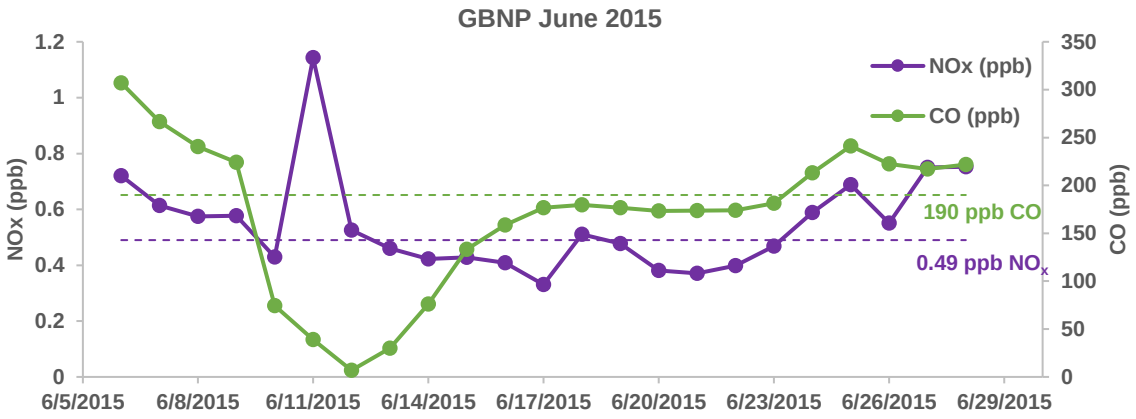

c)

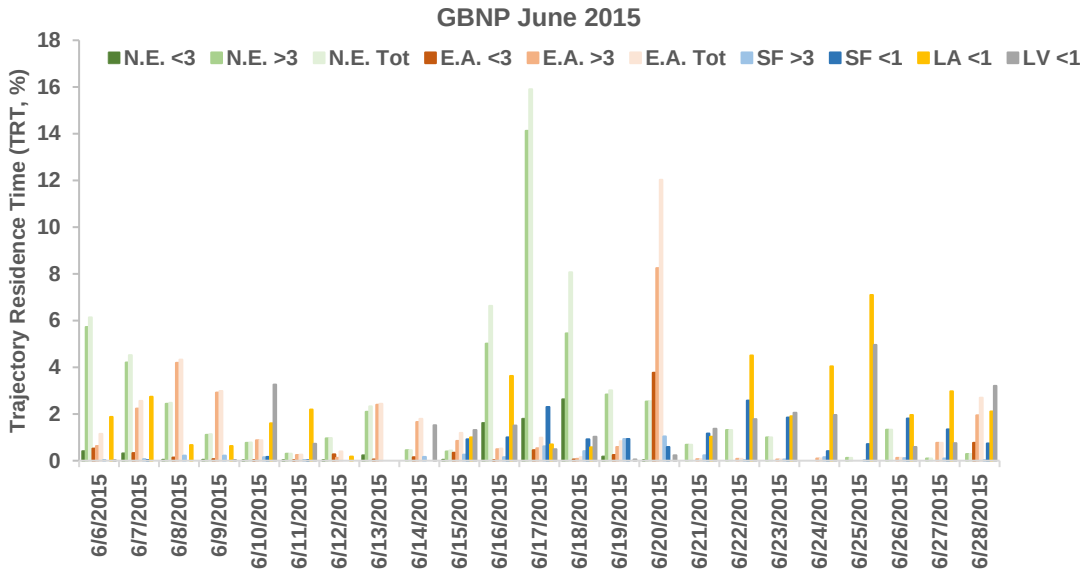

Figure 25: Surface weather maps from NOAA for June 8 and June 9, 2015.

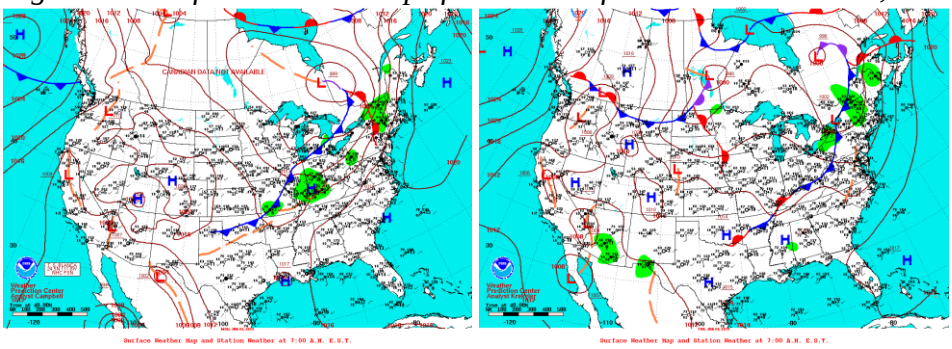

Figure 26: 500 millibar weather maps from NOAA for June 8 and June 9, 2015.

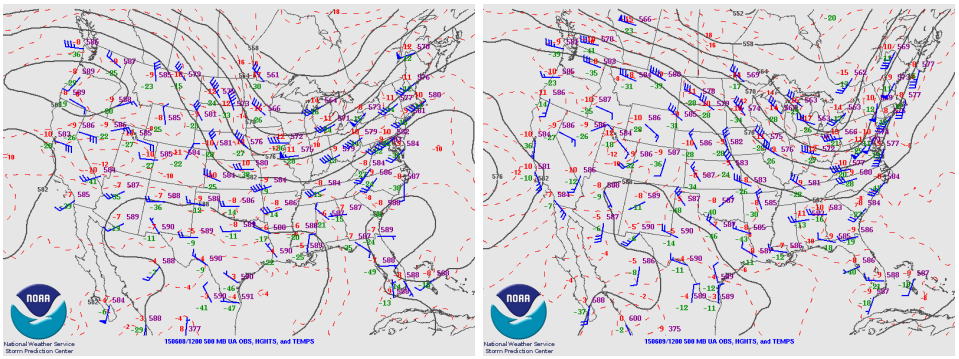

IMPROVE:

Figure 27: IMPROVE $PM_{2.5}$ chemical composition from GBNP on days with lead analysis (grey) compared to the monthly average (black).

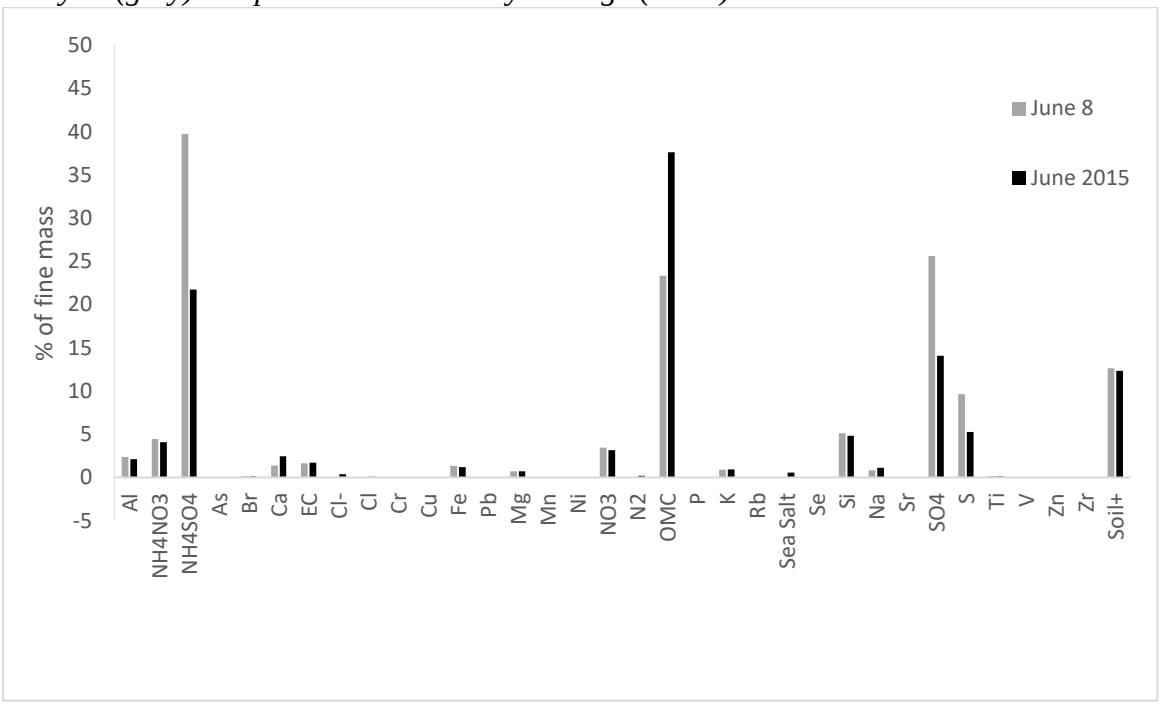

Figure 28: University of Nevada, Reno, Greenhouse, USA June 2015 a) time series of pollutants and RH, b) CO and NOx time series, and c) trajectory residence times. Dashed lines indicate the monthly median and the NAAQS for O_3. Grey shading indicates high-pressure.

a)

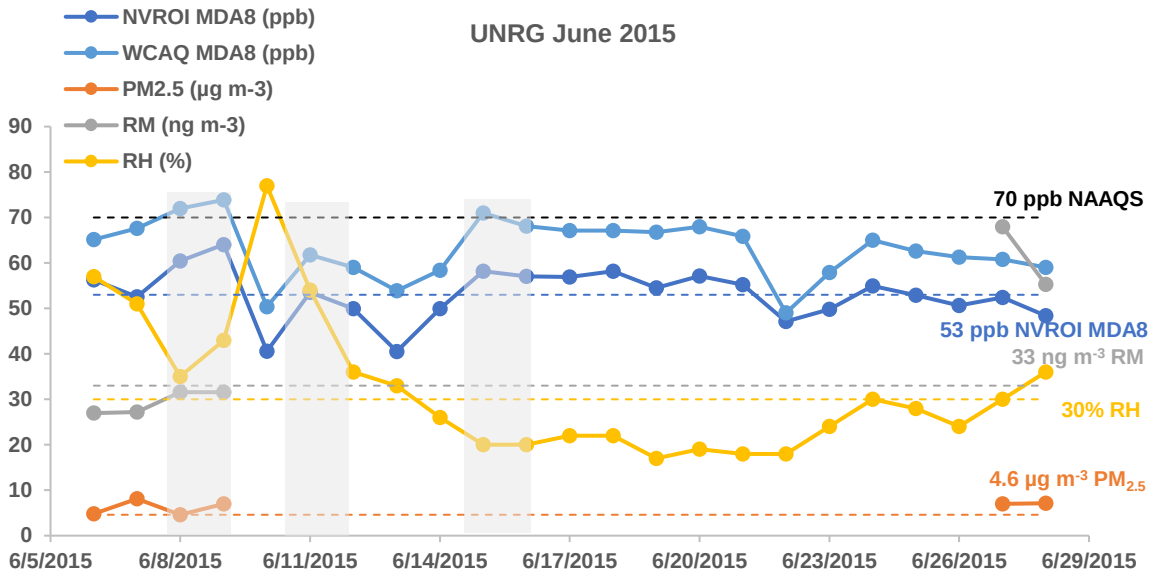

b)

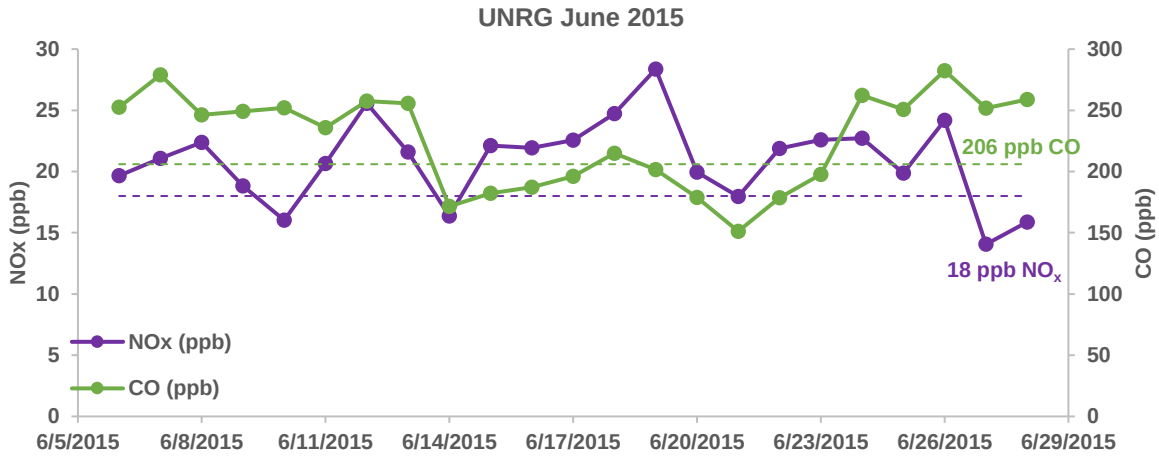

c)

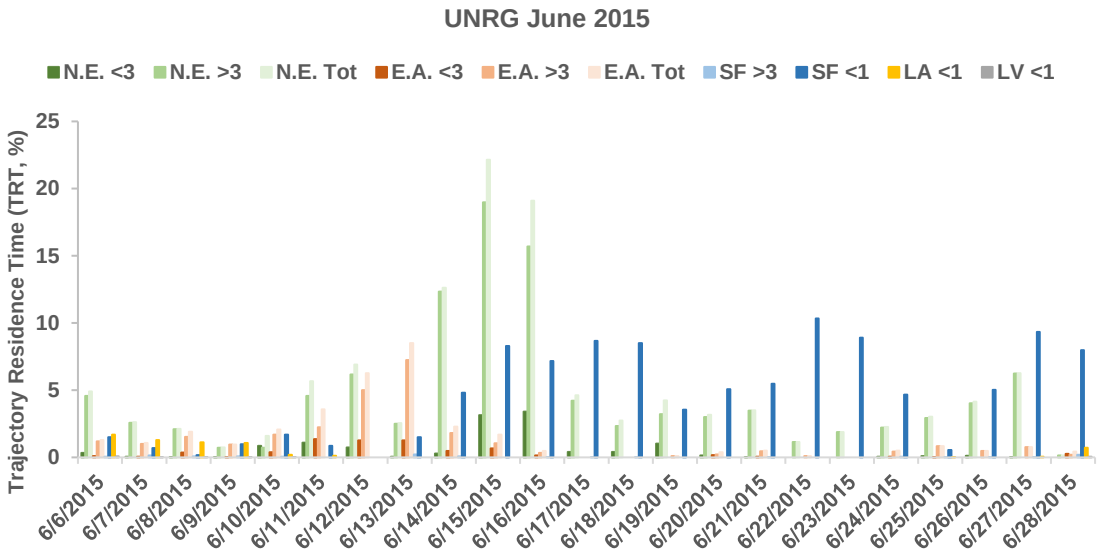

Figure 29: Surface weather maps from NOAA for June 16, 17 and 18, 2015.

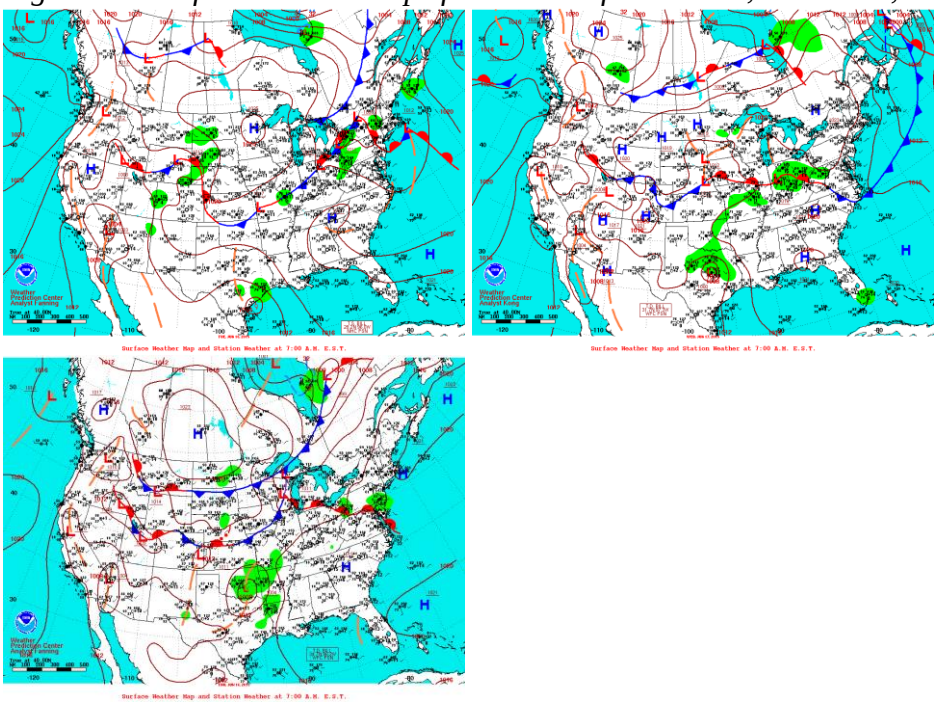

Figure 30: 500 millibar weather maps from NOAA for June 8 and June 9, 2015.

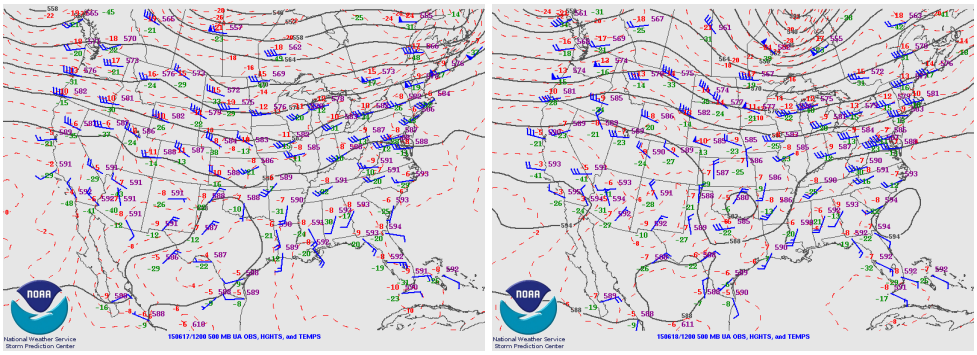

IMPROVE:

Figure 31: IMPROVE $PM_{2.5}$ chemical composition from GBNP on days with lead analysis (grey) compared to the monthly average (black).

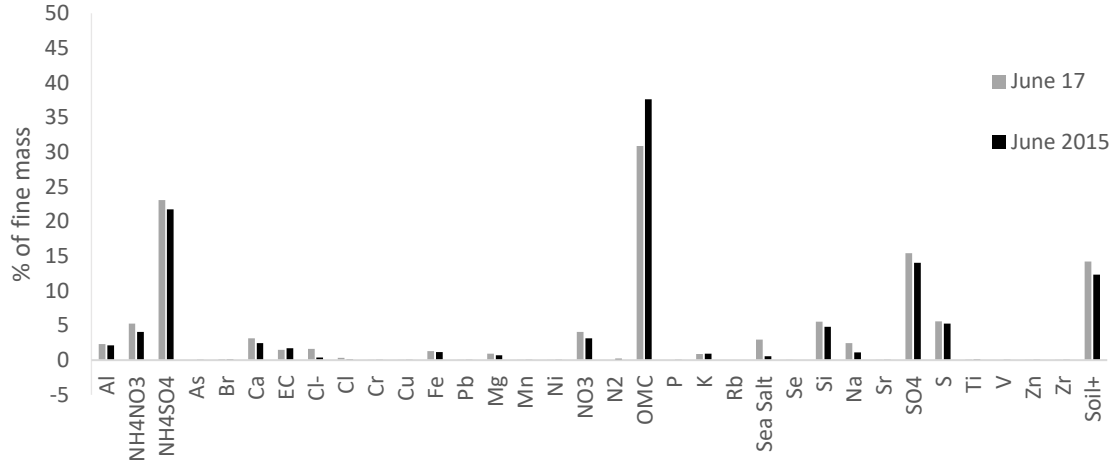

September 2015

Figure 32: Great Basin National Park, NV, USA, September 2015 a) time series of pollutants and RH, b) CO and NOx time series, and c) trajectory residence times. Dashed lines indicate the monthly median and the NAAQS for O_3. Grey shading indicates frontal activity.

a)

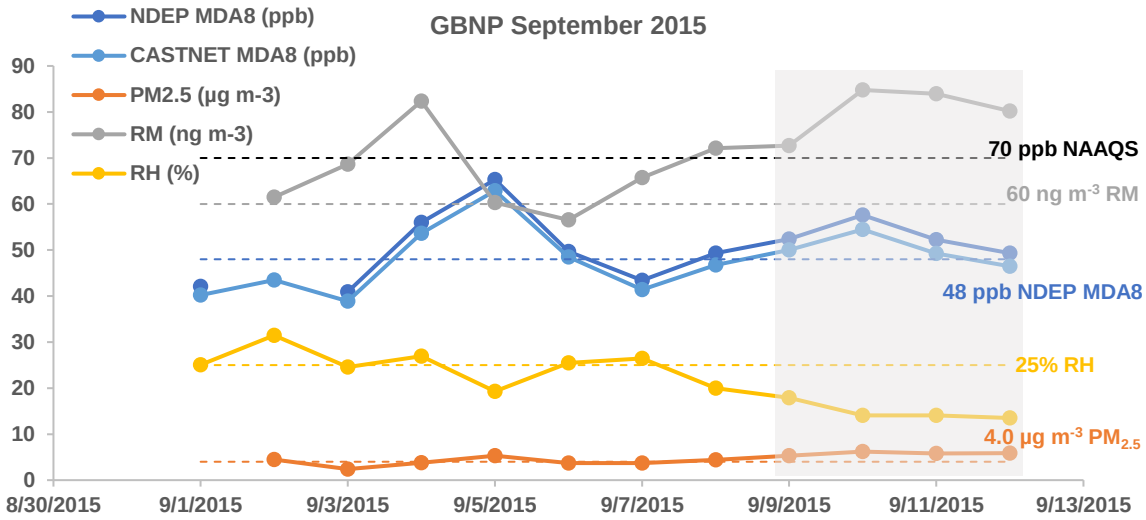

b)

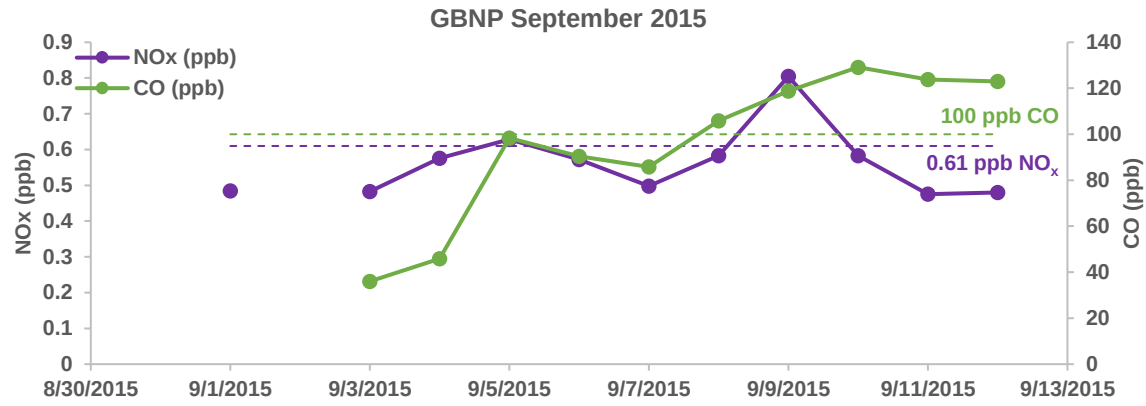

c)

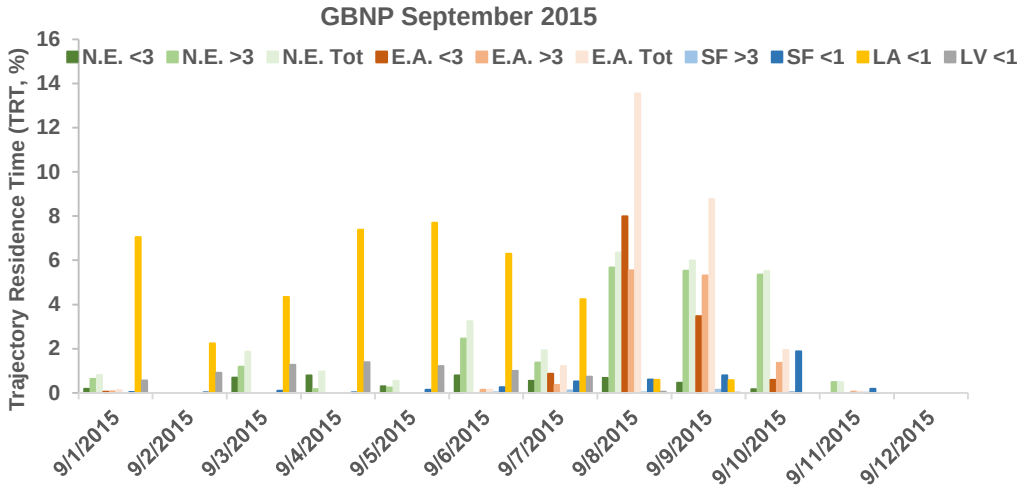

Figure 33: Percent Asian Pb for specific days in August and September 2015 at GBNP and UNRG. The horizontal grey line indicates the 75th percentile for GBNP (42%); the horizontal black line indicates the 75th percentile for UNRG (52%).

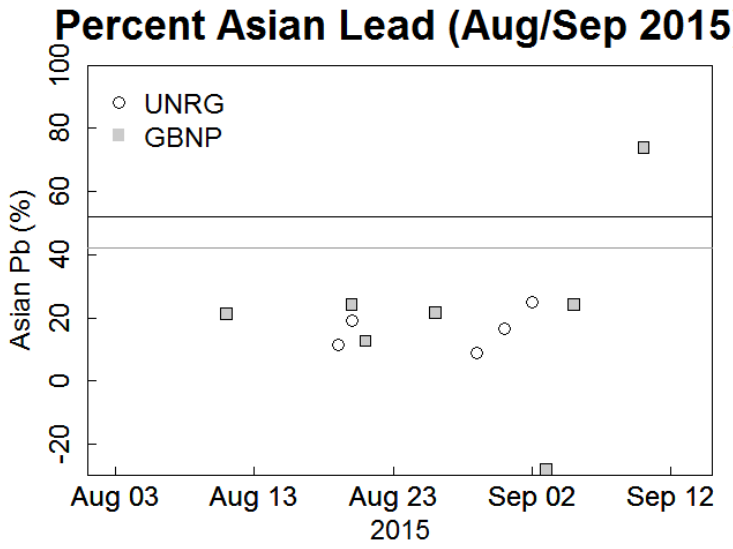

Figure 34: Surface weather maps from NOAA for September 10, 2015.

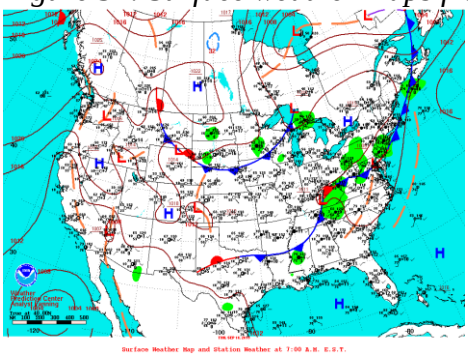

Figure 35: 500 millibar weather maps from NOAA for September 10, 2015.

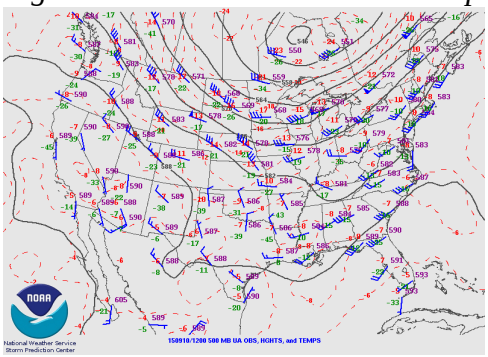

IMPROVE:

Figure 36: IMPROVE $PM_{2.5}$ chemical composition from GBNP on days with lead analysis (grey) compared to the monthly average (black). Grey bar charts indicate IMPROVE data for a day near but not directly on the same day as a lead analysis, parantheses indicate day with lead analysis.

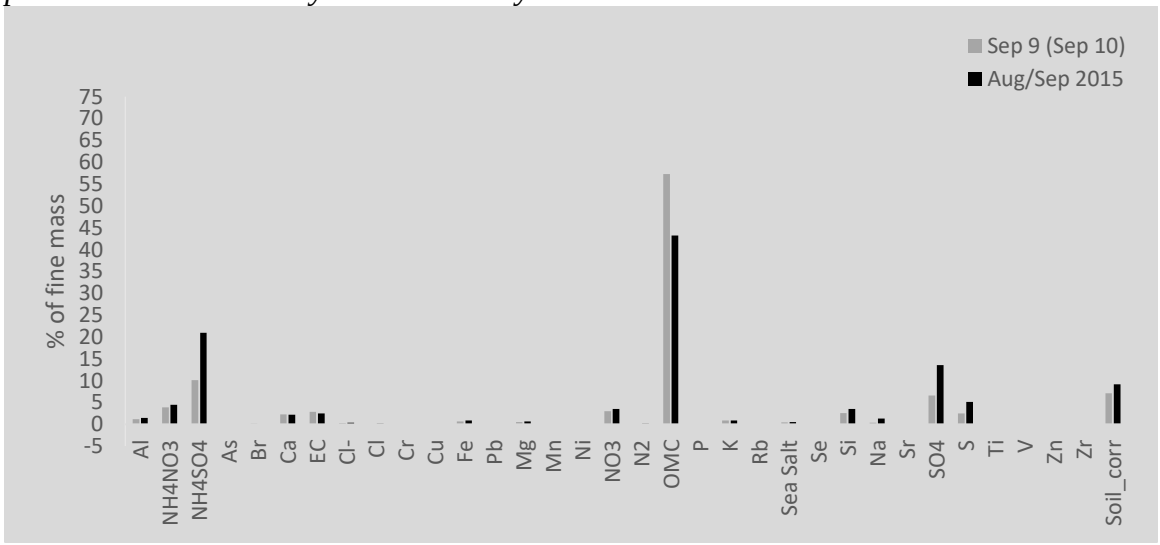

Figure 37: Naval Research Laboratory Aerosol Analysis and Prediction System (NRL NAAPS, https://www.nrlmry.navy.mil/aerosol/) smoke surface.

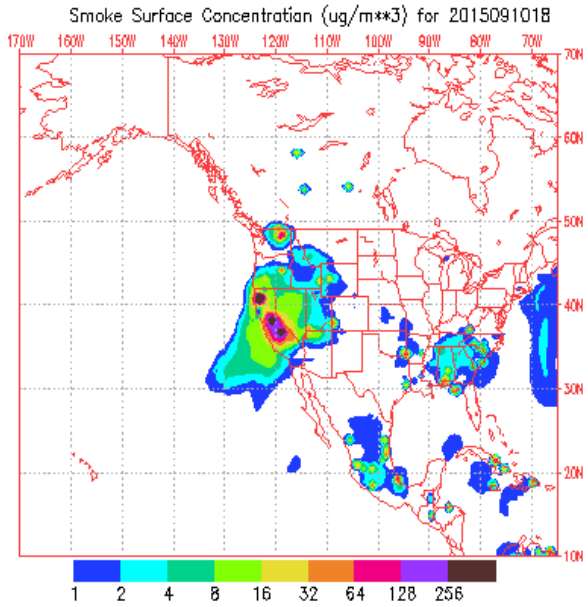

Figure 38: University of Nevada, Reno, Greenhouse, USA, September 2015 a) time series of pollutants and RH, b) CO and NOx time series, and c) trajectory residence times. Dashed lines indicate the monthly median and the NAAQS for O_3. Grey shading indicates frontal activity.

a)

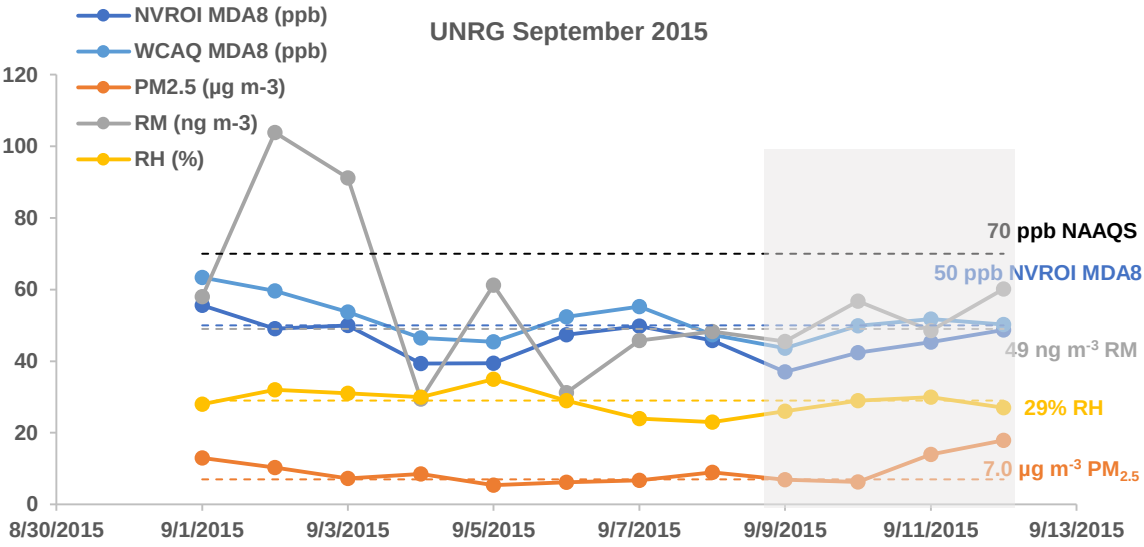

b)

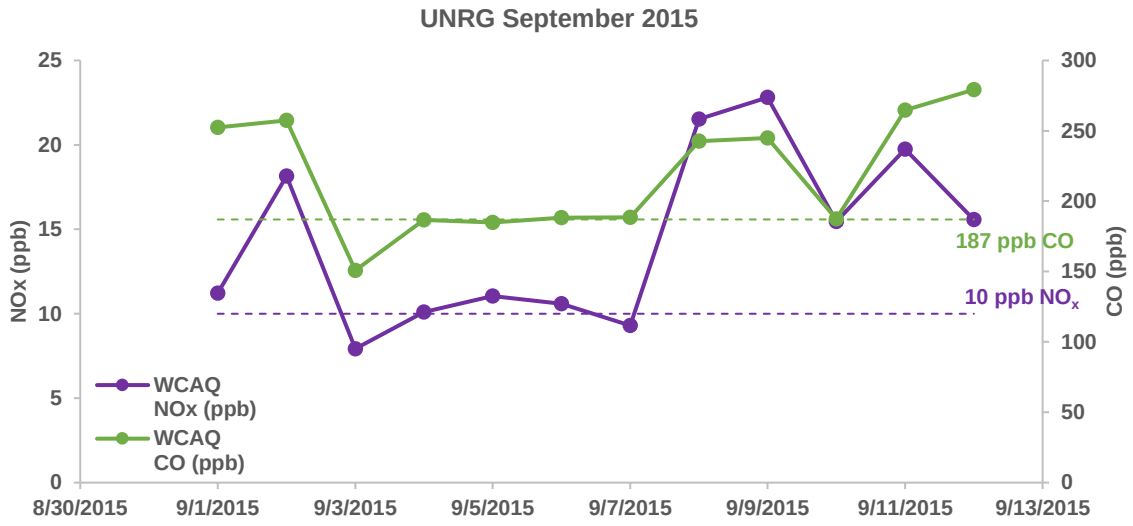
UNRG September 2015
NOx (ppb)
CO (ppb)
25
20
15
10
5
0
300
250
200
150
100
50
0
8/30/2015
9/1/2015
9/3/2015
9/5/2015
9/7/2015
9/9/2015
9/11/2015
9/13/2015
187 ppb CO
10 ppb NOx
WCAQ NOx (ppb)
WCAQ CO (ppb)

c)

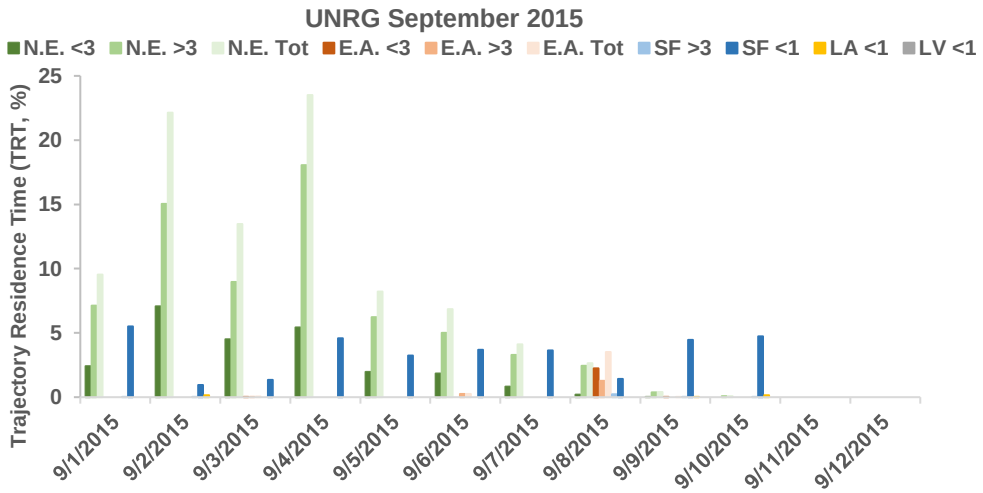
UNRG September 2015
N.E. <3
N.E. >3
N.E. Tot
E.A. <3
E.A. >3
E.A. Tot
SF >3
SF <1
LA <1
LV <1
Trajectory Residence Time (TRT, %)
25
20
15
10
5
0
9/1/2015
9/2/2015
9/3/2015
9/4/2015
9/5/2015
9/6/2015
9/7/2015
9/8/2015
9/9/2015
9/10/2015
9/11/2015
9/12/2015

References:

Ewing SA, Christensen JN, Brown ST, Vancuren RA, Cliff SS, Depaolo DJ. Pb Isotopes as an Indicator of the Asian Contribution to Particulate Air Pollution in Urban California. Environmental Science & Technology 2010; 44: 8911-8916.

Fine R, Miller MB, Burley J, Jaffe DA, Pierce RB, Lin M, et al. Variability and sources of surface ozone at rural sites in Nevada, USA: Results from two years of the Nevada Rural Ozone Initiative. Science of The Total Environment 2015; 530–531: 471-482.

Wright G, Gustin MS, Weiss-Penzias P, Miller MB. Investigation of mercury deposition and potential sources at six sites from the Pacific Coast to the Great Basin, USA. Science of The Total Environment 2014; 470–471: 1099-1113.

Appendix C

Supplemental Information

Investigating horizontal and vertical pollution gradients in the atmosphere associated with an urban location in complex terrain, Reno, Nevada, USA

Ashley M. Pierce[a,*], S. Marcela Loría-Salazar[b], Heather A. Holmes[b], Mae Sexauer Gustin[a]

*Corresponding author: ash.pie4@gmail.com

[a]Department of Natural Resources and Environmental Sciences, University of Nevada Reno, NV, USA 89557

[b]Atmospheric Science Program, Department of Physics, University of Nevada Reno, NV, USA 89557

Submitted: *Atmospheric Environment*

Statistical analysis

a)

Jun- Nov 2014	O_3 (1 h, ppbv)			O_3 (max 1 h, ppbv)			O_3 (MDA8, ppbv)		
	UNRG	WCAQ	PEAV	UNRG	WCAQ	PEAV	UNRG	WCAQ	PEAV
Mean±Std	25±18	37±17	48±8.8	46±13	57±11	56±8.4	39±12	51±10	53±7.6
25^{th},50^{th}, 75^{th}	7.4, 24, 40	25, 39,50	43, 49, 54	36, 47, 54	50, 58, 66	50, 56, 61	28, 41, 48	45, 53, 59	48, 53, 58
Range	0.0-77	0.0-88	1.6-80	7.4-77	27-88	40-80	13-65	23-75	39-78
Number	2896	3635	3733	129	155	158	129	154	158

b)

Jun-Nov 2014	CO (1 h, ppbv)			$PM_{2.5}$ (24 h, µg m^{-3})			$PM_{2.5}$ (1 h, µg m^{-3})	NO_x (1 h, ppbv)		NO (1 h, ppbv)		SO_2 (1 h, ppbv)	
	UNRG	WCAQ	PEAV	UNRG	WCAQ	PEAV	WCAQ	UNRG	WCAQ	UNRG	WCAQ	UNRG	WCAQ
Mean± Std	342±236	232±182	137±76	8.9±7.7	9.4±13	5.4±5.2	9.4±17	37±31	16±17	11±20	4.2±10	0.20±0.25	0.29±0.31
25^{th}, 50^{th}, 75^{th}	182, 263, 421	135, 179, 257	112, 126, 143	5.6, 7.2, 9.4	4.7, 6.7, 8.4	2.3, 4.5, 5.9	3.0, 6.0, 10	14, 26, 50	5.8, 9.5, 19	1.2, 3.4, 11	0.60, 1.2, 2.9	0.050, 0.12, 0.24	0.10, 0.20, 0.40
Range	59-2550	5.0-3009	0.0-1697	0.0-63	0.0-101	0.0-42	0.0-270	0.0-218	0.90-171	0.0-173	0.0-118	0.0-3.8	0.0-3.2
Number	2263	3816	2751	135	160	121	3788	1900	3793	3302	3793	3303	3639

Table 1: Summary statistics for each site for June to November 2014, a) ozone and b) other gaseous data.

a)

Jun 2014 – Oct 2015	O_3 (1 h, ppbv)			O_3 (max 1 h, ppbv)			O_3 (MDA8, ppbv)		
	UNRG	WCAQ	PEAV	UNRG	WCAQ	PEAV	UNRG	WCAQ	PEAV
Mean±Std	28±21	33±19	46±8.5	49±16	52±14	53±9.0	43±15	47±14	50±8.0
25th,50th, 75th	7.4, 28, 44	18, 35, 48	40, 46, 52	40, 49, 57	43, 54, 63	45, 52, 59	33, 44, 52	38, 49, 57	44, 50, 56
Range	0.0-92	0.0-88	1.6-80	1.5-92	2.0-88	33-80	1.3-85	1.7-77	31-78
Number	9668	11040	8855	430	470	377	431	469	377

b)

Jun 2014 – Oct 2015	CO (1 h, ppbv)			$PM_{2.5}$ (24 h, µg m^{-3})		$PM_{2.5}$ (1 h, µg m^{-3})	NO_x (1 h, ppbv)		NO (1 h, ppbv)	
	UNRG	WCAQ	PEAV	UNRG	WCAQ	WCAQ	UNRG	WCAQ	UNRG	WCAQ
Mean±Std	349±269	266±226	137±76	7.7±5.6	8.2±8.3	8.2±12	35±35	21±28	18±29	8.0±20
25th, 50th, 75th	178, 253, 416	145, 189, 287	112, 126, 143	5.0, 6.7, 8.7	4.8, 6.6, 8.8	3.0, 6.0, 10	12, 22, 46	6.0, 10, 24	1.5, 4.6, 22	0.60, 1.4, 4.7
Range	0.0-2550	5.0-3009	0.0-1697	0.0-63	0.0-1001	0.0-270	0.0-297	0.0-294	0.0-248	0.0-240
Number	9199	11257	6646	380	483	11488	8337	11354	7665	11354

Table 2: Summary statistics for each site for June 2014 to October 2015, a) ozone and b) other gaseous data and $PM_{2.5}$.

Jun-Nov 2014	AOD (τ_{ext}, 1 h)	AOD (τ_{ext}, 24 h)
Mean±Std	0.11±0.15	0.11±0.11
25th, 50th, 75th	0.050, 0.070, 0.12	0.046, 0.070, 0.12
Range	0.010-2.1	0.017-0.85
Number	1382	121
Jun 2014 – Oct 2015		
Mean±Std	0.12±0.17	0.12±0.13
25th, 50th, 75th	0.050, 0.080, 0.12	0.049, 0.082, 0.12
Range	0.0-2.5	0.014-1.1
Number	2592	229

Table 3: Summary statistics for AERONET aerosol optical depth (AOD, τ_{ext}) 1 h and 24 h data for June to November 2014 and June 2014 to October 2015.

Results

Atmospheric stability

		Total HD (MJ m^{-2})	Surface layer HD (MJ m^{-2})	AM HD (MJ m^{-2})	PM HD (MJ m^{-2})	ΔT (°C)
Winter	Median	1.6	0.92	3.0	0.31	0.77
	(n)	(n = 90)	(n = 90)	(n = 87)	(n = 88)	(n = 90)
	range	-0.38 to 6.2	-0.25 to 2.8	0.30 to 8.1	-0.38 to 4.7	-3.9 to 5.2
Spring	Median	0.92	0.56	2.2	-0.35	-1.2
	(n)	(n = 92)	(n = 92)	(n = 92)	(n = 91)	(n = 92)
	range	-0.048 to 2.6	-0.038 to 1.6	0.041 to 5.6	-0.82 to 1.1	-3.9 to 2.9
Summer	Median	1.2	0.81	2.6	-0.33	-0.060
	(n)	(n = 184)	(n = 184)	(n = 184)	(n = 182)	(n = 184)
	range	0.12 to 7.0	0.022 to 2.8	0.60 to 7.0	-0.75 to 2.1	-3.5 to 3.3
Fall	Median	1.4	0.95	2.9	-0.038	1.3
	(n)	(n = 122)	(n = 122)	(n = 122)	(n = 121)	(n = 122)
	range	0.027 to 5.9	-0.017 to 2.5	0.026 to 7.3	-0.51 to 4.4	-3.0 to 7.1

Table 4: Median, number (n), and range of data for for average total heat deficit (Total HD, MJ m^{-2}, 1342 m to 2134 m), heat deficit in the first layer (Surface layer HD, 1342 m to 1516 m), morning heat deficit (AM HD, 04:00 PST), afternoon heat deficit (PM HD, 14:00 PST), and vertical temperature difference between FARM and GALE (ΔT, °C) for winter (DJF), spring (MAM), summer (JJA), and fall (SON) in Reno, NV, USA from June 2014 to October 2015.

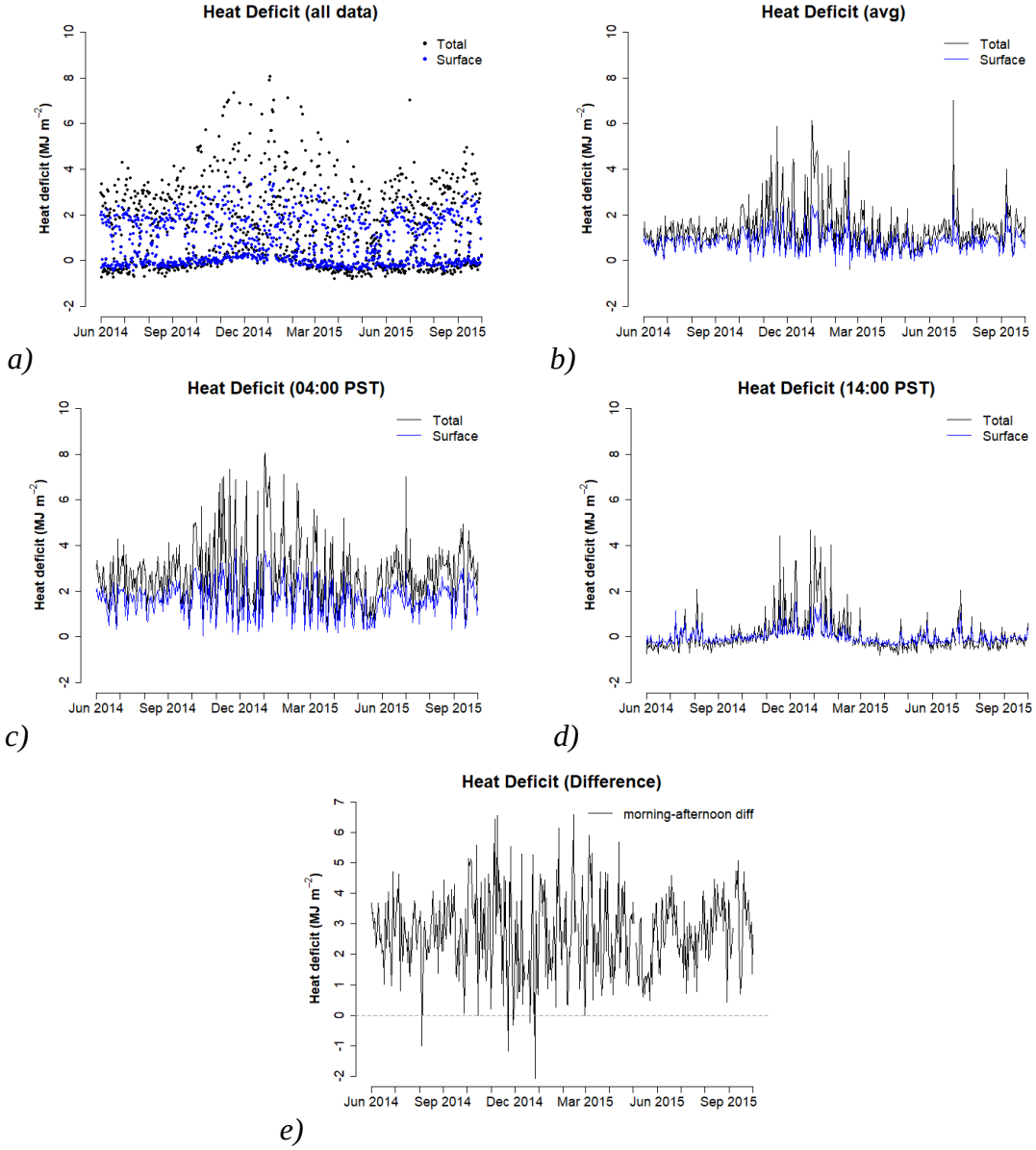

Figure 1: Heat deficit (MJ m^{-2}) for the Truckee Meadows valley calculated from balloon soundings twice daily and valley floor weather station data. Black data indicates total heat deficit from valley floor (1342 m) to ridge line (2134 m), blue data indicates heat deficit for the surface layer in the valley (1342 m to 1516 m) for a) all data, b) average data, c) morning data (04:00 PST), d) afternoon data (16:00 PST), and e) the difference between morning and afternoon total data in Reno, NV, USA from June 2014 to October 2015.

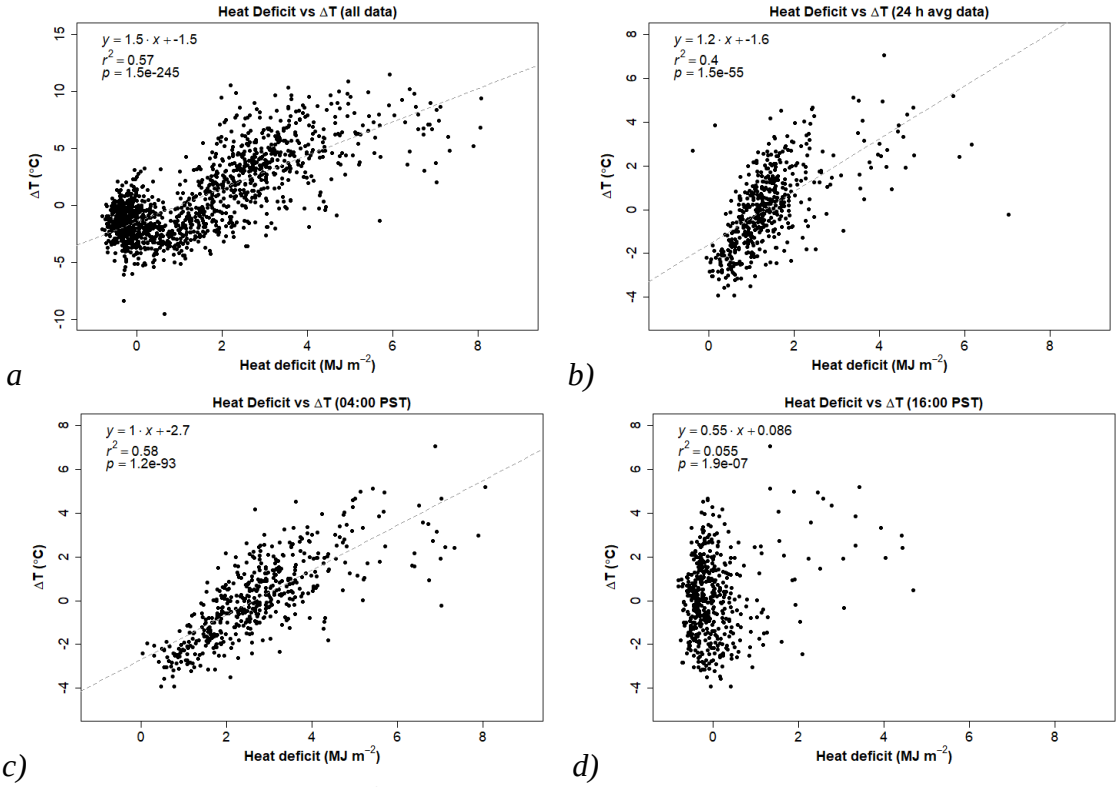

Figure 2: Heat deficit (MJ m^{-2}) and vertical temperature differences (ΔT, ºC) from Western Regional Climate Center Stations (ΔT = T_{GALE}-T_{FARM}) for a) all data, b) 24 h average data, c) morning (04:00 PST) heat deficit and 24 h ΔT data, and d) afternoon (16:00 PST) heat deficit and 24 h average ΔT data in Reno, NV, USA from June 2014 to October 2015.

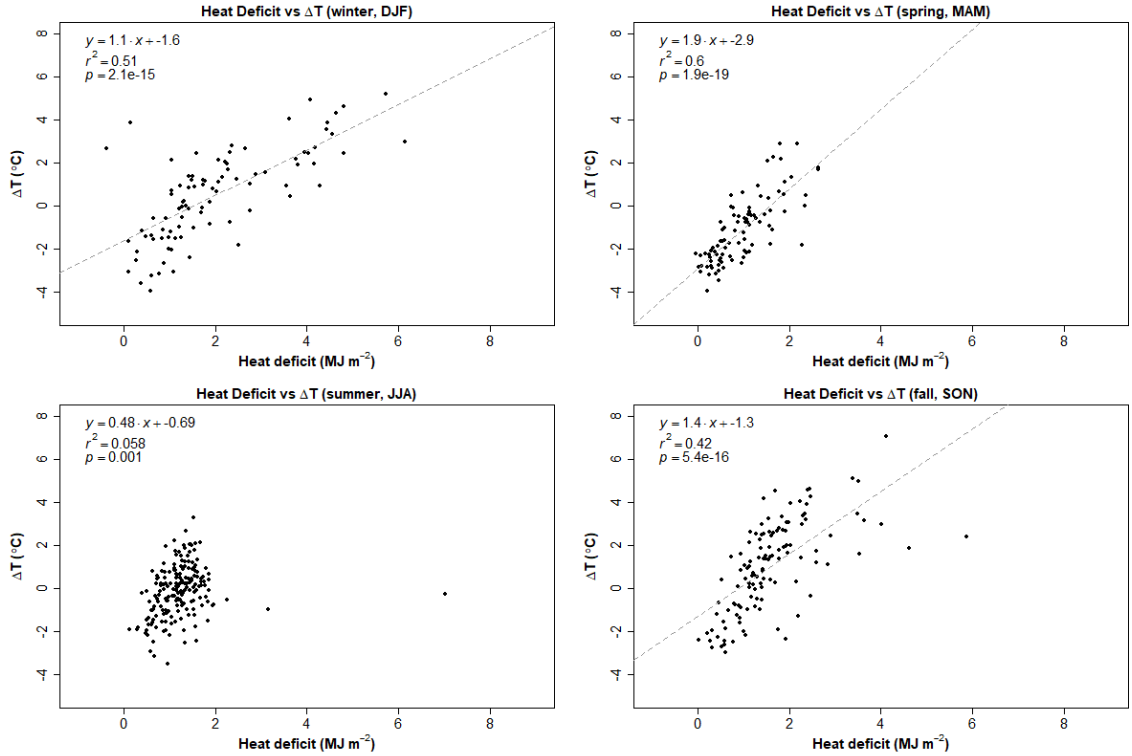

Figure 3: Total heat deficit (MJ m^{-2}) and vertical temperature differences (ΔT, ºC) from Western Regional Climate Center Stations (ΔT = T_{GALE}-T_{FARM}) for winter (DJF), spring (MAM), summer (JJA), and fall (SON) in Reno, NV, USA from June 2014 to October 2015.

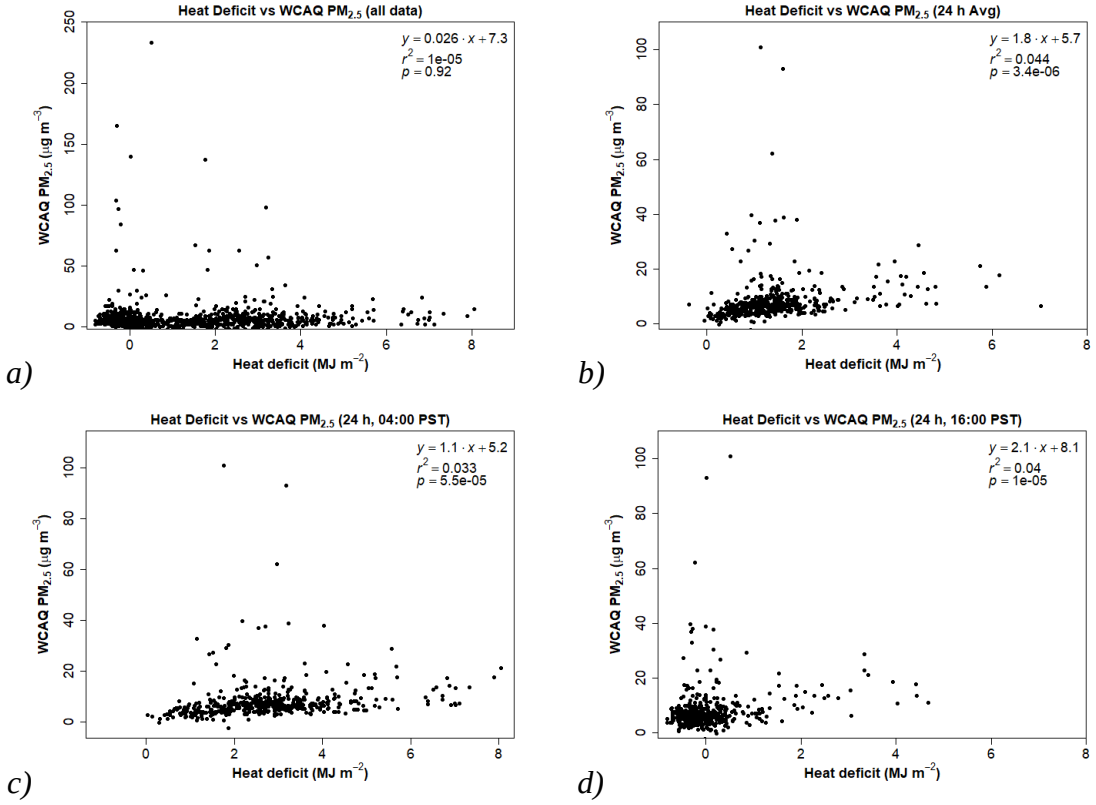

Figure 4: Heat deficit (MJ m^{-2}) and WCAQ $PM_{2.5}$ (µg m^{-3}) for a) all data, b) 24 h average data, c) morning (04:00 PST) heat deficit and 24 h $PM_{2.5}$ data, and d) afternoon (16:00 PST) heat deficit and 24 h $PM_{2.5}$ data in Reno, NV, USA from June 2014 to October 2015.

No Fire

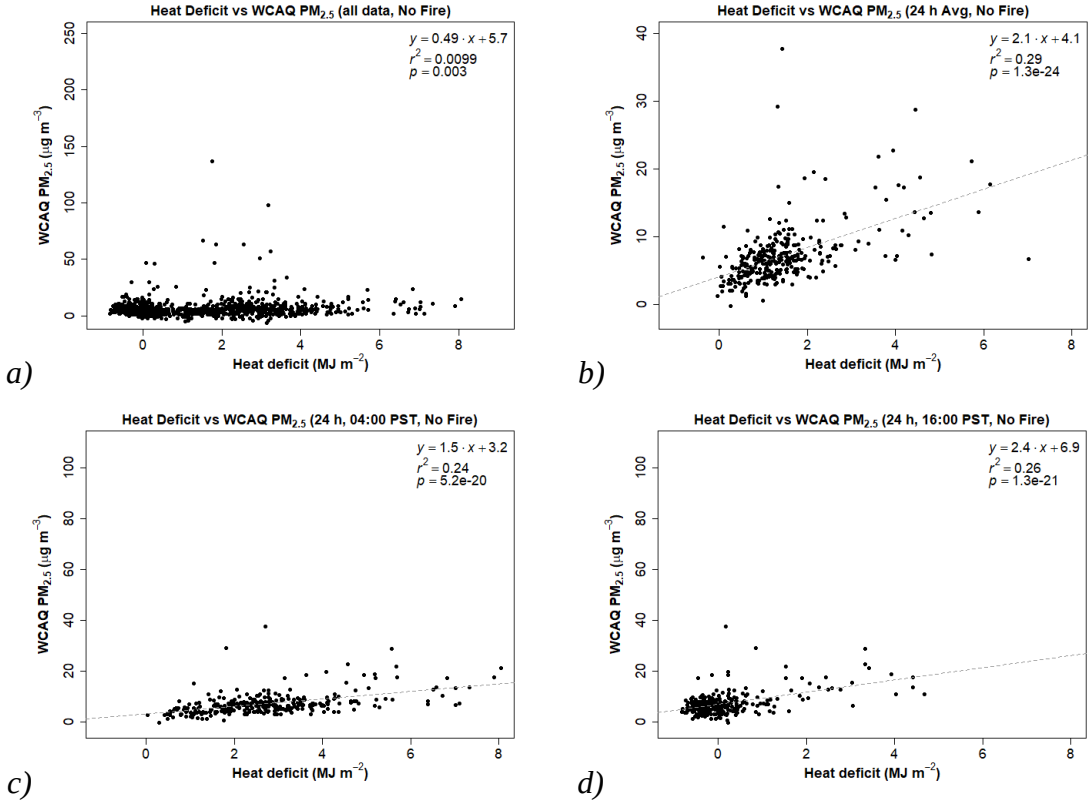

Figure 5: Heat deficit (MJ m^{-2}) and WCAQ $PM_{2.5}$ (µg m^{-3}) with fire flagged data removed for a) all data, b) 24 h average data, c) morning (04:00 PST) heat deficit and 24 h $PM_{2.5}$ data, and d) afternoon (16:00 PST) heat deficit and 24 h $PM_{2.5}$ data in Reno, NV, USA from June 2014 to October 2015.

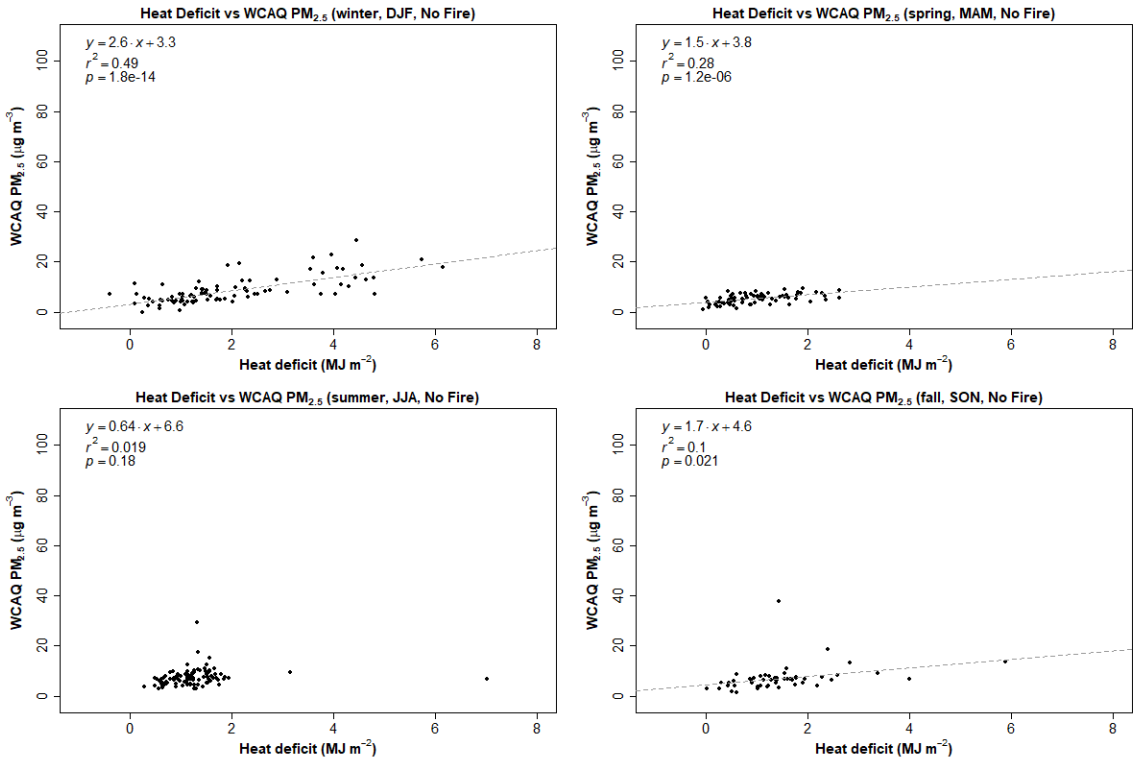

Figure 6: Total heat deficit (MJ m^{-2}) and 24 h WCAQ $PM_{2.5}$ (µg m^{-3}) with fire flagged data removed for winter (DJF), spring (MAM), summer (JJA), and fall (SON) in Reno, NV, USA from June 2014 to October 2015.

Vertical structure

		PBLH	AOH
Winter	Median	0.75 (n = 87)	NA
	range	0.010 to 2.8	NA
Spring	Median	1.7 (n = 90)	1.8 (n = 3)
	range	0.31 to 3.5	1.6 to 5.2
Summer	Median	2.5 (n = 183)	3.8 (n = 113)
	range	0.031 to 4.8	0.64 to 9.7
Fall	Median	1.9 (n = 122)	2.4 (n = 63)
	range	0.31 to 5.7	0.25 to 10

Table 5: Median, number (n), and range of data for planetary boundary layer height (PBLH, km) and apparent optical height (AOH, km) separated by winter (DJF, no AOH data), spring (MAM), summer (JJA), and fall (SON) in Reno, NV, USA from June 2014 to October 2015.

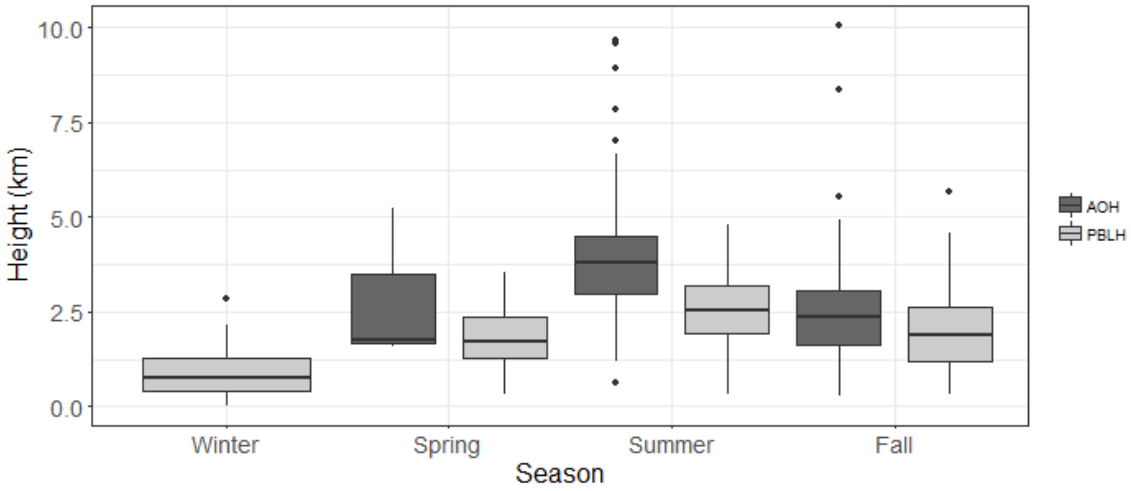

Figure 7: Box and whisker plot of planetary boundary layer height (PBLH, light grey) and apparent optical height (AOH, dark grey) for winter (DJF, no AOH data), spring (MAM), summer (JJA), and fall (SON) in Reno, NV, USA from June 2014 to October 2015.

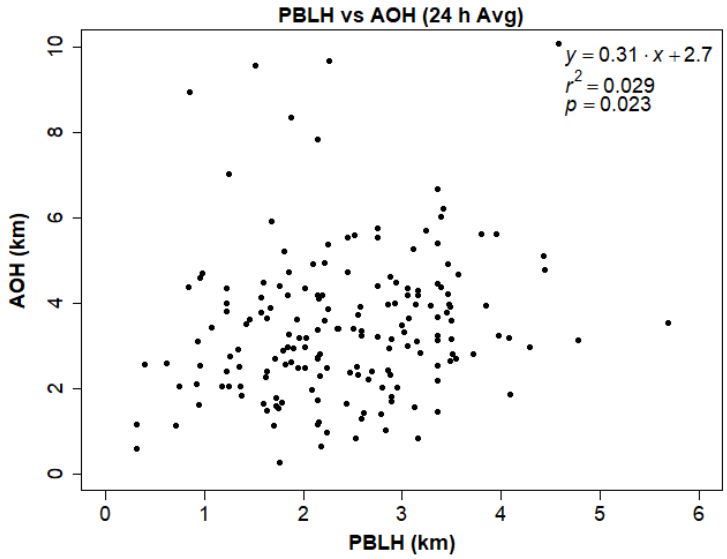

Figure 8: Planetary boundary layer height (PBLH, km) and apparent optical height (AOH, km) 24 h average data for Reno, NV, USA from June 2014 to October 2015.

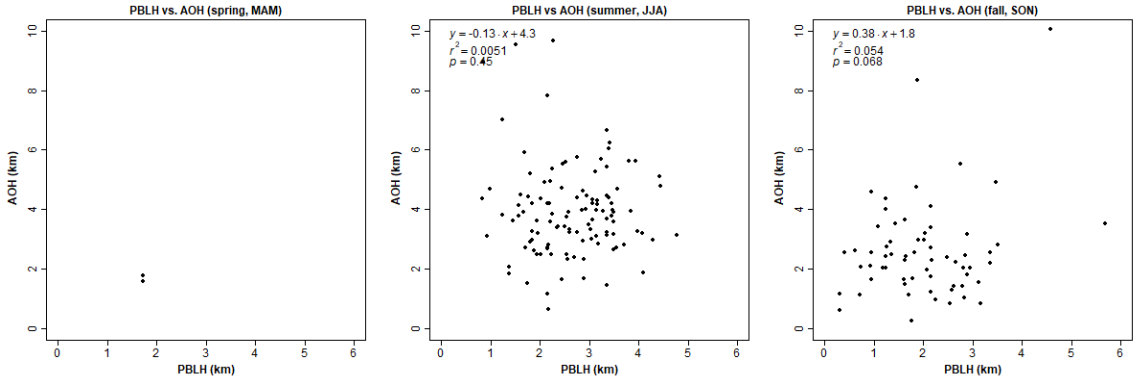

Figure 9: Planetary boundary layer height (PBLH, km) and apparent optical height (AOH, km) for spring (MAM), summer (JJA), and fall (SON) in Reno, NV, USA from June 2014 to October 2015. No winter data available.

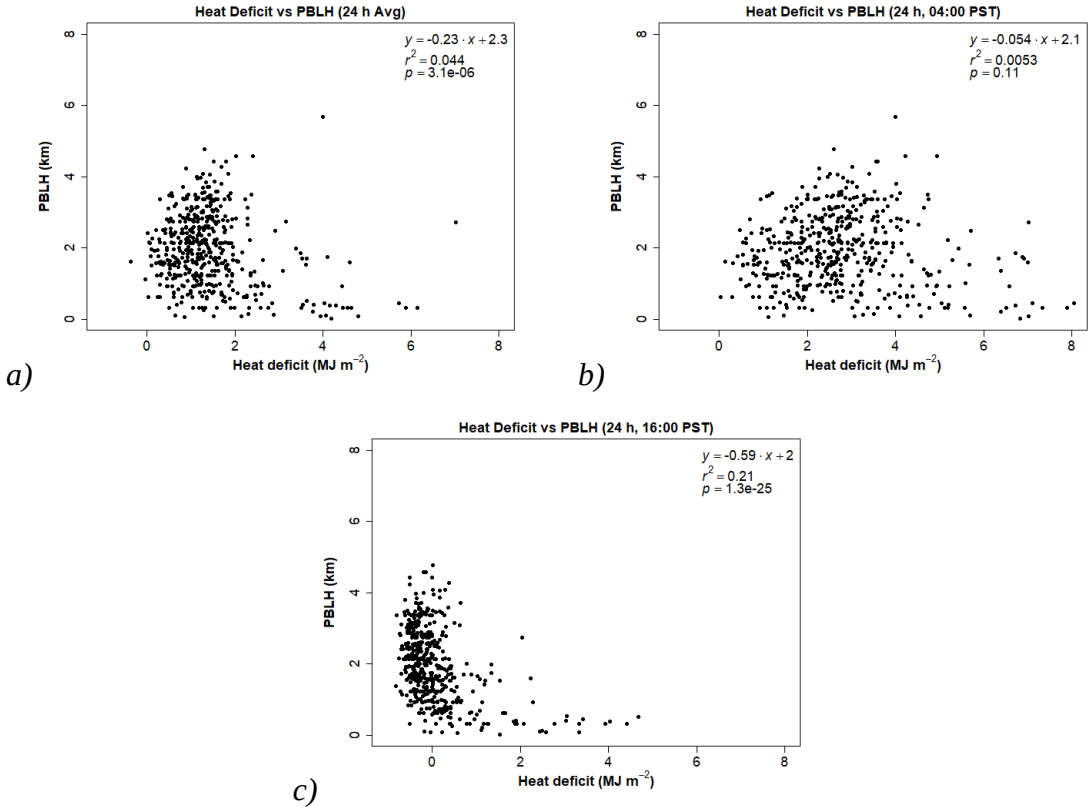

Figure 10: Heat deficit (HD, MJ m^{-2}) and planetary boundary layer height (PBLH, km) for a) 24 h average, b) morning HD (04:00 PST), and c) afternoon HD (16:00 PST) data for Reno, NV, USA from June 2014 to October 2015.

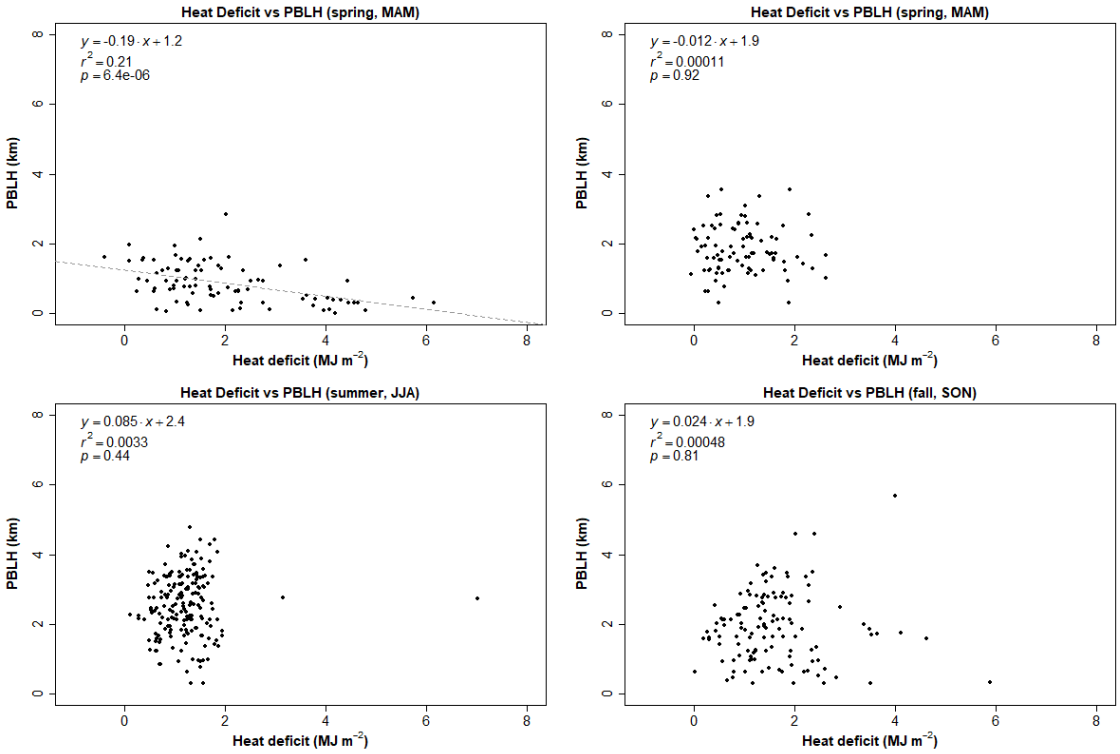

Figure 11: Heat deficit (HD, MJ m^{-2}) and planetary boundary layer height (PBLH, km) for winter (DJF), spring (MAM), summer (JJA), and fall (SON) in Reno, NV, USA from June 2014 to October 2015.

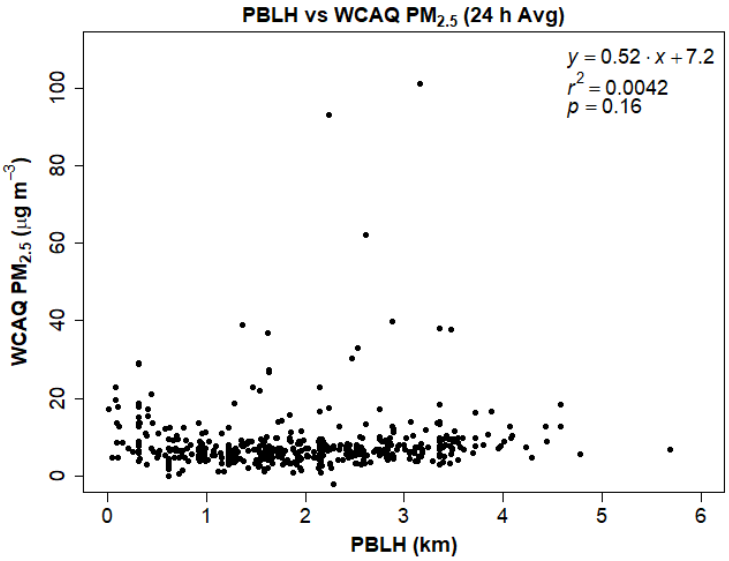

Figure 12: Planetary boundary layer height (PBLH, km) and WCAQ $PM_{2.5}$ (µg m^{-3}) for 24 h average data from Reno, NV, USA from June 2014 to October 2015.

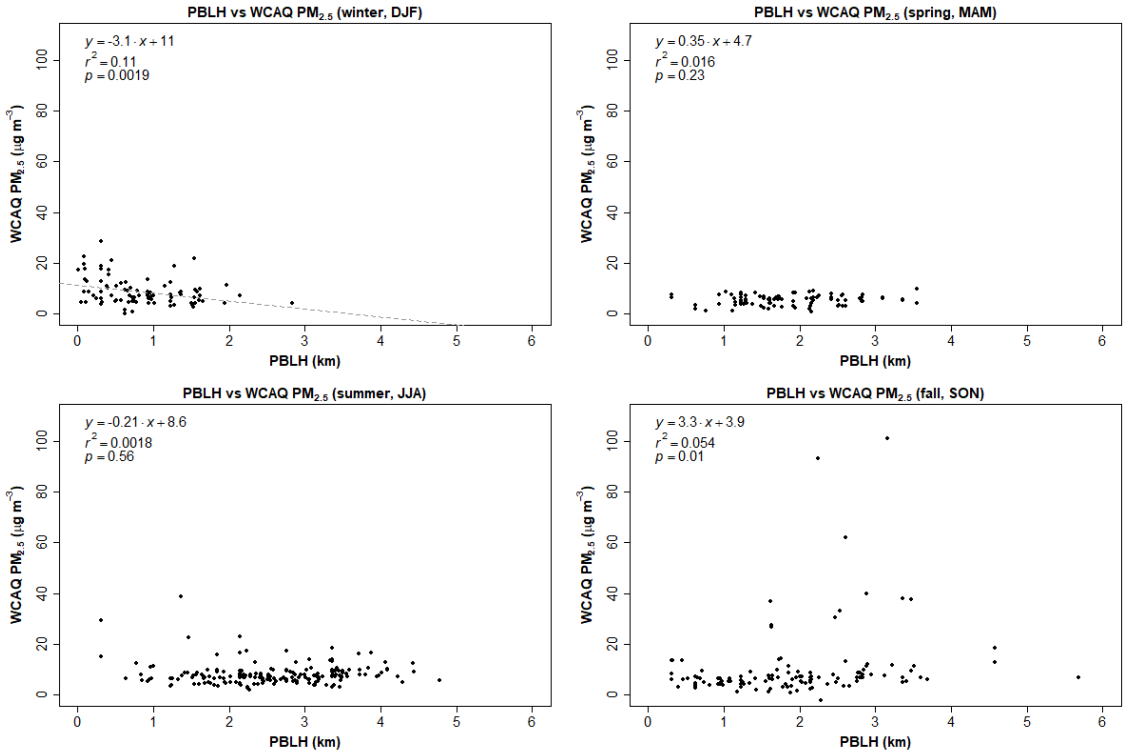

Figure 13: Planetary boundary layer height (PBLH, km) and WCAQ $PM_{2.5}$ (µg m^{-3}) for winter (DJF), spring (MAM), summer (JJA), and fall (SON) in Reno, NV, USA from June 2014 to October 2015.

Statistical analysis

Evaluation of the quadrant method using 24 h data

	WCAQ 24 h data (n=308)				WCAQ 1 h data (n=2122)			
	Q2 (n=34)		Q3 (n=50)		Q2 (n=25)		Q3 (n=59)	
	mean +/- std	median	mean +/- std	median	mean +/- std	median	mean +/- std	median
AEE (440-870 nm):	1.5±0.27	1.4	1.7±0.31	1.7	1.6±0.27	1.6	1.8±0.29	1.8
τ_{ext} (440 nm):	0.073±0.026	0.067	0.29±0.19	0.24	0.076±0.042	0.055	0.74±0.46	0.64
AOH (km):	1.9±1.3	1.6	3.6±1.8	3.6	0.77±1.1	0.43	2.4±2.3	2.1
Coarse mode:	0.29±0.11	0.3	0.15±0.13	0.11	0.29±0.12	0.25	0.054±0.082	0.032
Delta T (°C):	1.9±2.3	1.4	0.79±1.4	0.68	2.9±3.0	3	-0.55±1.9	-0.55
Fine mode:	0.71±0.11	0.7	0.85±0.13	0.89	0.71±0.12	0.75	0.95±0.082	0.97
Fire filter:	32%		72%		32%		46%	
O_3 (ppb):	24±18	26	44±8.0	45	22±20	11	54±17	55
PM (µg m^{-3}):	12±4.9	10	19±19	13	34±11	29	70±54	47
RH (%):	42±12	46	30±8.6	27	34±11	35	26±12	25
Temperature (°C):	13±10	11	24±3.1	25	15±10	12	26±4.8	26
Temp inversion (% of days):	79%		66%		84%		31%	
Temp inversion (strong, % of days):	29%		6%		16%		0%	
Wind speed (m s^{-1}):	1.1±0.27	1.1	1.2±0.22	1.1	0.88±1.1	0.51	1.5±1.0	1.2
	Q1 (n=198)		Q4 (n=26)		Q1 (n=1871)		Q4 (n=167)	
	mean +/- std	median	mean +/- std	median	mean +/- std	median	mean +/- std	median
AEE (440-870 nm):	1.4±0.35	1.1	1.4±0.32	1.4	1.4±0.34	1.4	1.7±0.32	1.8
τ_{ext} (440 nm):	0.064±0.027	0.062	0.14±0.022	0.13	0.078±0.041	0.07	0.38±0.30	0.28
AOH (km):	4.2±1.9	3.5	6.0±2.9	5.6	3.7±2.9	2.9	4.7±2.7	4.4
Coarse mode:	0.31±0.13	0.3	0.27±0.13	0.26	0.28±0.15	0.27	0.090±0.14	0.039
Delta T (°C):	0.018±1.7	-0.13	-0.57±1.2	-0.64	-0.61±2.1	-0.82	0.36±1.8	0.09
Fine mode:	0.69±0.12	0.7	0.73±0.13	0.74	0.72±0.15	0.73	0.91±0.14	0.96
Fire filter:	37%		31%		18%		47%	
O_3 (ppb):	38±10	40	42±6.5	42	44±15	46	49±17	51
PM (µg m^{-3}):	5.1±1.8	5.3	6.6±1.2	6.9	7.8±5.3	7	15±5.2	15
RH (%):	34±13	31	34±9.8	32	26±14	24	23±15	19
Temperature (°C):	17±6.8	19	19±5.0	21	21±7.9	22	26±6.2	27
Temp inversion (% of days):	48%		27%		31%		52%	
Temp inversion (strong, % of days):	2%		0%		2%		2%	
Wind speed (m s^{-1}):	1.4±0.39	1.3	1.3±0.28	1.3	1.4±1.0	0.98	0.96±0.74	0.72

Table 6: 24 h data (τ_{ext}: 0.12, $PM_{2.5}$: 8.4 µg m^{-3}, n=308) and 1 h data (τ_{ext}: 0.2, $PM_{2.5}$: 25 µg m^{-3}, n=370) for WCAQ. Mean ± one standard deviation and median.

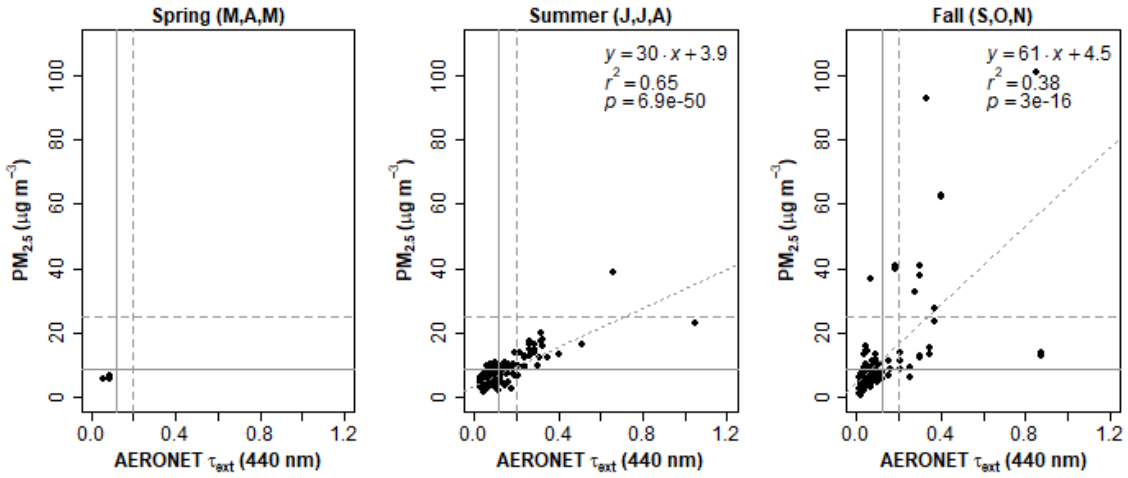

Figure 14: Scatter plot of seasonal AERONET τ_{ext} and $PM_{2.5}$ (µg m^{-3}) UNRG and WCAQ data for spring (March, April, May), summer (June, July, August), and fall (September, October, November). There was no data available in winter (December, January, February) and limited data in spring. Solid grey lines indicate τ_{ext}: 0.12 and $PM_{2.5}$: 8.8 µg m^{-3}, dashed grey lines indicate τ_{ext}: 0.2 and $PM_{2.5}$: 25 µg m^{-3}, dotted grey line is the fit line.

N=356	Q2 (n=29)		Q3 (n=64)	
	mean ± std	median	mean ± std	median
AEE (440-870 nm)	1.6±0.29	1.7	1.7±0.27	1.8
τ_{ext} (440 nm)	0.073±0.027	0.077	0.30±0.19	0.26
AOH (km)	2.0±1.3	1.8	3.9±2.1	3.7
Coarse mode fraction	0.24±0.11	0.23	0.12±0.11	0.082
Delta T (°C)	1.6±1.9	1.3	1.0±1.4	0.9
Fine mode fraction	0.76±0.11	0.77	0.88±0.11	0.92
fire flag (% of days)	62%		83%	
Heat Deficit (04:00 PST, total, MJ m^{-2})	3.7±1.4	3.2	2.9±0.77	2.9
Heat Deficit (avg, total, MJ m^{-2})	1.9±0.97	1.6	1.4±0.40	1.1
Max 1 h O_3 (ppb)	47±17	52	62±13	65
MDA8 O_3 (ppb)	40±18	46	55±11	57
O_3 (ppb)	26±15	30	39±10	40
PBLH (km)	2.1±1.1	1.8	2.9±0.79	2.9
$PM_{2.5}$ (µg m^{-3})	12±5.2	10	20±18	13
RH (%)	42±13	37	31±9.2	30
Temperature (°C)	16±8.4	21	24±2.7	24
Temp inversion (% of days)	86%		73%	
Temp inversion (% of days, strong)	10%		8%	
Wind speed (m s^{-1})	1.1±0.55	1.1	1.3±0.40	1.2
	Q1 (n=231)		Q4 (n=32)	
	mean ± std	median	mean ± std	median
AEE (440-870 nm)	1.5±0.37	1.5	1.5±0.21	1.5
τ_{ext} (440 nm)	0.063±0.028	0.059	0.14±0.031	0.13
AOH (km)	4.0±2.2	3.5	5.2±2.7	4.5
Coarse mode fraction	0.27±0.12	0.25	0.21±0.086	0.2
Delta T (°C)	0.41±1.6	0.3	0.037±1.4	-0.41
Fine mode fraction	0.73±0.12	0.75	0.79±0.086	0.8
fire flag (% of days)	53%		44%	
Heat Deficit (04:00 PST, total, MJ m^{-2})	2.7±1.1	2.7	2.5±0.81	2.4
Heat Deficit (avg, total, MJ m^{-2})	1.2±0.58	1.2	1.2±0.44	1.2
Max 1 h O_3 (ppb)	54±11	53	60±9.7	62
MDA8 O_3 (ppb)	49±10	48	54±8.8	55
O_3 (ppb)	35±10	35	39±9.1	41
PBLH (km)	2.2±0.81	2.2	2.8±0.86	3.0
$PM_{2.5}$ (µg m^{-3})	5.7±1.6	5.9	6.8±1.5	7.1
RH (%)	33±12	31	35±9.5	32
Temperature (°C)	20±4.8	22	23±3.2	24
Temp inversion (% of days)	58%		41%	
Temp inversion (% of days, strong)	3%		3%	
Wind speed (m s^{-1})	1.6±0.64	1.4	1.5±0.41	1.4

$PM_{2.5}$ (µg m^{-3})
8.8

0.12
AERONET τ_{ext} (440 nm)

Table 7: Mean ± standard deviation and median for 24 h combined data at UNRG and WCAQ June 2014 to October 2015 (n=356).

UNRG/WCAQ AOH	Q2 (n=44)	Q3 (n=44)
Mean±Std	2.0±1.3	3.9±2.1
25th, 50th, 75th	0.94, 1.8, 2.9	2.8, 3.7, 4.4
Range	0.25-5.8	0.83-10
	Q1 (n=268)	Q4 (n=39)
Mean±Std	4.0±2.2	5.2±2.7
25th, 50th, 75th	2.5, 3.5, 4.9	3.4, 4.5, 6.6
Range	0.59-12	1.2-12

Table 8: Summary statistics for AOH (km) for 24 h combined data at UNRG and WCAQ from June 2014 to October 2015.

PEAV $PM_{2.5}$	Q2 (n=8)	Q3 (n=17)
Mean±Std	2.9±2.6	12±8.9
25th, 50th, 75th	0.80, 1.9, 5.9	6.0, 11, 13
Range	0.0-6.2	3.1-42
	Q1 (n=62)	Q4 (n=7)
Mean±Std	3.8±1.9	4.7±1.3
25th, 50th, 75th	2.0, 3.8, 5.2	3.9, 4.3, 6.0
Range	0.70-8.0	3.1-6.9

Table 9: Summary statistics for $PM_{2.5}$ ($\mu g\ m^{-3}$) for 24 h data at PEAV from June 2014 to November 2014 separated by the valley quadrants.

Quadrant 2 (Q2): Stable conditions, shallow PBLH, and local pollutants

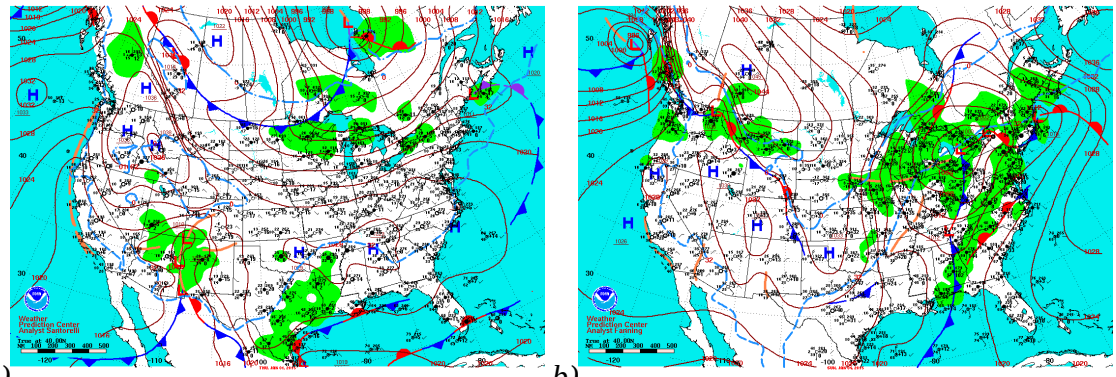

a) *b)*

Figure 15: Surface weather maps from NOAA for a) January 1, 2015 and b) January 4, 2015.

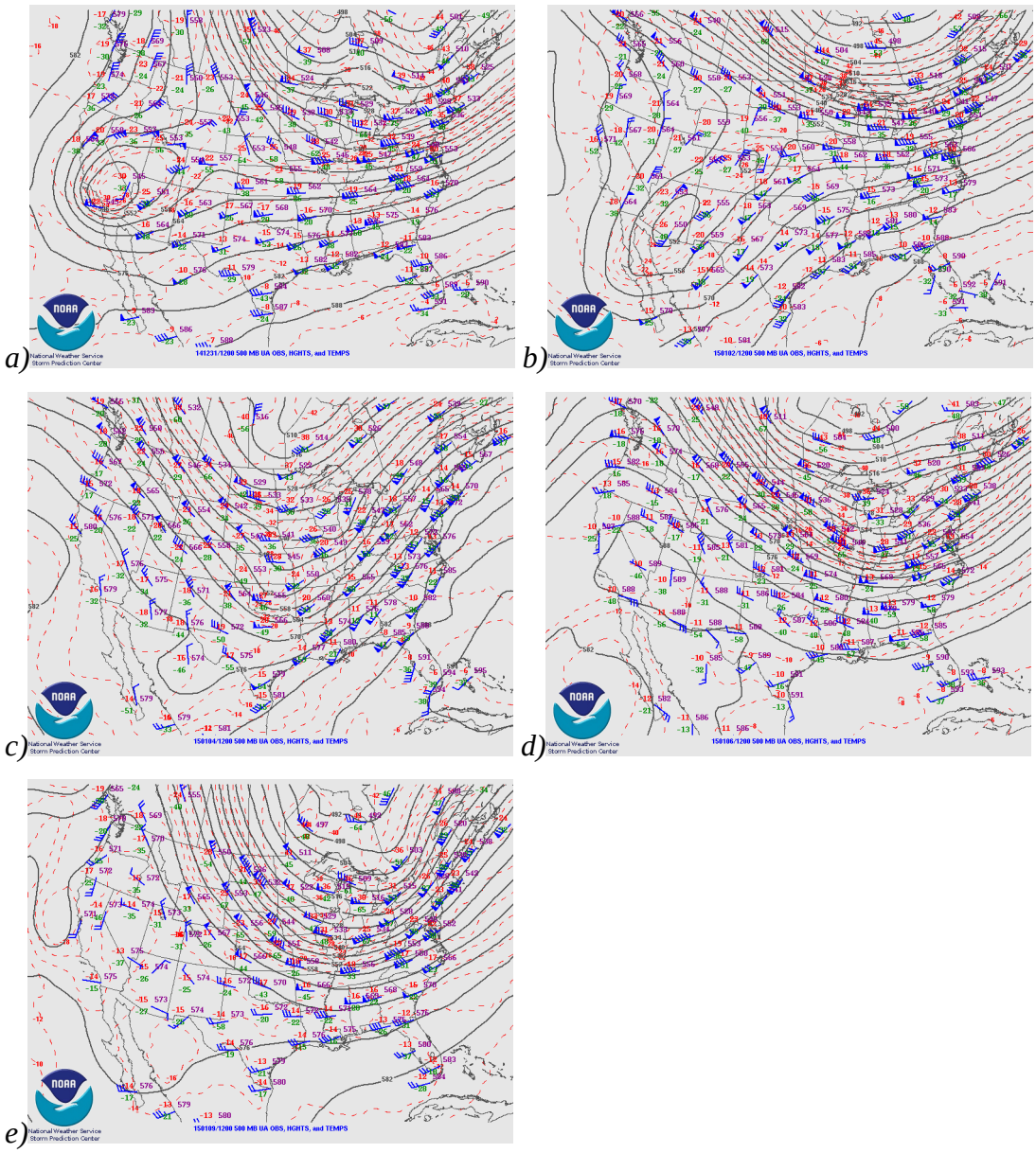

Figure 16: 500 millibar weather maps from NOAA for a) December 31, 2014 (04:00 PST), b) January 2, 2015 (04:00 PST), c) January 4, 2015 (04:00 PST), d) January 6, 2015 (04:00 PST), and e) January 9, 2015 (04:00 PST).

Quadrant 3 (Q3): transport and mixing of smoke plumes

September 2014

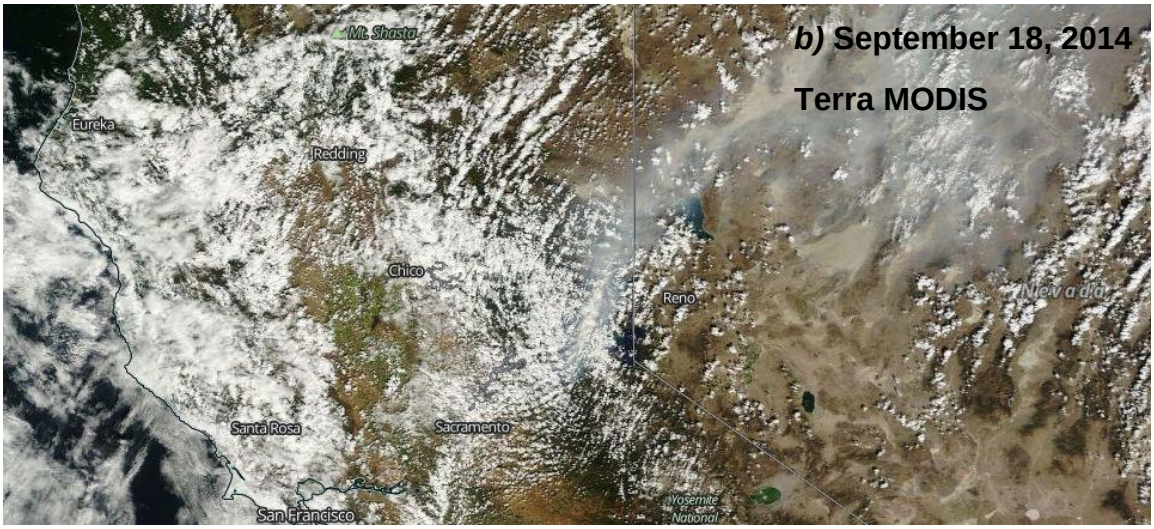

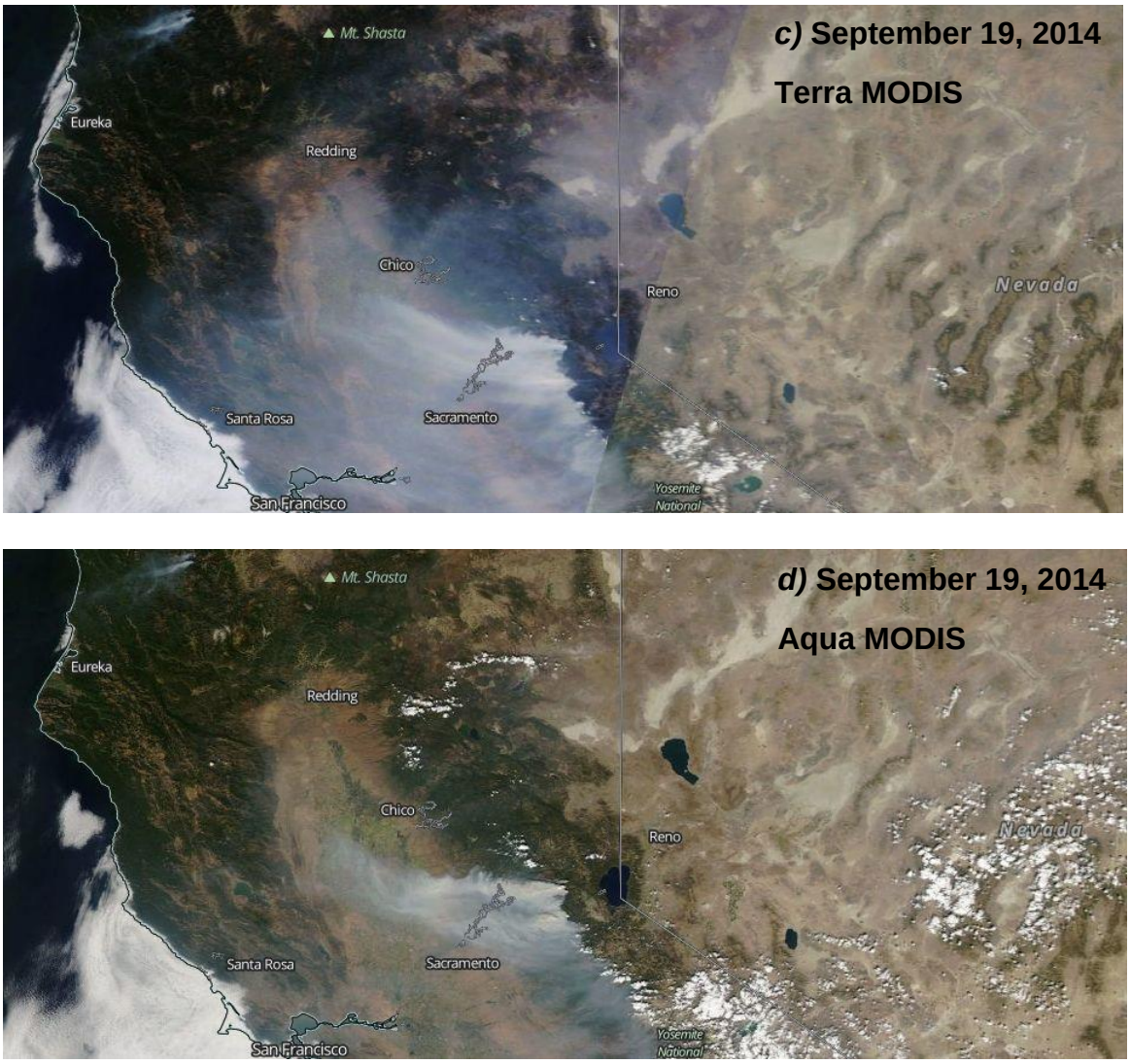

Figure 17: MODIS visible product for a) September 17, 2014 Terra (morning) overpass, b) September 18 Terra (morning) overpass, c) September 19, 2014 Terra (morning) overpass, and c) September 19, 2014 Aqua (afternoon) overpass.

	September 18 to September 19				September 19	
	Decrease	**Increase**	**Similar**	**Quadrant**	**AOH vs PBLH**	**Fire flag?**
Truckee Meadows	τ_{ext}, coarse mode, PBLH, HD	fine mode, ΔT, AOH, AEE			AOH>> PBLH	yes
UNRG[a]	WS, O_3, max 1 h O_3, MDA8 O_3, CO, SO_2	NO_x, NO, pressure	Temp, RH	NA to Q3		
WCAQ	$PM_{2.5}$, WS, O_3, max 1 h O_3, MDA8 O_3,, CO, SO_2	NO_x, NO	Temp, RH	Q3 to Q3		
PEAV[a]	RH, WS, O_3, max 1 h O_3, MDA8 O_3, CO	Temp, pressure				

Table 10: Trends at each site and in the Truckee Meadows valley for September 19, 2014 compared to the previous day. Grey parameters indicate variables not measured at all three sites.

[a]*$PM_{2.5}$ data is missing for the previous day for PEAV and UNRG.*

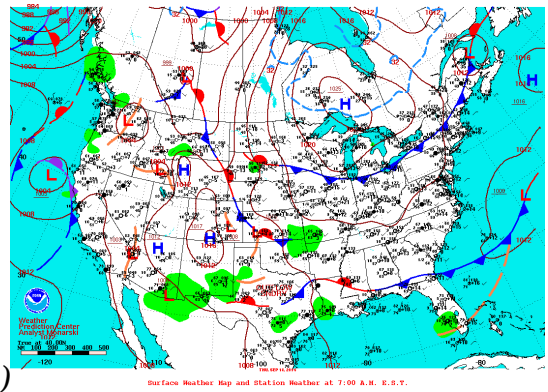

a)

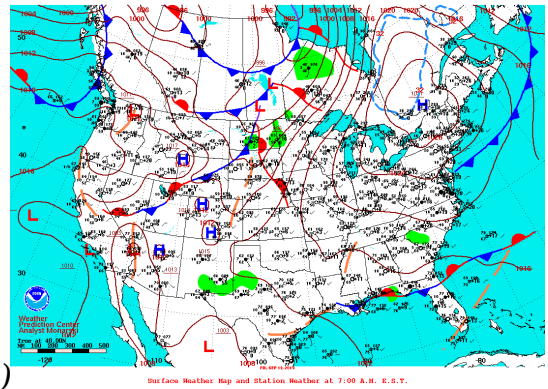

b)

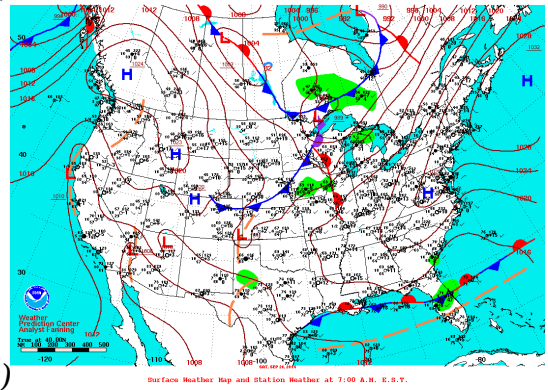

c)

Figure 18: Surface weather maps from NOAA for a) September 18, 2014, b) September 19, 2014, and c) September 20, 2014

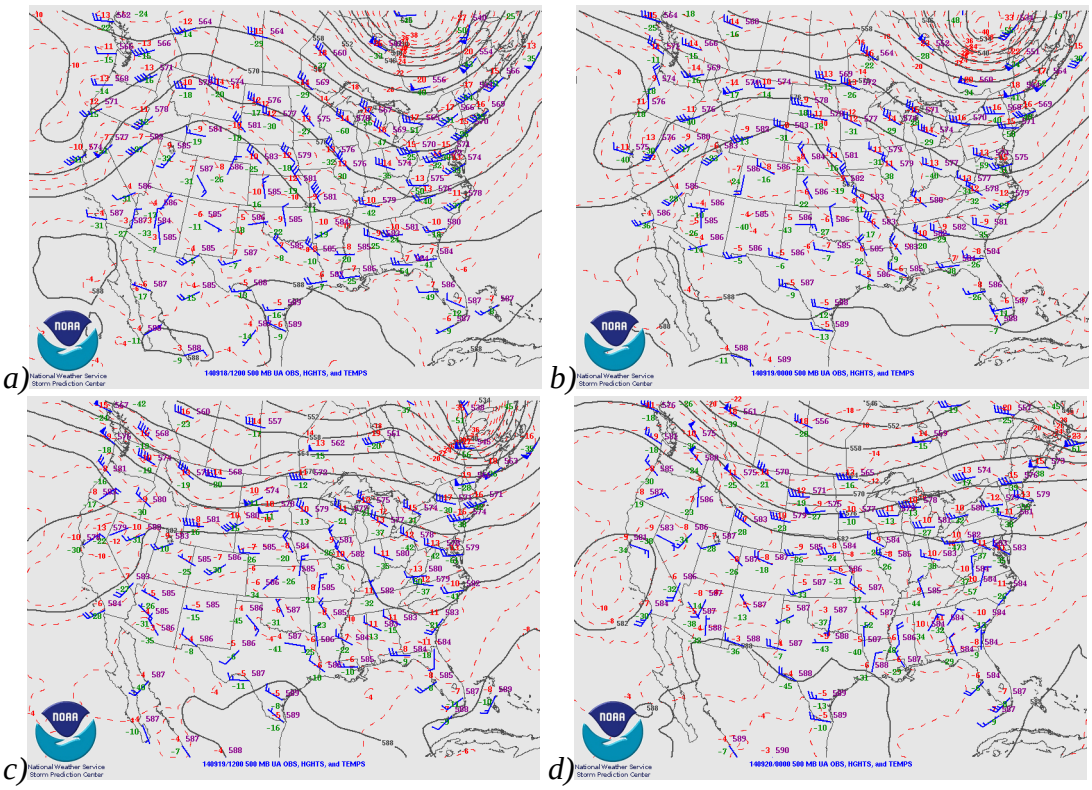

Figure 19: 500 millibar weather maps from NOAA for a) September 18, 2014 (04:00 PST), b) September 18, 2014 (16:00 PST), c) September 19, 2014 (04:00 PST), and d) September 19, 2014 (16:00 PST).

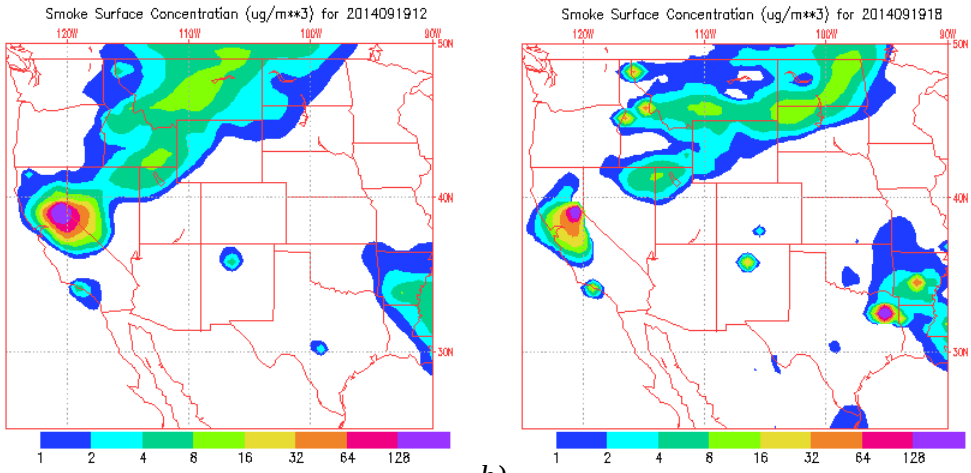

a)

b)

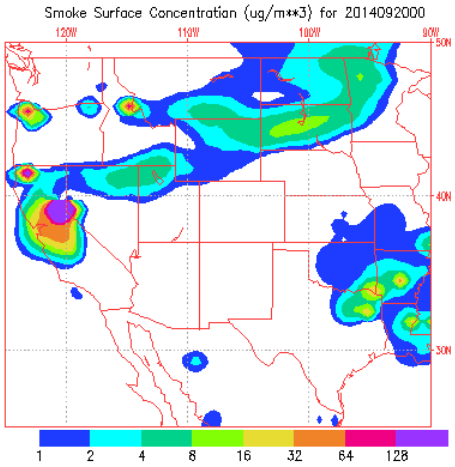

c)

Figure 20: Naval Research Laboratory Aerosol Analysis and Prediction System (NRL NAAPS, https://www.nrlmry.navy.mil/aerosol/) smoke surface for a) September 19, 2014 (04:00 PST), b) September 19, 2014 (10:00 PST), and c) September 19, 2014 (16:00 PST).

Quadrant 4 (Q4): Pollution aloft

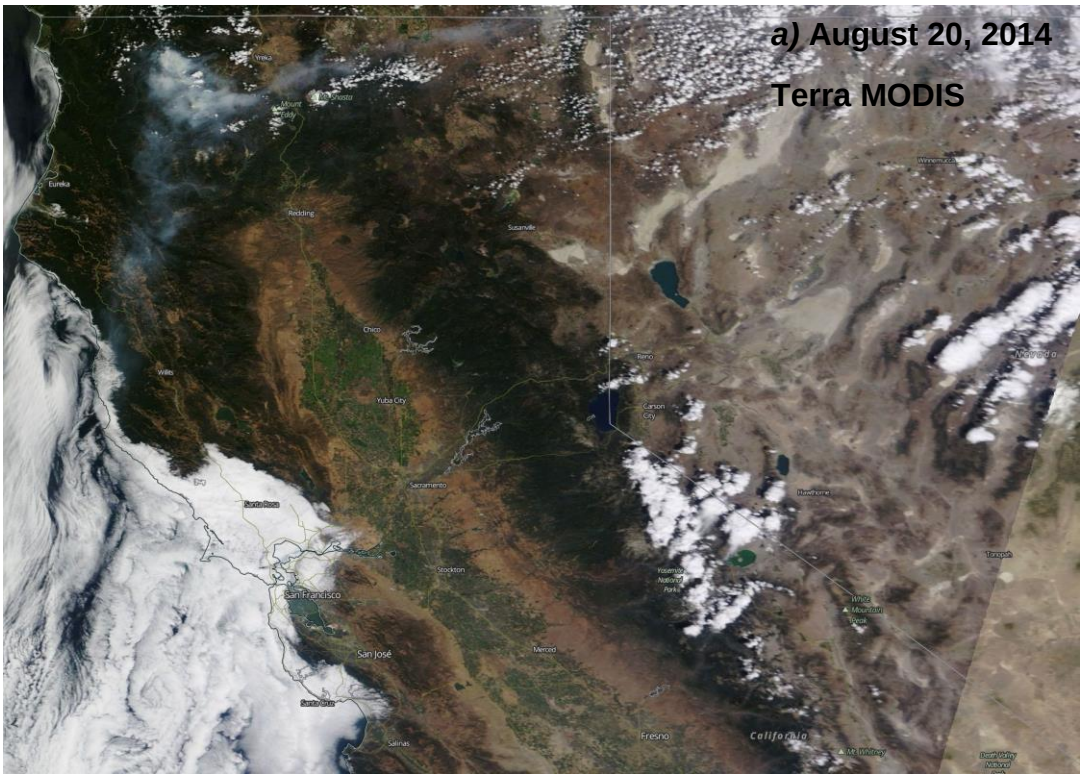

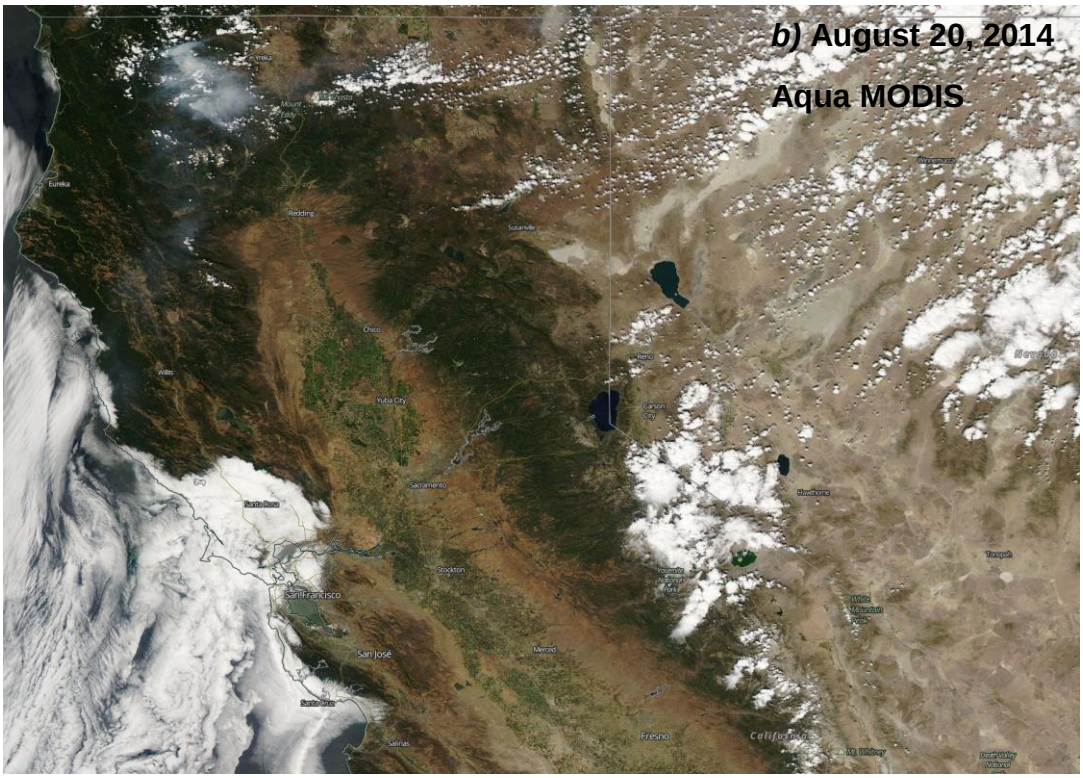

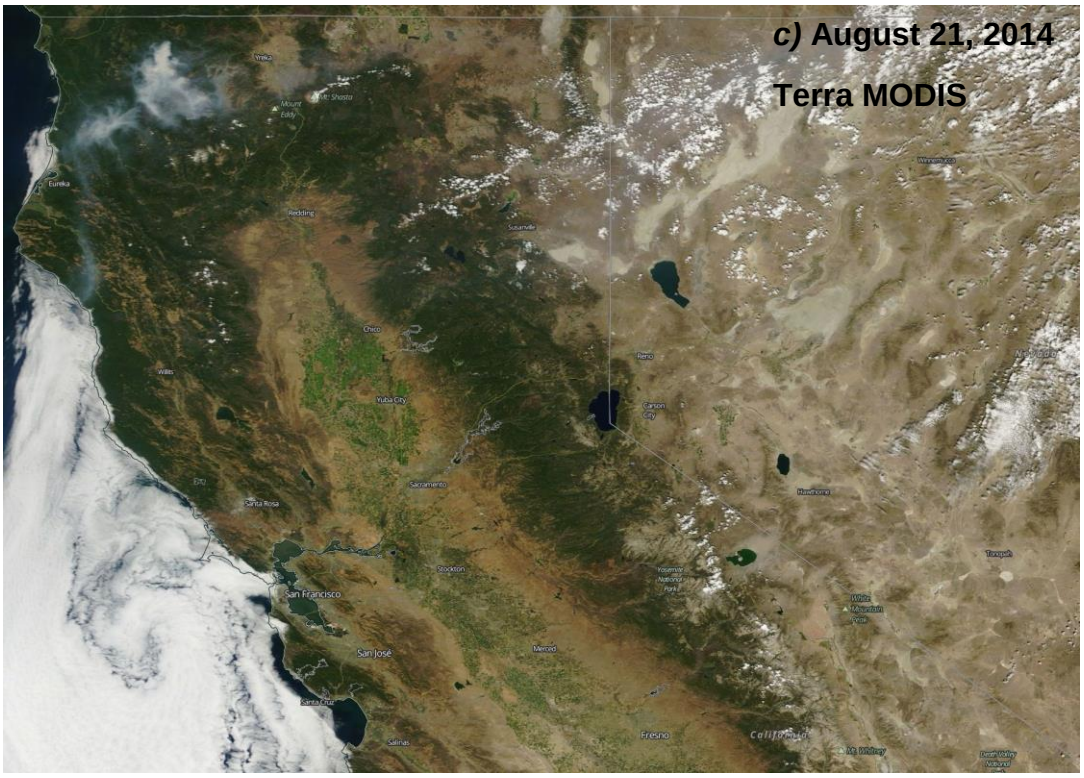
c) August 21, 2014
Terra MODIS
Eureka
Redding
Susanville
Chico
Reno
Yuba City
Carson City
Sacramento
Santa Rosa
Stockton
San Francisco
San José
Merced
Santa Cruz
Salinas
Fresno
Yosemite National Park
Hawthorne
Tonopah

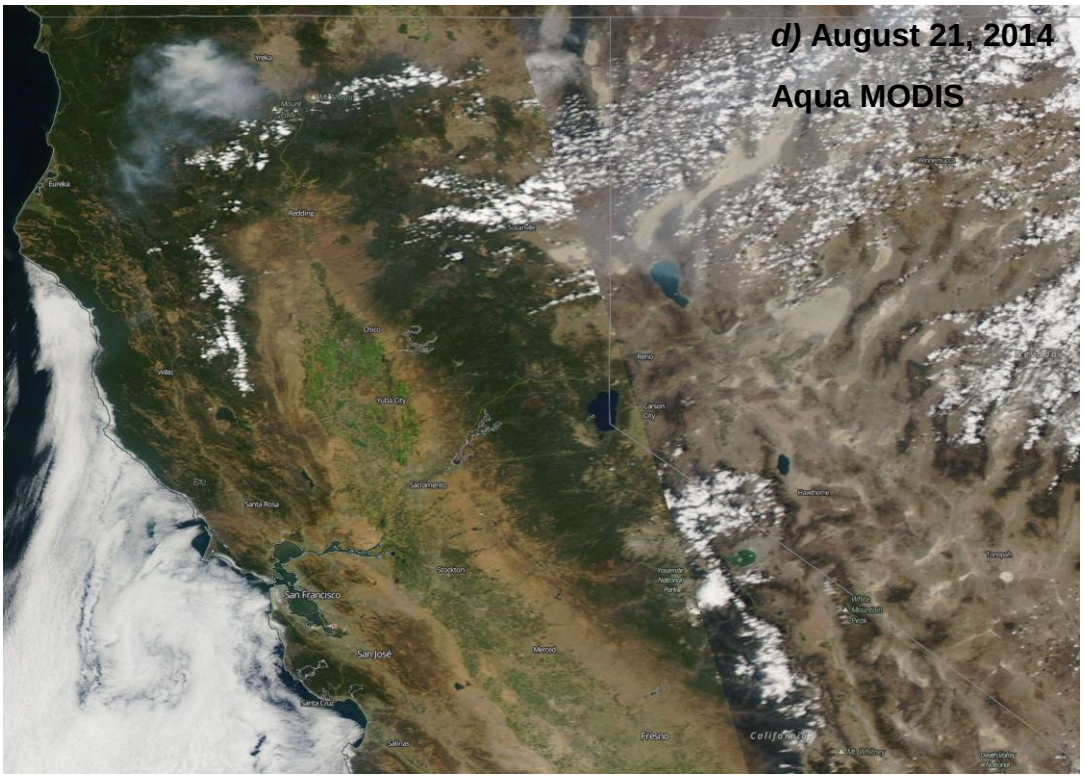
d) August 21, 2014
Aqua MODIS
Eureka
Redding
Susanville
Chico
Reno
Yuba City
Carson City
Sacramento
Santa Rosa
Stockton
San Francisco
San José
Merced
Santa Cruz
Salinas
Fresno
Yosemite National Park
Hawthorne
Tonopah

Figure 21: MODIS visible product for a) August 20, 2014 Terra (morning) overpass, b) August 20, 2014 Agua (afternoon) overpass, c) August 21, 2014 Terra (morning) overpass, and c) August 21, 2014 Aqua (afternoon) overpass.

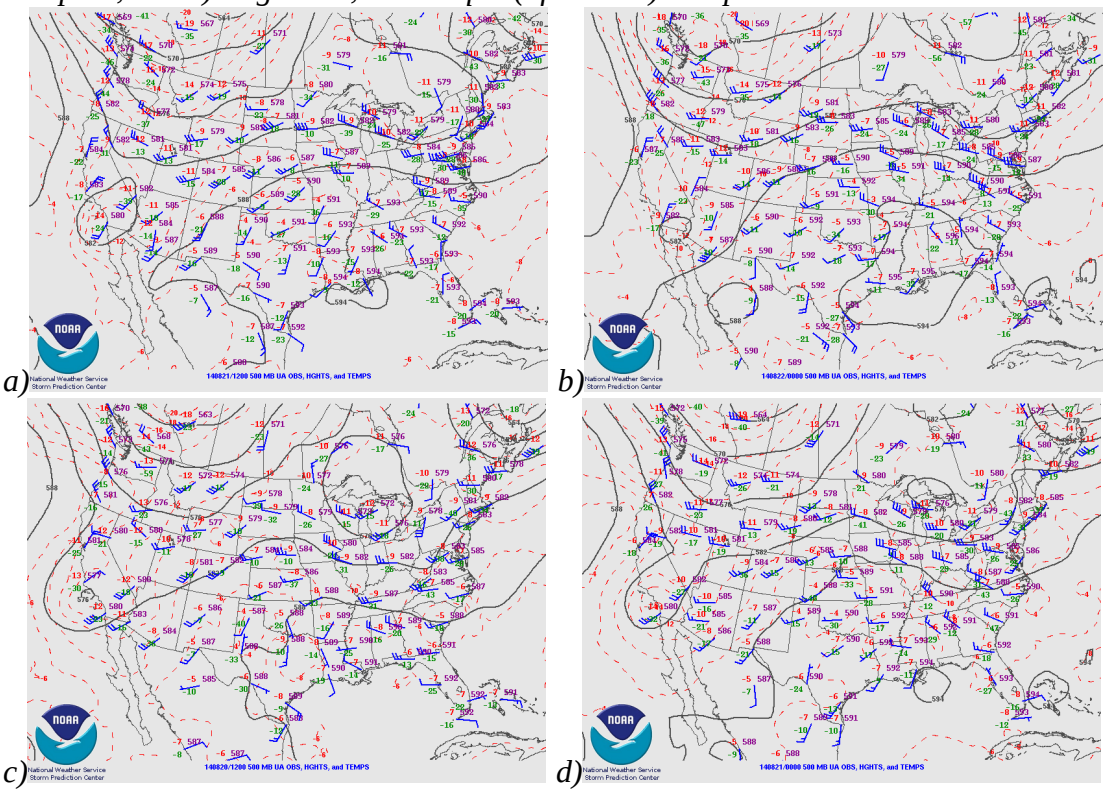

Figure 22: 500 millibar weather maps from NOAA for a) August 20, 2014 (04:00 PST), b) August 20, 2014 (16:00 PST), c) August 21, 2014 (04:00 PST), and d) August 21, 2014 (16:00 PST).

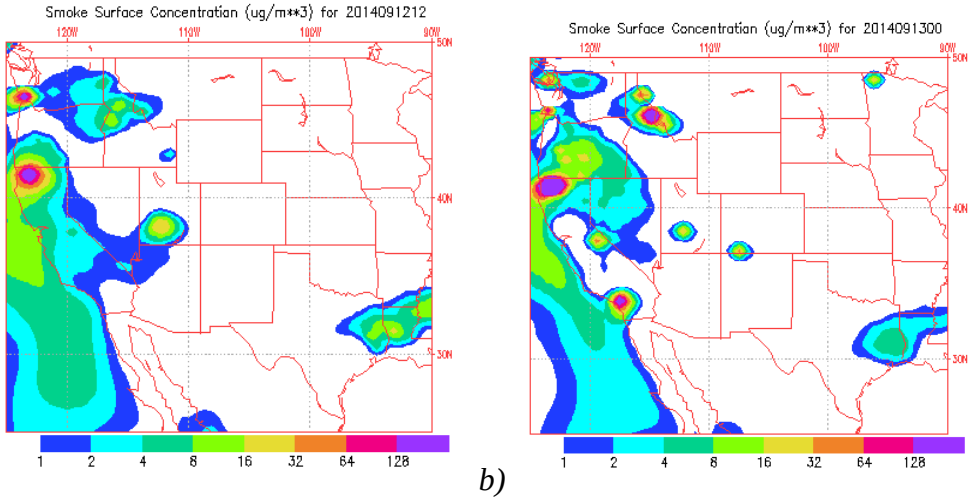

Figure 23: Naval Research Laboratory Aerosol Analysis and Prediction System (NRL NAAPS, https://www.nrlmry.navy.mil/aerosol/) smoke surface for a) August 12, 2014 (04:00 PST) and b) August 12, 2014 (16:00 PST).

References

Batterman S. The Near-Road Ambient Monitoring Network and Exposure Estimates for Health Studies. EM (Pittsburgh, Pa.) 2013; 2013: 24-30.

EPA. Near-road NO2 Monitoring. 2017, 2016.

Green MC, Chow JC, Watson JG, Dick K, Inouye D. Effects of Snow Cover and Atmospheric Stability on Winter PM2.5 Concentrations in Western U.S. Valleys. Journal of Applied Meteorology and Climatology 2015; 54: 1191-1201.

Hao H., Chang H. H., Holmes H.A., Mulholland J. A., Klein M., Darrow L. A., et al. Air pollution and preterm birth in the U.S. state of Georgia (2002–2006): associations with concentrations of 11 ambient air pollutants estimated by combining Community Multiscale Air Quality Model (CMAQ) simulations with stationary monitor measurements. Environmental Health Perspectives 2016; 124: 875–880.

HEI HEI. Traffic-related air pollution: A Critical review of the literature on emissions, exposure, and health effects, Boston, MA, 2010.

Whiteman CD, Bian X, Zhong S. Wintertime Evolution of the Temperature Inversion in the Colorado Plateau Basin. Journal of Applied Meteorology 1999; 38: 1103-1117.

WHO WHO. Urban Population Growth. 2017, 2017.